U.S.NRC
United States Nuclear Regulatory Commission
Protecting People and the Environment

NUREG/CR-7281
ORNL/SPR-2020/1572

Radiation Evaluation Methodology for Concrete Structures

Office of Nuclear Regulatory Research

AVAILABILITY OF REFERENCE MATERIALS IN NRC PUBLICATIONS

NRC Reference Material

As of November 1999, you may electronically access NUREG-series publications and other NRC records at the NRC's Library at www.nrc.gov/reading-rm.html. Publicly released records include, to name a few, NUREG-series publications; *Federal Register* notices; applicant, licensee, and vendor documents and correspondence; NRC correspondence and internal memoranda; bulletins and information notices; inspection and investigative reports; licensee event reports; and Commission papers and their attachments.

NRC publications in the NUREG series, NRC regulations, and Title 10, "Energy," in the *Code of Federal Regulations* may also be purchased from one of these two sources:

1. **The Superintendent of Documents**
   U.S. Government Publishing Office
   Washington, DC 20402-0001
   Internet: www.bookstore.gpo.gov
   Telephone: (202) 512-1800
   Fax: (202) 512-2104

2. **The National Technical Information Service**
   5301 Shawnee Road
   Alexandria, VA 22312-0002
   Internet: www.ntis.gov
   1-800-553-6847 or, locally, (703) 605-6000

A single copy of each NRC draft report for comment is available free, to the extent of supply, upon written request as follows:

Address: **U.S. Nuclear Regulatory Commission**
Office of Administration
Digital Communications and Administrative Services Branch
Washington, DC 20555-0001
E-mail: distribution.resource@nrc.gov
Facsimile: (301) 415-2289

Some publications in the NUREG series that are posted at the NRC's Web site address www.nrc.gov/reading-rm/doc-collections/nuregs are updated periodically and may differ from the last printed version. Although references to material found on a Web site bear the date the material was accessed, the material available on the date cited may subsequently be removed from the site.

Non-NRC Reference Material

Documents available from public and special technical libraries include all open literature items, such as books, journal articles, transactions, *Federal Register* notices, Federal and State legislation, and congressional reports. Such documents as theses, dissertations, foreign reports and translations, and non-NRC conference proceedings may be purchased from their sponsoring organization.

Copies of industry codes and standards used in a substantive manner in the NRC regulatory process are maintained at—

The NRC Technical Library
Two White Flint North
11545 Rockville Pike
Rockville, MD 20852-2738

These standards are available in the library for reference use by the public. Codes and standards are usually copyrighted and may be purchased from the originating organization or, if they are American National Standards, from—

American National Standards Institute
11 West 42nd Street
New York, NY 10036-8002
Internet: www.ansi.org
(212) 642-4900

Legally binding regulatory requirements are stated only in laws; NRC regulations; licenses, including technical specifications; or orders, not in NUREG-series publications. The views expressed in contractor prepared publications in this series are not necessarily those of the NRC.

The NUREG series comprises (1) technical and administrative reports and books prepared by the staff (NUREG–XXXX) or agency contractors (NUREG/CR–XXXX), (2) proceedings of conferences (NUREG/CP–XXXX), (3) reports resulting from international agreements (NUREG/IA–XXXX),(4) brochures (NUREG/BR–XXXX), and (5) compilations of legal decisions and orders of the Commission and the Atomic and Safety Licensing Boards and of Directors' decisions under Section 2.206 of the NRC's regulations (NUREG–0750).

NUREG/CR-7281
ORNL/SPR-2020/1572

U.S.NRC
United States Nuclear Regulatory Commission
Protecting People and the Environment

Radiation Evaluation Methodology for Concrete Structures

Manuscript Completed: December 2020
Date Published: July 2021

Prepared by:
J. Risner
A. Alpan
J. Yang (formerly with ORNL)

Oak Ridge National Laboratory
Oak Ridge, TN 37831-6283

Madhumita Sircar, NRC Project Manager

Office of Nuclear Regulatory Research

ABSTRACT

The ability to accurately calculate neutron fluence levels, radiation heating rates (neutron and gamma), and gamma dose rates in the concrete biological shields (bioshields) of light water reactors has become increasingly important as plant life extensions of 60 years have become common and extensions to 80 years of operation are proceeding This study evaluates the impact of concrete composition, the size and location of reinforcing steel, the presence of a bioshield liner or reflective thermal insulation, and the size of the reactor cavity gap on neutron flux, total heating rate (the rate of radiation energy deposition), and gamma dose rate using parametric studies with a representative three-loop pressurized water reactor (PWR) model. The analyses are performed using state-of-the-art hybrid radiation transport calculations, which provide the ability to explicitly model complex geometries and eliminate the discretization effects in space, energy, and angle that are present in the commonly used discrete ordinates transport methodology. The results of these analyses provide insights into the effect of material and geometrical variations in the representative PWR model on the magnitude of the neutron flux, heating rate, and gamma dose rate incident to the bioshield as well as their attenuation through the reinforced concrete structure.

TABLE OF CONTENTS

LIST OF FIGURES

LIST OF TABLES

EXECUTIVE SUMMARY

In October 2014 the U.S. Nuclear Regulatory Commission (NRC) published the Expanded Materials Degradation Assessment (EMDA) Report as NUREG/CR-7153. Volume 4 of the EMDA, "Aging of Concrete and Civil Structures", identified radiation effects on concrete as a technical area needing further research and having a high structural significance for concrete structures in the vicinity of the reactor vessel. This is a particular area of concern due to the extension of plant licensing from 60 to 80 years by subsequent license renewals (SLRs).

A thorough assessment of radiation effects in concrete requires not only materials science research into the radiation damage effects caused by exposure to neutron and gamma radiation, but also accurate methods for predicting the neutron and gamma radiation fields in the concrete and in associated steel components including reinforcing steel (rebar) and embedded support columns.

This evaluation reviews methodologies available for radiation transport calculations in light water reactor (LWR) shielding analyses and provides recommendations on appropriate methods for evaluating radiation fields in the concrete structures around the reactor pressure vessel (RPV) at locations within and outside the traditional beltline region. Sensitivity analyses using a representative three-loop pressurized water reactor (PWR) model provide insights into the effects of key parameters on the radiation quantities of interest, including neutron flux, gamma dose rates, and total (neutron plus gamma) heat generation rates[1].

Radiation Transport Methodology

Previous analyses of neutron and gamma radiation levels in concrete biological shields (bioshields) have relied primarily on discrete ordinates calculations and have focused on the traditional beltline region (i.e., elevations within the axial extent of the active fuel). In discrete ordinates calculations the solution of the Boltzmann radiation transport equation requires discretization of the spatial, energy, and angular variables for the particle flux. Regulatory Guide 1.190 provides guidance on appropriate selection of spatial, angular, and energy discretization for RPV fluence applications within the traditional beltline region; however, there is no regulatory guidance for bioshield fluence calculations either within or outside of the traditional beltline region.

Monte Carlo calculations inherently provide higher-fidelity solutions than discrete ordinates calculations, as they do not require the discretization in energy, space, and angle that is imposed by all discrete ordinates radiation transport codes. Because of this, Monte Carlo simulations are generally considered to be the most accurate method for radiation transport calculations. The primary limitation in the use of Monte Carlo radiation transport calculations for LWR shielding applications has historically been the amount of computer time required to obtain a well-converged solution (i.e., a solution with acceptable relative errors), particularly for deep penetration shielding calculations such as those encountered in predictions of neutron and gamma radiation fields in the bioshield and associated steel structures.

With the advent of the hybrid radiation transport methodology, Monte Carlo calculations can provide well-converged solutions with substantial reductions (often orders of magnitude) in computational time. In this study hybrid radiation transport calculations were applied to obtain

[1] Throughout this report the terms 'heat generation rate' and 'heating rate' refer to the rate at which energy from ionizing radiation is deposited in a material on a volumetric basis (e.g., W/cm^3). See Section 9 for a glossary of terms used in this report.

high-fidelity predictions of neutron fluxes for a range of energies, total heat generation rates, and gamma dose rates in the concrete, reinforcing steel (rebar), and RPV support columns in a three-loop pressurized water reactor (PWR) model.

Parametric Studies

Parametric studies were conducted to assess the sensitivity of the radiation quantities of interest to variations in the following parameters.

1) Concrete composition
   It is well known that the attenuation of neutrons in concrete is strongly dependent on the hydrogen content of the concrete. In this study we consider four types of concrete, with hydrogen contents ranging from 0.00484 to 0.029 g/cm^3. The hydrogen content affects not only the attenuation of neutrons in the concrete, but also the location and magnitude of the maximum heating rate and gamma dose rate.

2) Size and location of reinforcing steel (rebar)
   The primary radiation damage mechanism caused by the presence of rebar (as well as other steel, such as the embedded support columns in the current three-loop model) is the production of gamma radiation due to radiative capture of neutrons in the steel. These 'capture gamma' sources become the dominant contributor to the total heating rate and the gamma dose rate at a relatively short distance into the bioshield. The effect of rebar is considered in this analysis for two different rebar sizes (#8 and #14). The #8 rebar is modeled with a 3-inch concrete cover. The #14 rebar is modeled with a 3-inch concrete cover and also with a 10-inch concrete cover.

3) Presence of a steel bioshield liner
   Some bioshields include a steel liner on the inner radial surface (i.e., the surface adjacent to the cavity gap). The effect of a 0.25-inch steel liner was evaluated for both carbon steel and stainless steel compositions.

4) Presence of reflective thermal insulation in the cavity gap
   The effect of reflective thermal insulation in the cavity gap was assessed by including a 3-inch layer of reflective thermal insulation near the RPV.

5) Cavity gap width
   The effect of changes in the cavity gap width (i.e., the distance between the outer edge of the RPV and the inner edge of the bioshield) was evaluated using three models with gap widths 13, 71, and 120 cm. These values are expected to cover the range of gap widths in two-loop and three-loop plants.

ACKNOWLEDGEMENTS

The work described in this report was sponsored by the U.S. Nuclear Regulatory Commission (NRC), Office of Nuclear Regulatory Research (RES). The authors thank Madhumita Sircar for her support and guidance as the NRC project manager. Her knowledge on the subject of irradiated concrete and insightful comments were invaluable to the success of this project and report. Marcus Rolon also contributed to this project as the alternate Contracting Officer's Representative (COR). A number of NRC staff contributed constructive comments on draft versions of this report and provided helpful insights and suggestions during project review meetings. Among those, special thanks are due to Jose Pires, Jay Wallace, Jinsuo Nie, Andrew Prinaris, George Thomas, Huan Li, and Ben Parks.

ABBREVIATIONS AND ACRONYMS

1D	one-dimensional
2D	two-dimensional
3D	three-dimensional
ADAMS	Agencywide Documents Access and Management System
ANL	Argonne National Laboratory
ANS	American Nuclear Society
ANSI	American National Standards Institute
BWR	boiling water reactor
CE	continuous energy
dpa	displacements per atom
EMDA	Expanded Materials Degradation Assessment
EVND	Ex-vessel neutron dosimetry
LWR	light water reactor
MG	multigroup
NPP	nuclear power plant
NRC	United States Nuclear Regulatory Commission
ORNL	Oak Ridge National Laboratory
PNNL	Pacific Northwest National Laboratory
PWR	pressurized water reactor
RCCA	rod cluster control assembly
RPV	reactor pressure vessel
SLR	Subsequent License Renewal
TWE	TransWare Enterprises
UFSAR	Updated Final Safety Analysis Report
U.S.	United States
Voxel	volume element
w/c	water-to-cement ratio

1 INTRODUCTION

Nuclear power plants (NPPs) in the United States (U.S.) were initially licensed to operate for 40 years. As of May 2020, 94 units (88 operating NPPs) have been approved for 60-year licenses [1], and 4 units (4 operating NPPs) have been approved for 80-year licenses. Two NPP units have scheduled submittals in 2020, and three have scheduled submittals in 2021 [2].

In 2008, the U.S. Nuclear Regulatory Commission (NRC) initiated discussions on the topic of radiation effects on concrete with the national and international research communities and other stakeholders to address potential issues related to Subsequent License Renewal (SLR) applications. NRC-sponsored research at Oak Ridge National Laboratory (ORNL) reviewed the effects of radiation on the microstructure and properties of concrete used in NPPs to assess the state of knowledge and identify areas for further investigations during 2010–2013 [3]. In October 2014 the NRC published the Expanded Materials Degradation Assessment (EMDA) Report as NUREG/CR-7153. Volume 4 of NUREG/CR-7153, “Aging of Concrete and Civil Structures” [4], identified radiation effects on concrete as a technical area needing further research and having a high structural significance for concrete structures in the vicinity of the reactor vessel during the subsequent period of extended operation from 60 to 80 years. Based on this assessment and the Office of Nuclear Reactor Regulation (NRR) User Need Request for Research on the Effects of Irradiation on Concrete Structures, the Office of Nuclear Regulatory Research (RES) initiated a research activity to confirm the effects of irradiation on the noted concrete structures and the structural implications of these effects to support SLR applications.

Having neutron and gamma radiation measurements for the concrete biological shield (bioshield) is important in validating computational solutions in the analysis of irradiation effects. Ex-vessel neutron dosimetry (EVND) [5] that is commonly used for validation of reactor pressure vessel (RPV) neutron fluences would provide validation of neutron fluences calculated on the inner surface of the bioshield, but would not provide any information on neutron flux, radiation heating levels, and gamma dose rates within the bioshield. NPP-specific EVND data is generally not readily available in the public domain with the exception of the H. B. Robinson Unit 2 Cycle 9 RPV benchmark [6], [7]. Gamma dosimetry for the bioshield and measurements that provide information on the attenuation of neutron and gamma radiation within the bioshield are typically not available for operating NPPs.

Enveloping neutron fluences for neutron energies greater than 0.1 MeV ($E > 0.1$ MeV) have been determined on the bioshield inner radial surface considering 27 two-loop, 13 three-loop, and 28 four-loop pressurized water reactors (PWRs) and 35 boiling water reactors (BWRs) at 80 years of plant operation [8]. Maximum gamma doses at the concrete inner radial surface for two-loop and three-loop Westinghouse plants and a Mark 6 BWR are also provided in [8]. The analyses concluded that two-loop and three-loop NPPs provided the limiting neutron fluences ($E > 0.1$ MeV) on the bioshield inner surface. A two-loop Westinghouse plant provided the limiting gamma dose on the inner radial surface of the bioshield. The gamma dose for a three-loop Westinghouse plant was slightly lower (~2%) than that for the two-loop Westinghouse plant. Comparisons of neutron and gamma fluxes and heat generation rates in the bioshield of a Westinghouse two-loop PWR and a Westinghouse three-loop PWR are also available in [10]. Those results suggest the two-loop design is more limiting with respect to fluxes and heating rates in the bioshield, but, unlike the data reported in [8], they include only a single plant of each type. Based on the review of all the data in [8] and [9], a three-loop Westinghouse design NPP was selected for the current analysis. For the RPV support modeling in the current study, the Category 4A short-column-type support described in [9] was used. Modeling this support configuration provides the ability to assess the effect of large and complex embedded steel structures on

neutron flux, gamma dose rates, and total radiation heating rates within those structure and in the surrounding concrete.

The objective of the research described in this report is to apply rigorous computational approaches to provide an analysis of neutron fluxes, total (neutron + gamma) heat generation rates, and gamma dose rates through the bioshield as well as in the RPV support structures embedded in or attached to concrete and the included reinforcing steel bars (rebar). These studies provide insight on the spatial distribution of neutron fluxes, total heat generation rates, and gamma dose rates from the inner radial surface of the bioshield structure to a specified depth within the bioshield. These results will provide the necessary input for the calculation of radiation-induced concrete damage as well as the development of temperature profiles through the bioshield.

2 RADIATION PARAMETERS OF INTEREST FOR THIS STUDY

The radiation parameters of interest with regard to irradiation-induced concrete damage are neutron fluence and neutron and gamma dose and heat generation rates. Each of these radiation effects are discussed in the following sections.

2.1 Neutron Radiation

Analysis of legacy data for mechanical properties of irradiated concrete by Hilsdorf et al. [11] indicated that, for some concretes, a neutron fluence level of 1.0E+19 n/cm^2 may cause a reduction in compressive and tensile strengths and modulus of elasticity, and a marked increase in volume of the aggregates. Research conducted by Hilsdorf et al. on the effect of neutron radiation on concrete strength provided no specification of a neutron energy cutoff value associated with the 1×10^{19} n/cm^2 fluence value. Hilsdorf et al. presented neutron radiation–related test results under energy categories of "slow neutrons," "fast neutrons," and "no information." Kontani et al. [12] used a reference neutron fluence value of 1.0E+20 n/cm^2 for assessing the reduction of concrete strength using Hilsdorf et al.'s compilation of test data but also indicated that several concrete samples and test conditions (fluence levels and temperatures) used in that paper were not representative of light water reactor (LWR) concrete compositions and conditions. Removing test data that were not representative of LWR concrete compositions and conditions (fluence levels and temperatures) resulted in an unclear conclusion about the trend in the decrease of concrete strength as a function of neutron irradiation. Fujiwara et al. [13] performed irradiation tests with temperatures lower than 65°C and a maximum neutron fluence (E > 0.1 MeV) of 1.2E+19 n/cm^2. They concluded that neutron exposure does not significantly affect the compressive strength of concrete within the range of fluences considered in that study. In [8], test results by Fujiwara et al. were combined with another data point from Dubrovskii et al. [14] for a fast neutron fluence (E > 0.1 MeV) of 2.3E+19 n/cm^2. In [8], the new compressive strength plot as a function of fast neutron fluence (E > 0.1 MeV) using data from Fujiwara and Dubrovskii et al. was judged to be reliable and consistent.

Field et al. [15] evaluated the neutron flux spectrum in the bioshield of a three-loop PWR model using different energy cutoffs (E < 0.41 eV, E > 0.0 MeV,[2] E > 0.1 MeV, and E > 1.0 MeV). They also determined estimates of the neutron fluence at 40, 60, and 80 years of operation for two-loop and three-loop PWRs using energy cutoffs of E > 0.0 MeV, E > 0.1 MeV, and E > 1.0 MeV. Field et al. compared these estimated fluences with the suggested threshold fluence of 1E+19 n/cm^2 of Hilsdorf et al. and demonstrated that determining the correct energy cutoff for neutron fluence calculations in the bioshield is crucial for a proper assessment of concrete degradation resulting from neutron radiation.

Radiation-induced volumetric expansion (RIVE) of aggregates is an important contributor to the degradation of concrete mechanical properties [16]. This effect is driven by radiation-induced displacement of atoms (particularly those in siliceous [quartz type] aggregates), which is dominated by neutron contributions [17]. Remec et al. [18] showed that approximately 95% of the displacements per atom (dpa) for several minerals that are common constituents of concrete are caused by neutrons with energies above 0.1 MeV, while neutrons above 1.0 MeV contribute approximately 20% to 25% of the dpa. It is to be noted, however, that the notion of dpa is less meaningful for damage in ionic bonding dominated calcareous (amorphous) aggregates.

[2] The lower energy limit of the BUGLE-B7 multigroup library used for the transport calculations in [14] is 1.0E-5 eV. The tabulated results are reported as E > 0.0 MeV, which is essentially equivalent.

A recent evaluation of the effects of neutron radiation on concrete is available in [17]. This evaluation suggests that for temperatures applicable to LWR concrete (below 100°C), neutron fluences (E > 0.1 MeV) above 1.0E+19 n/cm^2 should be used as a threshold value for regulatory purposes. Experiments suggest that the main effect of neutron radiation on concrete is the disordering effect of neutrons on aggregates, which results in volume expansion of aggregates and causes a bonding mismatch with the cement paste. Since there are different mineral types in aggregates, the different expansion of minerals within aggregates may also lead to cracking.

2.2 Gamma Radiation

Gamma radiation test results presented by Hilsdorf et al. indicated that the effects of gamma radiation on the mechanical properties of concrete are not clear [11]. Kontani et al. reviewed the gamma radiation test data in the paper by Hilsdorf et al. and identified the data points that should be removed. While removing data points provided a trend that was not well defined, Kontani et al. considered a gamma dose of 2.0E+10 rad as the threshold to consider for concrete degradation [8], [12]. Further testing with gamma radiation was performed such as those presented in [19]–[21]; however, [8] indicates that test results for the effect of gamma radiation on concrete degradation are inadequate and suggests that acquisition of additional data representative of NPPs should be pursued.

The effects of gamma radiation on concrete are primarily due to heat generation and radiolysis [12], [16], [21]–[23]. Both of these mechanisms can affect the water content in concrete. The hydrogen peroxide generated in radiolysis may also affect the concrete properties. Changes in the water content of the concrete—whether due to thermal conditions or radiation effects—will affect the hydrogen content and hence affect the transmission of neutrons through the concrete. Because the total heating rate and gamma dose rate are largely due to “self-heating” gammas that are produced by neutron capture within the bioshield, changes in the transmission characteristics of neutrons in the concrete will also affect the behavior of the total heating and gamma dose rate profiles through the concrete.

A recent evaluation of the effects of neutron radiation on concrete is available in [17]. This evaluation suggests that for temperatures applicable to LWR concrete (below 100°C), neutron fluences (E > 0.1 MeV) above 1.0E+19 n/cm^2 should be used as a threshold value for regulatory purposes. Experiments suggest that the main effect of neutron radiation on concrete is the disordering effect of neutrons on aggregates, which results in volume expansion of aggregates and causes a bonding mismatch with the cement paste. Since there are different mineral types in aggregates, the different expansion of minerals within aggregates may also lead to cracking.

A recent evaluation of the effects of gamma radiation on concrete is available in [17]. This evaluation suggests that there is limited data on the effect of gamma radiation on concrete, but indicates that gamma doses greater than 1.0E+10 rad may cause a degradation in concrete properties. However, there is no data that isolates gamma irradiation of concrete in an air environment and the synergistic effects of neutron and gamma irradiation on concrete are not known. The main effect of gamma radiation on concrete is identified as water loss in the cement paste as a result of heating and radiolysis. The water loss in cement causes shrinkage in cement and opens pores; however, the gamma-induced carbonation of portlandite to calcite results in the calcite occupying more space compared to portlandite, which partly makes up for the opening of pores.

2.3 Quantification of Radiation Parameters

The results of this study for predictions of radiation effects on concrete are based on the following quantities obtained from radiation transport calculations.

1) Neutron flux levels throughout the first 60 cm (radially) of the bioshield for a range of elevations extending from the bottom of the RPV to the RPV nozzle elevation, with data provided for the following neutron energy ranges:
    a. E > 1.0 MeV
    b. E > 0.1 MeV
    c. E > 1.0E-05 eV (total neutron flux)

2) Total (sum of neutron and gamma) heat generation rates (W/cm^3) in the first 60 cm of the concrete and in structural steel (reinforcing steel and embedded support columns) within the bioshield

3) Gamma dose rates (rad/s) in the same locations as the heat generation rates

3 ANALYSIS METHODOLOGY

The primary analysis methods that are currently applied to calculation of neutron and gamma fluxes, heating rates, and dose rates are discrete ordinates calculations, Monte Carlo calculations, and hybrid calculations[3]. Monte Carlo methods have long been considered to be superior to discrete ordinates methods. This is primarily because discrete ordinates calculations require discretization of the space, energy, and angle variables in the radiation transport equation to produce a set of equations that are solved iteratively. In contrast, Monte Carlo calculations provide a more 'exact' solution, as they use geometry described by linear and quadratic surfaces (planes, spheres, cylinders, cones, ellipsoids, hyperboloids, and paraboloids) rather than cartesian or cylindrical mesh structures, and continuous energy (CE) cross sections rather than multigroup (MG) cross sections that are averaged values which may not be appropriate at all locations in a given model. The hybrid method, which uses the results of discrete ordinates calculations to substantially reduce the computational time of Monte Carlo calculations, is applied to the current analysis.

Previous analyses of neutron and gamma radiation levels in bioshields have relied primarily on discrete ordinates calculations and have focused on the traditional beltline region (i.e., elevations within the axial extent of the active fuel) [10], [18]. In discrete ordinates calculations the Boltzmann transport equation is solved by discretizing the spatial, energy, and angular variables for the particle flux to obtain a system of equations that is solved iteratively. Regulatory Guide 1.190 provides guidance on appropriate selection of spatial, angular, and energy discretization for RPV fluence applications within the traditional beltline region [5]; however, there is no regulatory guidance for bioshield fluence calculations.

For the current study an improved prediction of neutron flux, gamma dose rates, and neutron and gamma heat generation rates for the bioshield within axial locations extending below and above the active fuel elevation, including the location of RPV supports, is needed. Studies performed for RPV flux levels in the extended beltline region have demonstrated that discrete ordinates solutions become increasingly less accurate as the distance from the traditional beltline increases [25]–[27]. The primary causes of this reduced solution accuracy are angular quadrature effects and limitations imposed by using multigroup (MG), rather than continuous energy (CE), cross-section libraries. These issues are briefly discussed in Sections 3.1 and 3.2. Section 3.3 describes the analysis methodology applied in this study. Section 3.4 identifies the major assumptions in the development of the calculational model.

The calculational model used for the results discussed in Sections 3.1 and 3.2 is a four-loop PWR model based on Watts Bar Unit 1 [24]–[27]. While the analyses for the current study employ a three-loop model (see Section 4), the four-loop calculations are suitable for demonstrating quadrature and cross-section library considerations for discrete ordinates calculations of fluxes and dose rates in the bioshield. Figure 3-1 shows a plan view of the four-loop model at an elevation near the core midplane. Figure 3-2 and Figure 3-3 show elevation views of the four-loop model at the azimuthal locations with the maximum and minimum amounts of water between the core and the RPV, respectively.

3.1 Quadrature Sensitivity with Discrete Ordinates Calculations

In a discrete ordinates radiation transport calculation, the directional variation of the flux is represented using a set of discrete directions (or ordinates) to represent the continuous angular

[3] A brief overview of the calculational methods used for radiation transport analyses is provided in APPENDIX B.

variable (see Appendix B.1.3 *Level-symmetric* (S_N) quadrature sets have been widely used for discrete ordinates calculations. Typical S_N quadratures include S8, which has 10 discrete directions in each octant of the unit sphere, and S16, which has 36 angles per octant.

While S_N sets are widely used, they are not optimal for geometries where particle transport along directions near a coordinate axis, such as streaming of neutrons in the cavity gap between the RPV and the bioshield. Abu-Shumays developed *quadruple range* (QR) quadratures to provide superior accuracy for problems in which there are material discontinuities across octants of the unit sphere, such as the edges of fuel assemblies and gaps near any of the coordinate axes [28][29]. Regulatory Guide 1.190 provides guidance on the selection of angular quadrature for RPV fluence analyses in the traditional beltline region and suggests the use of an S8 quadrature as a minimum for determining RPV fluence, with the added requirement that the adequacy of S8 quadrature used in off-midplane locations for radiation transport calculations in the cavity region must be demonstrated.

Figure 3-4 through Figure 3-7 illustrate quadrature sensitivity effects in the bioshield by comparing Denovo [30] discrete ordinates calculations with various quadratures to a Shift [31] Monte Carlo calculation. The Denovo and Shift calculations used the BUGLE-B7 multigroup cross-section library [32]. The Denovo calculations were run using a spatial mesh that was resolved finely enough to provide convergence with respect to mesh (i.e., further mesh refinement does not change the Denovo solution). This comparison provides a means of effectively isolating the impact of the quadrature set on the Denovo solution.

Figure 3-4 and Figure 3-5 show the ratios of Denovo solutions with S8 and S16 quadratures to the Shift solution near the core midplane. While the S8 solution agrees to within ~6% at all locations, there is clear evidence of quadrature artifacts (which appear as 'fringe patterns' beginning at each corner fuel assembly) in the S8 solution. The S16 solution shows a substantial improvement in agreement with the Shift solution, though there are still some indications of minor quadrature artifacts.

Figure 3-6 and Figure 3-7 demonstrate the increasing deviation between Denovo solutions and the Shift solution at an elevation above the traditional beltline region. At this elevation, which is approximately 5 cm below the start of the RPV nozzle supports, there are significant ray effects[4] in and immediately adjacent to the cavity gap in the S16 solution. Use of QR8T quadrature, which has the same number of angles per octant (36) as S16 quadrature, provides an improved solution, but there are still ray effects, particularly in the cavity gap.

Figure 3-8 and Figure 3-9 illustrate the solution improvement that results from using higher-order QR quadratures: a QR12T set with 78 angles per octant and a QR16T set with 136 angles per octant. While these solutions significantly reduce the magnitude of the ray effects, they do not eliminate them. Furthermore, it can be impractical to use quadrature sets of this size with large three-dimensional (3D) discrete ordinates models due to memory limitations in computing systems.

[4] *Ray effects* refer to anomalies in the flux solution that are most likely to occur in regions with very little if any scattering, such as the cavity gap.

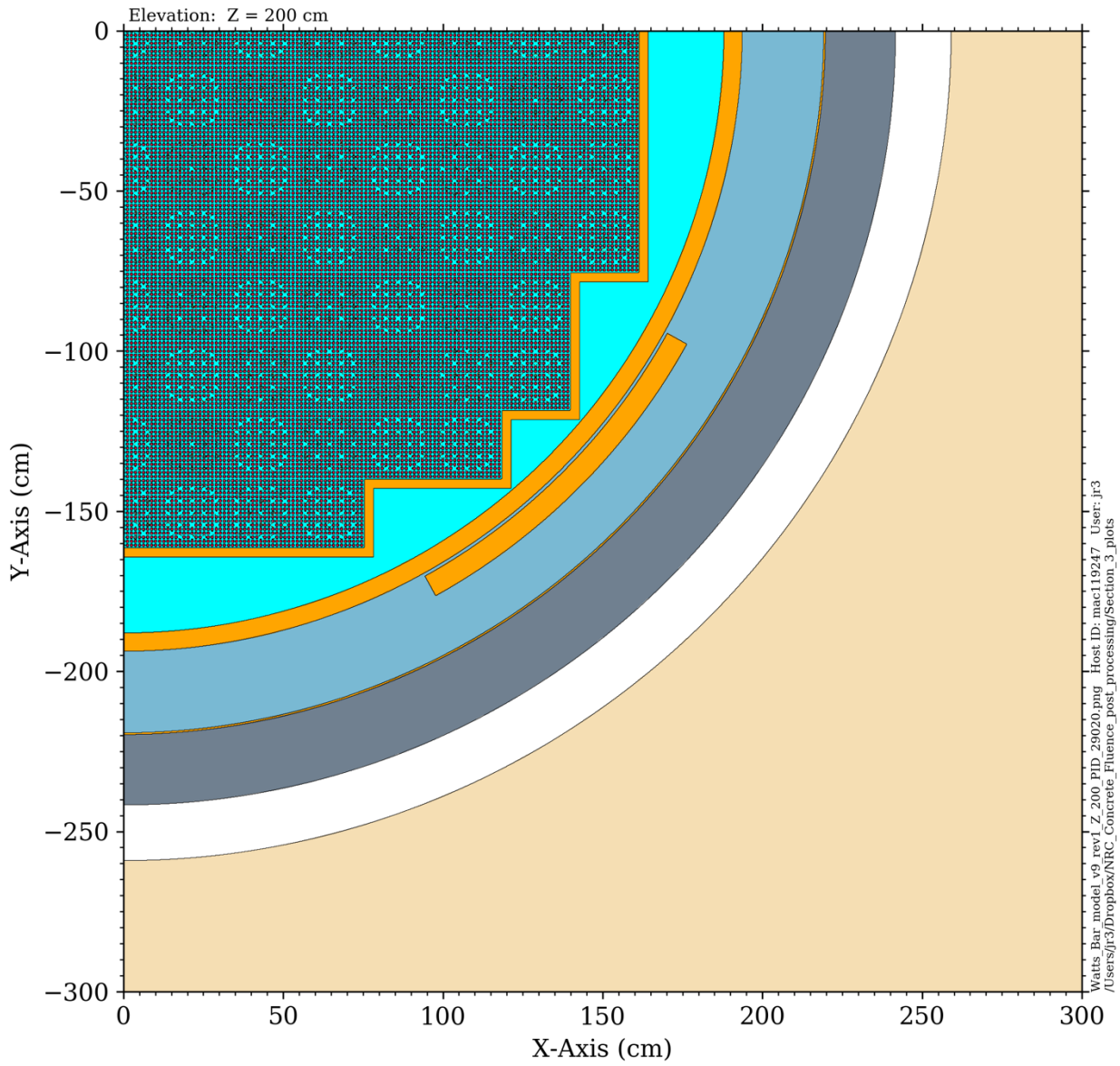

Figure 3-1 Plan view of the four-loop PWR model at an elevation near the core midplane

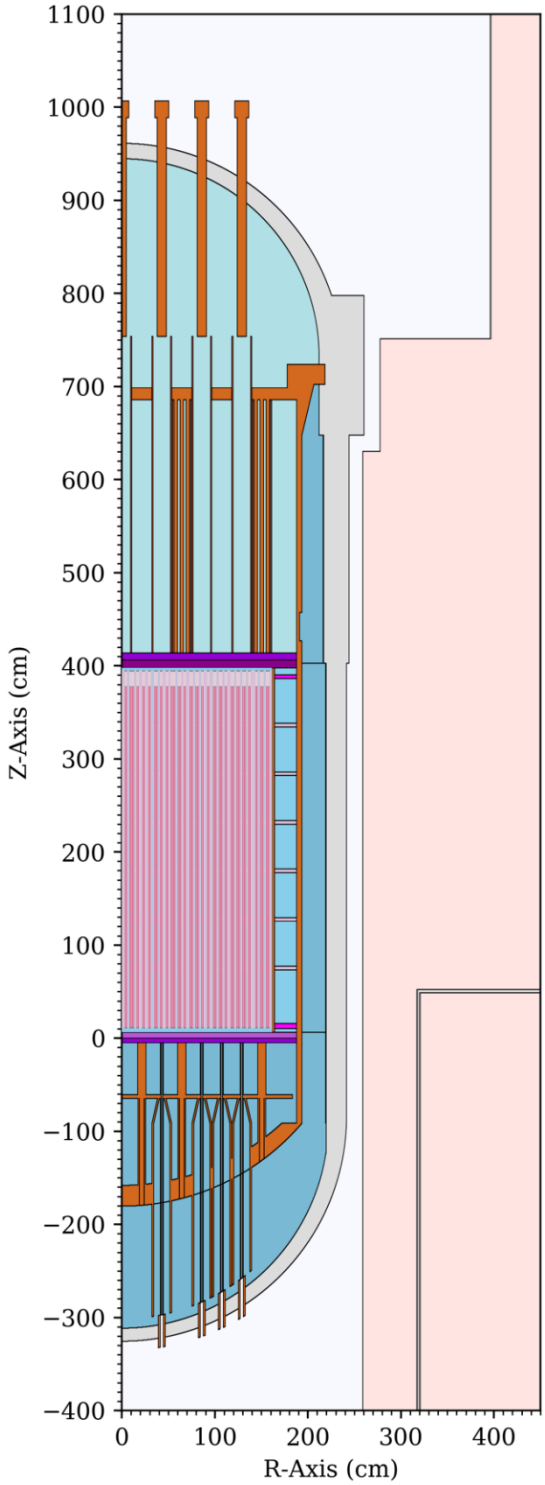

Figure 3-2 **Elevation view of the four-loop PWR model at the azimuthal location with the maximum amount of water between the core and the RPV**

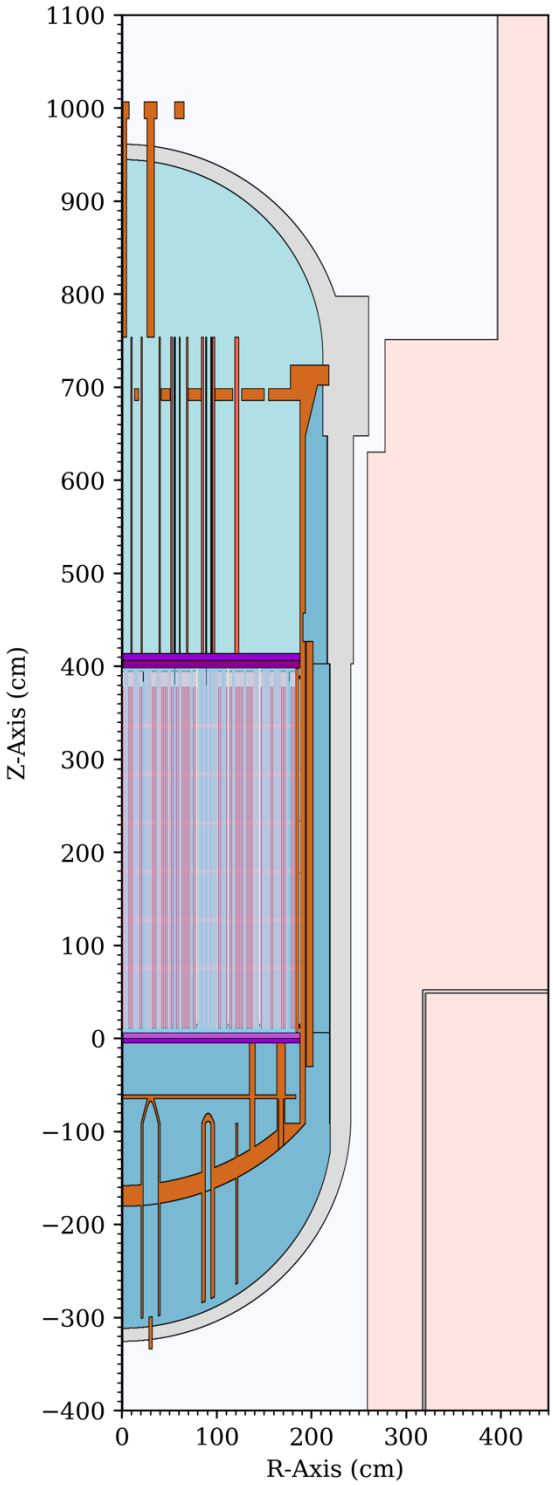

Figure 3-3 **Elevation view of the four-loop PWR model at the azimuthal location with the minimum amount of water between the core and the RPV**

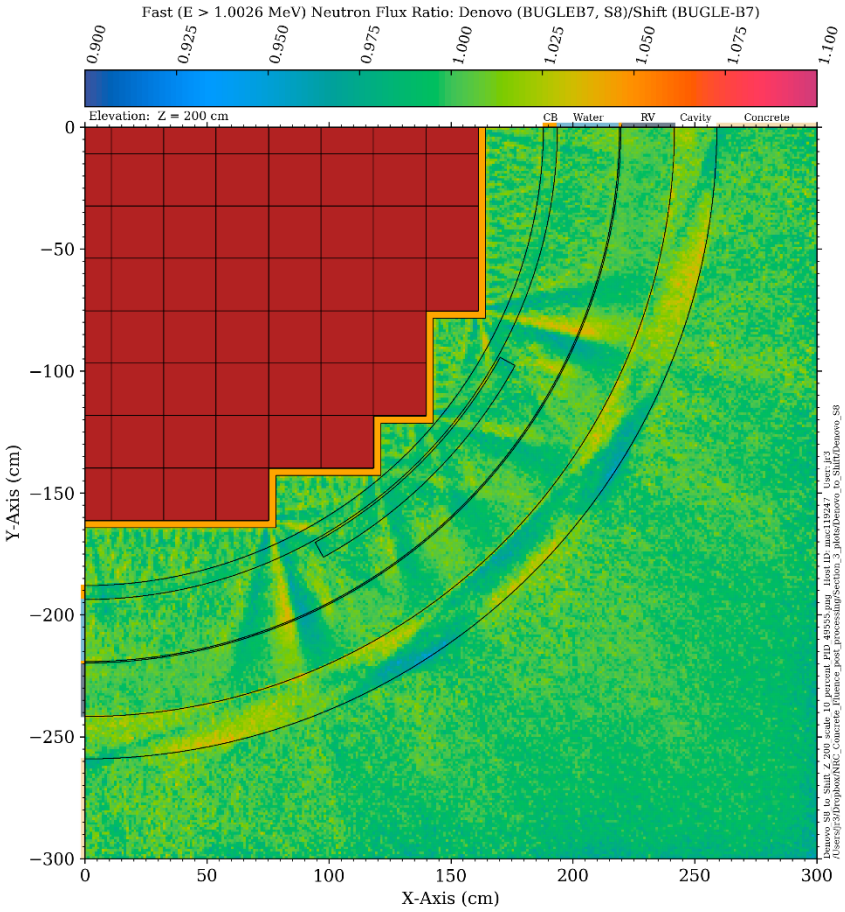

Figure 3-4 **Ratio of the neutron flux (E > 1.0 MeV) from an S8 Denovo calculation to a multigroup Shift calculation near the core midplane in a four-loop PWR model (Both calculations used the BUGLE-B7 cross-section library)**

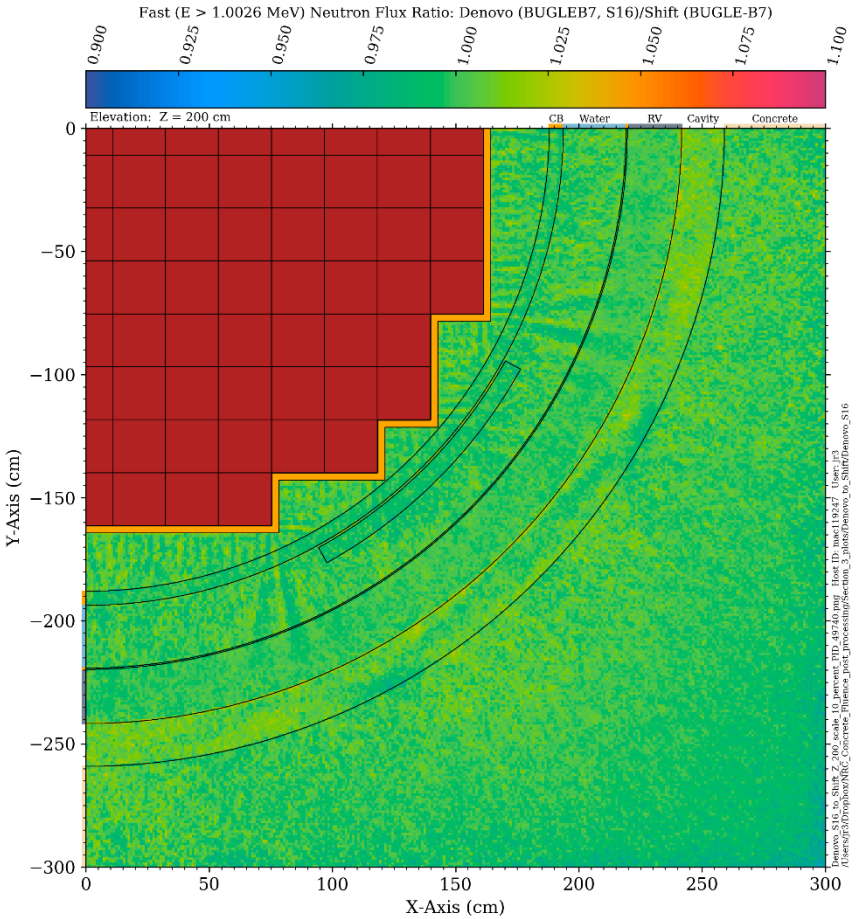

Figure 3-5 **Ratio of the neutron flux (E > 1.0 MeV) from an S16 Denovo calculation to a multigroup Shift calculation near the core midplane in a four-loop PWR model (Both calculations used the BUGLE-B7 cross-section library)**

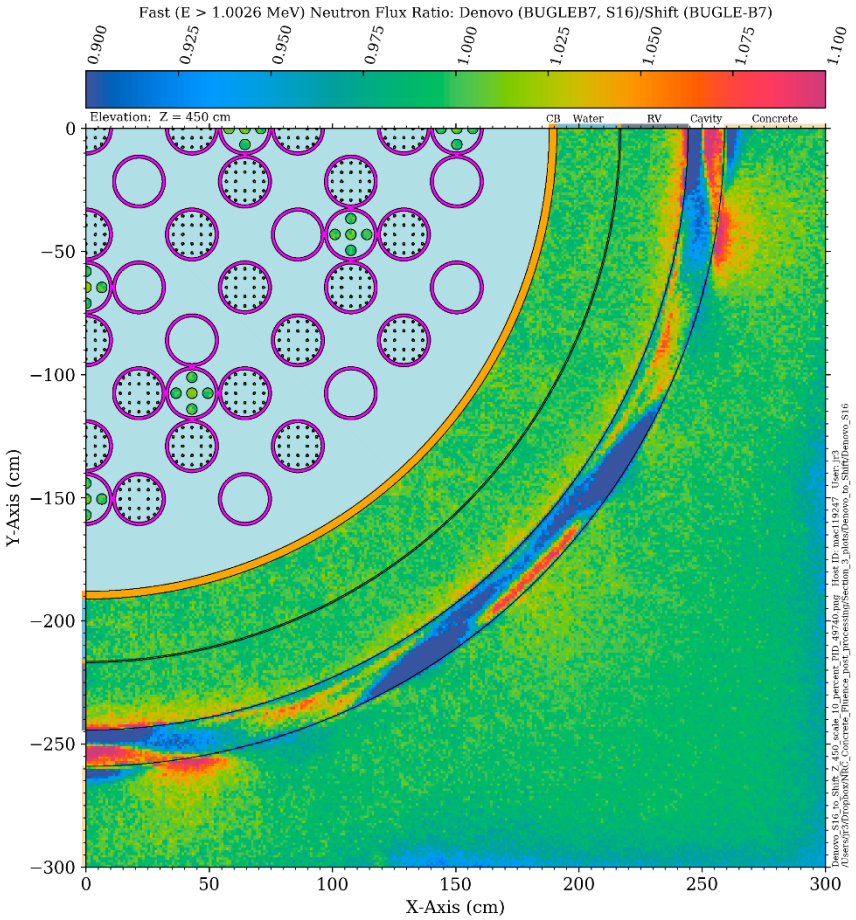

Figure 3-6 **Ratio of the neutron flux (E > 1.0 MeV) from an S16 Denovo calculation to a multigroup Shift calculation just below the elevation of the RPV supports in a four-loop PWR model (Both calculations used the BUGLE-B7 cross-section library)**

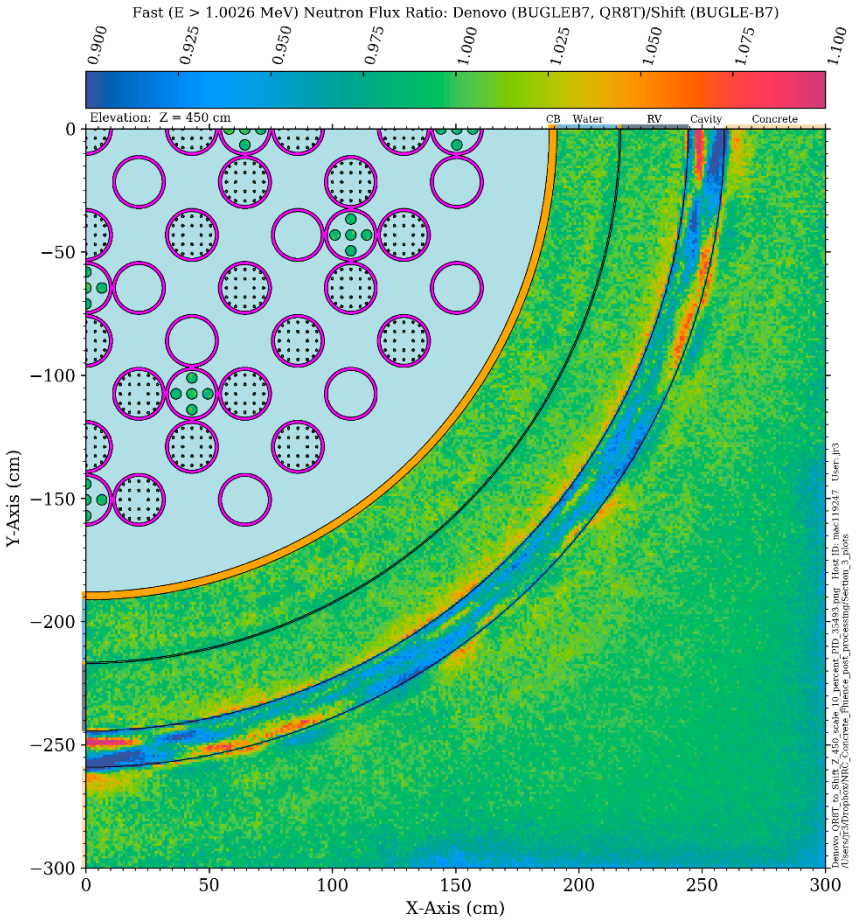

Figure 3-7 **Ratio of the neutron flux (E > 1.0 MeV) from a QR8T Denovo calculation to a multigroup Shift calculation just below the elevation of the RPV supports in a four-loop PWR model (Both calculations used the BUGLE-B7 cross-section library)**

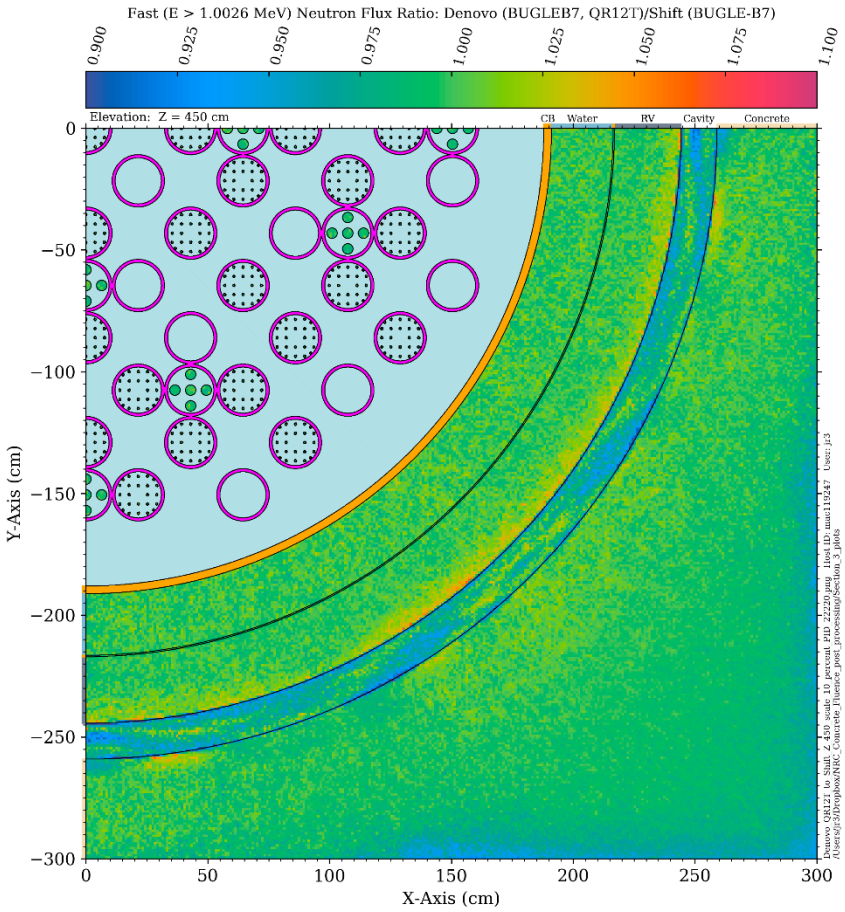

Figure 3-8 **Ratio of the neutron flux (E > 1.0 MeV) from a QR12T Denovo calculation to a Shift calculation just below the elevation of the RPV supports in a four-loop PWR model (Both calculations used the BUGLE-B7 cross-section library)**

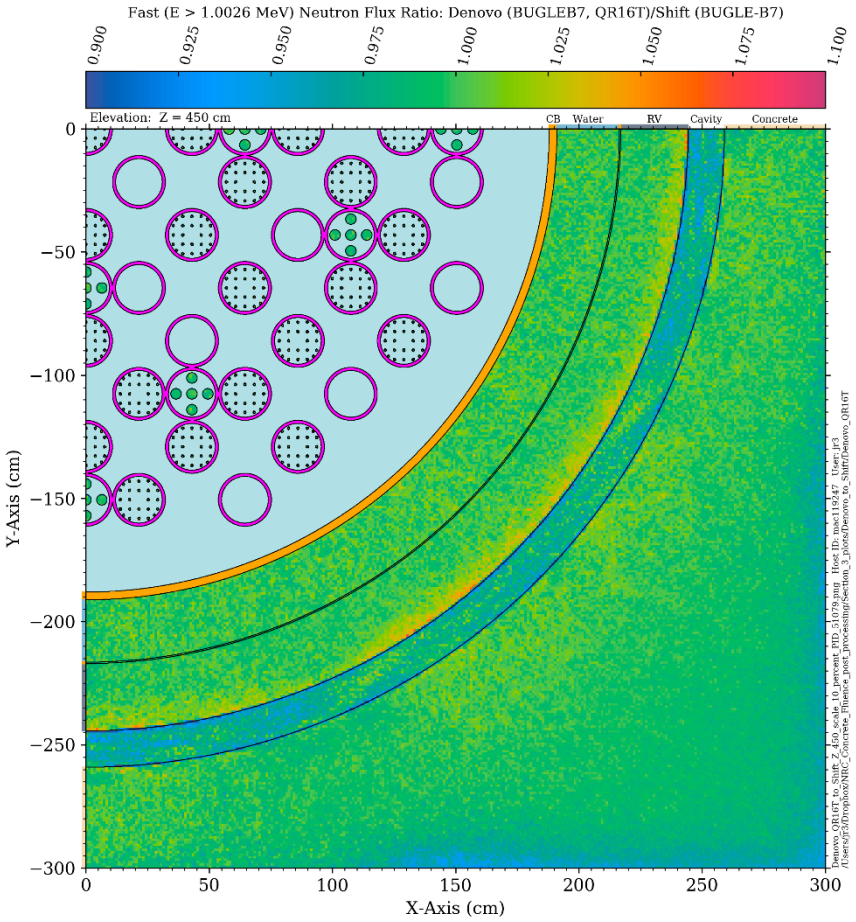

Figure 3-9 **Ratio of the neutron flux (E > 1.0 MeV) from a QR16T Denovo calculation to a Shift calculation just below the elevation of the RPV supports in a four-loop PWR model (Both calculations used the BUGLE-B7 cross-section library)**

3.2 Multigroup Cross-Section Library Sensitivity with Monte Carlo Calculations

In discrete ordinates calculations, the energy dependence of the flux is represented by *energy groups*. The particle (neutron or photon) flux in each group is solved using MG cross-section libraries that are prepared by averaging CE cross-section data over the energy groups using a specific weighting function or functions. Because of this averaging process, MG calculations are inherently less accurate than CE calculations. The accuracy that can be obtained from an MG library is dependent on the number of energy groups and on the weighting function(s) used to average the CE data over the energy groups.

The BUGLE-B7 MG library was developed specifically for LWR shielding applications and are frequently used for RPV fluence analyses. To assess the adequacy of MG calculations using the BUGLE-B7 library for prediction of neutron fluence levels in a bioshield, MG and CE calculations were performed using the Shift Monte Carlo radiation transport code with the four-loop PWR model. Figure 3-10 through Figure 3-15 demonstrate the tendency of MG calculations using the BUGLE-B7 library to underpredict neutron flux levels for energies above 1.0 MeV and above 0.1 MeV relative to the more accurate CE solution. These plots show how the MG/CE differences increase with increasing distance from the core. Similar MG/CE underprediction also occurs using the VITAMIN-B7 [27], [32] and SCALE X200N47G [33] MG libraries.

Within the beltline region, the BUGLE-B7 fluxes in the bioshield for E > 0.1 MeV and E > 1.0 MeV are up to ~13% lower than the CE fluxes. At elevations in the vicinity of the RPV supports, the BUGLE-B7 solution is up to ~15% lower than the CE solution for neutron energies greater than 1.0 MeV. The difference between the BUGLE-B7 and CE solutions for neutron energies greater than 0.1 MeV at this elevation is typically 15–25%, with maximum differences up to ~31% at the elevation through the RPV supports (Figure 3-15).

Figure 3-16 through Figure 3-19 show MG/CE solution comparisons when a very-fine-group MG library with 956 neutron groups (vs. 47 neutron groups in the BUGLE-B7 library) is used. This library was developed internally at ORNL to assess whether the deviations between MG and CE Shift solutions could be reduced to a specified value (< 5%). The 956-group library has 540 groups between 1.0026 MeV and 10.0 MeV, compared to 46 groups over the same energy range in the VITAMIN-B7 library. The agreement between the MG and CE solutions is significantly improved with the 956-group library, with maximum differences for both energy ranges and both elevations of less than ~9%, and overall agreement typically within 5%. While the MG/CE agreement is substantially improved for the RPV support elevation at E > 0.1 MeV, the size of this MG library is prohibitive for multidimensional calculations using typical discrete ordinates codes.

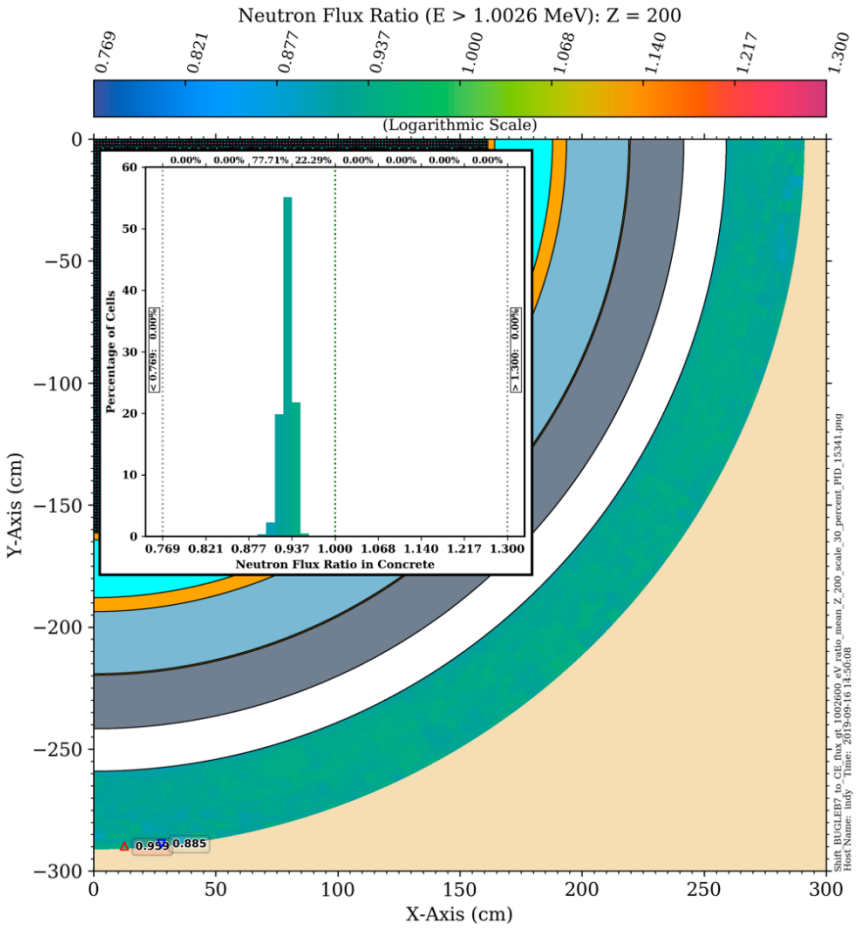

Figure 3-10 Ratio of the neutron flux (E > 1.0 MeV) from a Shift calculation using the BUGLE-B7 library to a Shift calculation using continuous-energy cross sections (The elevation is near the core midplane in a four-loop PWR model. The histogram plot shows the distribution of ratio values within the first 60 cm of the bioshield)

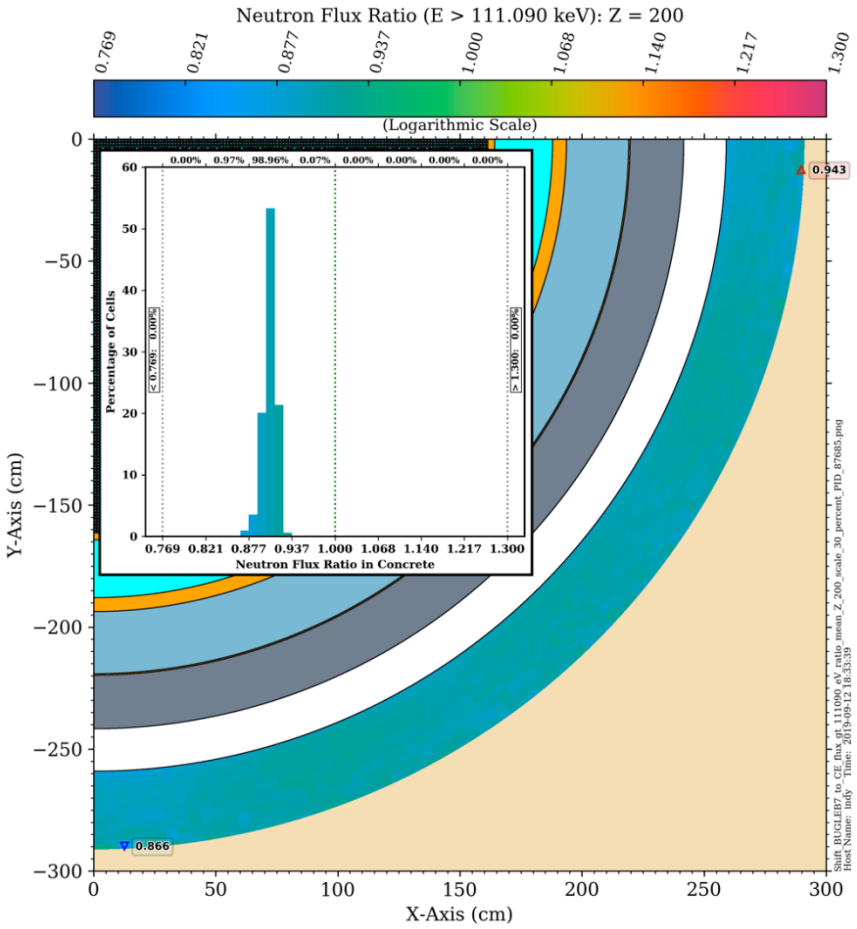

Figure 3-11 Ratio of the neutron flux (E > 111.09 keV) from a Shift calculation using the BUGLE-B7 library to a Shift calculation using continuous-energy cross sections (The elevation is near the core midplane in a four-loop PWR model. The histogram plot shows the distribution of ratio values within the first 60 cm of the bioshield)

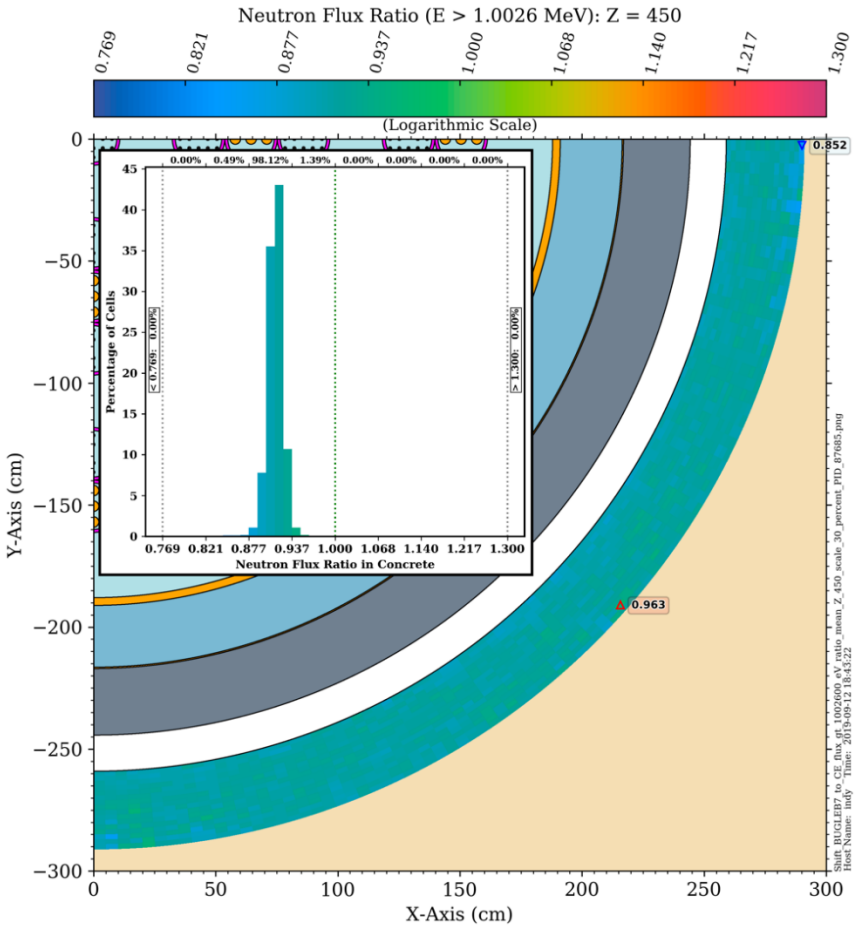

Figure 3-12 Ratio of the neutron flux (E > 1.0 MeV) from a Shift calculation using the BUGLE-B7 library to a Shift calculation using continuous-energy cross sections (The elevation is just below the RPV supports in a four-loop PWR model. The histogram plot shows the distribution of ratio values within the first 60 cm of the bioshield.)

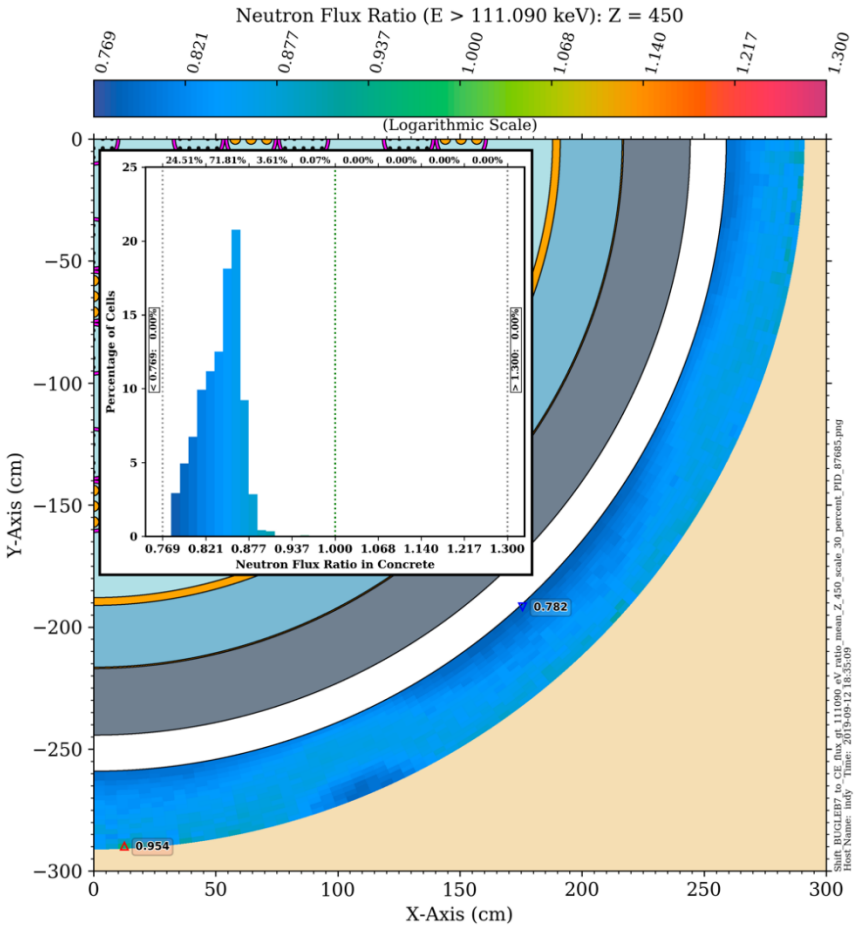

Figure 3-13 Ratio of the neutron flux (E > 111.09 keV) from a Shift calculation using the BUGLE-B7 library to a Shift calculation using continuous-energy cross sections (The elevation is just below the RPV supports in a four-loop PWR model. The histogram plot shows the distribution of ratio values within the first 60 cm of the bioshield.)

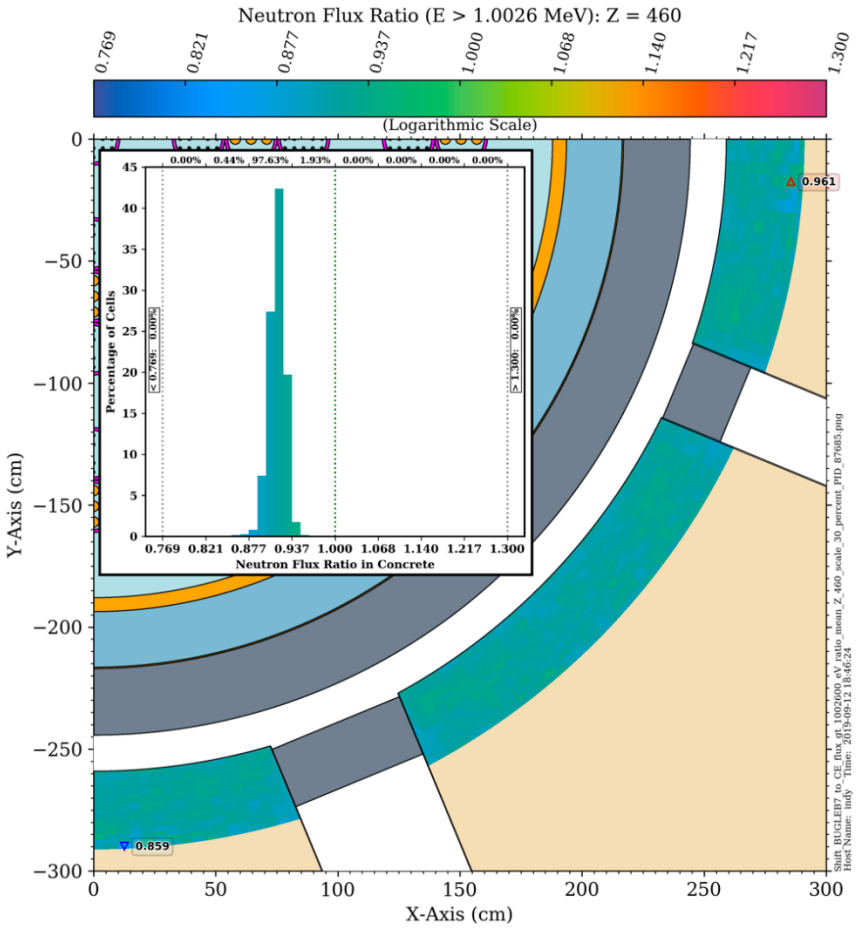

Figure 3-14 Ratio of the neutron flux (E > 1.0 MeV) from a Shift calculation using the BUGLE-B7 library to a Shift calculation using continuous-energy cross sections (The elevation is through the lower part of the RPV supports in a four-loop PWR model. The histogram plot shows the distribution of ratio values within the first 60 cm of the bioshield.)

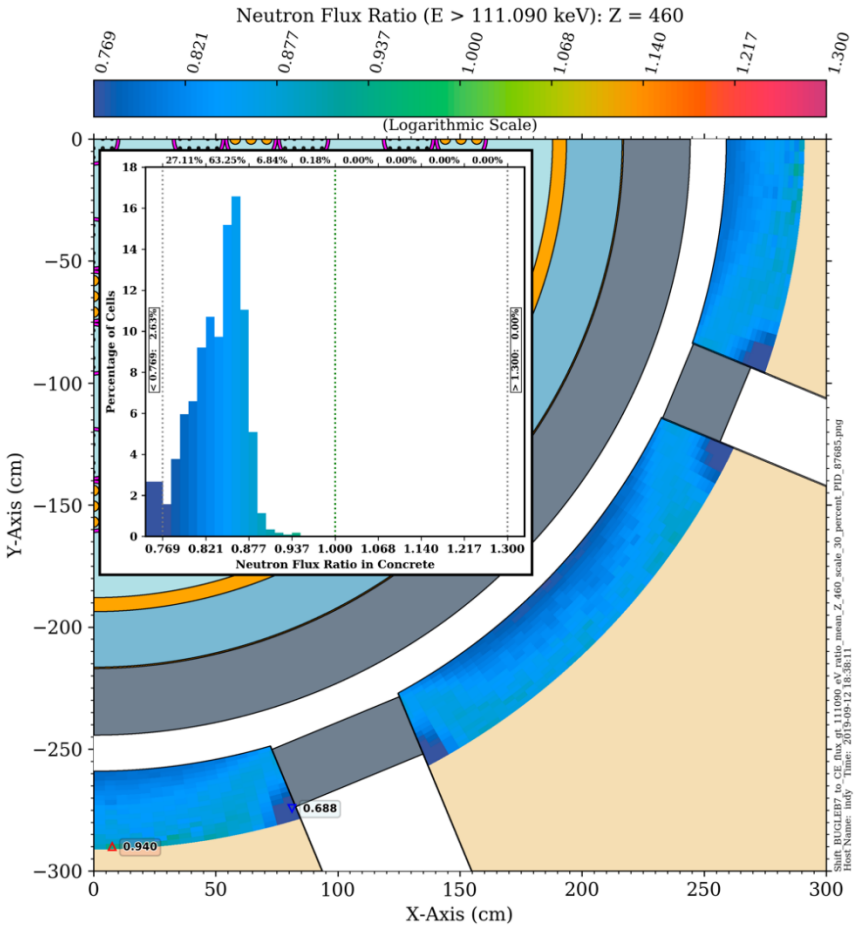

Figure 3-15 Ratio of the neutron flux (E > 111.09 keV) from a Shift calculation using the BUGLE-B7 library to a Shift calculation using continuous-energy cross sections (The elevation is through the lower part of the RPV supports in a four-loop PWR model. The histogram plot shows the distribution of ratio values within the first 60 cm of the bioshield.)

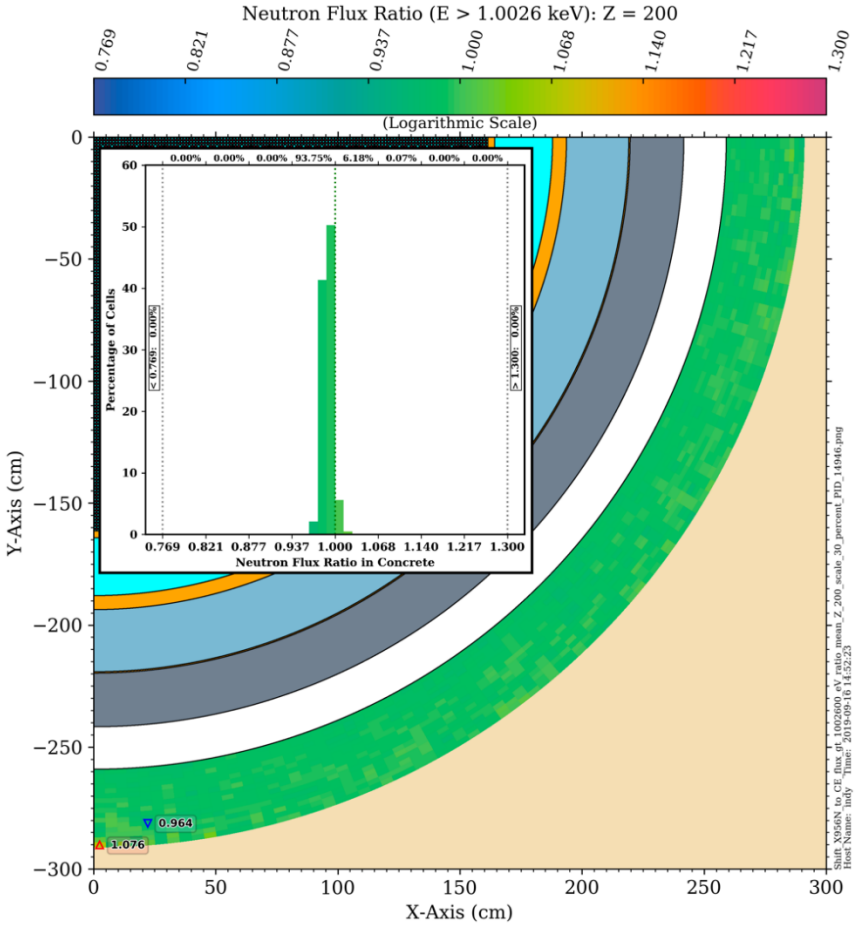

Figure 3-16 Ratio of the neutron flux (E > 1.0 MeV) from a Shift calculation using a multigroup library with 956 neutron groups to a Shift calculation using continuous-energy cross sections (The elevation is near the core midplane in a four-loop PWR model. The histogram plot shows the distribution of ratio values within the first 60 cm of the bioshield.)

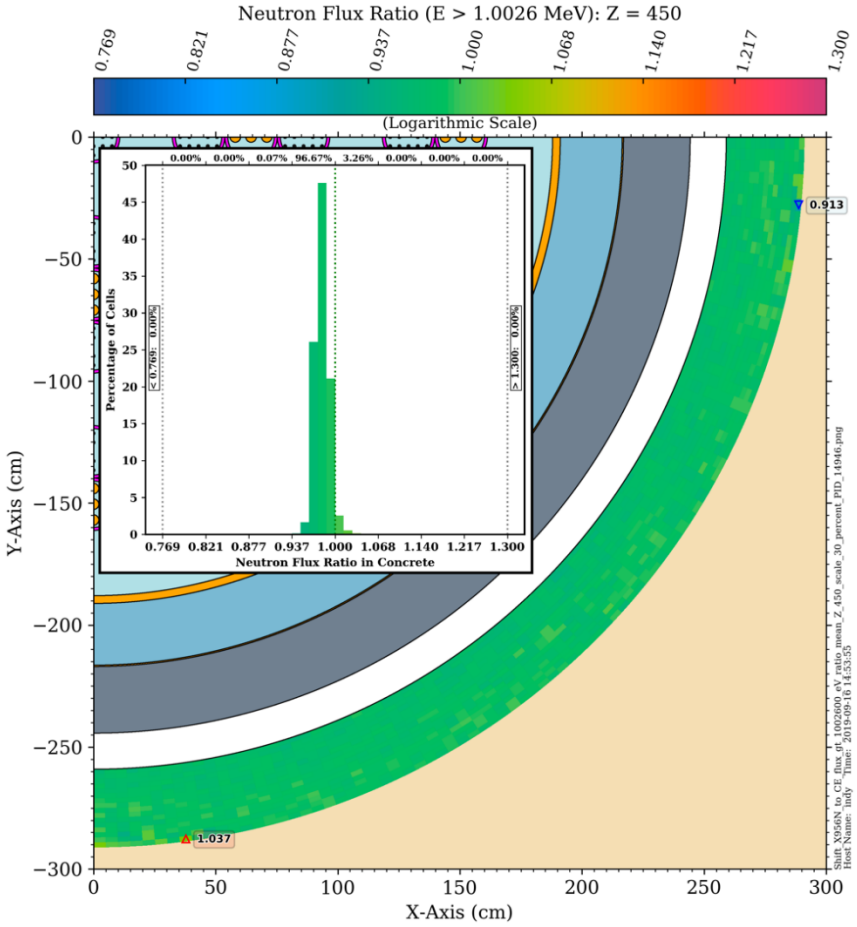

Figure 3-17 Ratio of the neutron flux (E > 1.0 MeV) from a Shift calculation using a multigroup library with 956 neutron groups to a Shift calculation using continuous-energy cross sections (The elevation is just below the RPV supports in a four-loop PWR model. The histogram plot shows the distribution of ratio values within the first 60 cm of the bioshield.)

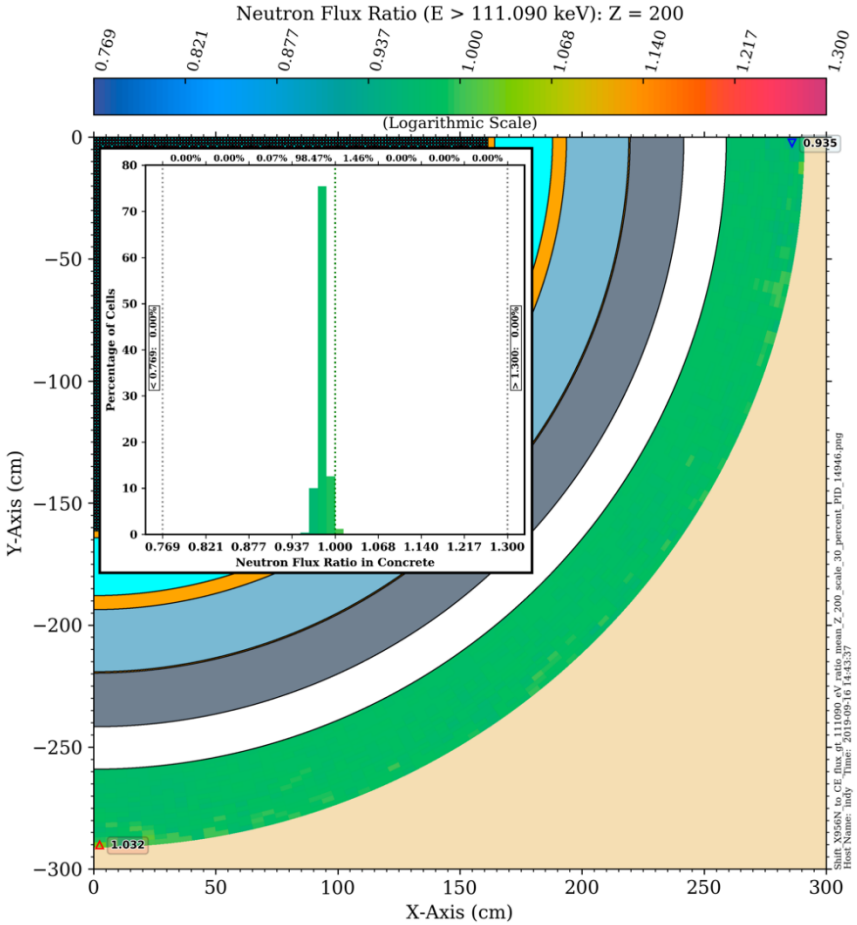

Figure 3-18 Ratio of the neutron flux (E > 111.09 keV) from a Shift calculation using a multigroup library with 956 neutron groups to a Shift calculation using continuous-energy cross sections (The elevation is near the core midplane in a four-loop PWR model. The histogram plot shows the distribution of ratio values within the first 60 cm of the bioshield.)

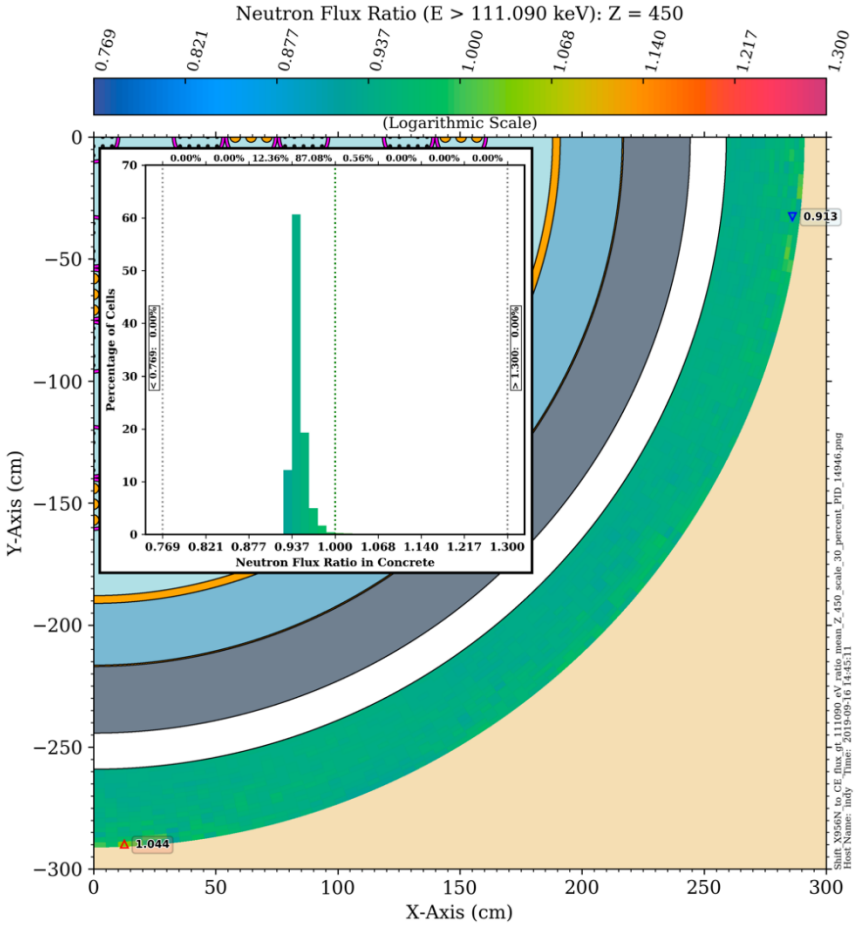

Figure 3-19 Ratio of the neutron flux (E > 111.09 keV) from a Shift calculation using a multigroup library with 956 neutron groups to a Shift calculation using continuous-energy cross sections (The elevation is just below the RPV supports in a four-loop PWR model. The histogram plot shows the distribution of ratio values within the first 60 cm of the bioshield.)

3.3 Use of Hybrid Radiation Transport Calculations for Radiation Evaluations in Concrete Bioshields

While discrete ordinates radiation transport calculations are widely used for RPV fluence analyses and for the evaluation of neutron and gamma radiation levels in bioshields, their range of application has primarily been in the traditional beltline region. The parameter studies presented in Sections 3.1 and 3.2 demonstrate the inherent limitations in using discrete ordinates methods for radiation transport calculations that extend into the bioshield, especially for elevations near the RPV supports. In particular, the use of a typical MG cross-section library (i.e., BUGLE-B7) was shown to result in neutron flux (E > 0.1 MeV) solution differences that may exceed 20% relative to more accurate CE calculations in the axial region above the active fuel. These MG/CE solution differences vary as a function of axial, radial, and azimuthal location (see especially Figure 3-13 and Figure 3-15).

Monte Carlo calculations are not subject to the discretization effects in space, energy, and angle that are an inherent limitation of discrete ordinates calculations and, as such, are considered to be a superior analysis method. In studies evaluating RPV fluence methodologies in the extended beltline region [25]–[27], it was conclusively demonstrated that hybrid radiation transport calculations provide the accuracy of well-converged Monte Carlo calculations— even with detailed mesh tallies —with solution times that are readily achievable on modern computing clusters. The calculations for this report were performed on a Linux cluster with 40 nodes and 48 processors per node. A typical MCNP® calculation was run for 2E9 histories with a wall-clock time in the range of 6 to 8 hours running on 16 nodes with 48 processors each.

Because of the clear benefits associated with hybrid radiation transport calculations, this solution methodology was adopted for the evaluation of neutron flux and neutron and gamma dose rate and heat generation rate distributions for this study. This selection does not imply that other analysis methods are not suitable but recognizes that more rigorous predictions of radiation levels can be obtained using this state-of-the-art methodology.

3.4 Uncertainty Quantification

Any radiation transport analysis is subject to uncertainties resulting from modeling approximations, lack of complete information on material specifications and dimensions, and uncertainties in the nuclear cross-section data that is used. The availability of benchmark quality experimental measurements is invaluable in quantifying the effects of these uncertainties.

Access to benchmark data for neutron flux distributions in bioshields and to radiation heating rate measurements would provide the ideal means of assessing the uncertainty in the analyses performed in Section 6 Given the current lack of such benchmark data, a rigorous uncertainty analysis is not feasible.

The hybrid methodology used in the present analysis, though, does provide a clear improvement in the accuracy that can be expected for calculations of neutron flux, heating rates, and gamma dose rates. As noted above, use of the hybrid method eliminates the methodological uncertainties due to quadrature effects and multigroup libraries in discrete ordinates calculations.

While there is no available benchmark data for calculated-to-measured comparisons of neutron flux, heating rates, or gamma dose rates in an LWR bioshield, there is measured data for neutron dosimetry reactions in the reactor cavity gap of the ORNL Pool Critical Assembly (PCA) pressure vessel wall benchmark facility (PVWBF) [34]. A recent PCA analysis [35] using

ADVANTG and MCNP®, the same codes that are used in the present analysis, demonstrated the ability of the hybrid method to obtain agreement that is generally within 5% of the measurements, even at a location in the simulated cavity outside a 22.5-cm-thick pressure vessel.

4 DEVELOPMENT OF A REFERENCE THREE-LOOP PWR MODEL

The initial phase of this project focused on creating an analysis model that could be used to evaluate neutron fluxes, heat generation rates, and gamma dose rates for a plant design that is representative of the limiting plant type with respect to radiation levels in the bioshield. The selection of the plant type to model was informed by the work of Esselman and Bruck [8], who used reports from the NRC Agencywide Documents Access and Management System (ADAMS) that included neutron fluences (E > 1.0 MeV) at the RPV inner radius for the U.S. PWR and BWR fleet. Extrapolation of data to calculate neutron fluences (E > 1.0 MeV) at 80 calendar years, attenuation of neutron fluences (E > 1.0 MeV) from the RPV inner radius to the RPV outer radius, conversion of neutron fluences for E > 1.0 MeV to E > 0.1 MeV, and calculation of concrete inner radius fluences (E > 0.1 MeV) were performed using studies by ORNL and TransWare Enterprises (TWE). Summary plots of neutron fluences at 80 calendar years from [8] are shown in Figure 4-1 through Figure 4-4. Additionally, gamma doses at the bioshield were estimated using gamma fluxes and/or dose rates from ORNL and TWE studies for two-loop and three-loop Westinghouse plants as well as an ORNL BWR study. Gamma fluxes at the RPV outer radius of a four-loop PWR and BWR reactor were also considered.

In [8], the maximum neutron fluence (E > 0.1 MeV) at the bioshield inner radius at 80 calendar years is estimated as 6.1E+19 n/cm^2 for the two-loop and three-loop U.S. PWR fleet. The four-loop U.S. PWR fleet and the U.S. BWR fleet have significantly lower neutron fluence and gamma dose levels and consequently are not limiting. From Safety Evaluation Reports of SLRs, the limiting neutron fluences (E > 0.1 MeV) calculated on the concrete biological shield at 80 calendar years are 3.57E+19 n/cm^2, 1.9E+18 n/cm^2, and 3.17E+18 n/cm^2 for a three-loop PWR, a BWR, and a three-loop PWR with a neutron shield tank, respectively [36]–[38].

The maximum gamma doses at the inner radius of the concrete biological shield at 80 calendar years are estimated as 1.23E+10 rad (ORNL study) for two-loop Westinghouse plants, 1.21E+10 rad (TWE study) and 5.04E+09 rad (ORNL study) for three-loop Westinghouse plants, and 4.27E+09 rad for a BWR (ORNL study) [8]. From Safety Evaluation Reports of SLRs, the limiting gamma doses calculated on the concrete biological shield at 80 calendar years are 1.9E+10 rad, 1E+10 rad, and 2.97E+8 rad for a three-loop PWR, a BWR, and a three-loop PWR with a neutron shield tank, respectively [36]–[38].

Based on these estimated neutron fluence (E > 0.1 MeV) and gamma dose projections on the bioshield inner radius at 80 calendar years of operation, a generalized three-loop Westinghouse plant was chosen for the current analysis. For the RPV support structure, the Category 4A short-column type support described in [9] was used as noted in Section 1

4.1 Three-Loop Model Description

Three-dimensional radiation transport calculations for the bioshield were performed using a quarter model of a Westinghouse three-loop PWR. Geometrical dimensions and materials of this baseline model were obtained from several three-loop PWR documents, including Updated Final Safety Analysis Reports (UFSARs) [39]–[42] and U.S. Nuclear Regulatory Commission contractor reports (NUREG/CRs) [6], [9]. A few modeling parameters that were not available in the three-loop reactor documents were obtained from a Westinghouse four-loop PWR model that was available to the authors.

The core region included modeling of 157 fuel assemblies having a 15 x 15 rod array per fuel assembly. Fuel, fuel cladding, fuel plenum, fuel end plugs, bottom and top nozzles, spacer grids,

guide thimbles, rod cluster control assembly (RCCA), instrument tubes, burnable poison rods, and thimble plugs were explicitly included in the core modeling. RPV internals surrounding the core in the radial direction consisted of baffle plates, former plates, core barrel, and a fully circumferential thermal shield. RPV internals below and above the core consisted of the lower and upper core plates, respectively. The four-loop-reactor-specific geometrical data were used for the fuel end plug, RCCA, burnable poison rods, thimble plugs, baffle plates, and lower and upper core plates.

The RPV clad, RPV, short-column type RPV supports, inlet and outlet nozzles, and bioshield were included in the model. The RPV thickness was selected to be within the range of RPV thicknesses of three-loop plants. For the RPV support structure, the Category 4A short-column type support described in [9] was used. In this RPV support structure, each nozzle rests on support pads that have rollers underneath. Rollers as well as lateral restraints are located on top of girders. Each girder is bolted to cantilever beams that extend in the cavity. Cantilever beams are also partially embedded in the bioshield. Each cantilever beam is welded to supporting columns embedded in the bioshield.

The baseline three-loop reactor model for the transport calculations included reinforcing steel in the bioshield. The reinforcing steel (rebar) consisted of #8 rebar (1-inch diameter) at 12-inch spacings azimuthally and vertically with a 3-inch concrete cover (i.e., the distance between the inner radius of the bioshield and the near edge of the rebar was 3 inches).

The reflective thermal insulation and bioshield liner were not in the baseline model, but their impact was evaluated in parametric studies. Surveillance capsule holders and surveillance capsules were not included in the model. The nonexistence of surveillance capsule holders and surveillance capsules has no impact on the conclusions of this work as the focus is on parametric studies for the bioshield.

The three-loop reactor used in this study has octant symmetry with the exception of the coolant nozzles and RPV supports. In the current analysis, modeling one-quarter of the reactor instead of a full model (i.e., 360º azimuthal modeling) was found to be sufficient for the purposes of this work, which was a parametric study. Moreover, this simplification of modeling one-quarter of the reactor results in significant reductions in computational time and resources (processors and memory) as compared to those required for a full-core model.

Plan and elevation views of the three-loop model are provided in APPENDIX A

4.2 Major Modeling Assumptions

Several simplifications were made in developing the three-loop model used in this analysis. Because the current work performs studies to understand the impact of various parametric changes on neutron and gamma radiation levels in the bioshield and RPV supports and does not calculate plant-specific neutron fluxes, heat generation rates, or gamma doses, these modeling simplifications, listed below, will not impact the conclusions of the study.

a. The neutron source was defined as having a U-235 Watt fission energy spectrum with a uniform spatial distribution within each fuel assembly.

b. With the exception of the lower and upper core plates, details of the upper and lower RPV internals were not included in the geometrical model, and the composition of these regions were specified as water. There is very little neutron transport to the bioshield through these regions.

c. Three types of coolant temperatures were used in this study without taking into consideration a detailed axial temperature change. One coolant temperature was used for the inlet temperature and for the core, bypass, and downcomer regions along the active fuel height. Two outlet temperatures were used above the core.

d. Ex-core detector wells were outside the scope of the project and were not modeled. Neglecting the presence of detector wells is not expected to affect the conclusions of this analysis.

e. Surveillance capsules and capsule holders were not modeled.

The analysis is performed for a three-loop Westinghouse PWR, but the parametric studies in this work can be extended to apply to two-loop PWRs as well since the impact of the parametric studies on neutron and gamma radiation levels in the bioshield and RPV supports are not plant specific to two-loop or three-loop PWRs. As noted in Section 4 two-loop and three-loop PWRs are more limiting than four-loop PWRs or BWRs with regard to concrete fluence concerns.

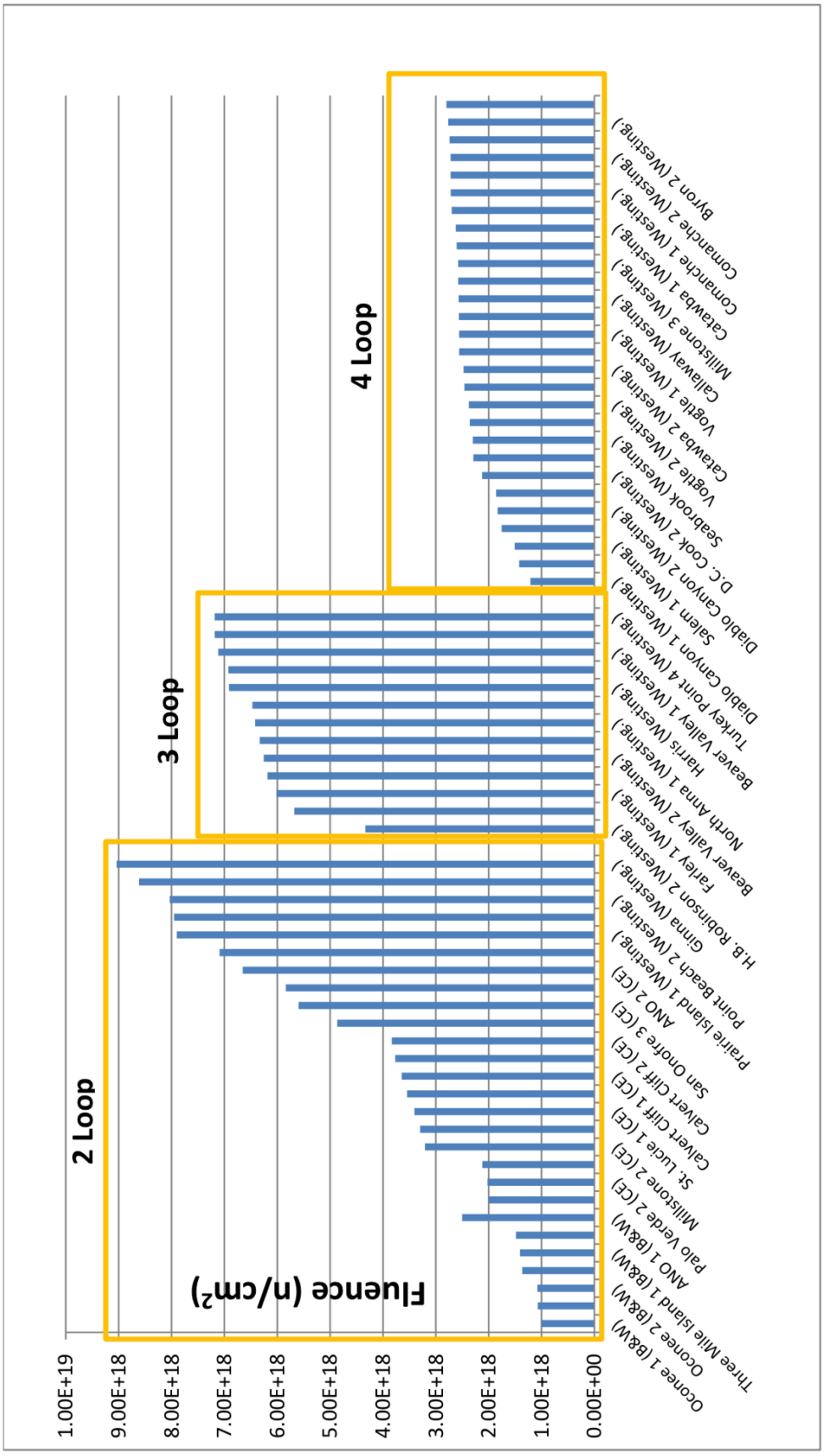

Figure 4-1 Summary of accumulated maximum neutron fluence (E > 1.0 MeV) at the outer surface of the RPV for the US PWR fleet extrapolated to 80 calendar years [8]

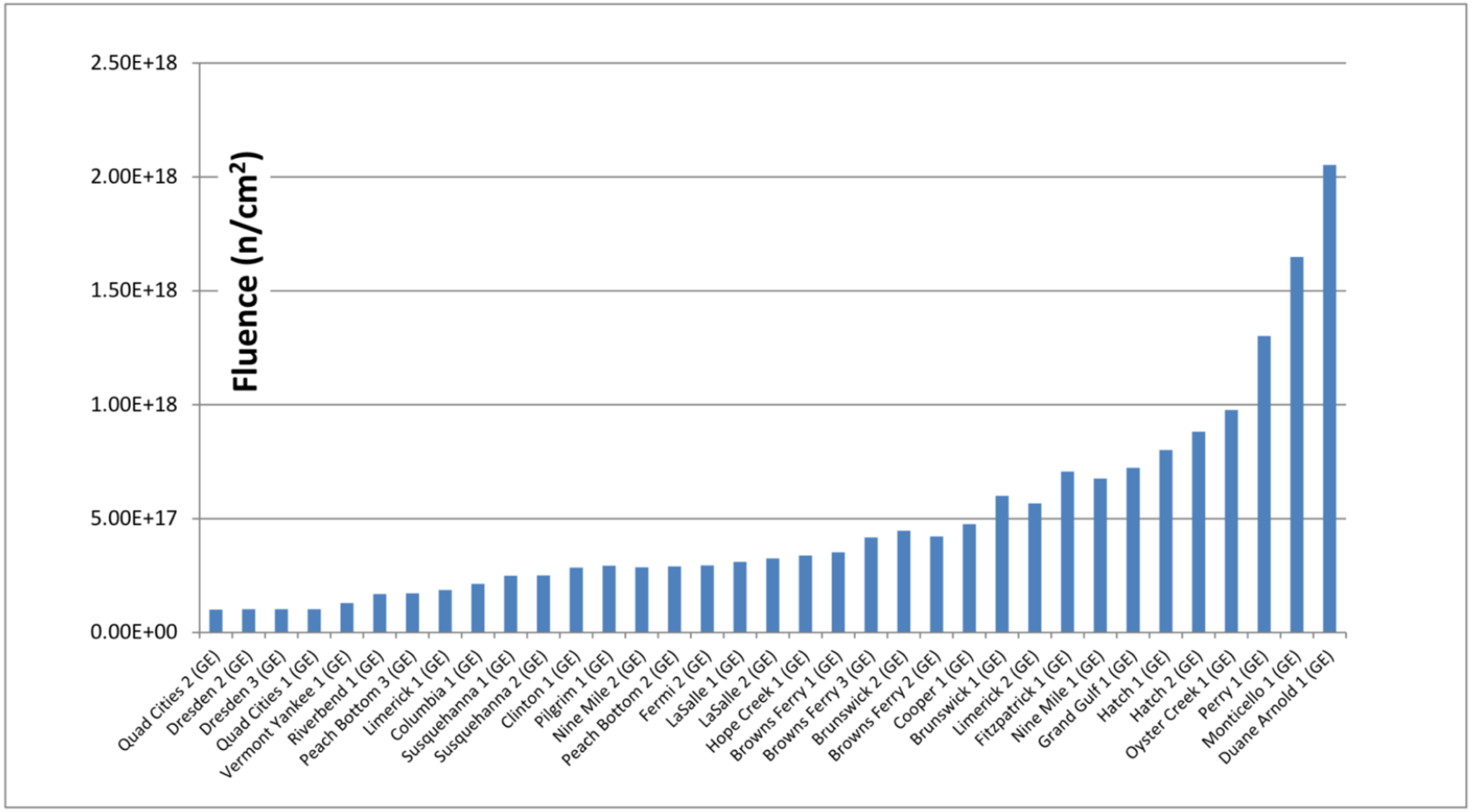

Figure 4-2 Summary of accumulated maximum neutron fluence (E > 1.0 MeV) at the outer surface of the RPV for the US BWR fleet extrapolated to 80 calendar years [8]

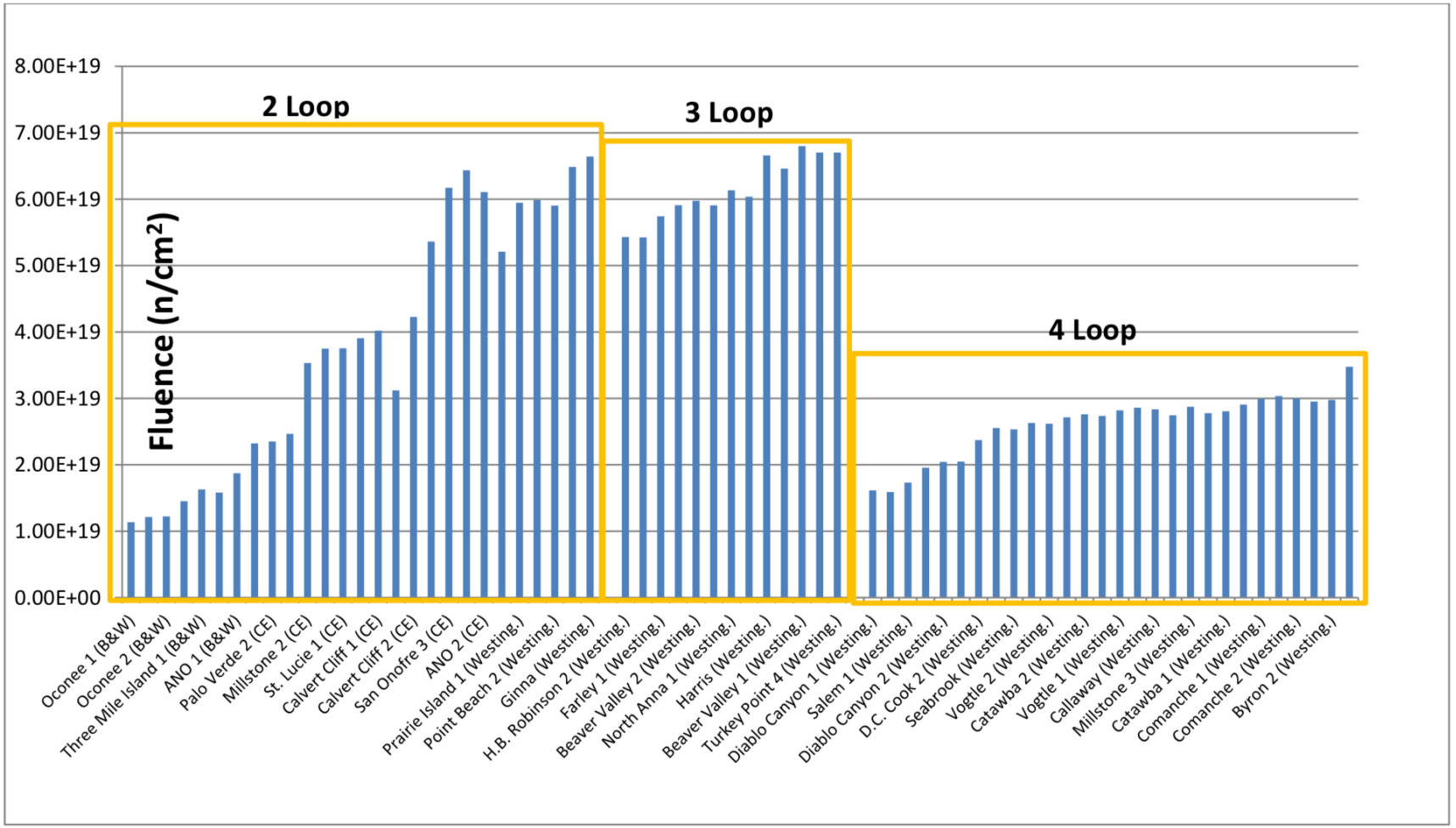

Figure 4-3 Summary of accumulated maximum neutron fluence (E > 0.1 MeV) at the outer surface of the RPV for the US PWR fleet extrapolated to 80 calendar years [8]

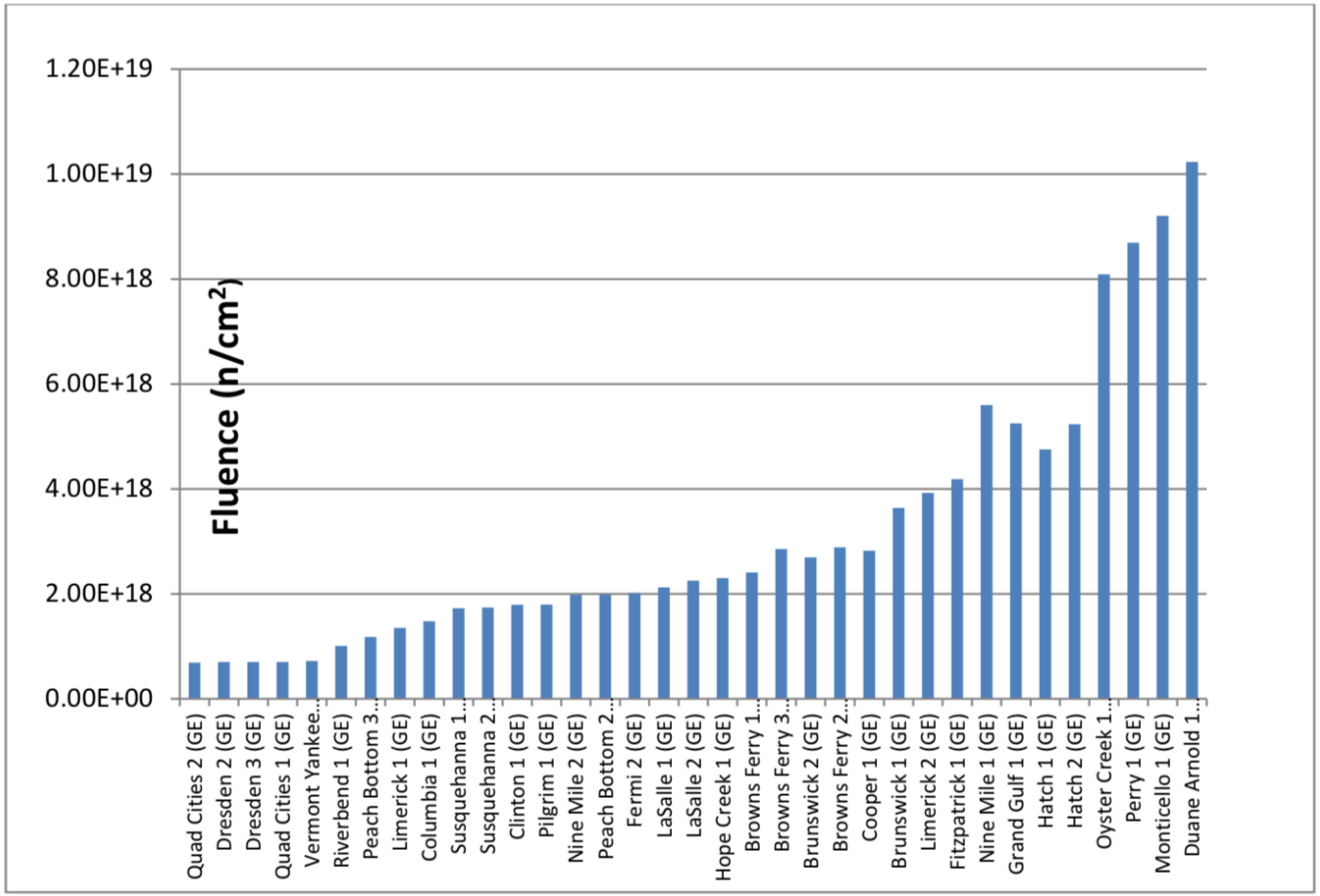

Figure 4-4 Summary of accumulated maximum neutron fluence (E > 0.1 MeV) at the outer surface of the RPV for the US BWR fleet extrapolated to 80 calendar years [8]

5 INPUTS FOR PARAMETER STUDIES

5.1 Concrete Hydrogen Content

The attenuation of neutrons in concrete is known to be sensitive to the moisture level (specifically the hydrogen content) of the concrete. The selection of a typical range of hydrogen content in concrete bioshields was informed by the following information [43] as well as information in references [39]–[42].

- Typical cement density in concrete ranges from 325 to 375 kg/m^3.
- Typical water-to-cement ratio (w/c) ranges from 0.45 to 0.55.
- The minimum hydrogen density was calculated using a cement density of 325 kg/m^3 and w/c of 0.45 The maximum hydrogen density was calculated using a cement density of 375 kg/m^3 and w/c of 0.55.
- Minimum hydrogen density = 0.01625 g/cm^3.
- Maximum hydrogen density = 0.02292 g/cm^3.

The calculation of the minimum and maximum hydrogen densities listed above considers 100% water retention in the concrete. An assumed 70% reduction of water for a very dry environment for concrete without a liner plate results in a minimum hydrogen density of 0.00487 g/cm^3. The above calculation assumes no hydrogen in aggregates. If the aggregate is hydrogen bearing, the maximum hydrogen density may be increased by ~0.03 g/cm^3.

Different concrete compositions were investigated in [44]–[46]. Three concrete compositions with minimum, maximum, and typical hydrogen densities selected for this study are presented in Table 5.1. In addition, the typical water density of Type 04 concrete was reduced by 50% to evaluate the effect of keeping the composition of Type 04 concrete the same with the exception of the water content [47].

Table 5.1. Concrete Types Used in the Analysis.

Type	Reference	Hydrogen Density (g/cm^3)	Concrete Density (g/cm^3)	Note
01	ANL-6443 [45]	0.00484	2.33	Minimum hydrogen density
Hanford Wet	PNNL-15870, Rev. 1 [46]	0.029	2.35	Maximum hydrogen density
04	ANS-6.4-2006 (R2016) [44]	0.013	2.35	ANS-6.4-2006 (R2016) recommendation
Type 04 with 50% water reduction (Type 04 Mod)	ISRD10 Proceedings [47]	0.0065	2.29	Case performed to evaluate the effect of keeping the composition of Type 04 the same with the exception of water, which is reduced 50%

Note that this study does not include modeling of a hydrogen profile within the bioshield. In all calculations, a spatially uniform hydrogen content in concrete was assumed. This approach is consistent with standard modeling practice for concrete fluence analyses but may not be a conservative assumption. However, by examining a range of hydrogen contents with a total variation of nearly a factor of six, it is likely that bounding behaviors have been obtained. For a design basis calculation, though, it may be necessary to have details of any hydrogen variation in the bioshield.

5.2 Reinforcing Steel within the Bioshield

A sensitivity study addressing the impact of reinforcing steel (rebar) in the bioshield on neutron and gamma levels in the bioshield was performed using the following four cases.

(i) No rebar

(ii) #8 rebar (1-inch diameter) with a 3-inch concrete cover (i.e., the near edge of the rebar is located 3 inches inside the bioshield from the inner radius)

(iii) #14 rebar (1.75-inch diameter) with a 3-inch concrete cover

(iv) #14 rebar (1.75-inch diameter) with a 10-inch concrete cover

The configurations described in Cases (ii)–(iv) were provided by NRC Office of Nuclear Regulatory Research staff. In each case the horizontal and vertical rebar spacing was 12 inches, and the rebar was modeled explicitly following the guidance of ANSI/ANS-6.4-2006 (R2016) [44].

ANSI/ANS-6.4-2006 (R2016) indicates that for gamma sources, if rebar is considered, a homogenization of rebar and concrete is sufficient for the analysis. However, for neutron sources, if rebar is considered, a heterogenous treatment of rebar may be required in order to account for two competing effects: the increase in gamma radiation resulting from neutron capture in the rebar (i.e., radiative capture gammas) and an increase in gamma attenuation where rebar displaces concrete. In most cases, rebar composition is specified as low-carbon steel.

ANSI/ANS-6.4-2006 (R2016) evaluates the effect of the location of rebar in concrete and indicates that rebar within the first few inches of concrete causes an increase in capture gammas due to neutron thermalization and rebar in deeper locations of concrete causes an increased attenuation of gammas. The location effect of rebar is evaluated in the current analysis.

5.3 Bioshield Liner

The presence of a bioshield liner will impact neutron and gamma transmission into the bioshield and will also introduce an additional source of capture gamma radiation. In this study, the following two cases were considered.

(i) No liner

(ii) 0.25-inch-thick steel liner with no variation in thickness azimuthally. Both carbon steel and stainless steel were evaluated.

In case (ii), the thickness of the liner was taken from [6]. Note that in [6], the concrete surfaces of the ex-core detector wells are covered with a liner and other concrete surfaces are bare. In the current study, ex-core detector wells are not modeled, and the thickness of the concrete liner is assumed to be uniform. The existence and thickness of the liner may change on a plant-specific

basis. The purpose of the liner sensitivity study is to analyze the impact of a selected concrete liner plate thickness on neutron and gamma levels in the bioshield. Possible effects of ex-core detectors are outside the scope of this study.

5.4 Reflective Thermal Insulation

In order to perform a sensitivity study addressing the impact of reflective thermal insulation on neutron and gamma levels in the bioshield, the following two cases were considered.

(i) No reflective thermal insulation

(ii) 3-inch-thick reflective thermal insulation located between the RPV outer radius and bioshield inner radius

For case (ii), the thickness of the reflective thermal insulation was determined based on several UFSARs [39], [48]–[50] as well as the thickness provided in [6].

5.5 RPV-Bioshield Cavity Gap Width

The minimum and maximum cavity gap widths were determined by estimating the widths from reactor geometrical models presented in surveillance capsule analyses reports for one two-loop Westinghouse PWR, six three-loop Westinghouse PWRs, and five Combustion Engineering PWRs that were available in NRC ADAMS as well as data presented in the three-loop H. B. Robinson Unit 2 Cycle 9 benchmark [6] and the PWR pressure vessel benchmark prepared by Brookhaven National Laboratory for the NRC [51]. The minimum and maximum cavity gap widths were determined as ~16 cm and ~117 cm, respectively. In an attempt to cover other two-loop and three-loop PWR gap widths, this range was arbitrarily extended by 3 cm on both ends of the range, and the resultant gap width minimum and maximum were determined as 13 cm and 120 cm, respectively. In the current study, three cavity gap widths were analyzed:

(i) 13 cm (minimum gap width),
(ii) 71 cm (an intermediate gap width between the minimum and maximum widths), and
(iii) 120 cm (maximum gap width).

6 PARAMETER STUDY RESULTS

The parameter studies were carried out using hybrid radiation transport calculations with ADVANTG [52] and MCNP® [53]. ADVANTG generates variance reduction parameters that are used in subsequent MCNP® Monte Carlo simulations. The MCNP® calculations employed mesh tallies for each radiation quantity of interest (neutron fluxes, heating rates, and dose rates). Within the bioshield, the data were tallied using a cylindrical mesh tally with radial intervals of 1 cm, axial intervals of approximately 2.5 cm, and azimuthal intervals of 1º. Individual cylindrical mesh tallies were used for each rebar segment (hoop and vertical). Cartesian mesh tallies were used for each embedded support column and cantilever beam. A brief overview of mesh tallies is provided in Appendix B.2.1

Example mesh tally results are shown in Figure B-4 and Figure B-5. These plots illustrate the use of flooded (color-filled) contours and contour lines for the quantity of interest (e.g., gamma dose rate), markers to indicate the maximum values in the concrete, rebar, and column supports, and the mesh cell spacing for the cylindrical and cartesian mesh tallies. Examination of Figure B-4 and Figure B-5 will aid in understanding the features of the two-dimensional (2D) data plots throughout Section 6

The Monte Carlo simulation results provide statistical estimates of the mean and associated relative error for every mesh tally voxel (volume element). Common guidance for Monte Carlo calculations suggests that solutions should be converged such that the relative error for any tally value is less than 10%. For the calculations in this study, the solutions were typically converged to relative errors of less than 2%, and often less than 1%.

6.1 Concrete Composition

For the concrete composition parameter studies, neutron and coupled neutron/gamma calculations were performed using models with each of the four concrete types listed in Table 5-1. In each case #8 rebar with a 3-inch concrete cover was included in the bioshield. The cavity gap width was the intermediate gap width of 71 cm. No bioshield liner or reflective thermal insulation is present in these models. Plan and elevation views of this model are provided in APPENDIX A They may be referred to for orientation when viewing the one-dimensional (1D) and 2D data plots throughout Section 6 The dashed boxes labeled ‘A’ in the plan view plots of APPENDIX A show the spatial region that is included in most of the 2D data plots. As will be demonstrated in Section 6.5 the maximum incident neutron and gamma radiation levels occur near the X- and Y-axes of the quarter-core model (i.e., at azimuthal angles near 0º and near 90º).

6.1.1 Neutron Flux: Concrete Only

It is well known that the attenuation of neutrons through concrete is strongly dependent on the hydrogen content of the concrete [44]. The average energy loss from elastic scattering of neutrons by hydrogen is greater than the average energy loss for elastic scattering by any other element. Thus, the hydrogen content of the concrete plays a key role in the moderation (slowing down) of fast neutrons and in the subsequent thermalization of those neutrons. The thermal neutrons are absorbed by hydrogen and other elements in the concrete. Those absorption reactions typically produce secondary gamma rays which then contribute to heating and to gamma dose rates.

In this section we consider the attenuation of neutrons through the four concrete types for four energy ranges of interest.

1) E > 1.0 MeV
2) E > 0.1 MeV (100 keV)
3) E > 1.0E-05 eV
4) E < 1 eV

The first three energy ranges are those listed in Section 2.3 The fourth range is representative of the thermal neutron flux. While there is no single “cutoff” energy that is considered to be the upper limit for thermal neutrons, typical values are a fraction of 1 eV.

6.1.1.1 *Neutron flux by energy range: general characteristics*

While differences in the concrete compositions evaluated in this study have a marked effect on the neutron flux, gamma dose rates, and total heating rates, there are common characteristics of how the neutron flux behaves as a function of energy for each concrete type.

Figure 6-1 and Figure 6-2 show the neutron flux for five energy ranges (including the total flux) in Type 04 concrete at an elevation of 200 cm and azimuthal angles of 3.5º and 44.5º. This elevation was chosen because it is near the core midplane and is likely to see the highest fluence accumulation for plant designs similar to the model used in this study. In these and all other 1D plots in this report, the mean values are plotted using symbols, and the associated 95% confidence intervals are shown as error bars.

6.1.1.2 *The azimuthal angles of 3.5º and 44.5º were chosen for two reasons.*

1) They represent locations that have the minimum (at 3.5º) and maximum (at 44.5º) amounts of water between the outer edge of the fuel assemblies and the core barrel (see Figure A-1). This results in neutron flux levels incident to the bioshield that are at or near the maximum and minimum values, respectively.

2) These axial and azimuthal locations provide neutron flux traverses that are entirely within concrete and do not pass through any steel (rebar or support columns) in the bioshield. This provides the optimal “concrete-to-concrete” comparisons.

The following observations can be made from Figure 6-1.

1) The neutron flux for E > 1.0 MeV and for E > 0.1 MeV decrease monotonically through the concrete.

2) For the energy range 1 eV < E < 0.1 MeV, there is a peak (maximum) value at ~2 cm into the concrete. This peak occurs as neutrons with E > 0.1 MeV are down scattered (scattered to lower energies) in the concrete.

3) The neutron flux for E < 1 eV undergoes an initial increase in the concrete as higher-energy neutrons are moderated and thermalized by successive scatters. For the Type 04 concrete, the thermal peak occurs at a depth of ~12 cm.

4) Because of the peaking noted in observation 2 and, to a lesser extent in observation 3, the total flux undergoes a slight peak at ~2 cm into the concrete.

5) The fraction of the total flux due to neutrons with E < 1 eV increases monotonically through the concrete before reaching an asymptotic value.

At an azimuthal location of 44.5º (Figure 6-2), there is no peaking of the neutron flux for the energy range 1 eV < E < 0.1 MeV, and the thermal flux peak occurs ~10 cm into the concrete. These differences relative to the 3.5º location are due to changes in the incident neutron flux spectrum at the inner radial surface of the bioshield as shown in Figure 6-3. Due to the greater amount of water between the outer edge of the fuel assemblies and the core barrel at 44.5º, the incident neutron spectrum is 'softer' (shifted toward lower energies), so there are fewer neutrons with E > 0.1 MeV available to down scatter into the lower energy ranges.

Figure 6-4 through Figure 6-6 show the neutron flux by energy range at an elevation of 200 cm and an azimuthal angle of 3.5º for the Type 01 concrete, Type 04 mod concrete, and Hanford wet concrete. For the Type 01 concrete (Figure 6-4), which has the minimum hydrogen content, there is less moderation and thermalization of the neutrons with E > 0.1 MeV compared to the Type 04 concrete, and the peaks in the neutron flux for 1 eV < E < 0.1 MeV and for E < 1 eV occur at greater depths. The flux behavior in the Type 04 mod concrete (Figure 6-5) is similar to that in the Type 01 concrete. The Hanford wet concrete (Figure 6-6), which has the maximum hydrogen content, has flux peaks at < 2 cm into the concrete for 1 eV < E < 0.1 MeV and at ~7 cm into the concrete for E < 1 eV. These 'rapid' peaks are due to the increased moderation and thermalization resulting from the higher hydrogen content.

6.1.1.3 *Neutron energies E > 1.0 MeV and E > 0.1 MeV*

Figure 6-7 through Figure 6-9 show the attenuation of the neutron flux in each concrete type for E > 1.0 MeV and E > 0.1 MeV at an elevation of 200 cm and azimuthal angles of 3.5º and 44.5º.

Figure 6-10 and Figure 6-11 show the neutron flux attenuation at the same azimuthal locations at an elevation of 400 cm.

For each of the curves in Figure 6-7 through Figure 6-11 (as well as in some of the subsequent 1D radial plots), an exponential function of the following form has been fitted to the data using a weighted least-squares fit:

$$\phi(r) = \phi_0 e^{-b(r-r_0)},$$

where $\phi(r)$ = the neutron flux at radial location r (cm),
r_0 = the radius of the first mesh tally voxel in the bioshield (cm),
ϕ_0 = the neutron flux at r_0, and
b = the attenuation coefficient (cm^{-1}).

These fits are applied to the radial extent at which the "incident" flux ϕ_0 has been attenuated by a factor of 10. Partial range fits over this range of values are employed because in many cases a single exponential attenuation does not adequately model the flux behavior through the entire bioshield.

The effect of the hydrogen content is clear in these figures. As expected, the most rapid attenuation of the neutron flux for both energy ranges (E > 1.0 MeV; E > 0.1 MeV) occurs with the Hanford wet concrete, while significantly less attenuation occurs with the Type 01 and modified Type 04 concretes. The following observations can be made from these results.

1) At each of the elevations shown, the flux for E > 1.0 MeV and E > 0.1 MeV at the inner surface of the bioshield at 3.5º is 2–4 times higher than the corresponding flux at 44.5º. This is due to the core geometry. Angles near 0º and 90º have the minimal amount of

water between the outer assemblies and the core barrel and hence have less attenuation of the neutron flux radially outward from the edge of the assemblies.

2) At each axial/azimuthal location, the attenuation coefficients for neutrons with E > 0.1 MeV are greater than the corresponding attenuation coefficients for E > 1.0 MeV. This increased attenuation rate of the flux for E > 0.1 MeV is a result of the energy dependence of the hydrogen scattering cross section, which decreases monotonically over an energy range from approximately 10 keV (0.01 MeV) to 20 MeV (the upper energy limit in typical neutron shielding calculations). As neutrons are scattered to lower energies, their probability of scattering from hydrogen continuously increases, resulting in a more rapid rate of attenuation as the neutron energy decreases.

3) The attenuation coefficients for neutrons with E > 1.0 MeV at a specific elevation are consistent at 3.5º and 44.5º. This is not the case for neutrons with E > 0.1 MeV. For that energy range, the attenuation coefficients are greater at 44.5º. This is due to differences in the spectrum of the incident neutron flux at these two azimuthal locations as noted in Section 6.1.1.1

4) The attenuation coefficients for each energy range are larger at an elevation of 400 cm than at 200 cm. This is due to differences in the incident neutron flux spectrum at these two elevations. At 400 cm the incident flux is affected more by the contribution of neutrons that have scattered in the cavity gap, including those that have scattered in the cantilever beams for the short column supports.

6.1.1.4 *Neutron energies E > 1.0E-05 eV*

The neutron flux as a function of radial position for E > 1.0 MeV and E > 0.1 MeV decreases monotonically with depth through the bioshield. However, for neutron energies below 0.1 MeV, the flux can exhibit a peak value at some distance into the concrete as noted in Section 6.1.1.1 This behavior can be seen in Figure 6-12, which illustrates the total flux through the concrete at an elevation of 200 cm. For an azimuthal angle of 3.5º (the maximum incident flux location), the peak value of the total flux for each concrete type occurs in the first few centimeters of the concrete. This peaking can be seen more clearly in Figure 6-13, which shows the total flux behavior in the first 12 cm of the concrete. At an azimuthal angle of 44.5º, the maximum total flux occurs at the inner surface of the concrete. At this location the neutron flux spectrum is degraded in energy relative to the 3.5º location, so there are fewer neutrons with E > 0.1 MeV to moderate. This can be seen in Figure 6-14, which shows the azimuthal variation of the fractions of the incident total neutron flux with E > 1.0 MeV and with E > 0.1 MeV.

6.1.1.5 *Neutron energies E < 1 eV*

Neutrons with energies less than 1 eV are not a significant concern with respect to neutron damage effects in concrete, but they are important due to their role in heating and dose rates. Much of the energy deposition within the bioshield is caused by gamma sources that are a result of radiative capture as neutrons are moderated and thermalized in the concrete. These effects are illustrated in Sections 6.1.3 and 6.1.4

The neutron flux for E < 1 eV initially increases with depth in the concrete as higher-energy neutrons are moderated and thermalized. The flux then decreases monotonically with additional depth into the concrete. Both the location and magnitude of the peak thermal flux value are affected by the hydrogen content of concrete as noted in Section 6.1.1.1 Those factors in turn

affect the spatial distribution of the total heating rate and the gamma dose rate. Figure 6-15 illustrates the flux distribution for neutrons with E < 1 eV at an elevation of 200 cm and azimuthal angles of 3.5º and 44.5º. The following observations can be made from the data in this figure.

1) Increases in the hydrogen content of concrete result in higher maximum flux levels for E < 1 eV. These higher peak values, which occur at "shallower" depths in the concrete (i.e., at locations closer to the inner surface of the bioshield), are due to increased moderation and thermalization of neutrons in concrete that contains high levels of hydrogen. In contrast, concretes with lower hydrogen content have thermal flux peaks that are lower in magnitude, broader, and are shifted to further depths in the concrete.

2) The higher thermal flux peaks in the concretes with higher hydrogen content are followed by more rapid attenuation of the thermal flux at locations beyond the thermal peak. This behavior has a direct effect on total heating rates and gamma dose rates, which will be seen in Section 6.1.3 and subsequent sections.

6.1.2 Neutron Flux: Effect of Rebar and Support Columns

The results presented in Section 6.1.1 are appropriate for neutron attenuation through portions of the bioshield that do not contain steel. The presence of rebar and the RPV support columns must also be considered with regard to the behavior of the neutron flux. For the energy ranges that are considered for neutron fluence effects in concrete, the presence of structural steel has a minor effect, as shown in Figure 6-16 (E > 1.0 MeV) and Figure 6-17 (E > 0.1 MeV).

The total neutron flux (E > 1.0E-05 eV) is sensitive to the presence of steel, as evidenced by the depression of the total flux contours in Figure 6-18. The flux depression effect due to steel is most pronounced for the low-energy neutrons (E < 1 eV), as shown in Figure 6-19. The flux depression of these low-energy neutrons is caused by neutron capture (absorption) in the steel, which produces capture gammas that are important contributors to heating and dose rates.

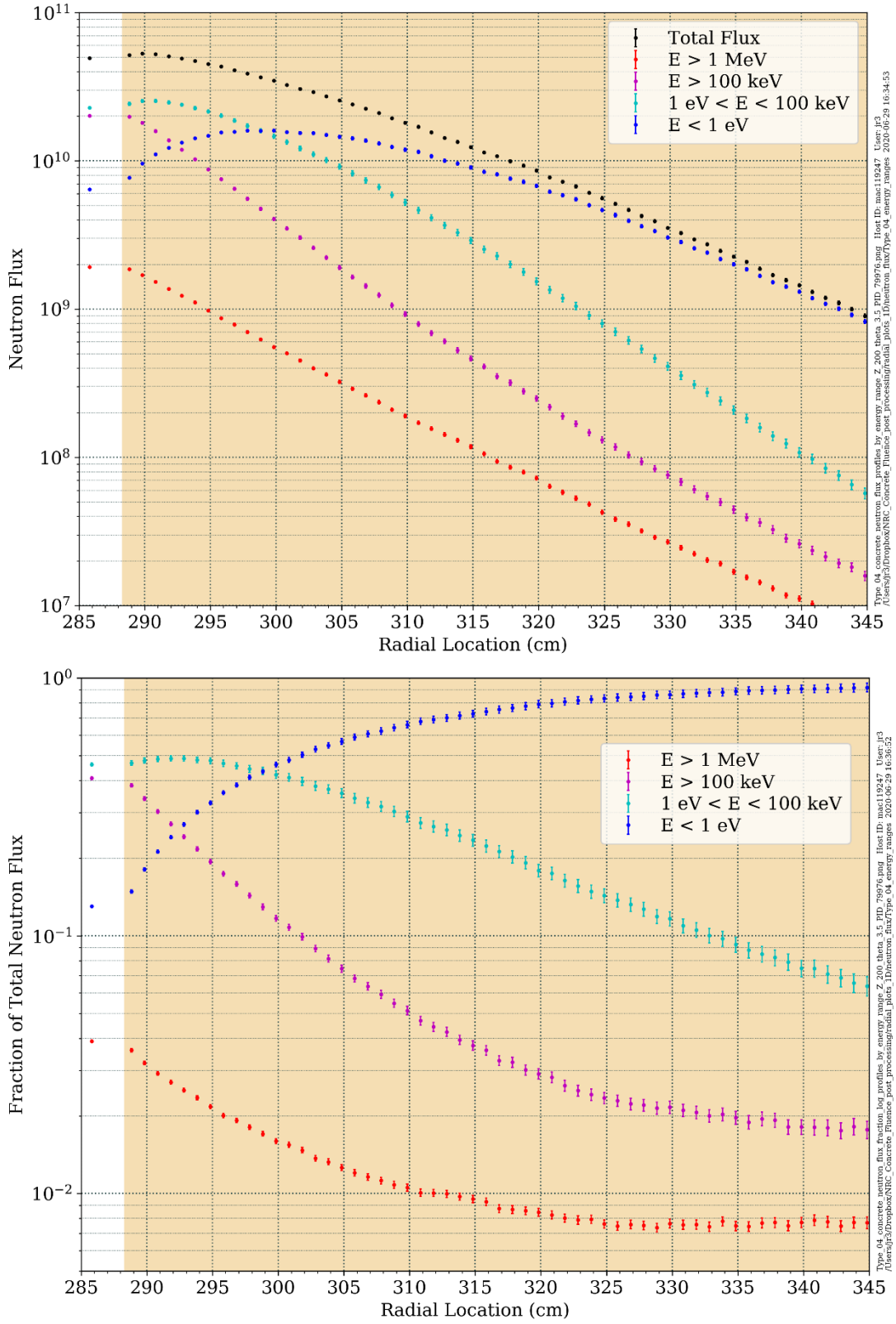

Figure 6-1 Neutron flux radial profiles by energy interval through Type 04 concrete at an elevation of 200 cm and an azimuthal angle of 3.5º

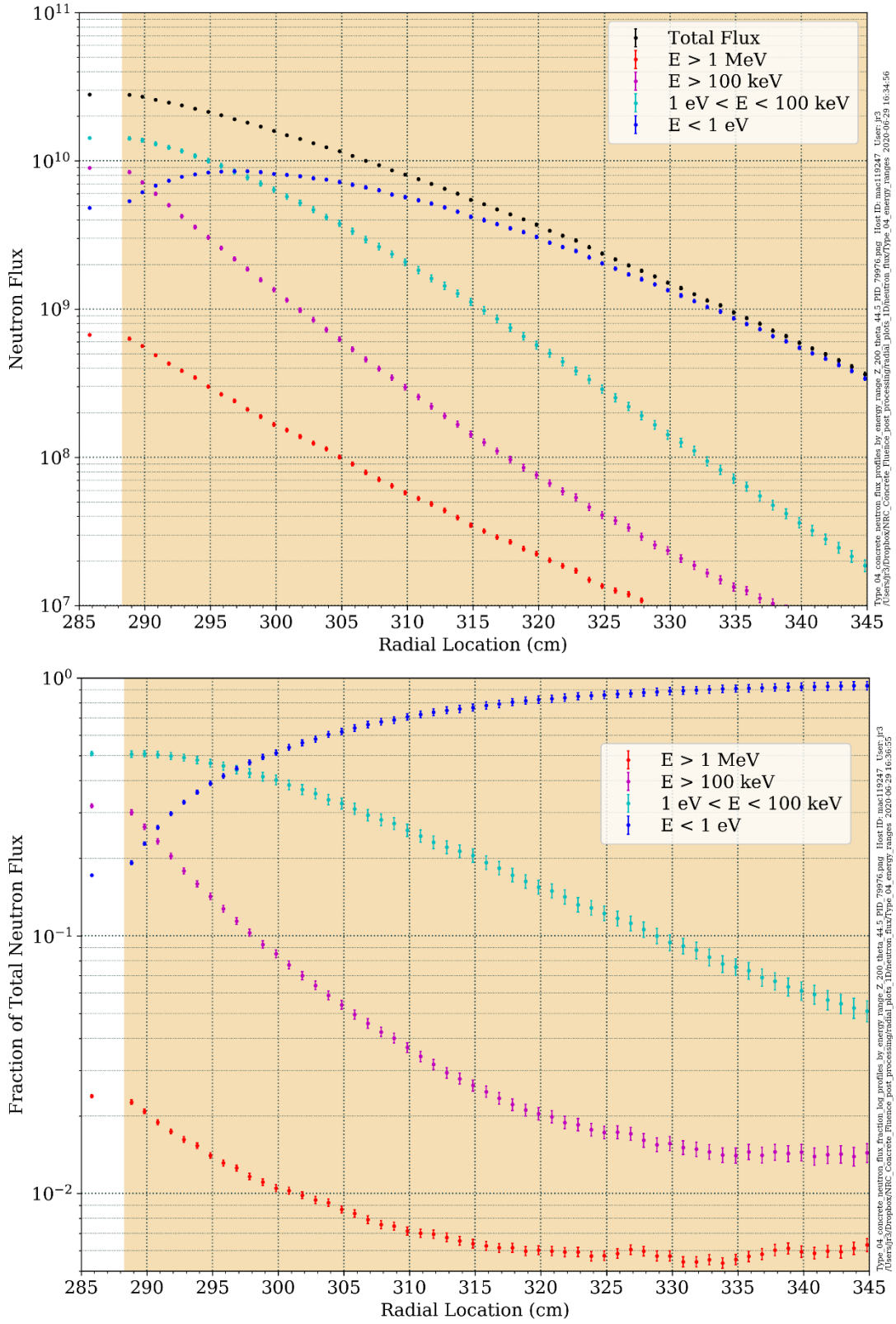

Figure 6-2 Neutron flux radial profiles by energy interval through Type 04 concrete at an elevation of 200 cm and an azimuthal angle of 44.5º

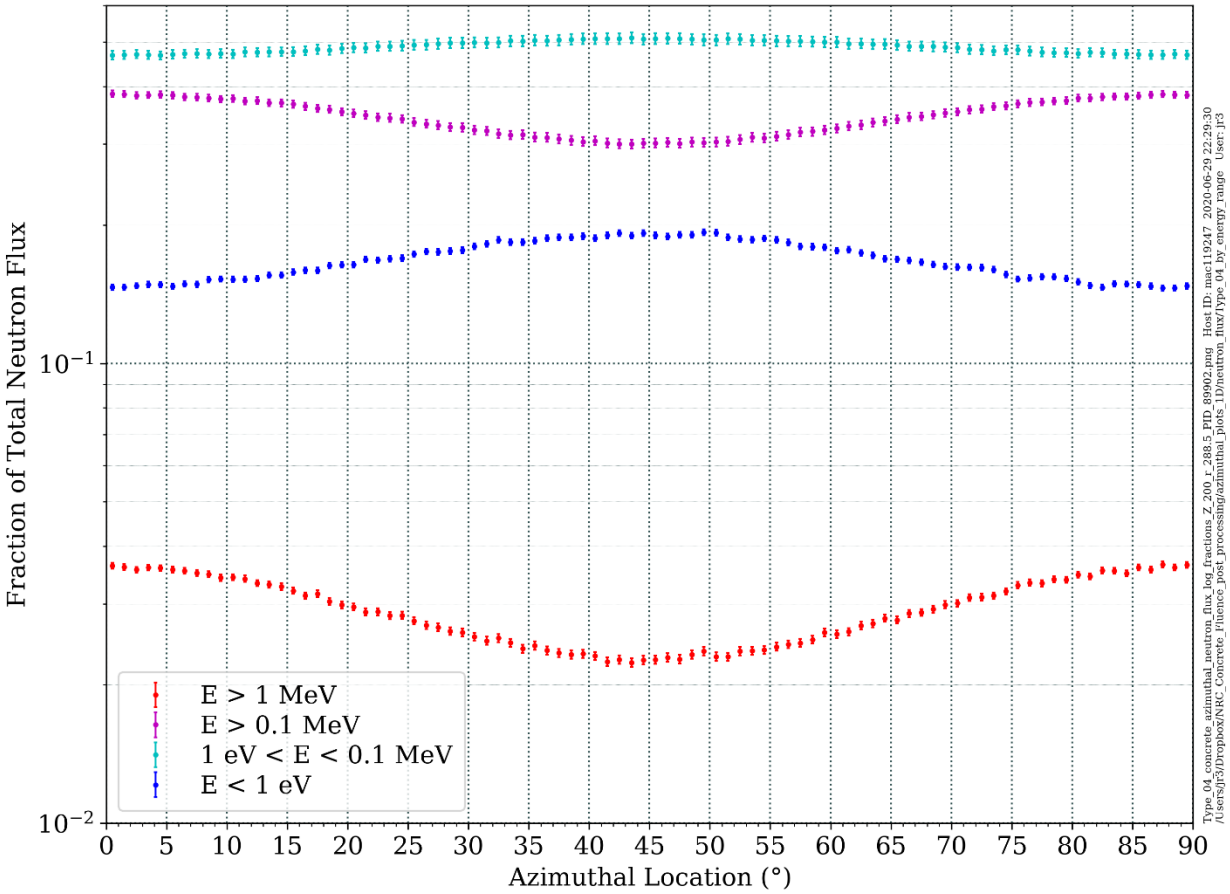

Figure 6-3 Azimuthal variation of the fraction of the total neutron flux for four energy ranges at the inner surface of the bioshield. Type 04 concrete

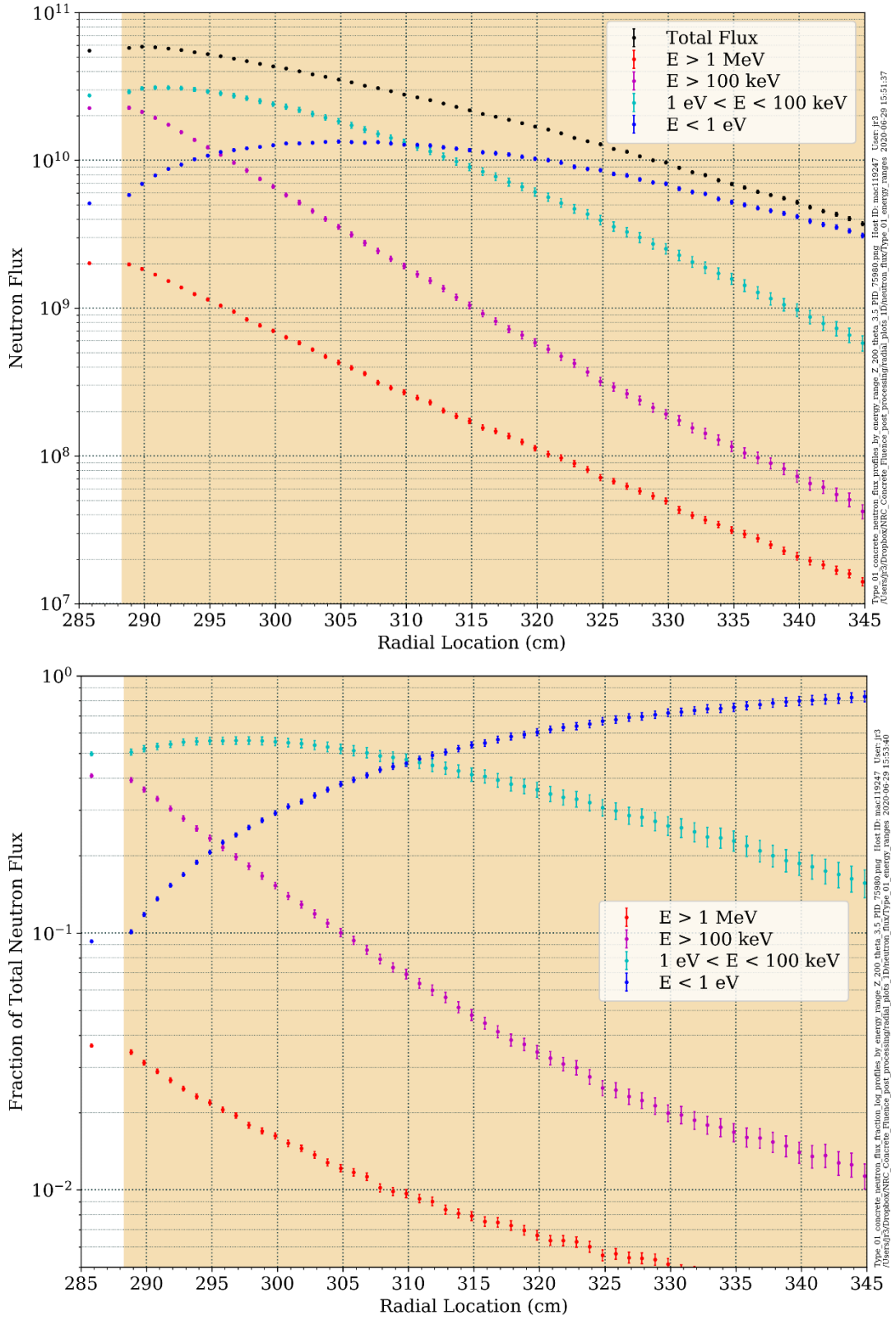

Figure 6-4 Neutron flux radial profiles by energy interval through Type 01 concrete at an elevation of 200 cm and an azimuthal angle of 3.5º

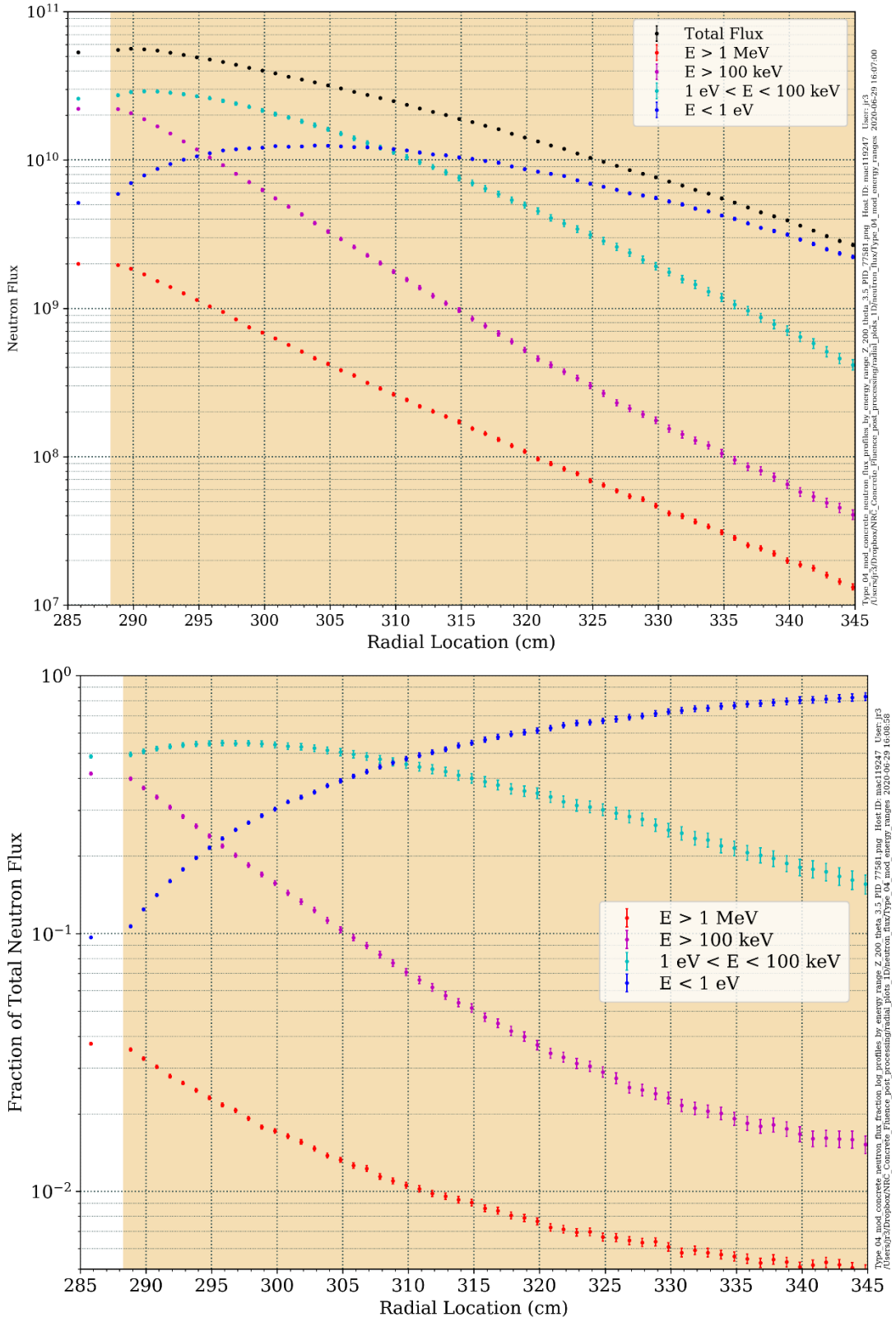

Figure 6-5 Neutron flux radial profiles by energy interval through Type 04 mod concrete at an elevation of 200 cm and an azimuthal angle of 3.5º

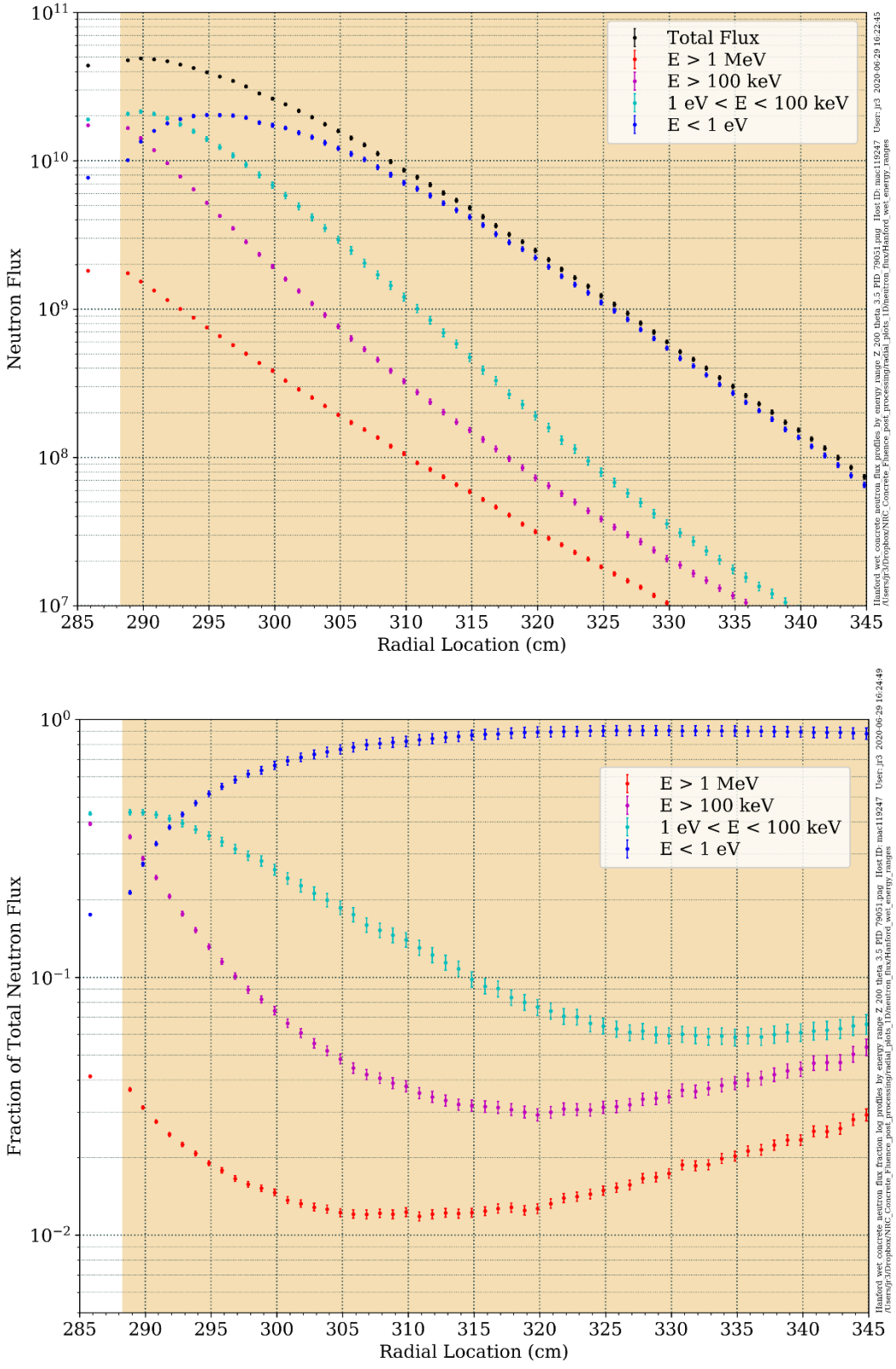

Figure 6-6 Neutron flux radial profiles by energy interval through Hanford wet concrete at an elevation of 200 cm and an azimuthal angle of 3.5º

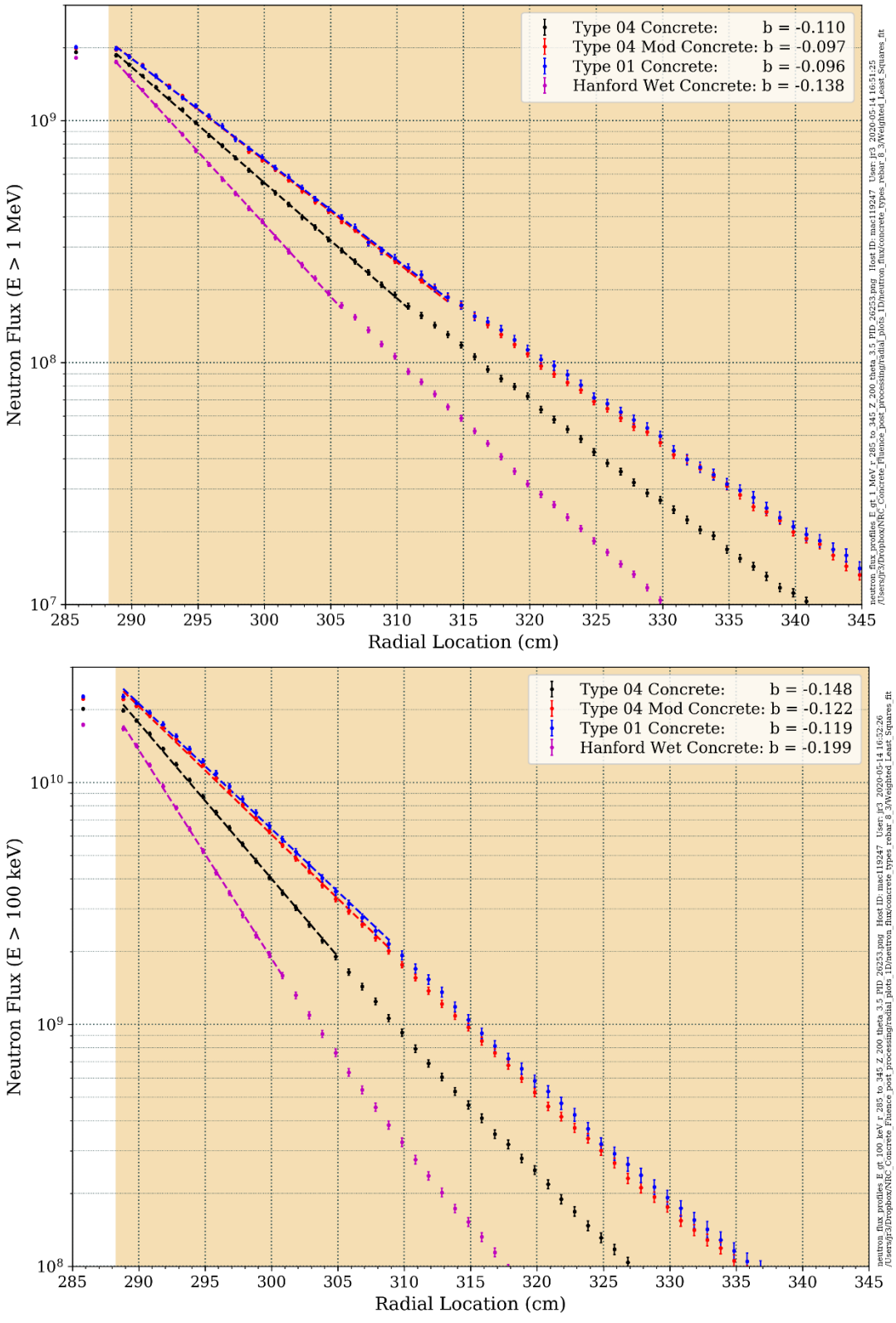

Figure 6-7 Neutron flux (E > 1.0 MeV and E > 0.1 MeV) radial profiles through four concrete types at an elevation of 200 cm and an azimuthal angle of 3.5º (See Section 6.1.1.2 for a discussion of the parameter 'b')

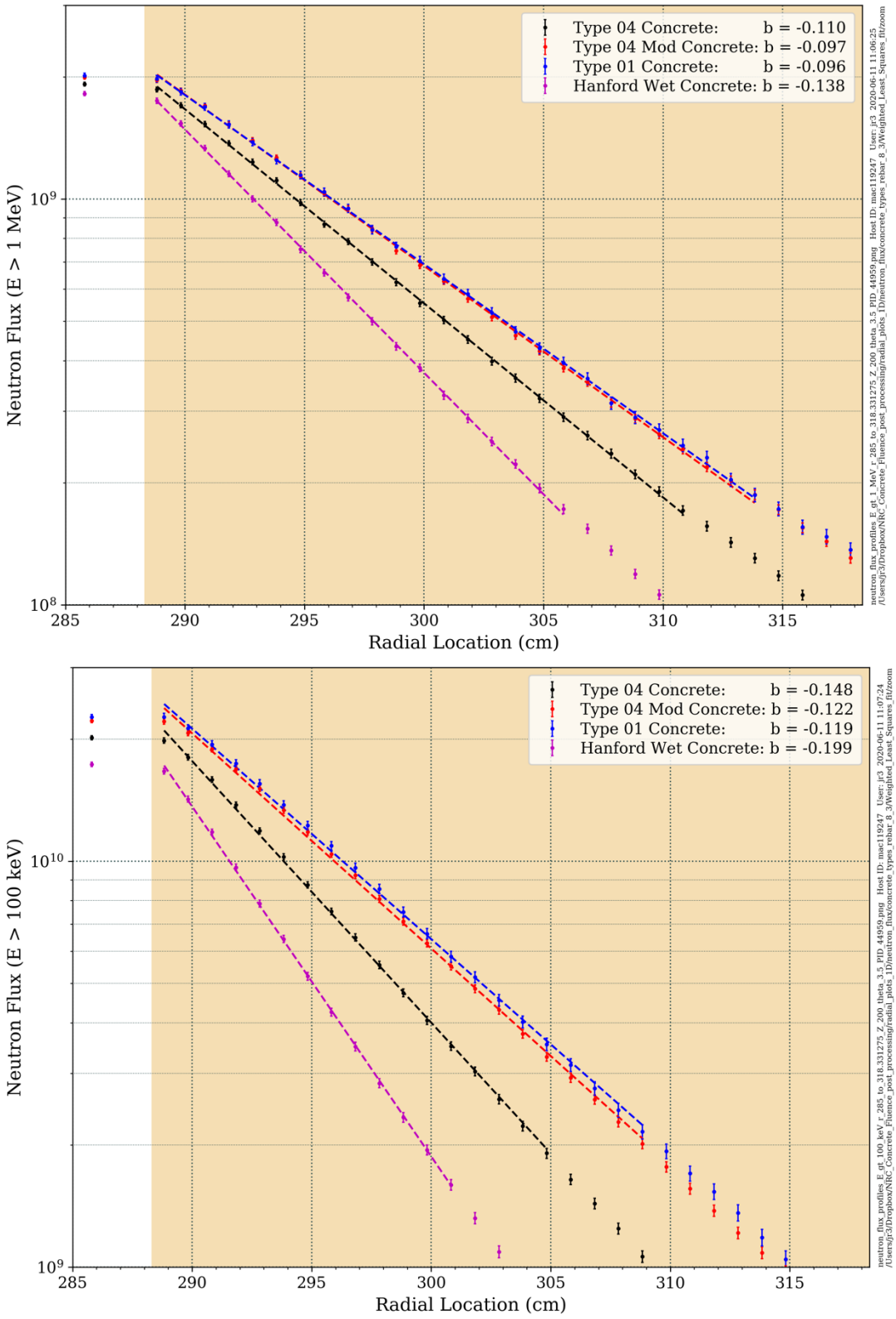

Figure 6-8 Neutron flux (E > 1.0 MeV and E > 0.1 MeV) radial profiles through the first 30 cm of the bioshield for four concrete types at an elevation of 200 cm and an azimuthal angle of 3.5º (See Section 6.1.1.2 for a discussion of the parameter 'b'

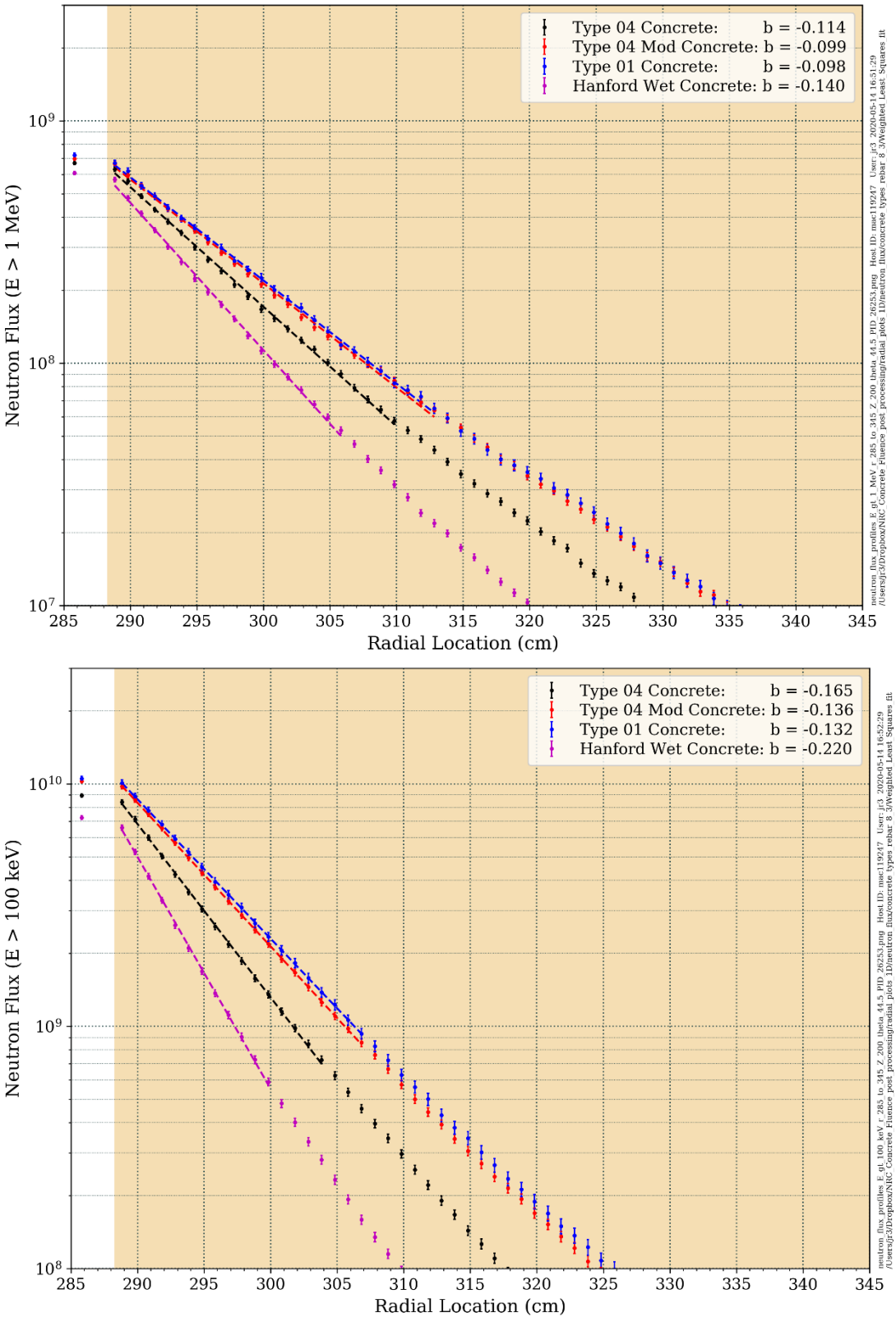

Figure 6-9 Neutron flux (E > 1.0 MeV and E > 0.1 MeV) radial profiles through four concrete types at an elevation of 200 cm and an azimuthal angle of 44.5º

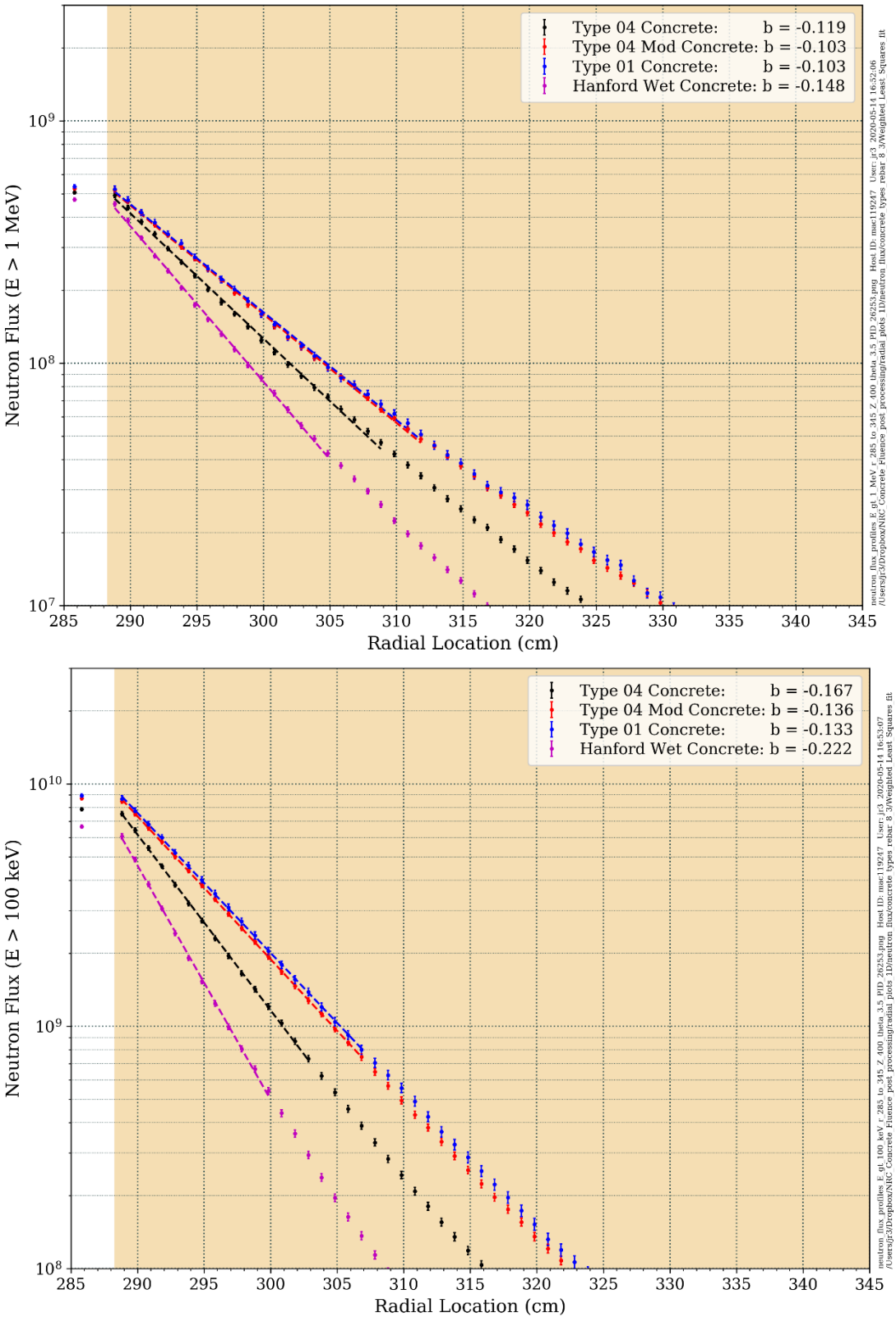

Figure 6-10 Neutron flux (E > 1.0 MeV and E > 0.1 MeV) radial profiles through four concrete types at an elevation of 400 cm and an azimuthal angle of 3.5º

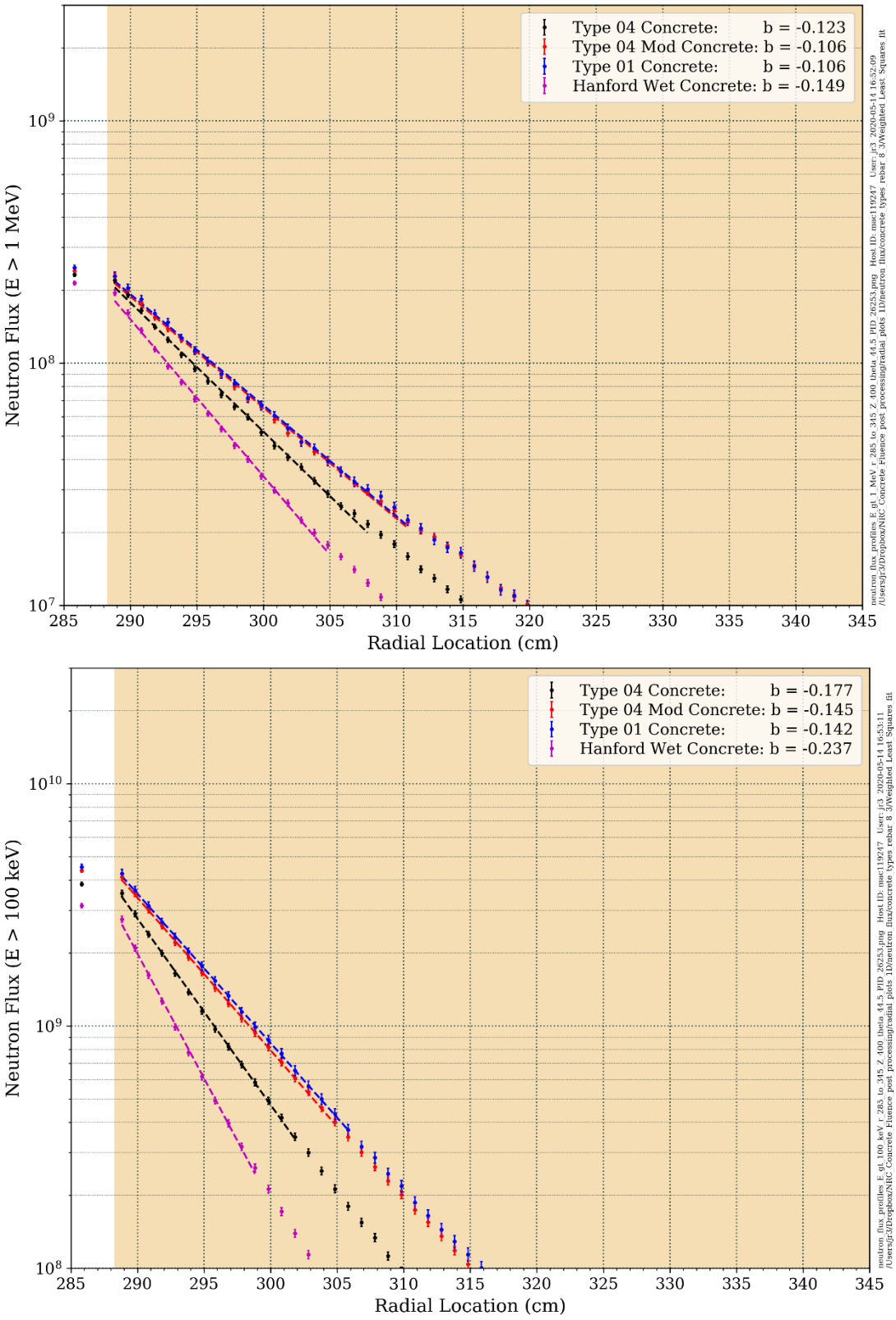

Figure 6-11 Neutron flux (E > 1.0 MeV and E > 0.1 MeV) radial profiles through four concrete types at an elevation of 400 cm and an azimuthal angle of 44.5º

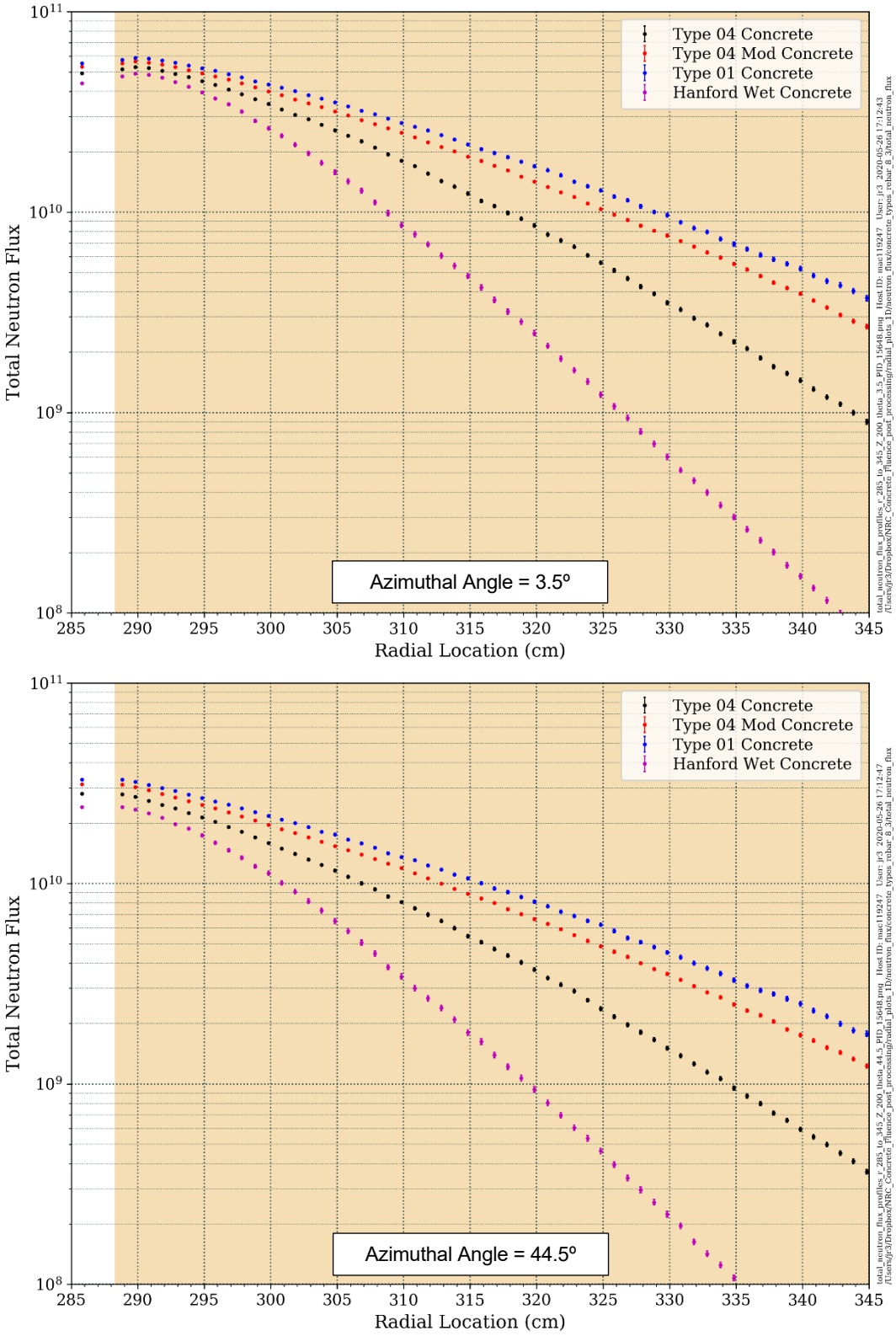

Figure 6-12 Total neutron flux (E > 1.0E-05 eV) radial profiles through four concrete types at an elevation of 200 cm and azimuthal angles of 3.5º and 44.5º

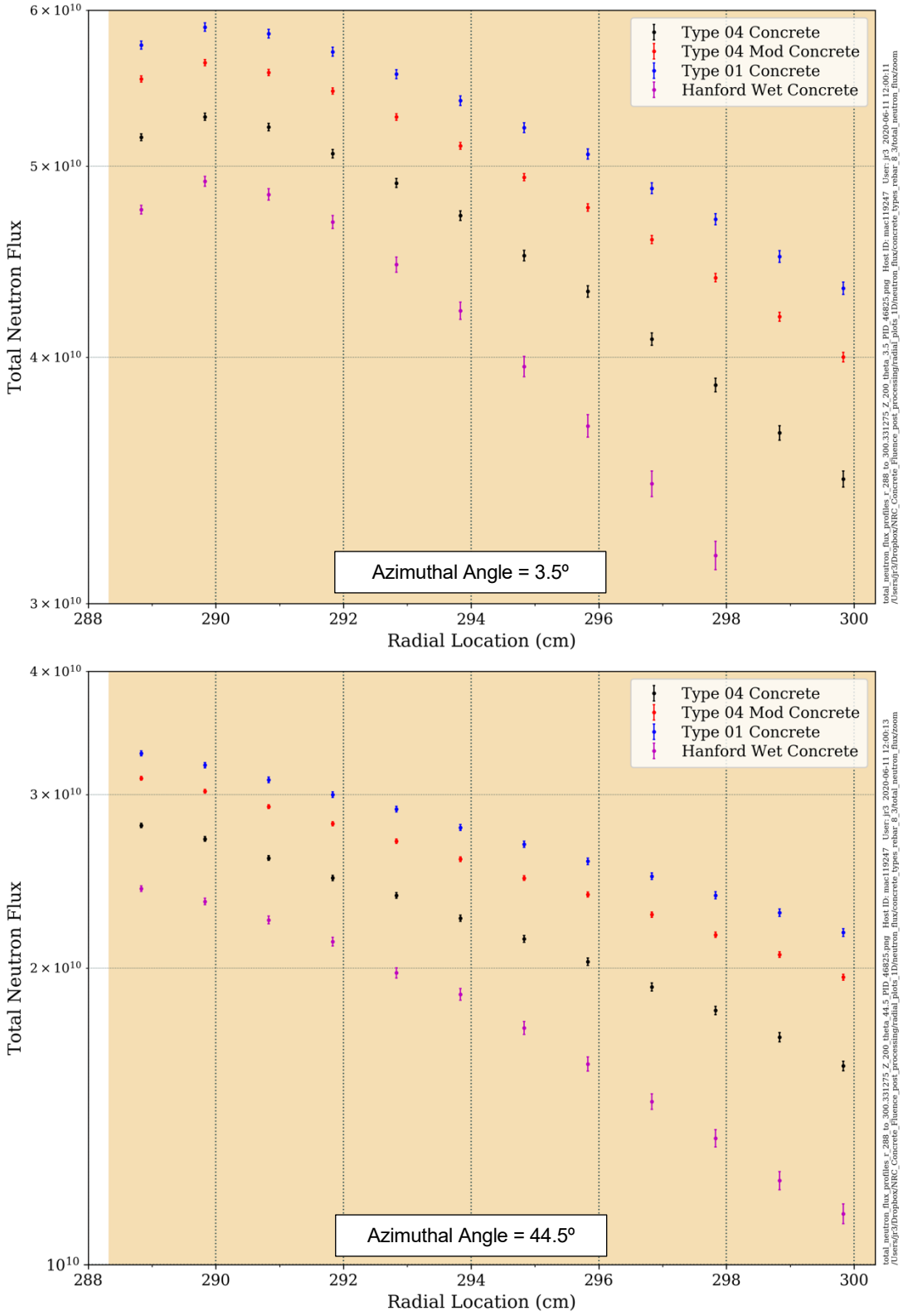

Figure 6-13 Total neutron flux (E > 1.0E-05 eV) radial profiles through four concrete types at an elevation of 200 cm and azimuthal angles of 3.5º and 44.5º. (Detail through the first 12 cm of the concrete)

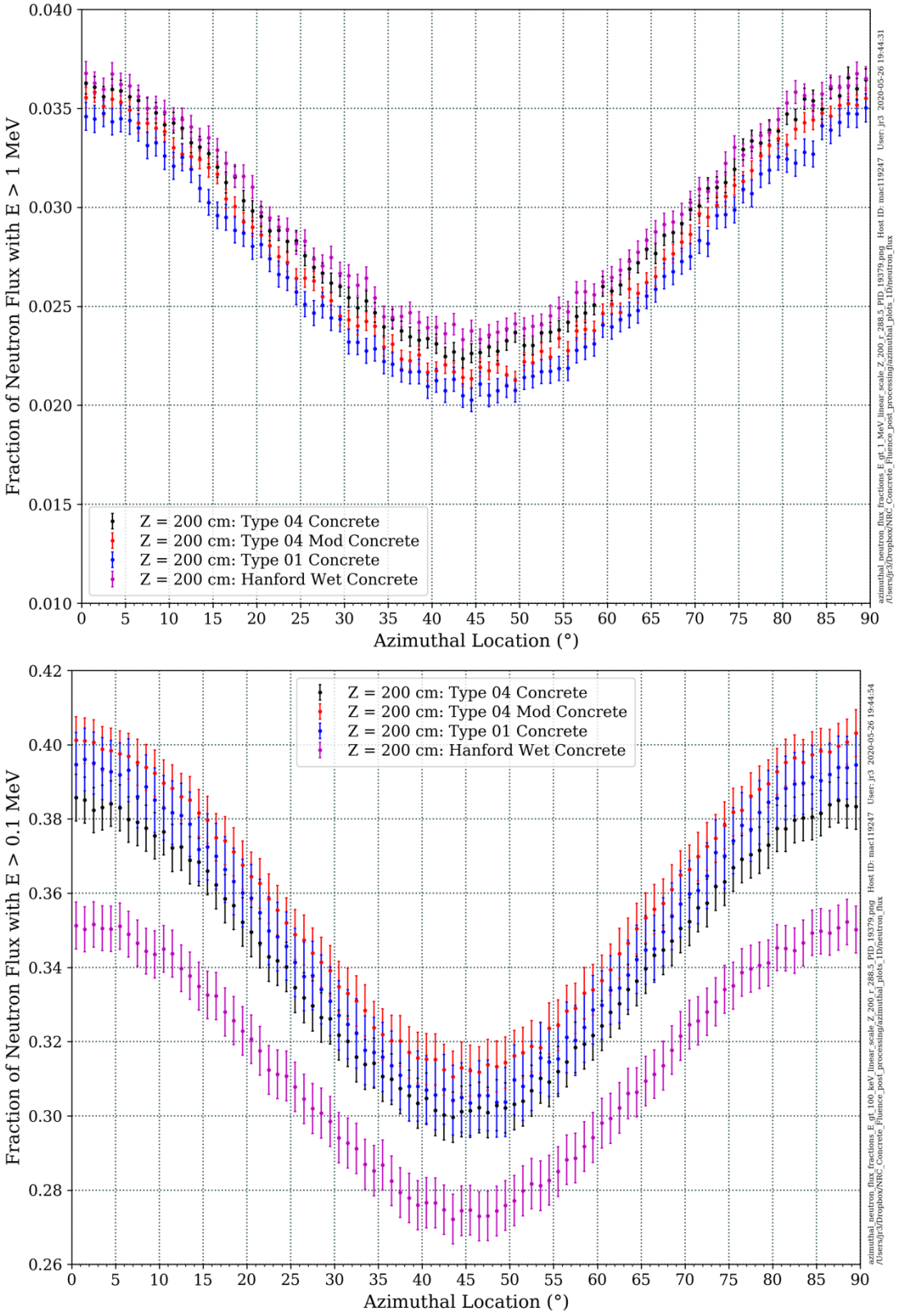

Figure 6-14 Fraction of the neutron flux incident at the inner surface of the bioshield with E > 1.0 MeV and with E > 0.1 MeV in four concrete types at an elevation of 200 cm

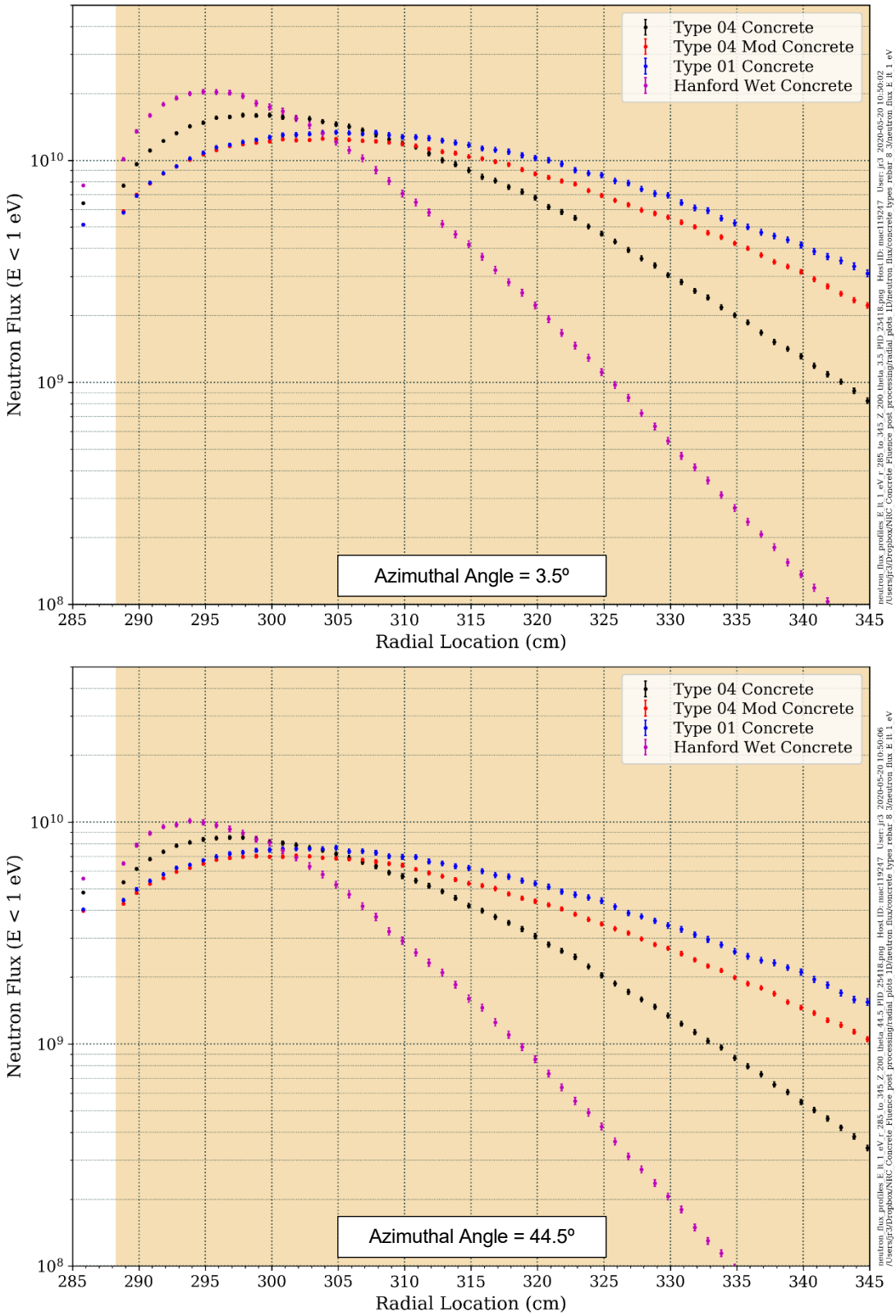

Figure 6-15 Neutron flux (E < 1 eV) radial profiles through four concrete types at an elevation of 200 cm and azimuthal angles of 3.5º and 44.5º

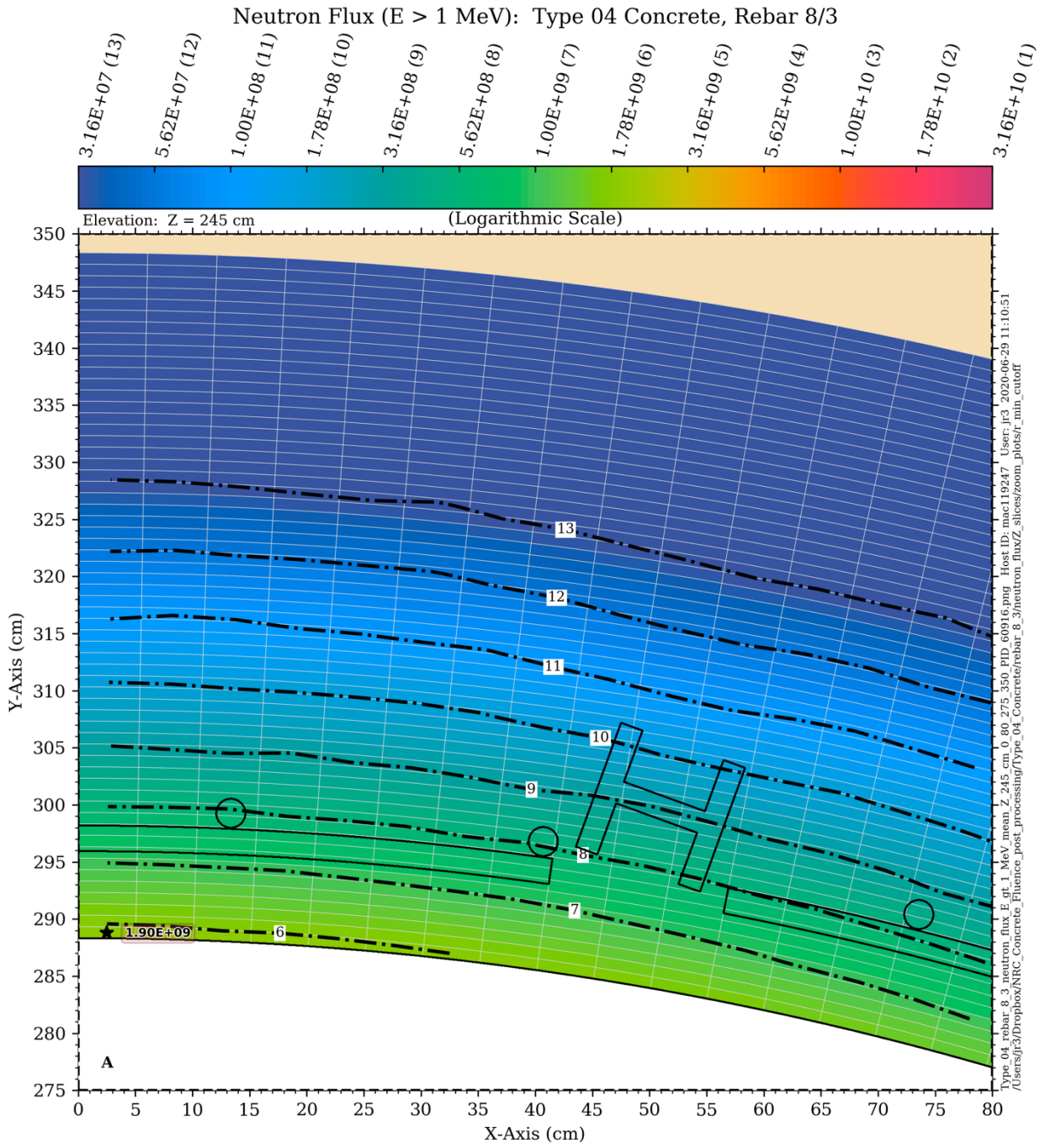

Figure 6-16 Neutron flux contours in Type 04 concrete for E > 1.0 MeV at an elevation of 245 cm. (This elevation includes hoop and vertical rebar and support columns)

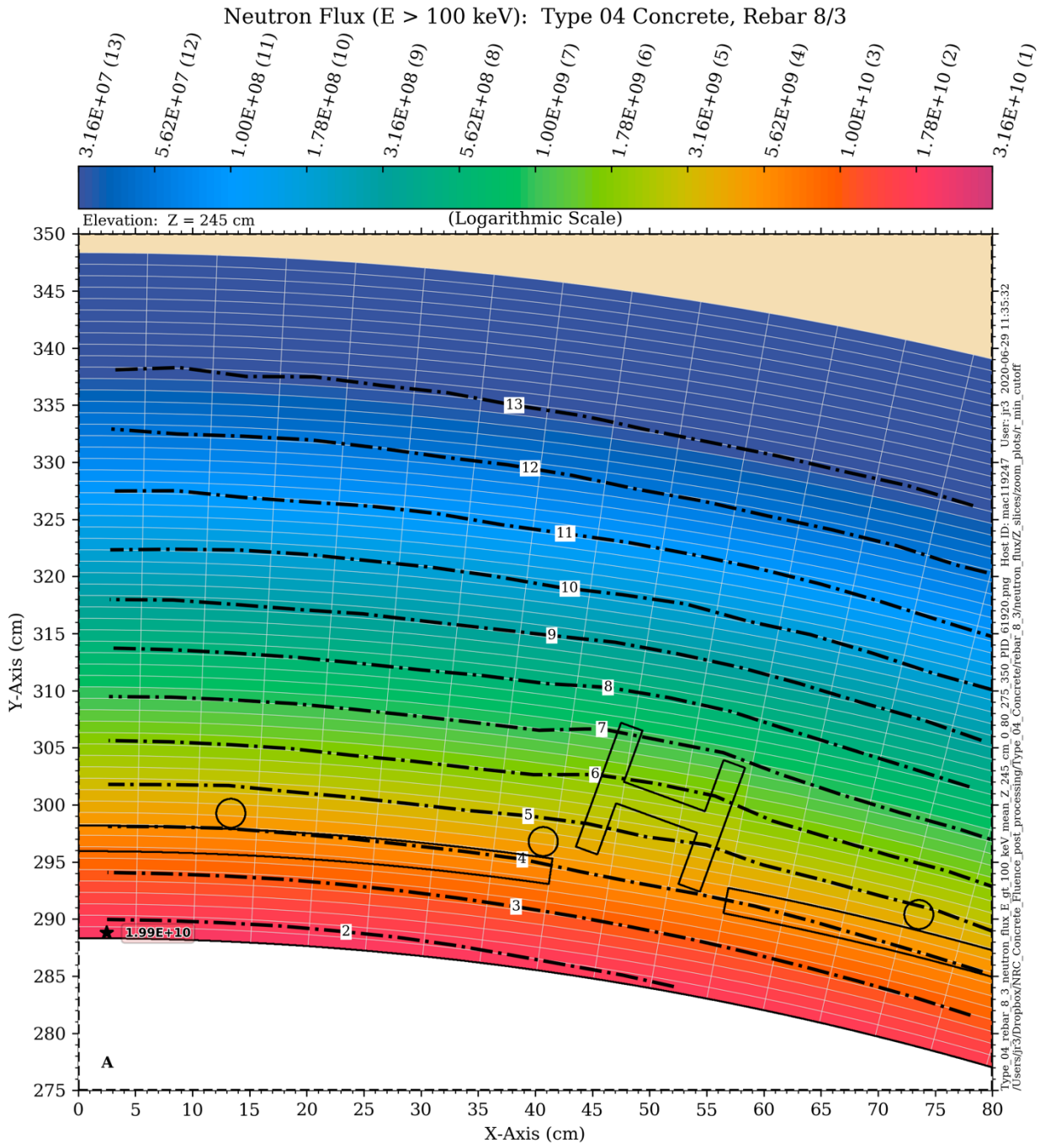

Figure 6-17 Neutron flux contours in Type 04 concrete for E > 0.1 MeV at an elevation of 245 cm. (This elevation includes hoop and vertical rebar and support columns)

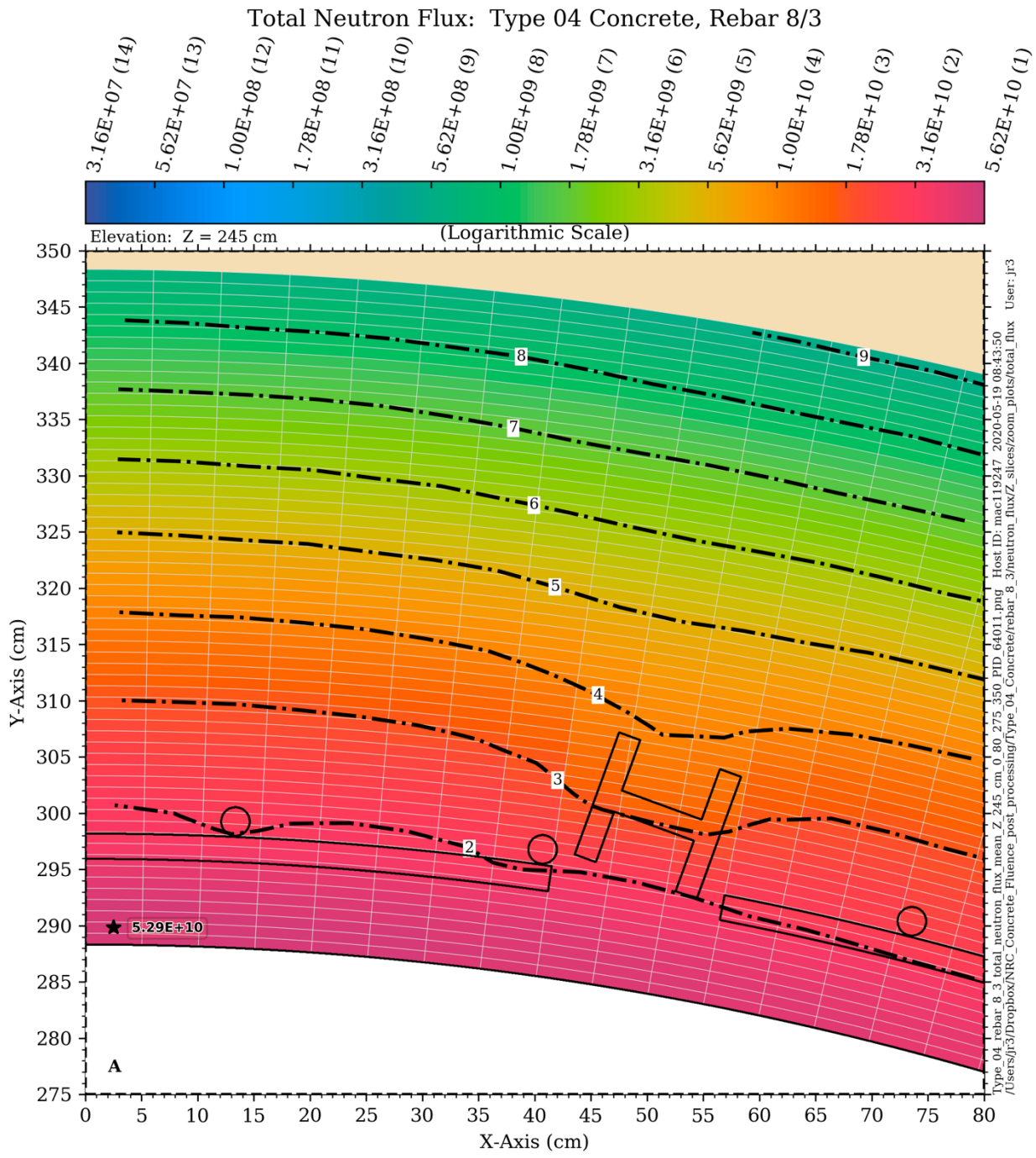

Figure 6-18 Total neutron flux contours in Type 04 concrete at an elevation of 245 cm. (This elevation includes hoop and vertical rebar and support columns)

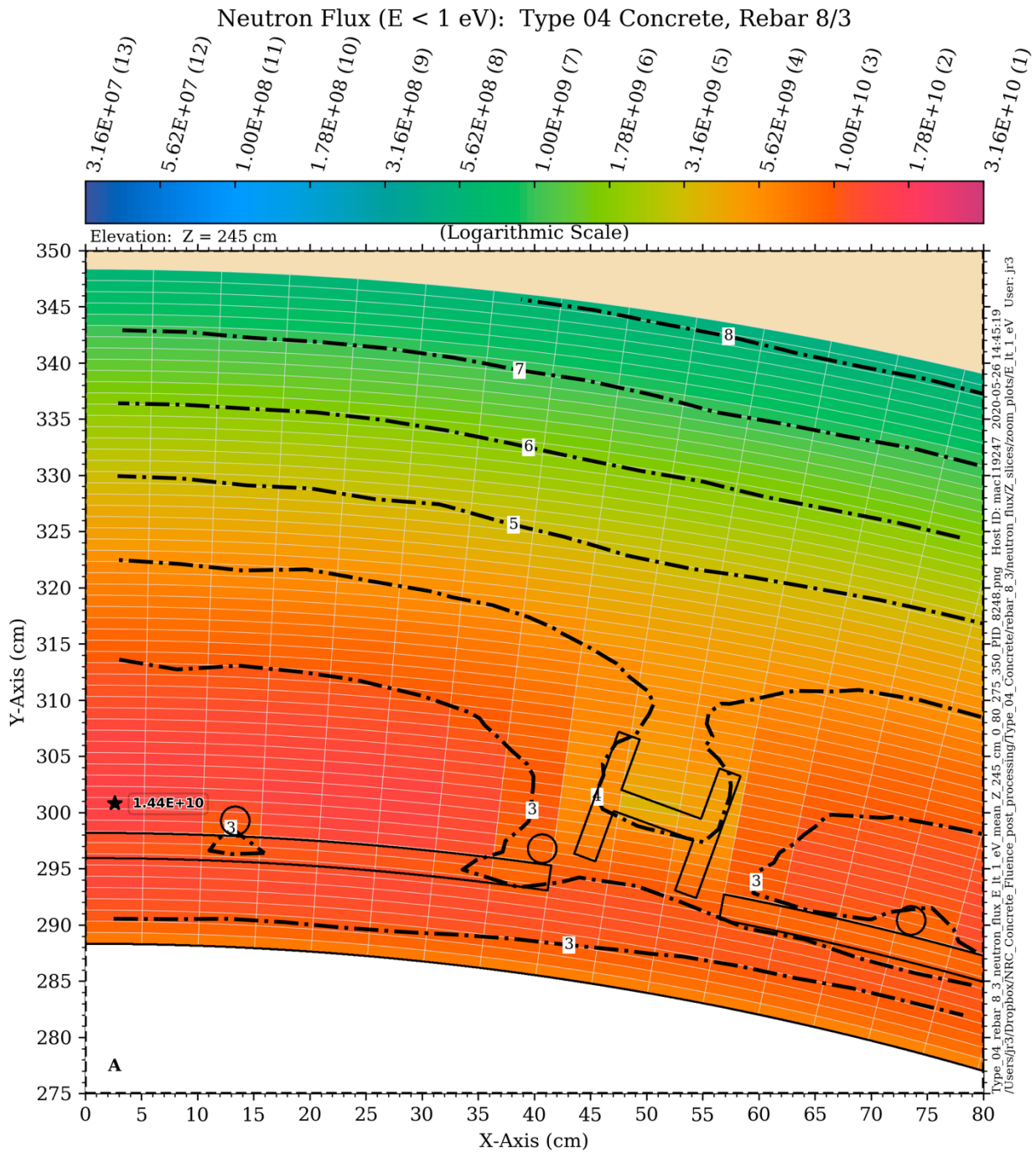

Figure 6-19 Neutron flux contours in Type 04 concrete for E < 1 eV at an elevation of 245 cm. (This elevation includes hoop and vertical rebar and support columns)

6.1.3 Total Heating Rate: Concrete Only

The total heating rate provides the radiation heat-generation rate in the bioshield concrete and the steel structural components and rebar. It includes contributions from neutron heating and gamma heating. Gamma heating can be further broken down into two components: "incident" gamma heating, which is due to gammas that are produced in the core and core structural components and reach the bioshield, and "self-heating", which is caused by gamma radiation that is produced by radiative capture within the concrete and steel in the bioshield. Figure 6-20 illustrates the contributions to the total heating rate in Type 04 concrete at an elevation of 200 cm and an azimuthal angle of 3.5º. At the inner surface of the bioshield, the incident gamma heating is slightly higher than the self-heating, but the incident gamma heating is rapidly attenuated and is lower than the self-heating within a few centimeters. The self-heating reaches a peak value about 15 cm into the concrete and then decreases monotonically. The combination of the two produces a gamma heating rate curve that is nearly uniform for ~12 cm before decreasing monotonically.

In considering this behavior, it must be remembered that the elevation and azimuthal angle for this plot were selected to avoid any steel structures and rebar. The presence of steel will have a significant impact on heating rates, as discussed below. Additionally, these results are only representative of Type 04 concrete. Changes in the hydrogen content will affect the results, particularly with regard to the shape of the self-heating curve.

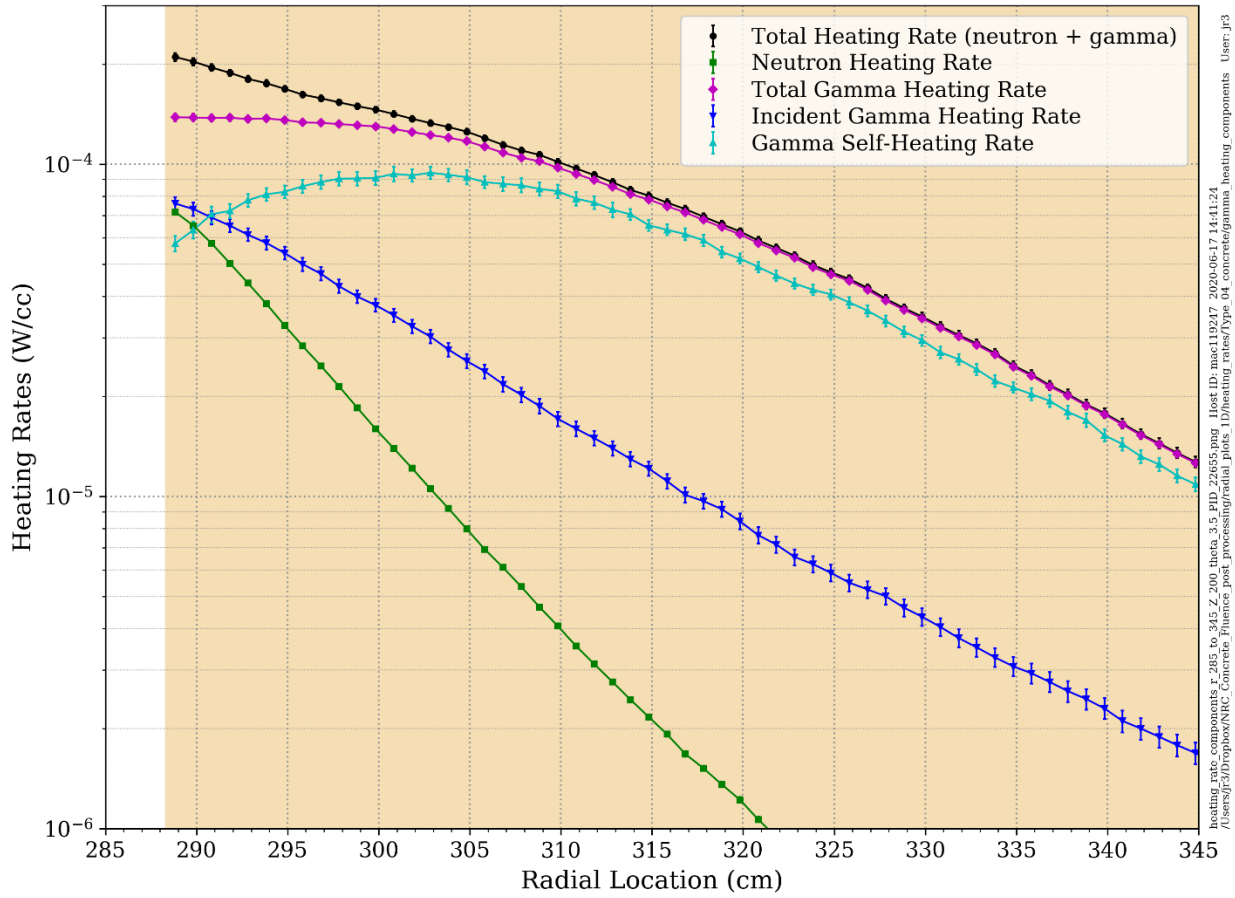

Figure 6-20 Components of the total heating rate in Type 04 concrete at an elevation of 200 cm and an azimuthal angle of 3.5º

Neutron heating rates in the bioshield decrease monotonically as a function of depth into the shield. This is shown in Figure 6-21 and Figure 6-22 for two azimuthal locations (3.5º and 44.5º) at an elevation of 200 cm. In each case, the neutron heating rate near the inner surface of the concrete is highest for the Hanford wet concrete (with the highest hydrogen content) and lowest for the Type 01 concrete (with the lowest hydrogen content). This behavior is due to changes in the magnitude of the neutron scattering cross section resulting from changes in the hydrogen content. Correspondingly, the neutron heating rate in the concrete is attenuated more rapidly with increasing hydrogen content.

As shown in Figure 6-20, the gamma heating rates do not always decrease monotonically through the concrete. This is because the self-heating rate is driven by the production of gammas due to neutron absorption and scattering. As neutrons enter the concrete from the cavity region, they are moderated in the concrete to lower energies, where their probability of absorption (and hence of producing capture gamma rays) increases. The Hanford wet concrete produces the most rapid moderation and thermalization, which results in a peak in the total gamma heating rate several centimeters into the concrete at the 3.5º azimuthal location (see Figure 6-21). The peaking effect at 44.5º (Figure 6-22) is substantially smaller due to differences in the incident neutron spectra at those two locations.

Figure 6-23 and Figure 6-24 show the total (neutron + gamma) heating rate profiles through the four concrete types at elevations of 200 cm and 400 cm and azimuthal angles of 3.5º and 44.5º. At each location the heating rates in the innermost portion of the concrete (i.e., the region nearest the inner surface) are proportional to the hydrogen content of each concrete type. At further distances into the concrete, the concretes with the higher hydrogen content (Hanford wet and Type 04) begin to experience a more rapid attenuation. This is due to the more rapid attenuation of the neutron flux in the Type 04 and Hanford wet concretes, which results in less gamma production and hence lower self-heating rates than the concretes with lower hydrogen contents.

6.1.4 Total Heating Rate: Effect of Rebar and Support Columns

The results presented in Section 6.1.3 are appropriate for heating rate comparisons in the concrete regions of the bioshield where there are no perturbations due to the presence of structural steel components or rebar. While the presence of rebar and the RPV support columns has a minor effect on the attenuation of neutrons with energies greater than 0.1 MeV as well as neutrons with energies greater than 1.0 MeV (see Section 6.1.2 those steel components have a significant effect on heating rates. The increased heating in the steel is due to two effects.

1) The gamma energy absorption coefficient μ_{en}, which is a measure of how much energy is deposited in a material due to gamma interactions, is significantly greater for steel than for concrete.

2) Absorption of thermal neutrons in the steel produces capture gamma rays, some of which can have energies as high as ~8 MeV.

The effects of the rebar and support columns are shown for each of the four concrete types at elevations of 245 cm and 391 cm in Figure 6-25 through Figure 6-32. The elevation at 245 cm includes vertical and hoop rebar and an embedded support column. The elevation at 391 cm includes vertical rebar and the upper cantilever beam.

In each of these eight plots, the maximum total heating rates occur within the structural steel components and rebar. The peak heating rates in the steel are typically three to four times higher

than the peak heating rate in the concrete. The peak heating rates in the steel occur in rebar at both elevations. There is a clear correlation between the hydrogen content of the concrete and the heating rates in the structural steel. At both elevations, the peak heating rates in the steel and in the concrete are proportional to the hydrogen content. Thus, the highest heating rates occur in the Hanford wet concrete (with a hydrogen content of 0.029 g/cm^3) and the lowest rates occur in the Type 01 concrete (with a hydrogen content of 0.00484 g/cm^3).

This behavior is caused by two effects: (1) more effective moderation and thermalization of the neutrons as the hydrogen content increases, which leads to higher rates of capture gamma production, and, to a lesser extent, (2) increased neutron heating in the concrete due to an increase in the macroscopic elastic scattering cross section as the hydrogen content increases. It may also be noticed that the total heating rates are attenuated more rapidly in the “wetter” concretes, but that may be a secondary concern relative to the maximum heating rates.

At the elevation of 391 cm, the peak heating rates occur in the vertical rebar and along the edges of the cantilever beam. The peaks along the edges of the cantilever beam are a result of thermal neutron capture in the steel. The capture rate decreases toward the center of the cantilever beam as the thermal flux is rapidly attenuated in the steel.

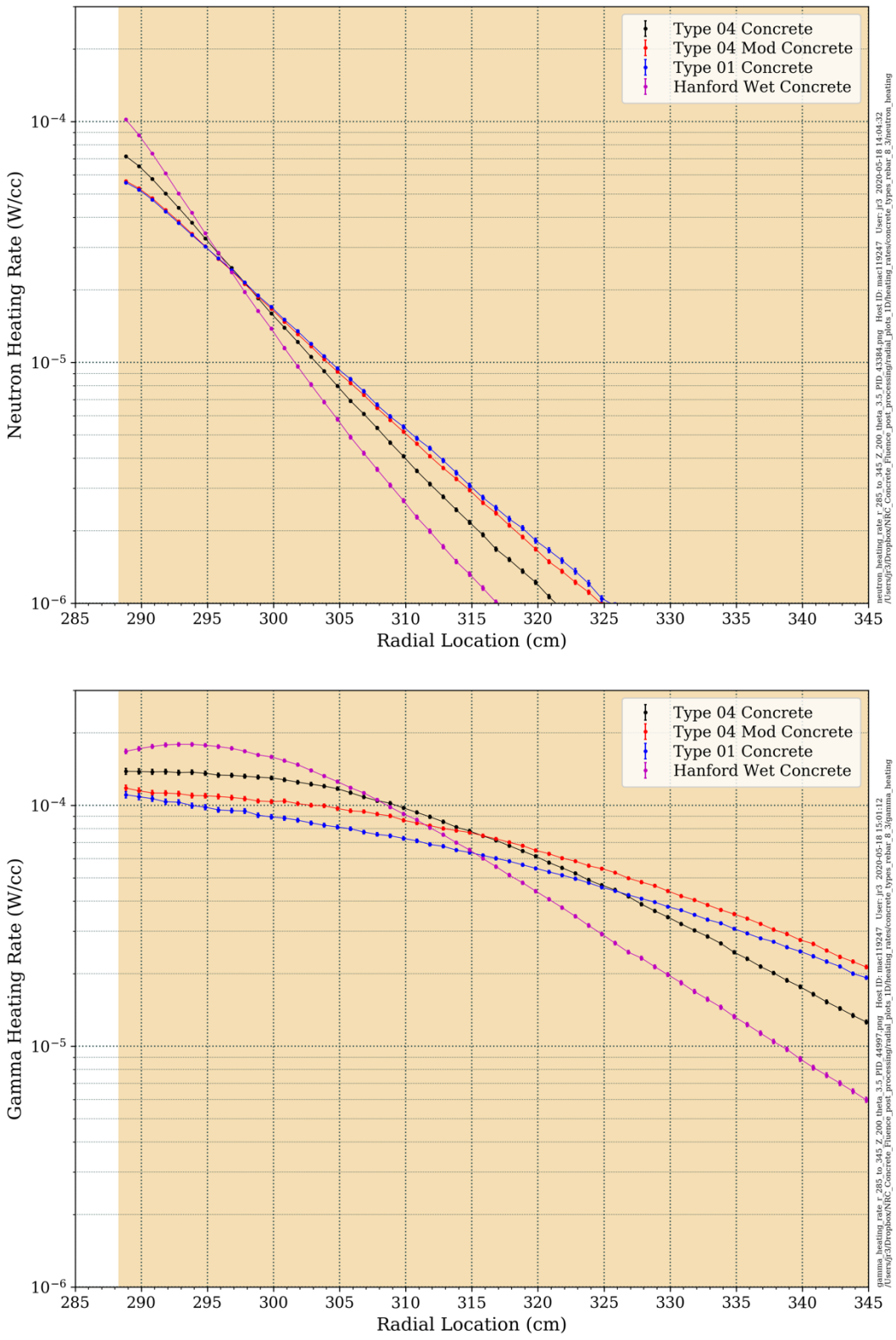

Figure 6-21 Neutron and gamma heating rate radial profiles through four concrete types at an elevation of 200 cm and an azimuthal angle of 3.5º

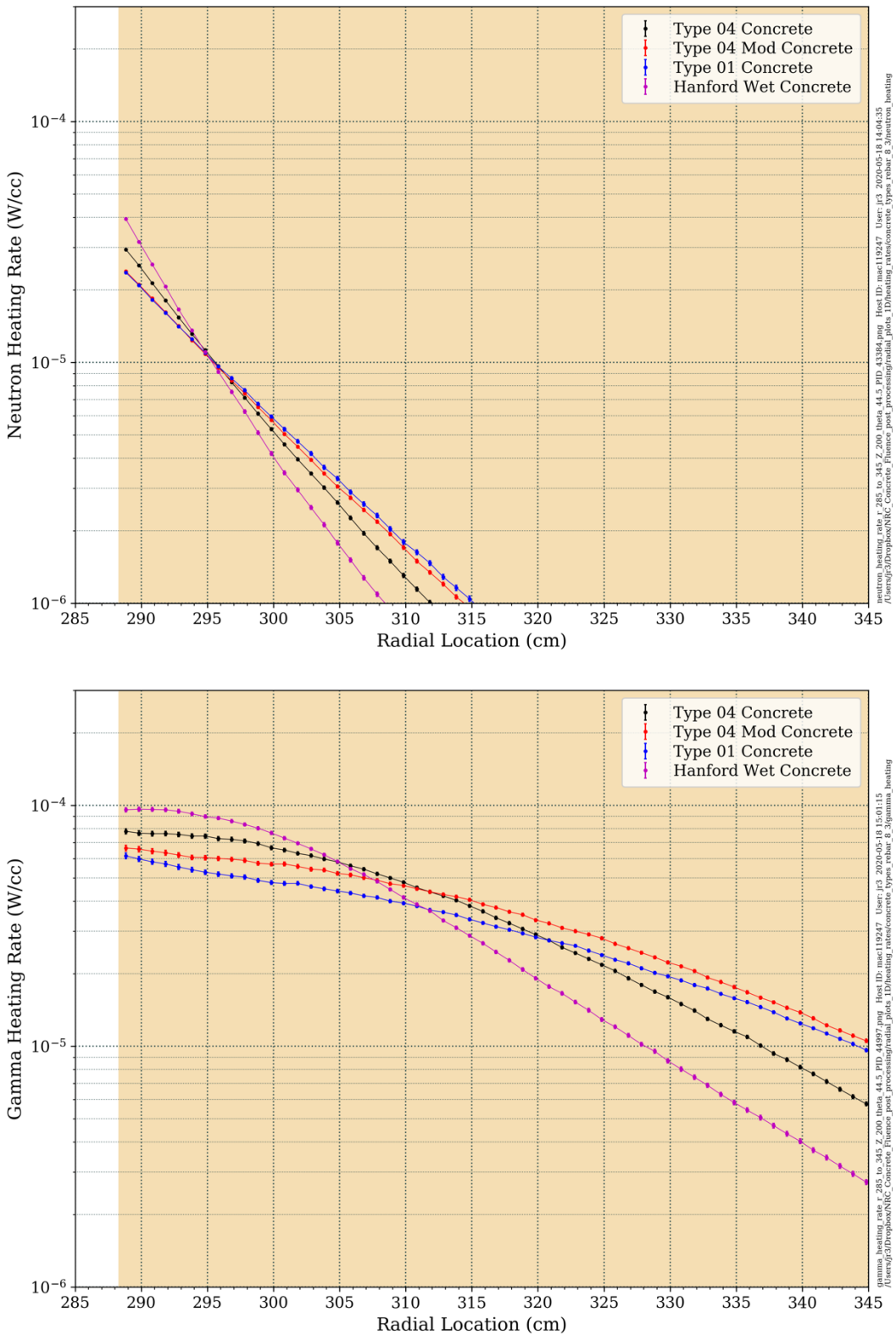

Figure 6-22 Neutron and gamma heating rate radial profiles through four concrete types at an elevation of 200 cm and an azimuthal angle of 44.5º

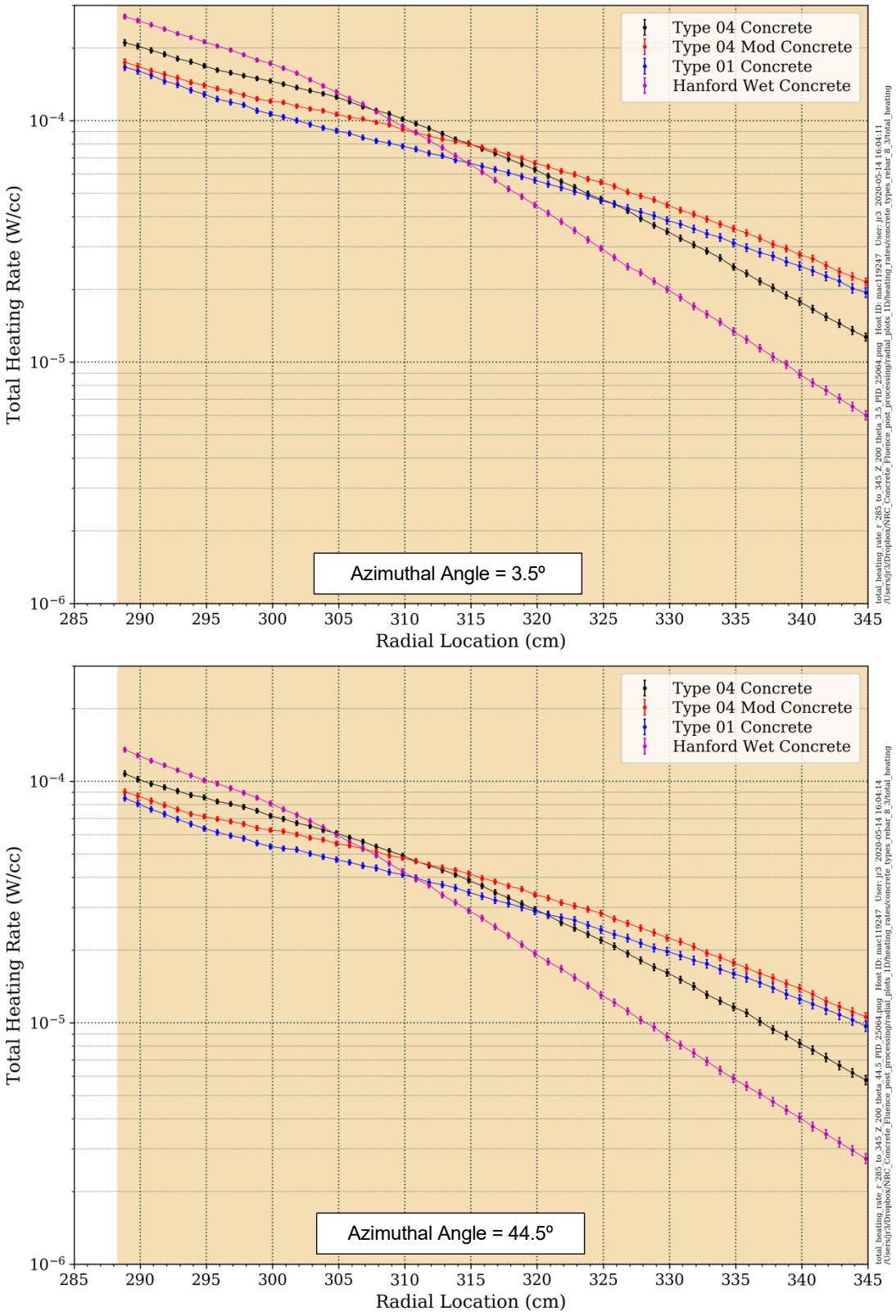

Figure 6-23 Total heating rate radial profiles through four concrete types at an elevation of 200 cm and azimuthal angles of 3.5º and 44.5º

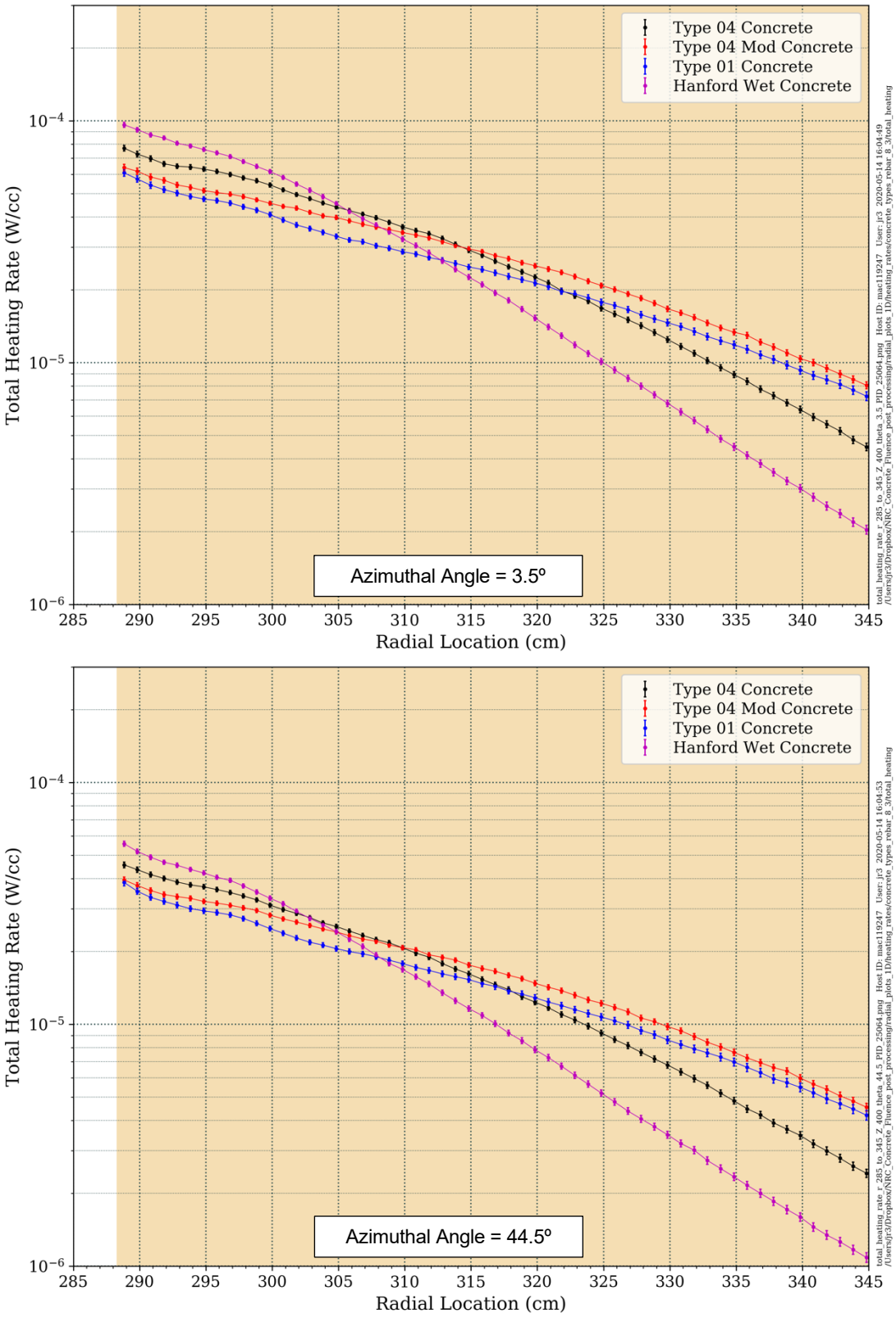

Figure 6-24 Total heating rate radial profiles through four concrete types at an elevation of 400 cm and azimuthal angles of 3.5º and 44.5º

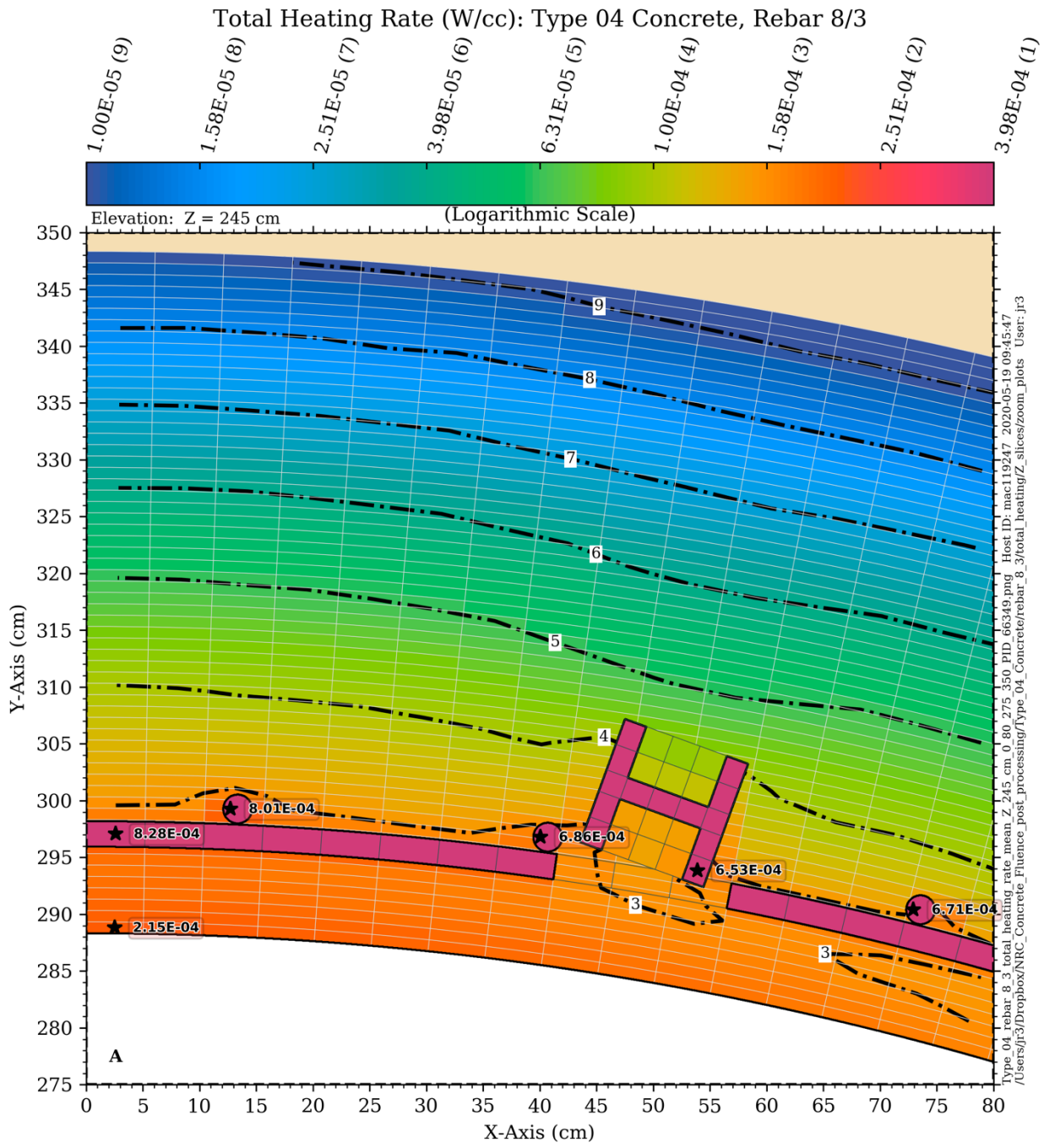

Figure 6-25 Total (neutron + gamma) heating rate contours at an elevation of 245 cm: Type 04 concrete

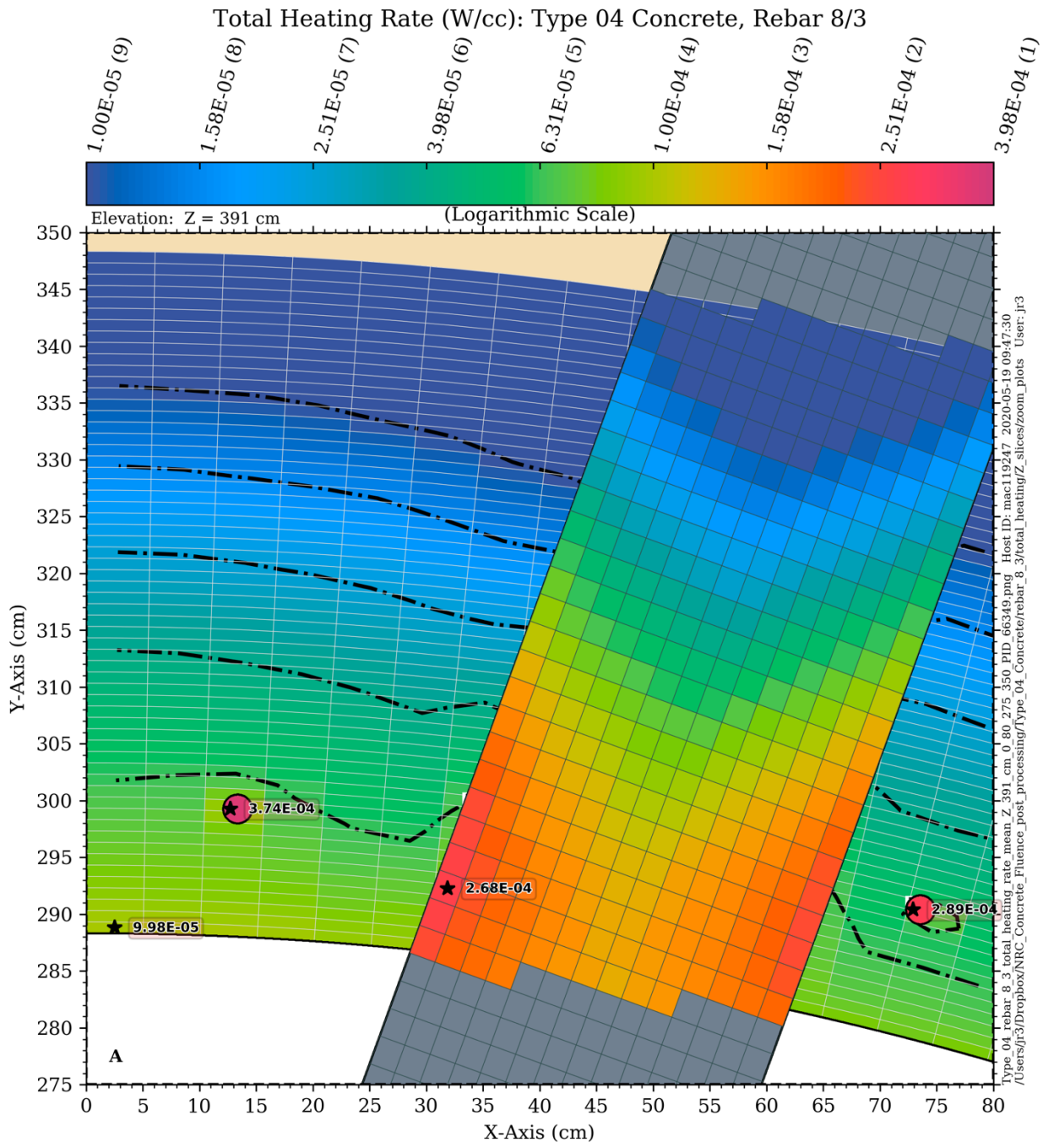

Figure 6-26 Total (neutron + gamma) heating rate contours at an elevation of 391 cm: Type 04 concrete

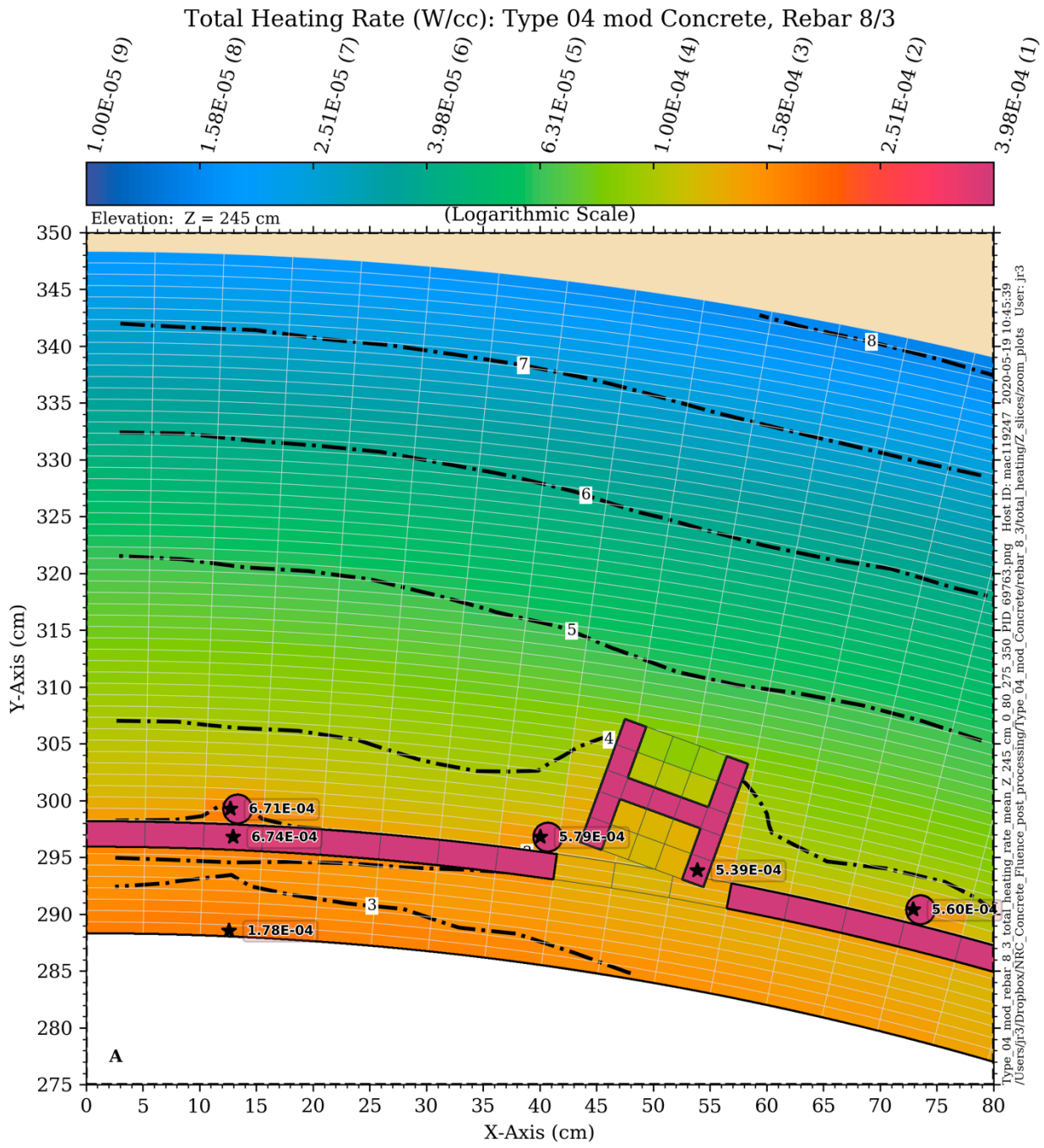

Figure 6-27 Total (neutron + gamma) heating rate contours at an elevation of 245 cm: Type 04 mod concrete

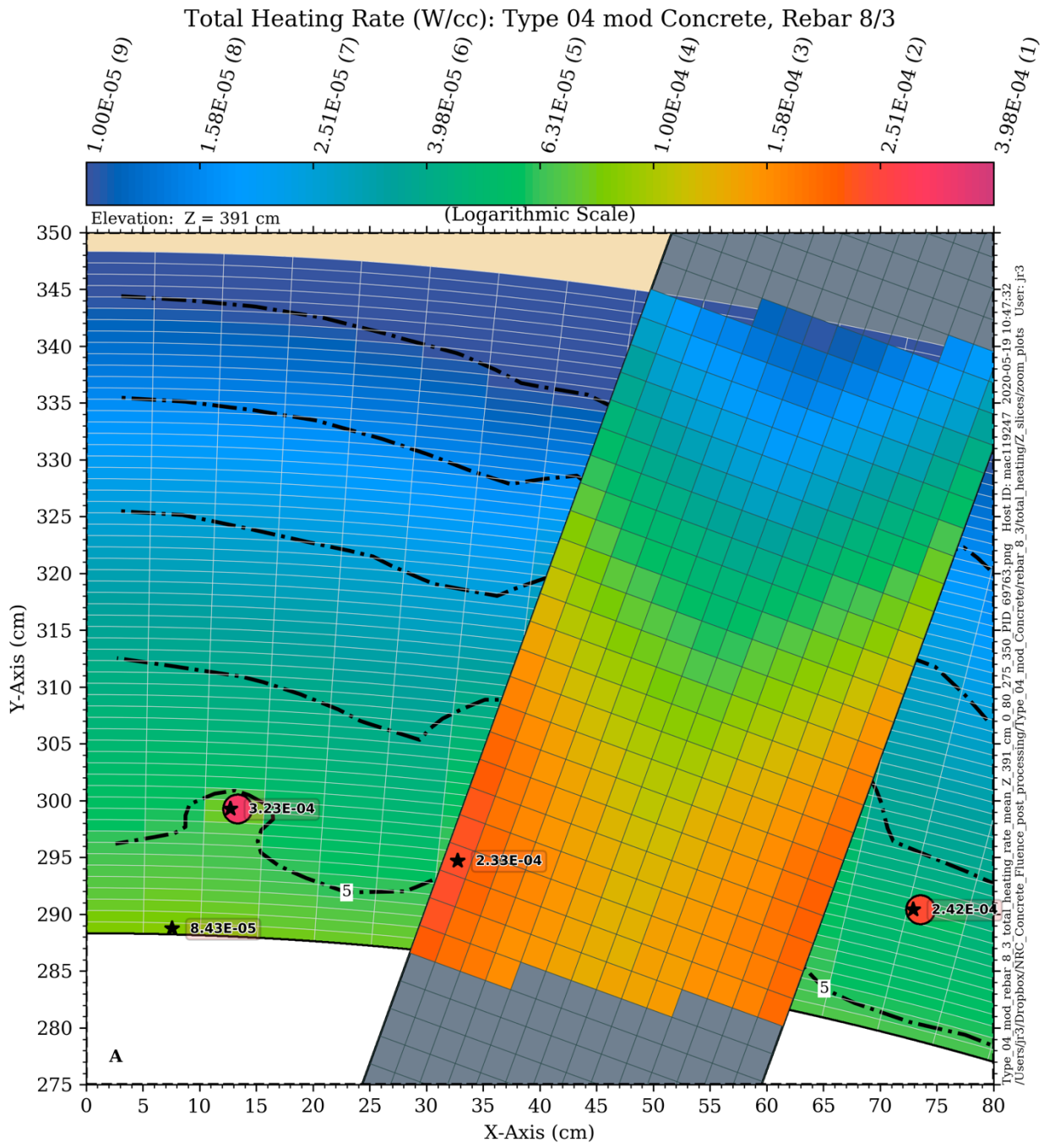

Figure 6-28 Total (neutron + gamma) heating rate contours at an elevation of 391 cm: Type 04 mod concrete

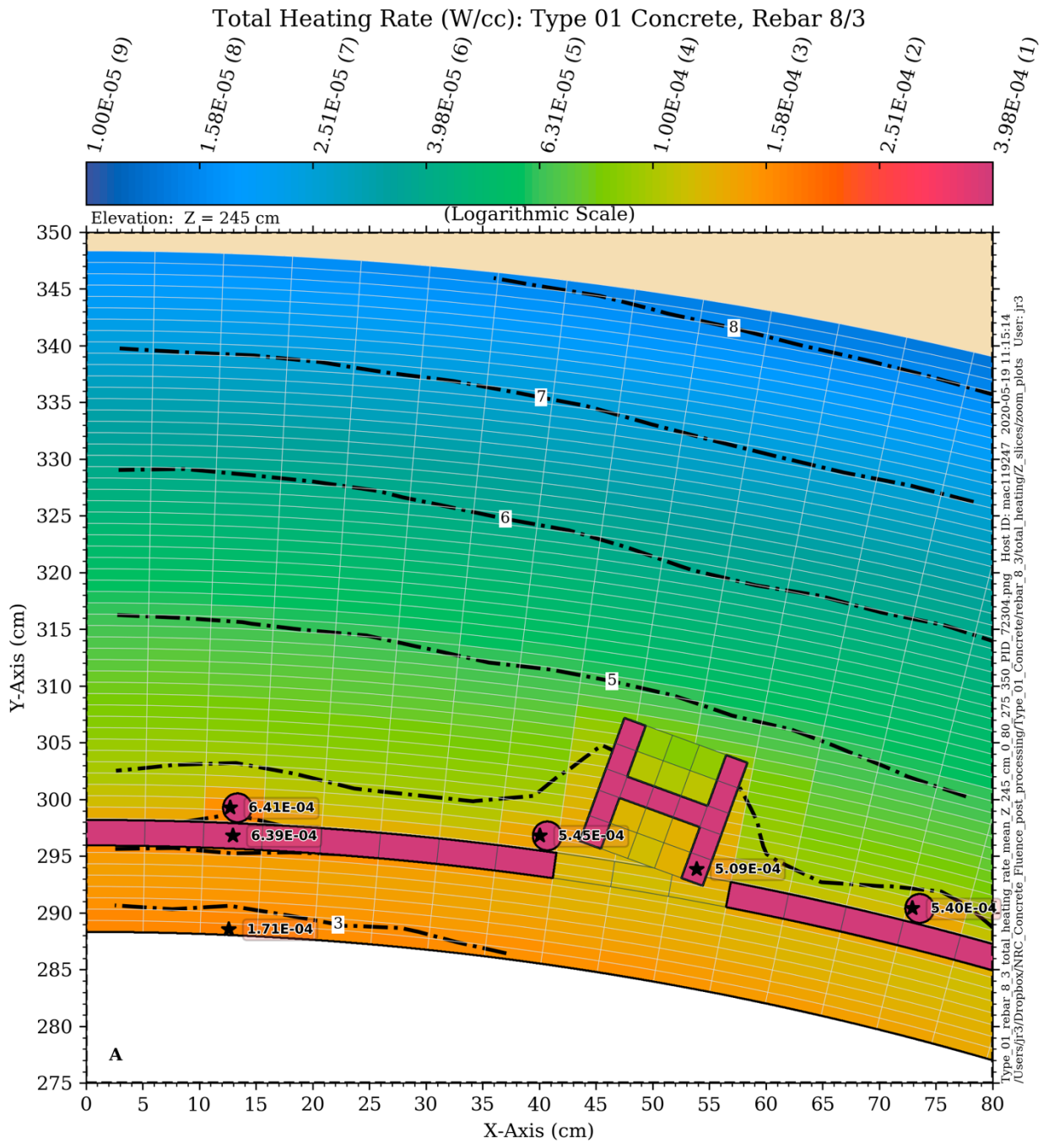

Figure 6-29 Total (neutron + gamma) heating rate contours at an elevation of 245 cm: Type 01 concrete

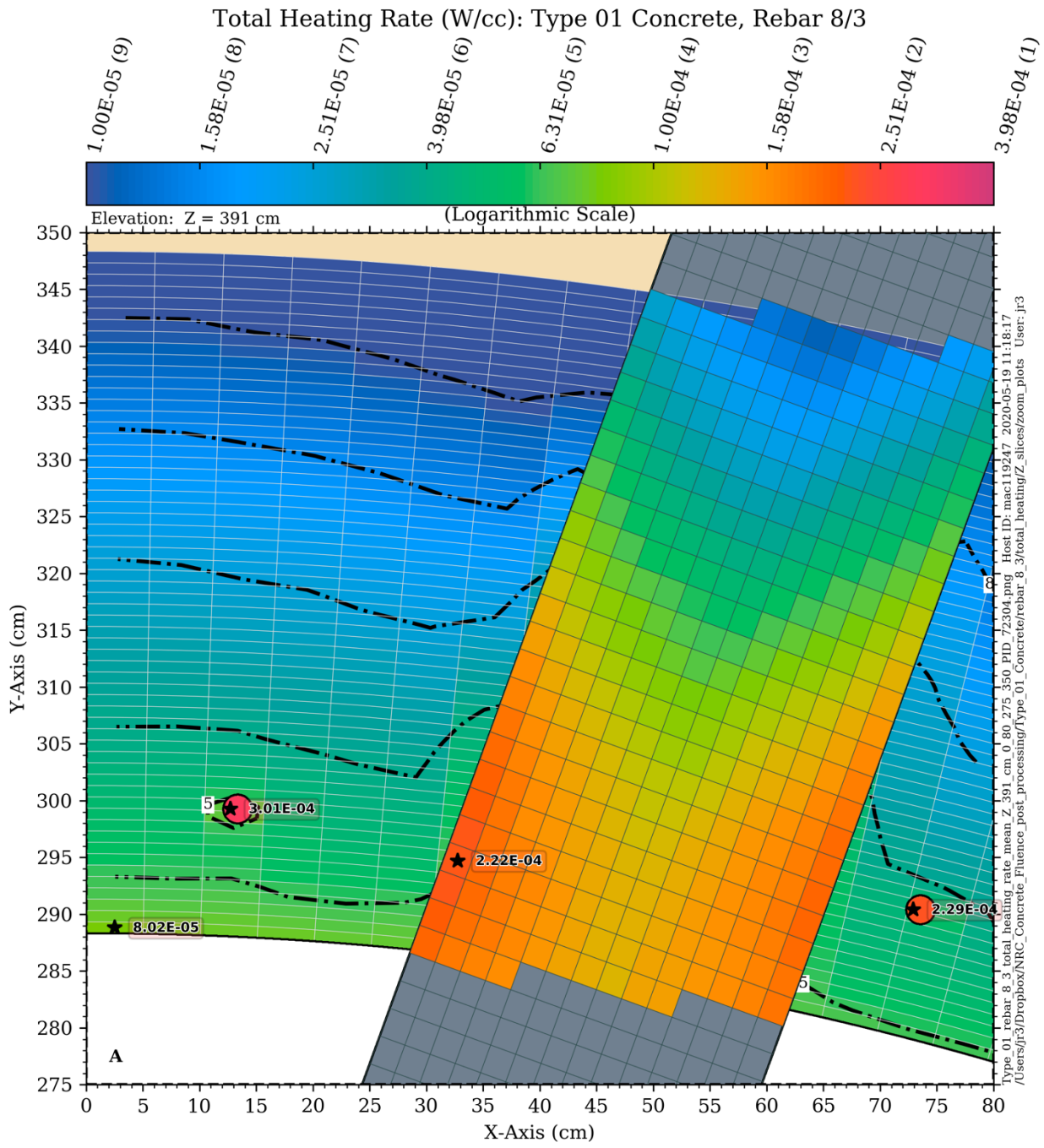

Figure 6-30 Total (neutron + gamma) heating rate contours at an elevation of 391 cm: Type 01 concrete

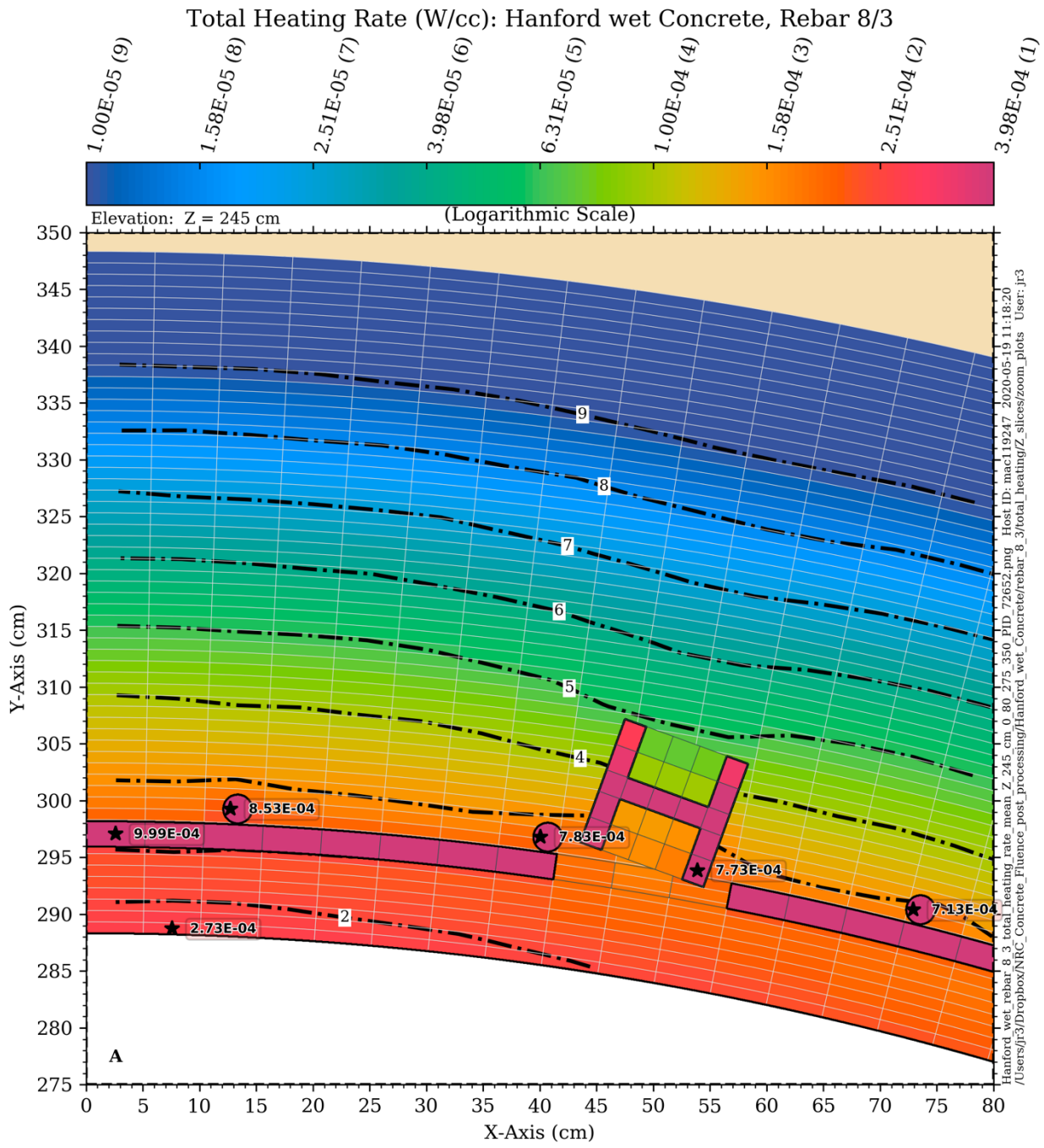

Figure 6-31 Total (neutron + gamma) heating rate contours at an elevation of 245 cm: Hanford wet concrete

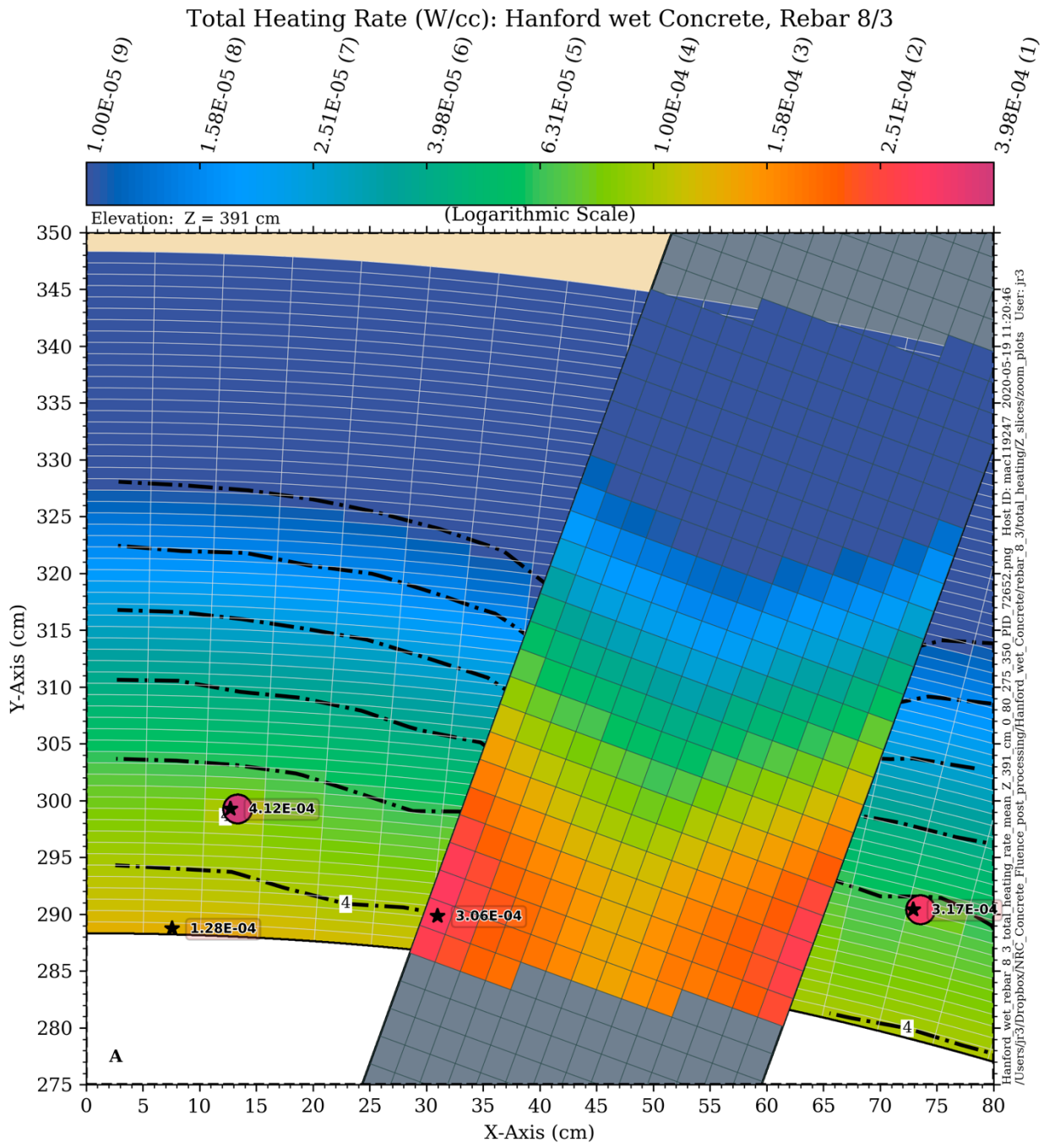

Figure 6-32 Total (neutron + gamma) heating rate contours at an elevation of 391 cm: Hanford wet concrete

6.1.5 Gamma Dose Rate: Concrete Only

The gamma dose rate provides another measure of energy deposition in the bioshield concrete and the steel structural components. It differs from the total heating rate in two ways.

1) The gamma dose rate includes energy deposition from gamma rays only. Note that, as with the total heating rate, there are contributions from incident gammas and self-heating gammas.

2) The total heating rate provides a measure of energy deposition on a volumetric (W/cm^3) basis. The gamma dose rate provides a measure or energy deposition on a mass basis (rad/s).

The conversion between the gamma heating rate and the gamma dose rate is given by

$$DR_\gamma = \dot{H}_\gamma \times \frac{10^5}{\rho},$$

where

DR_γ = the gamma dose rate (rad/s),
$\dot{H}_\gamma$ = the gamma heating rate (W/cm^3), and
ρ = the density of the material (g/cm^3).

The behavior of the gamma dose rate can be seen by examining the gamma heating rate plots in Figure 6-21 and Figure 6-22. The gamma dose rates can be obtained by multiplying the gamma heating rates by 10^5 and dividing by the concrete density. Thus, the same conclusions that were drawn for gamma heating as a function of concrete composition in Section 6.1.3 are applicable to the gamma dose rate.

6.1.6 Gamma Dose Rate: Effect of Rebar and Support Columns

The effect of structural steel and rebar on gamma dose rates in the bioshield is similar to the effect described for heating rates in Section 6.1.4 . The primary difference is that because the dose rate in rad/s is a measure of energy deposition per unit mass, while the heating rate in W/cm^3 is a measure of the energy deposition per unit volume, the variation in the gamma dose rate between the structural steel and the surrounding concrete is not as significant as the variation in the heating rates in the structural steel and the surrounding concrete. Furthermore, the total heating rate includes the effect of neutrons as well as gammas. Note that while neutron heating rates are less than gamma heating rates for the models used in this analysis, the total heating rate near the inner surface of the bioshield can have a significant neutron heating contribution.

The effects of these differences relative to the heating rates can be seen by comparison of Figure 6-25 through Figure 6-32 with Figure 6-33 through Figure 6-40. The differences can be summarized as follows.

1) As noted above, the difference in a mass-based versus a volume-based energy deposition rate significantly reduces the variation in the gamma dose rate in the concrete relative to the steel compared to the variation in the heating rates in concrete relative to the steel.

2) The peak gamma dose rates in the concrete at each location occur in mesh tally voxels immediately adjacent to rebar sections. With the total heating rates, the peak heating rate in the concrete occurs near the inner surface of the bioshield due to the contribution of neutron heating.

3) As is the case with the total heating rates, the maximum gamma dose rates occur with the Hanford wet concrete. The maximum dose rates decrease with decreasing hydrogen content of the concrete. This is again due to more effective moderation and thermalization of the neutrons as the hydrogen content increases, which leads to higher rates of capture gamma production and hence higher gamma dose rates.

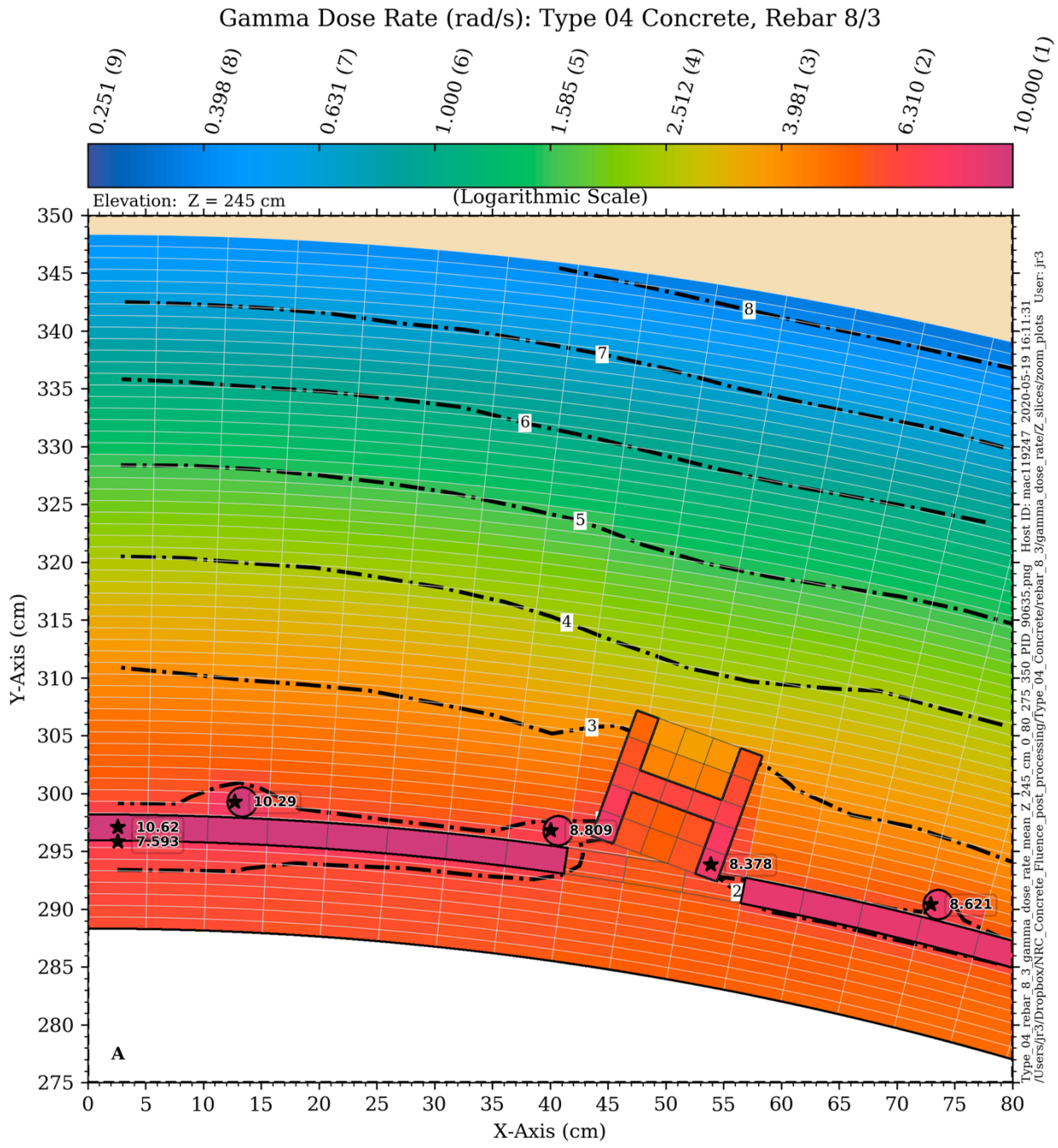

Figure 6-33 Gamma dose rate contours at an elevation of 245 cm: Type 04 concrete

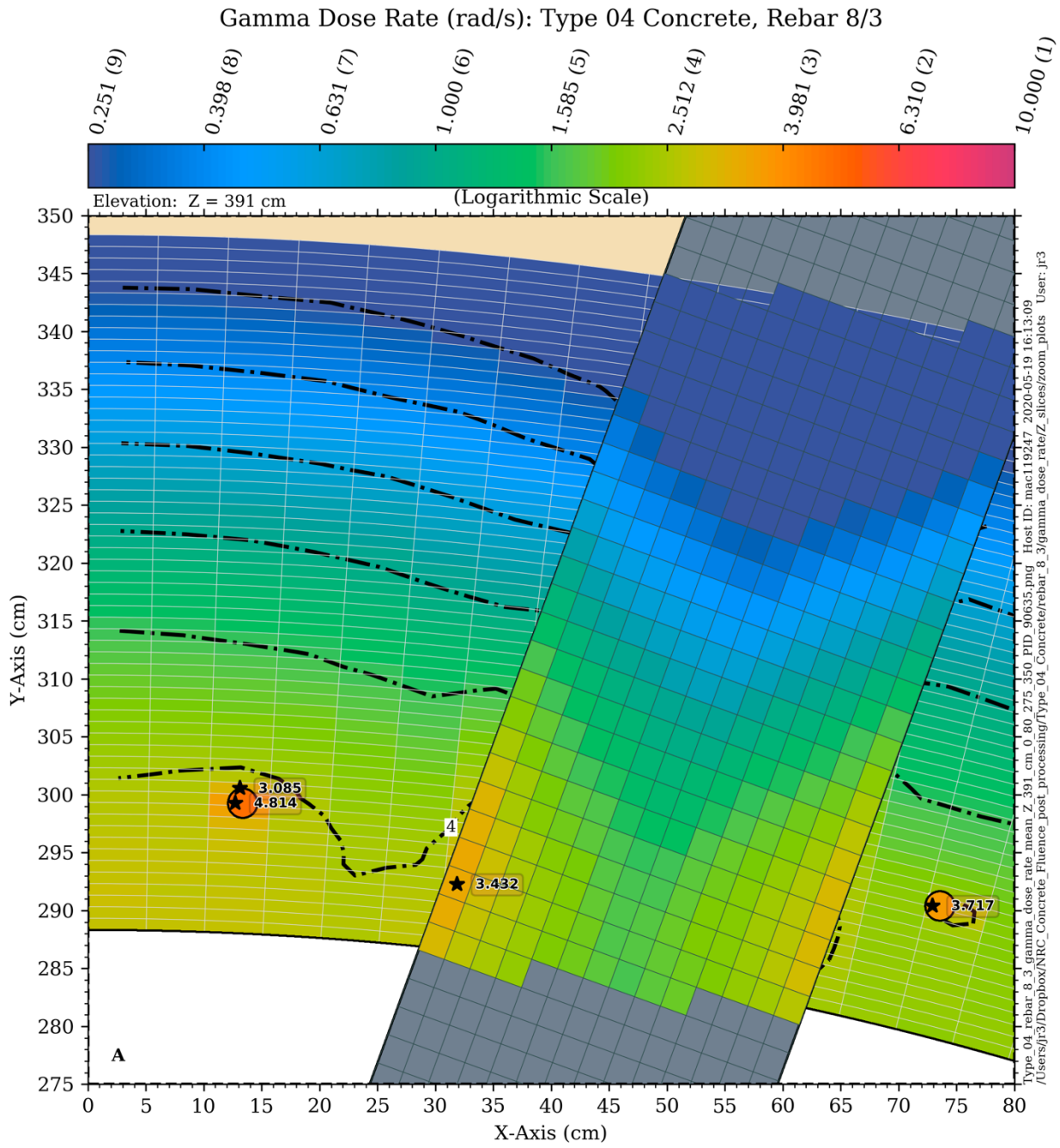

Figure 6-34 Gamma dose rate contours at an elevation of 391 cm: Type 04 concrete

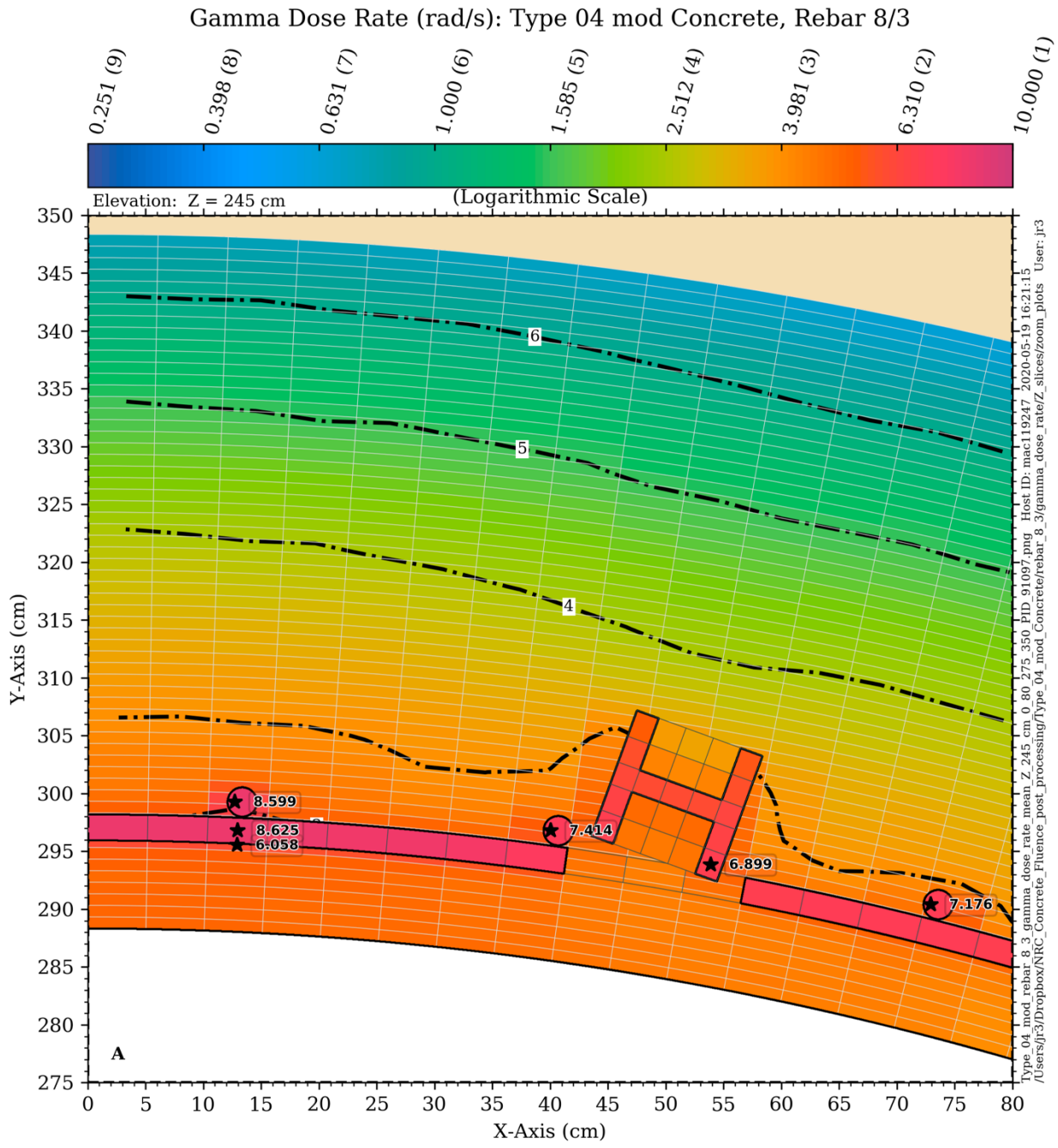

Figure 6-35 Gamma dose rate contours at an elevation of 245 cm: Type 04 mod concrete

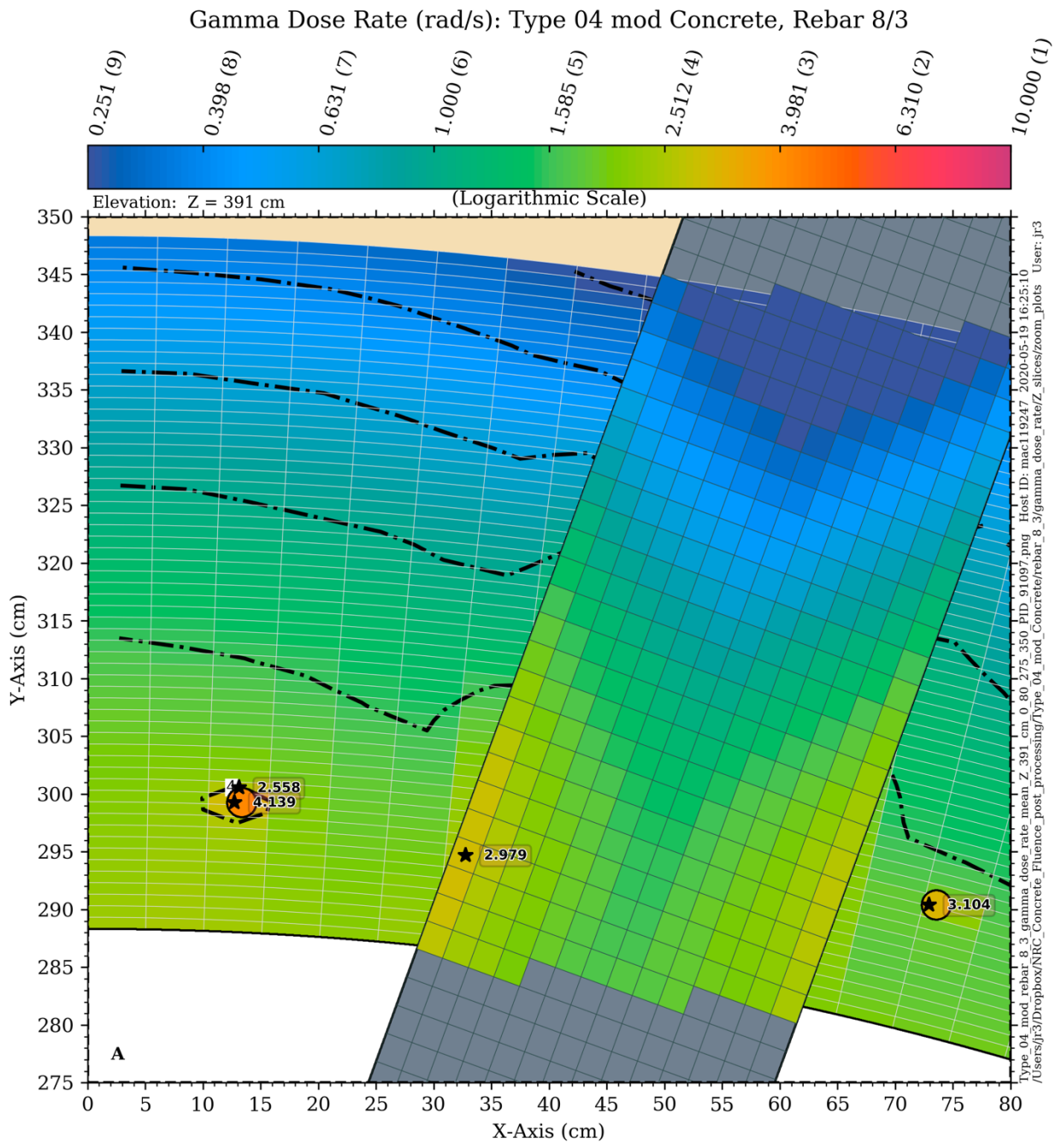

Figure 6-36 Gamma dose rate contours at an elevation of 391 cm: Type 04 mod concrete

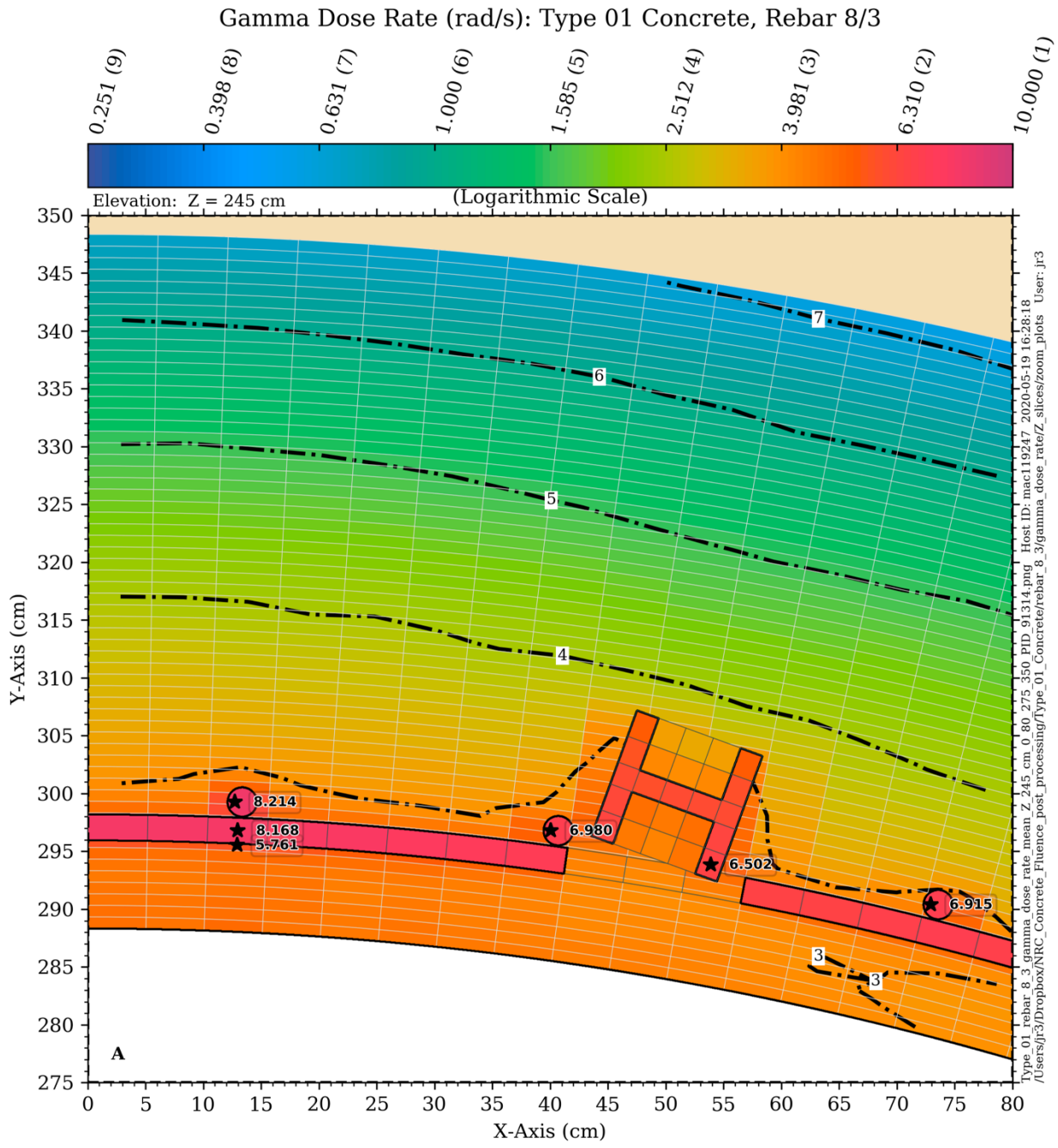

Figure 6-37 Gamma dose rate contours at an elevation of 245 cm: Type 01 concrete

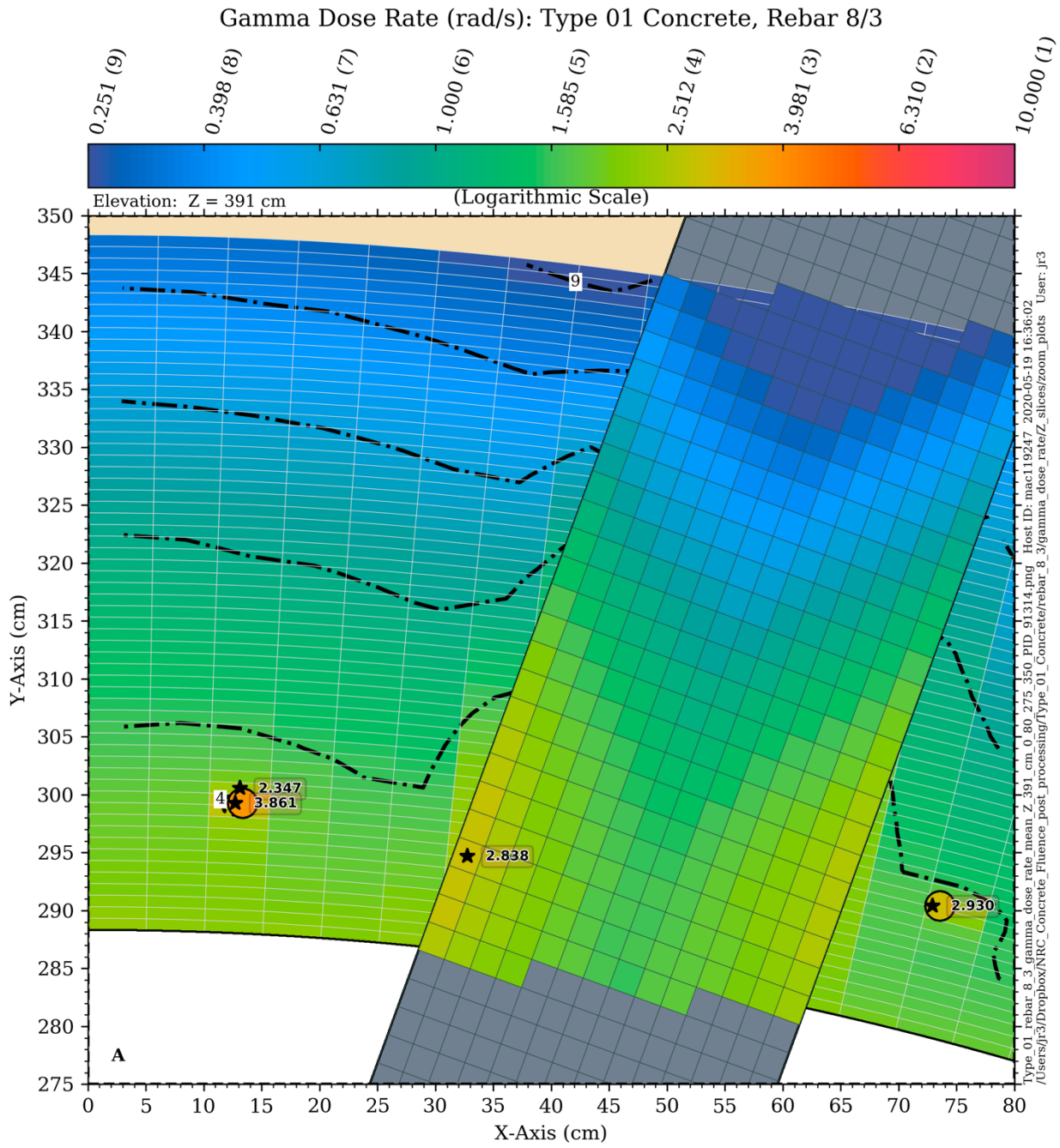

Figure 6-38 Gamma dose rate contours at an elevation of 391 cm: Type 01 concrete

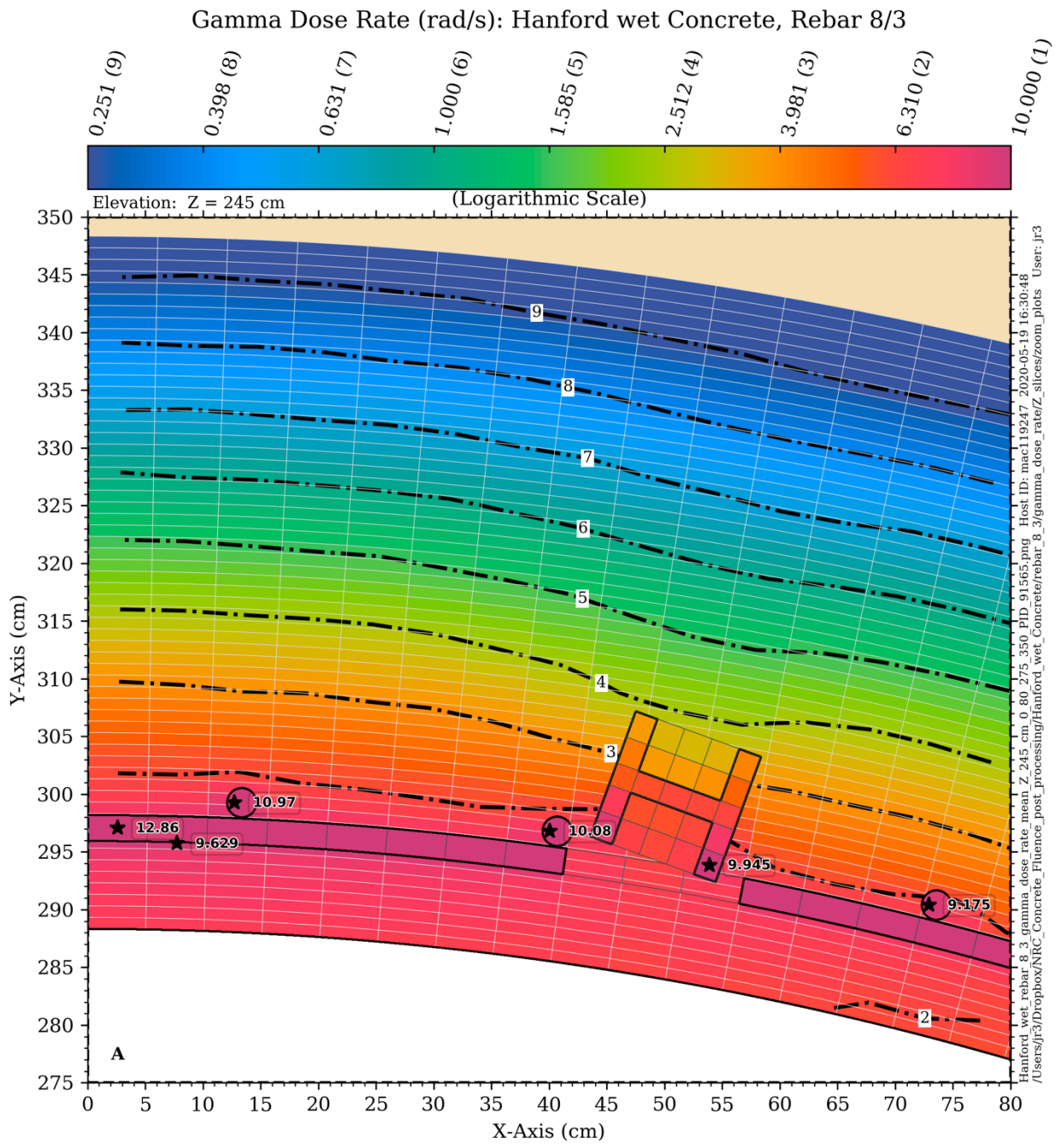

Figure 6-39 Gamma dose rate contours at an elevation of 245 cm: Hanford wet concrete

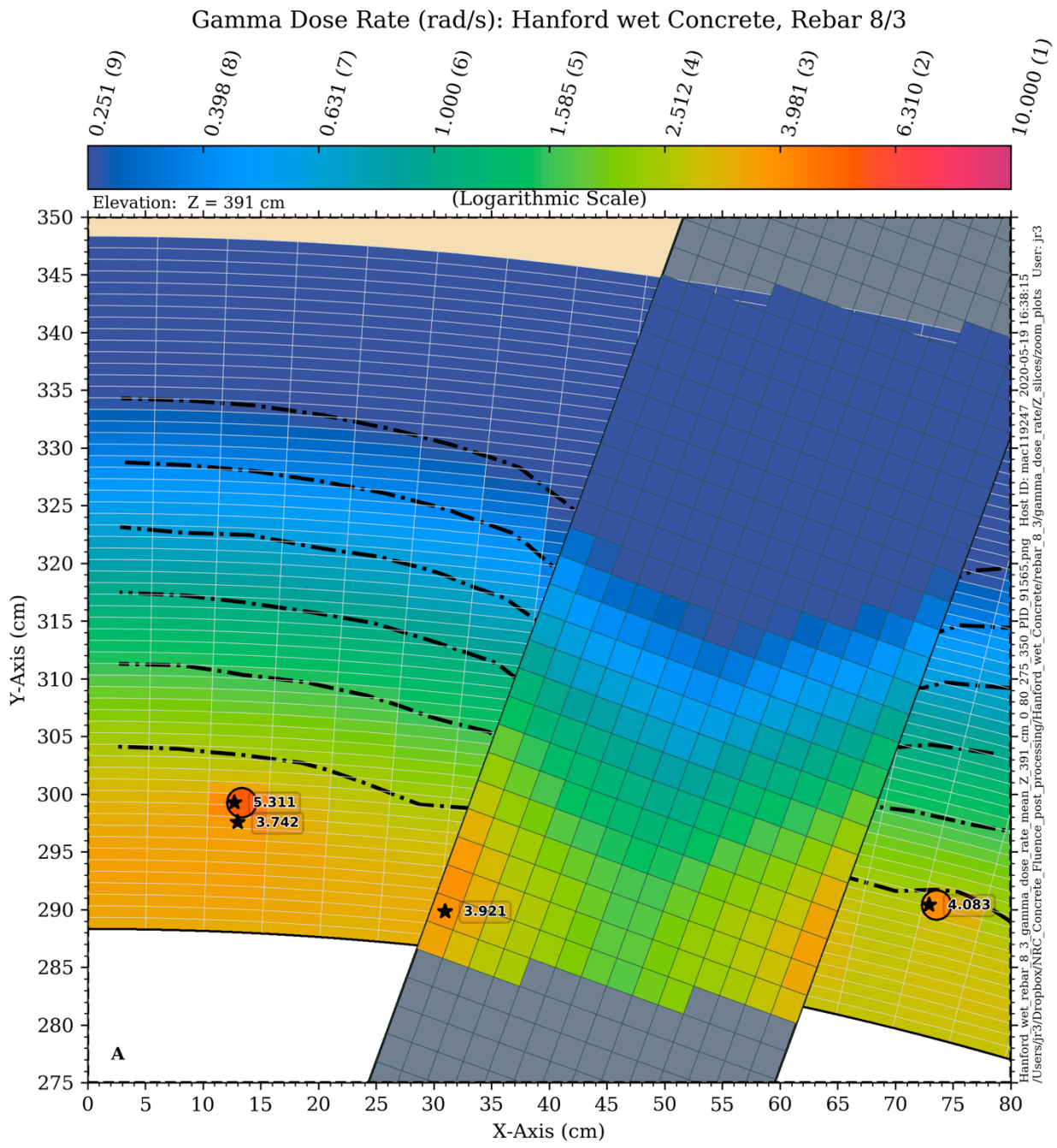

Figure 6-40 Gamma dose rate contours at an elevation of 391 cm: Hanford wet concrete

6.2 Composition and Location of Reinforcing Steel (Rebar)

It was shown in Section 6.1 that the presence of structural steel within the bioshield concrete has a relatively minor effect on neutron flux levels but a significant localized effect on total heating rates and gamma dose rates. In this section we consider the effect of changing the rebar size and the depth of the concrete cover (i.e., the amount of concrete between the inner surface of the bioshield and the first layer of rebar) using the following cases.

1) #8 rebar (1-inch diameter) with a 3-inch concrete cover
2) #14 rebar (1.75-inch diameter) with a 3-inch concrete cover
3) #14 rebar (1.75-inch diameter) with a 10-inch concrete cover
4) No rebar

These four cases are all based on a Type 04 concrete bioshield.

In cases 1–3 the rebar consists of hoops and vertical rods. The prescribed horizontal and vertical spacing intervals are 12 inches in each case. In some locations the rebar hoops had to be divided into azimuthal sections to avoid interference with the support columns. In the same way, vertical rebar rods were moved azimuthally in some cases to avoid interferences.

Because the effects of the rebar and column supports on neutron flux levels for E > 1.0 MeV and E > 0.1 MeV are relatively minor, we focus here on the effect of the rebar modeling on total heating rates and gamma dose rates.

The total heating rates for cases 2–4 are shown in Figure 6-41 through Figure 6-46. The following conclusions can be drawn from comparison of these figures with Figure 6-25 and Figure 6-26.

1) The highest heating rates occur for the #8 rebar with a 3-inch concrete cover.

2) Increasing the concrete cover for the #14 rebar from 3 inches to 10 inches results in a reduction in the heating rates in the rebar.

3) The maximum heating rates in the concrete occur at the inner edge of the bioshield in each case. The maximum heating rates in the steel occur in the rebar for the #8/3-inch and #14/3-inch models and in the support column in the #14/10-inch and no-rebar models.

The gamma dose rates for cases 2–4 are shown in Figure 6-47 through Figure 6-52. The following conclusions can be drawn from comparison of these figures with Figure 6-33 and Figure 6-34.

1) As with the total heating rates, the highest gamma dose rates occur for the #8 rebar with a 3-inch concrete cover.

2) Increasing the concrete cover for the #14 rebar from 3 inches to 10 inches results in a reduction in the gamma dose rates in the rebar. The peak gamma dose rate in the rebar hoop is ~42% lower in the #14/10-inch model. This reduction is essentially identical to that for the total heating rate in the #14/3-inch and #14/10-inch models. This equivalence is expected, as the contribution of neutron heating to the total heating rate in the rebar is very small.

3) The maximum gamma dose rates in concrete for the #8/3-inch and #14/3-inch models occur along the inner edge of the rebar hoop due to the significant capture gamma production in the rebar hoop. For the #14/10-inch and no-rebar models, the maximum gamma dose rates in the concrete occur a few centimeters from the inner surface of the bioshield. The location of the rebar in the #14/10-inch model is far enough from the inner surface of the concrete that its contribution to the peak gamma dose rate in the concrete is insignificant.

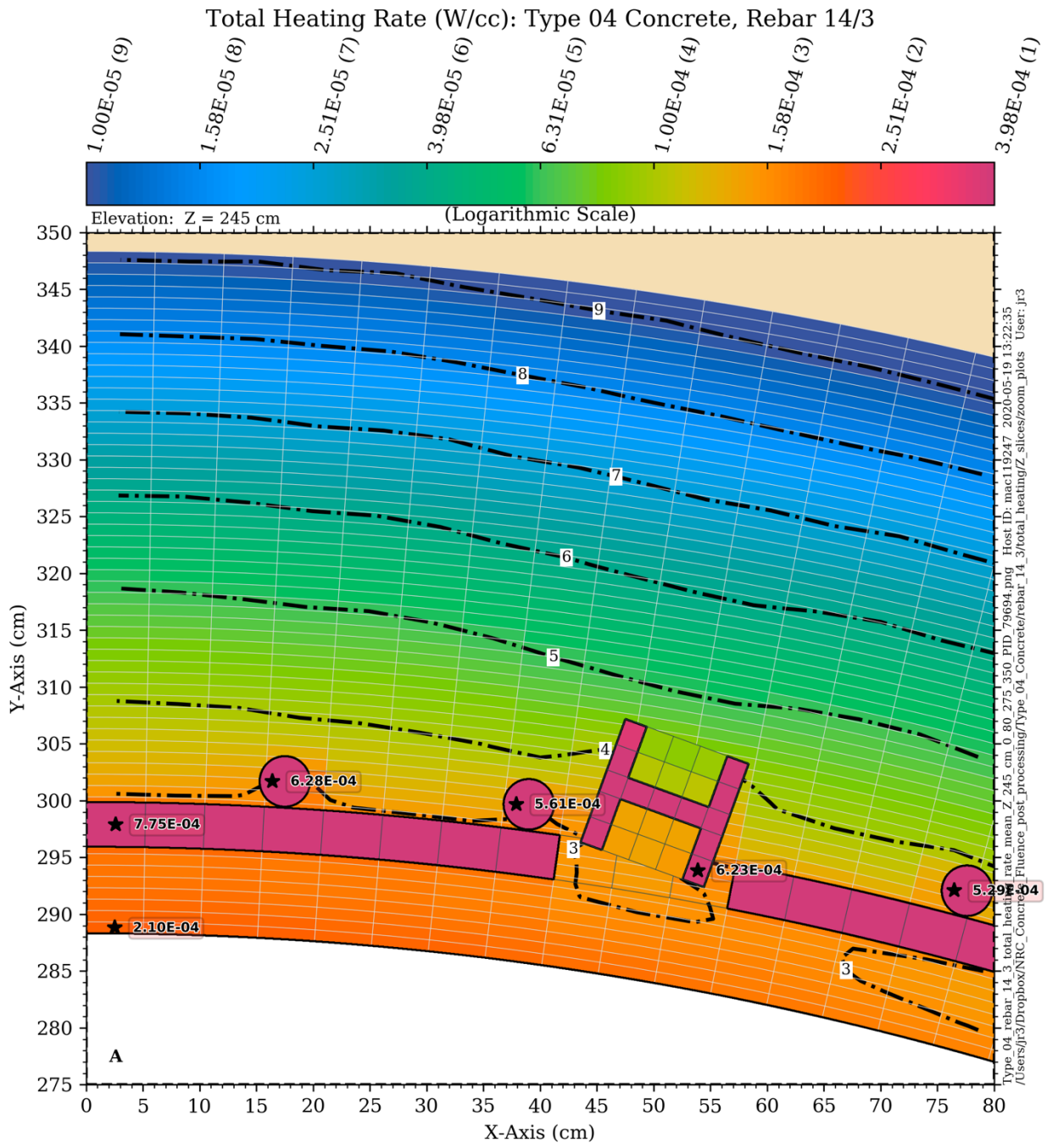

Figure 6-41 Total (neutron + gamma) heating rate contours at an elevation of 245 cm: Type 04 concrete with #14 rebar and a 3-inch concrete cover

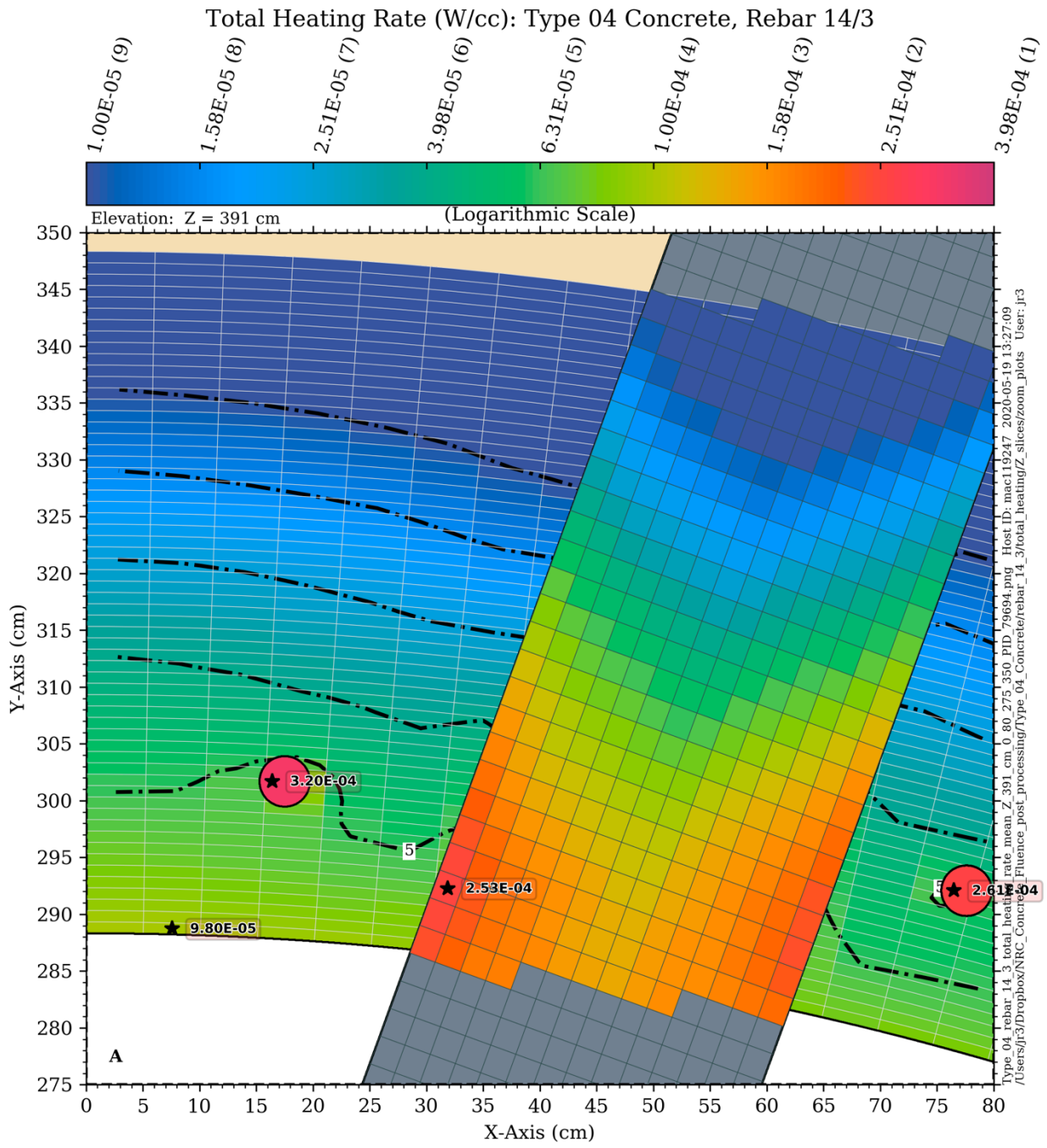

Figure 6-42 Total (neutron + gamma) heating rate contours at an elevation of 391 cm: Type 04 concrete with #14 rebar and a 3-inch concrete cover

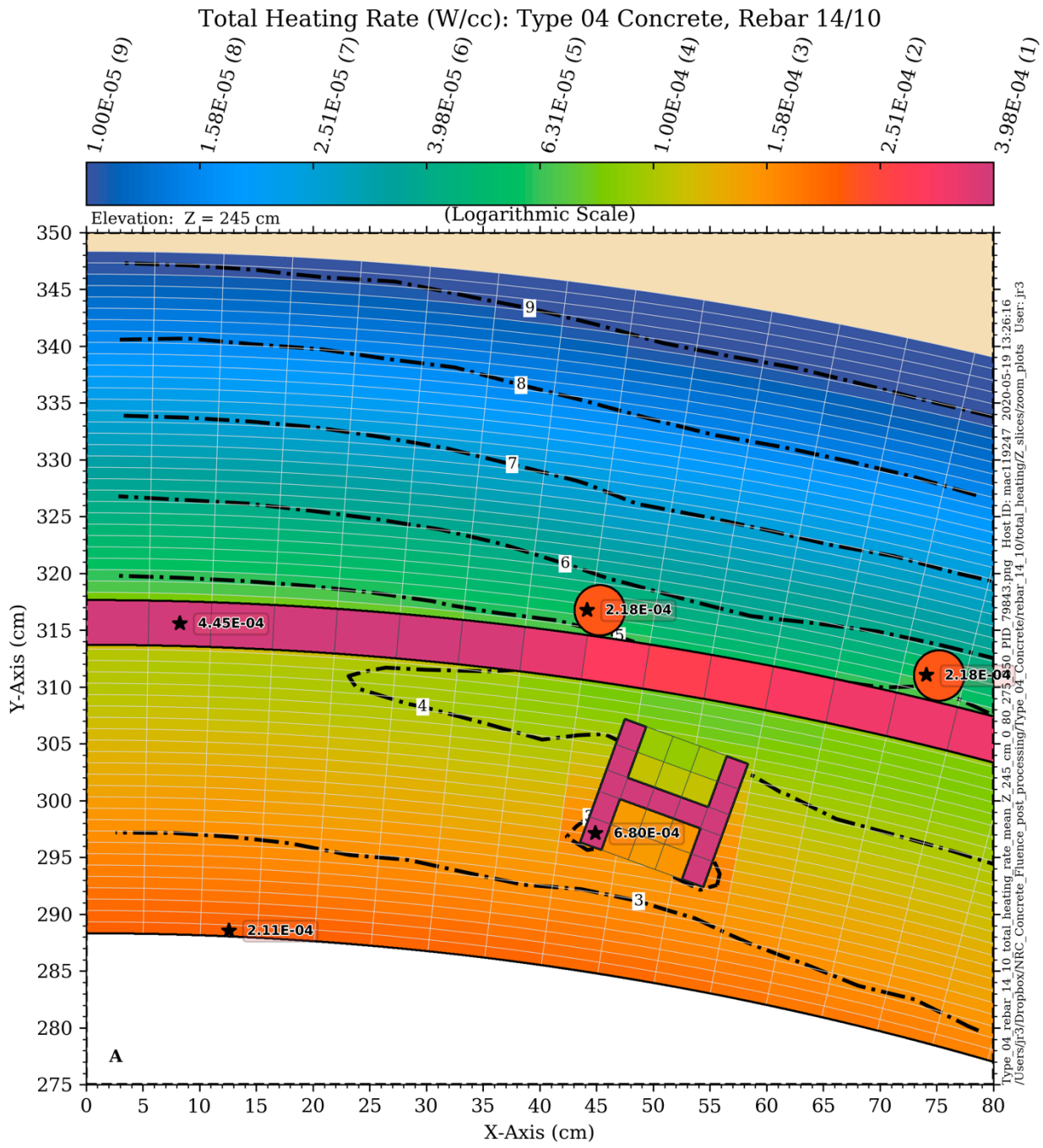

Figure 6-43 Total (neutron + gamma) heating rate contours at an elevation of 245 cm: Type 04 concrete with #14 rebar and a 10-inch concrete cover

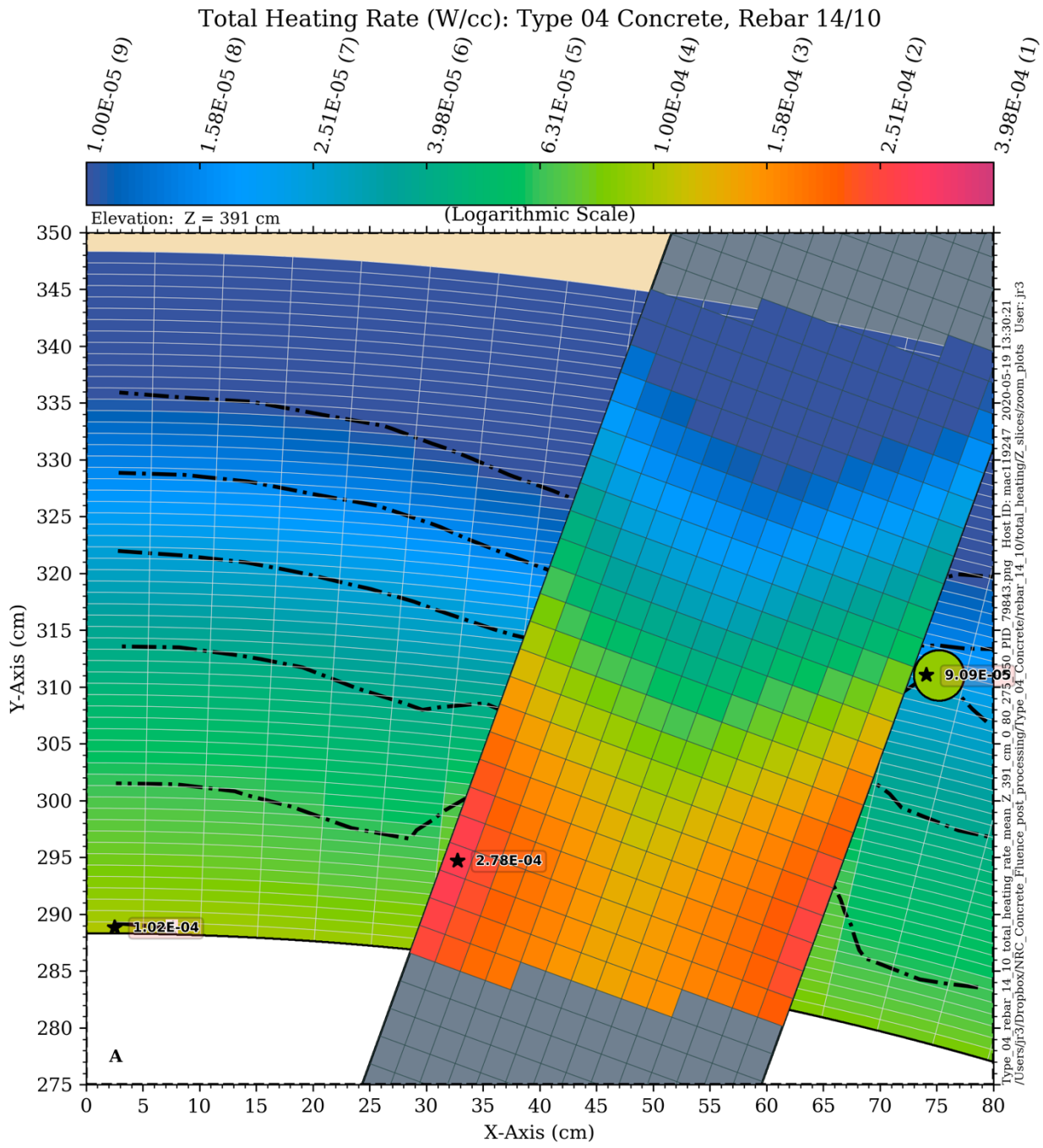

Figure 6-44 Total (neutron + gamma) heating rate contours at an elevation of 391 cm: Type 04 concrete with #14 rebar and a 10-inch concrete cover

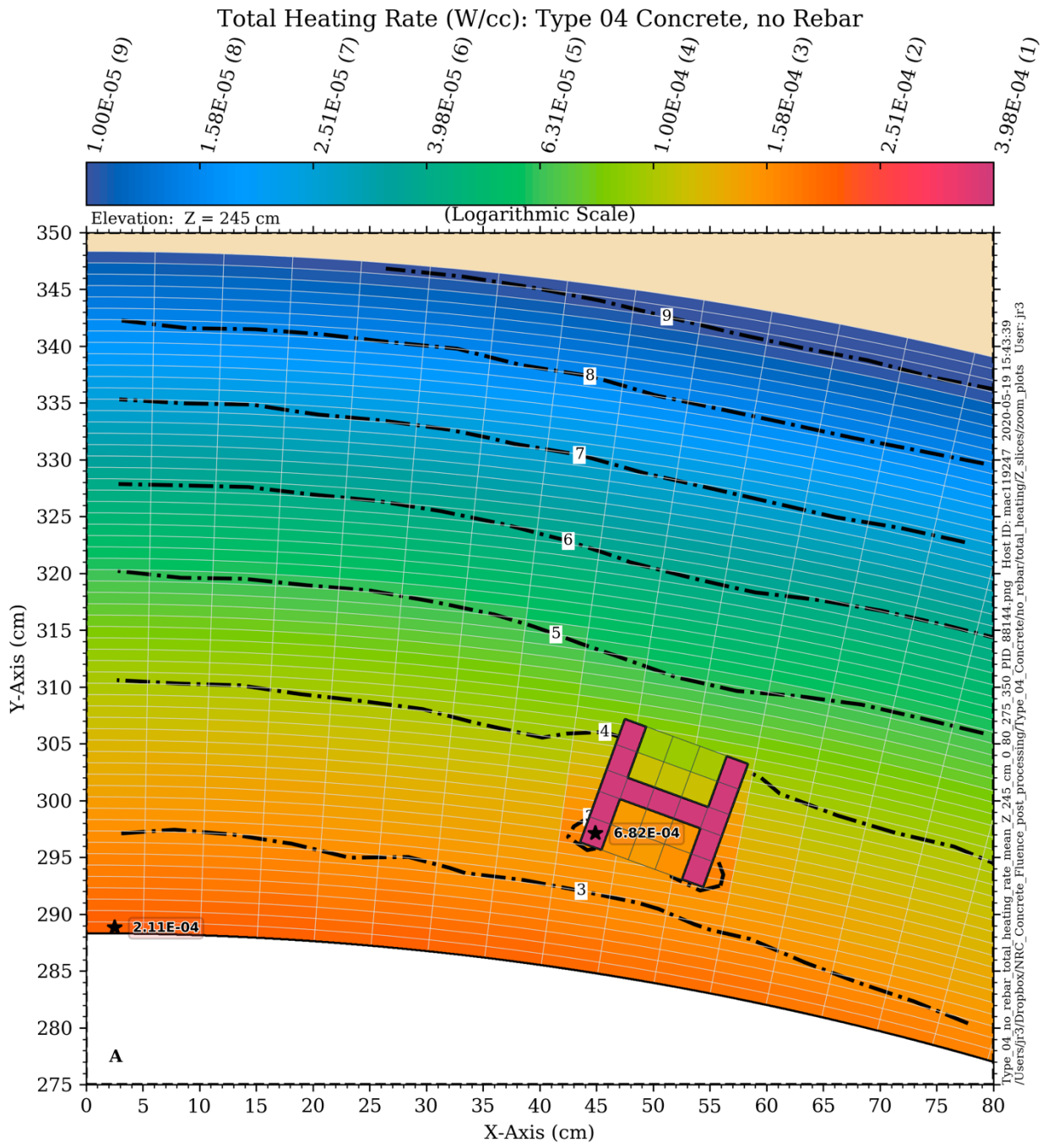

Figure 6-45 Total (neutron + gamma) heating rate contours at an elevation of 245 cm: Type 04 concrete with no rebar

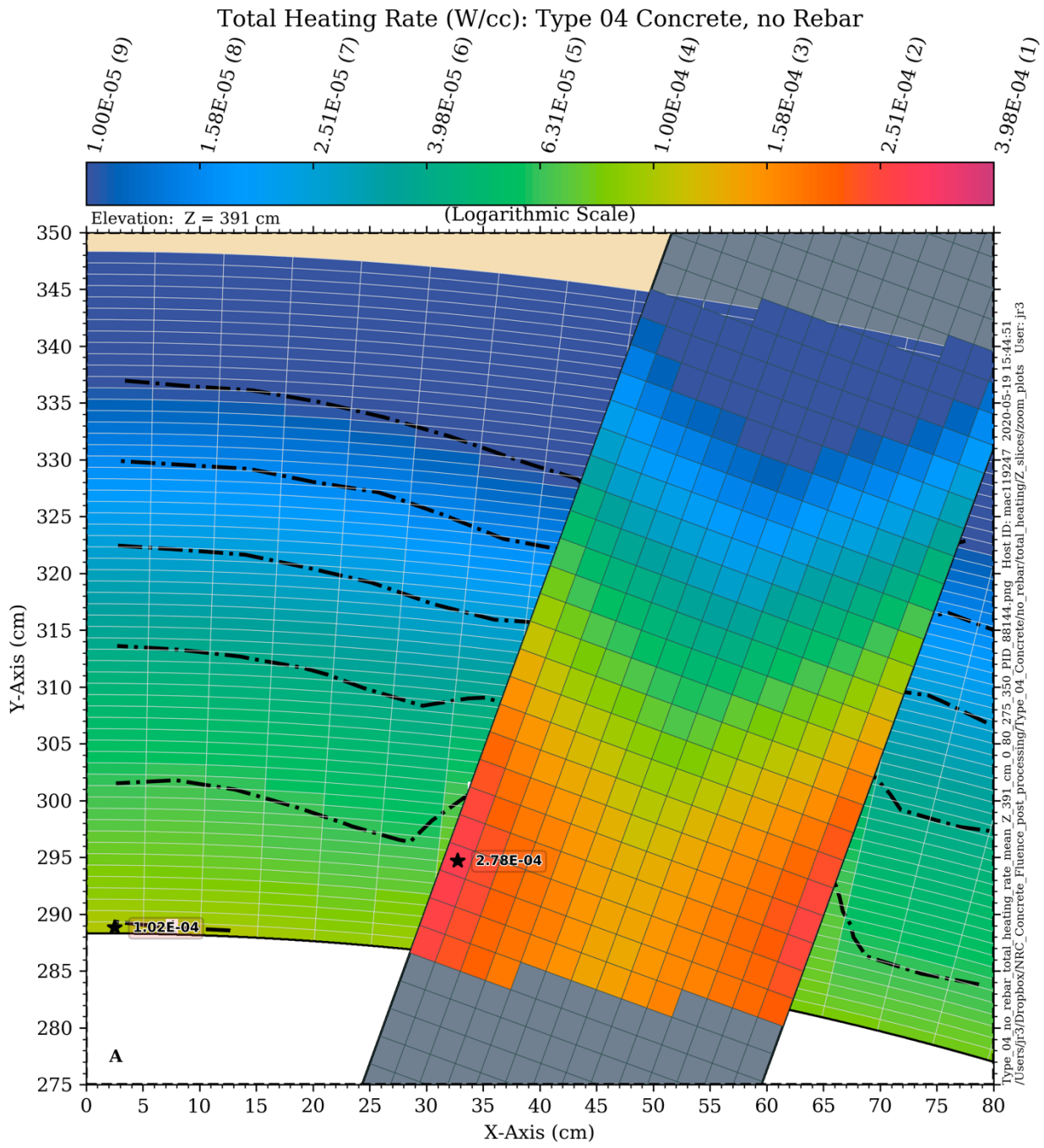

Figure 6-46 Total (neutron + gamma) heating rate contours at an elevation of 391 cm: Type 04 concrete with no rebar

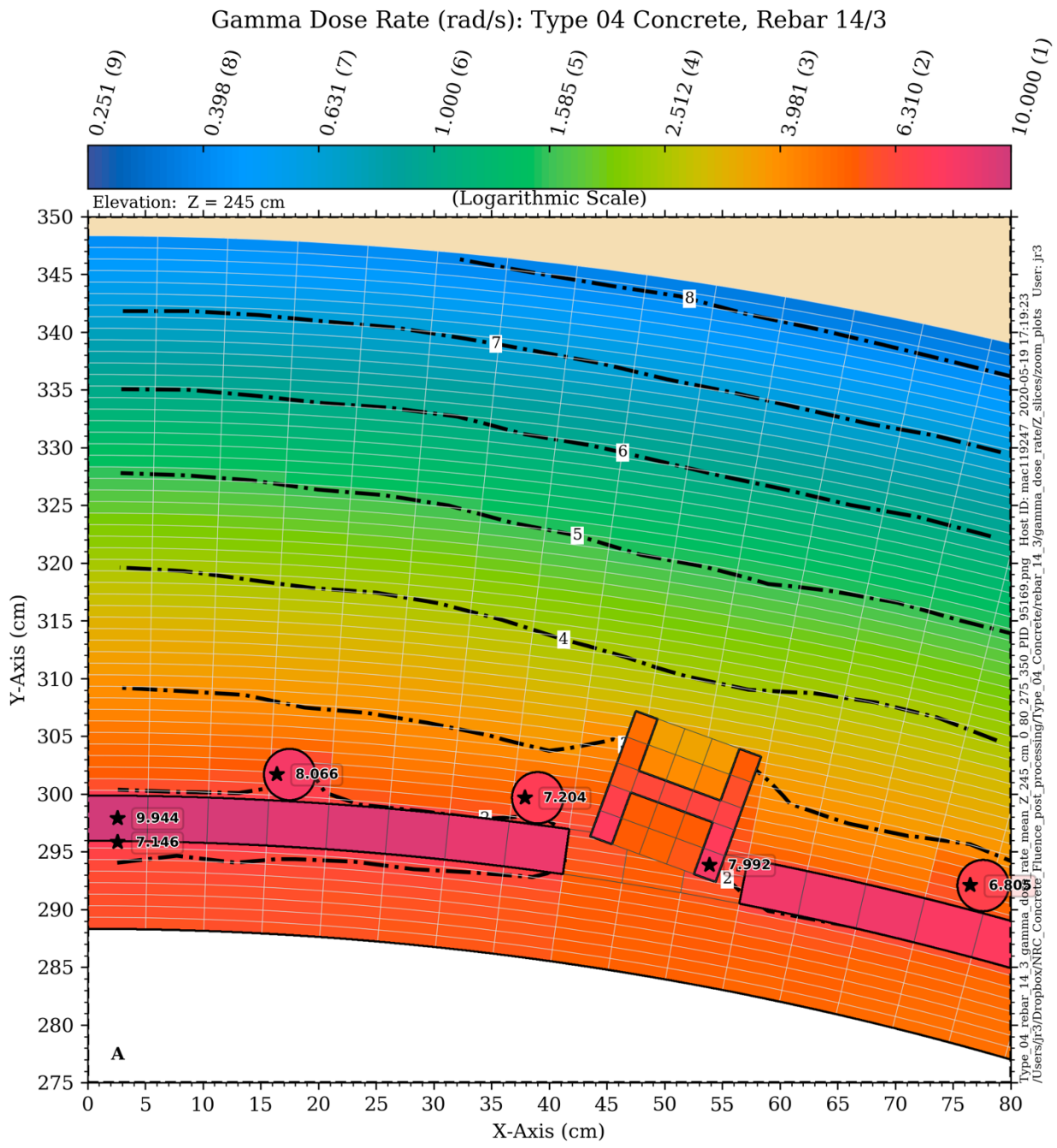

Figure 6-47 Gamma dose rate contours at an elevation of 245 cm: Type 04 concrete with #14 rebar and a 3-inch concrete cover

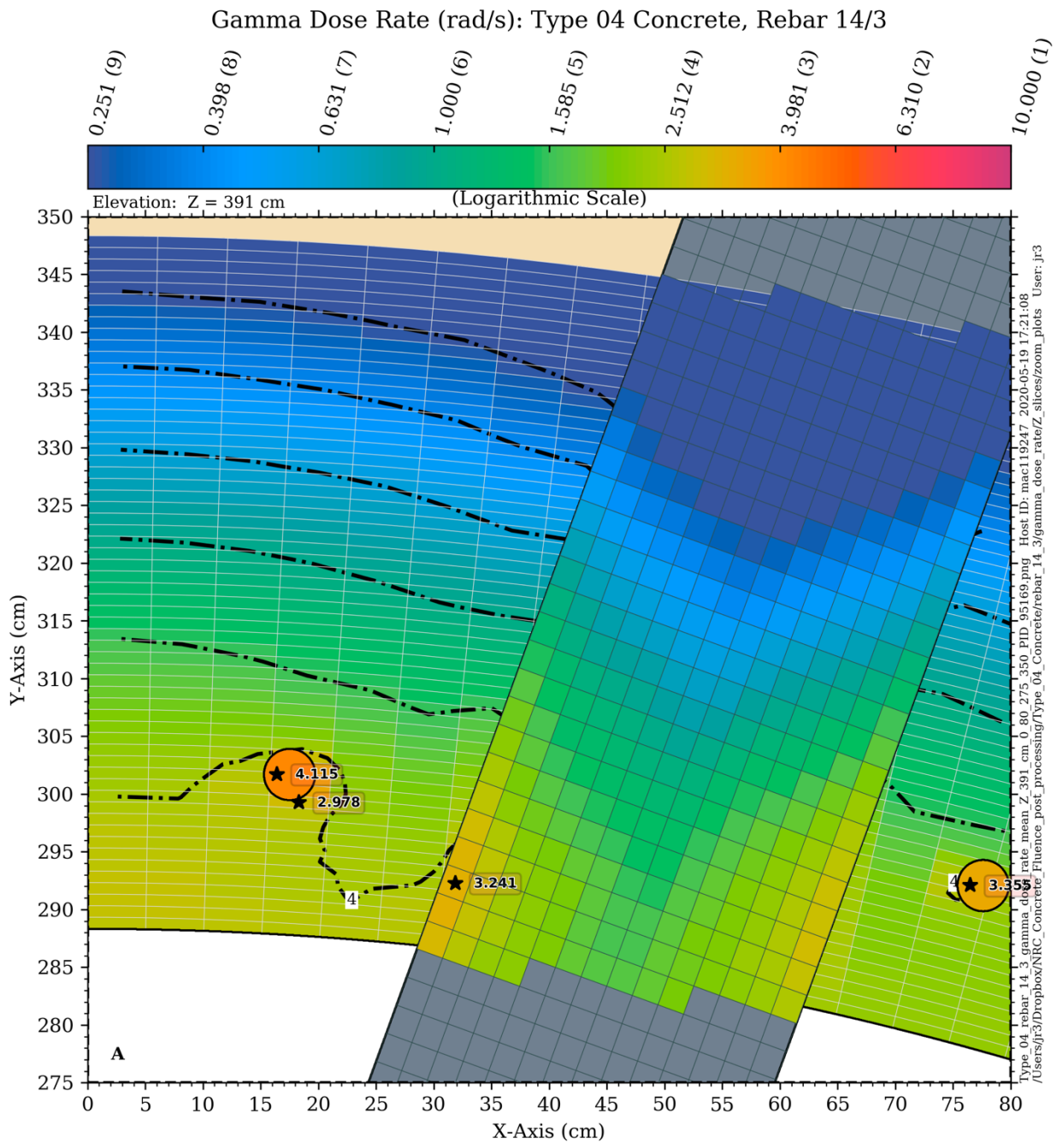

Figure 6-48 Gamma dose rate contours at an elevation of 391 cm: Type 04 concrete with #14 rebar and a 3-inch concrete cover

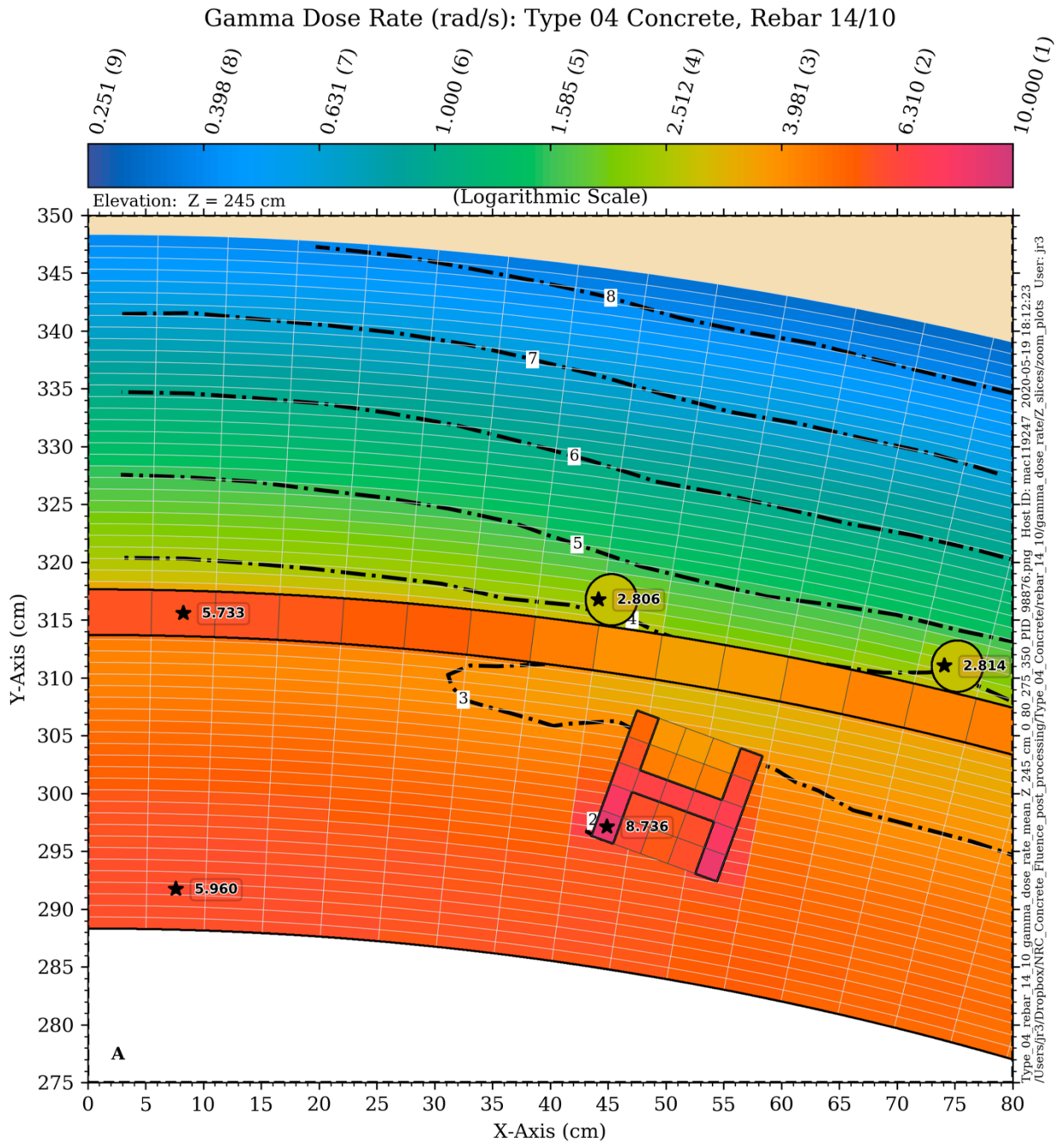

Figure 6-49 Gamma dose rate contours at an elevation of 245 cm: Type 04 concrete with #14 rebar and a 10-inch concrete cover

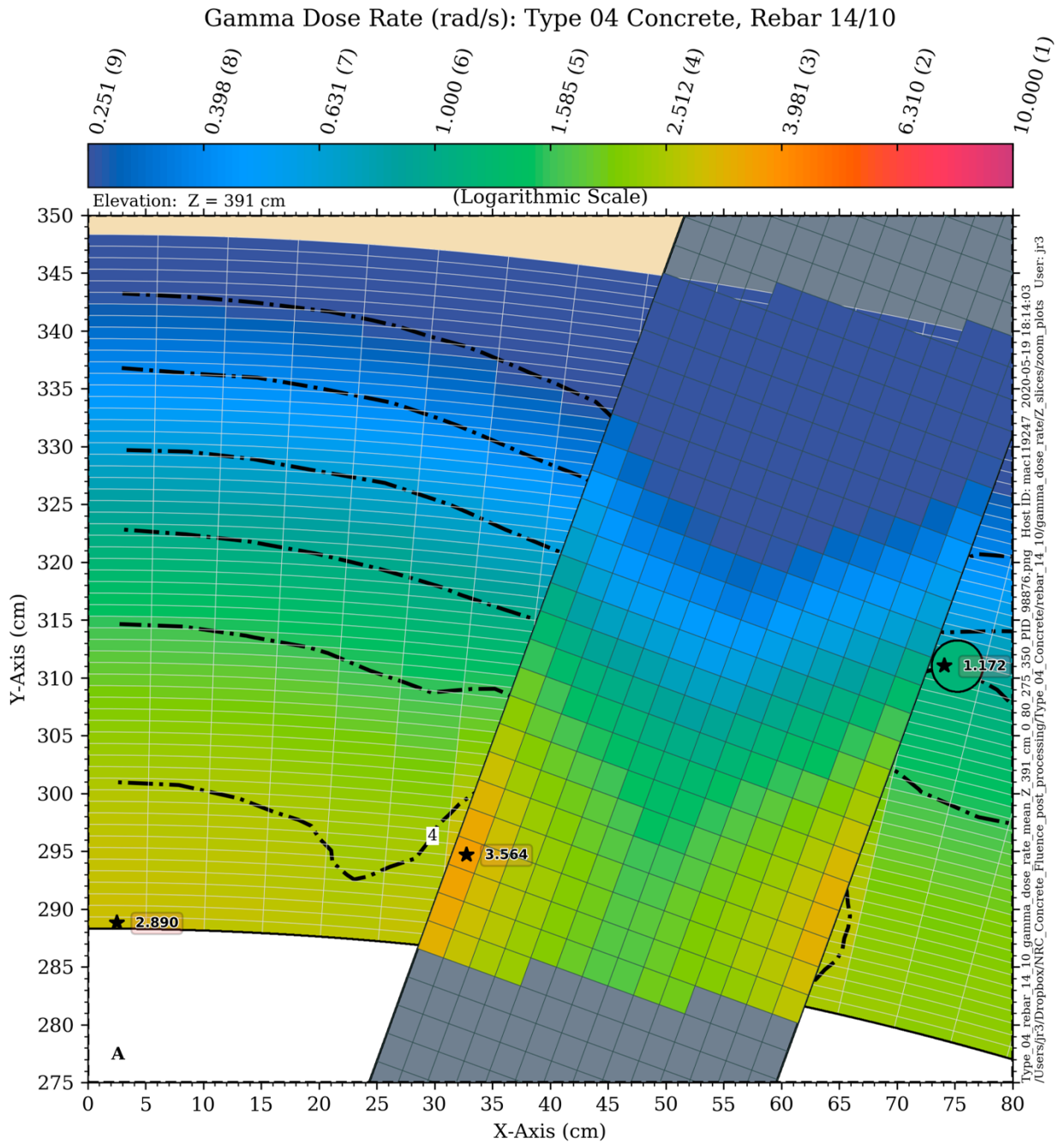

Figure 6-50 Gamma dose rate contours at an elevation of 391 cm: Type 04 concrete with #14 rebar and a 10-inch concrete cover

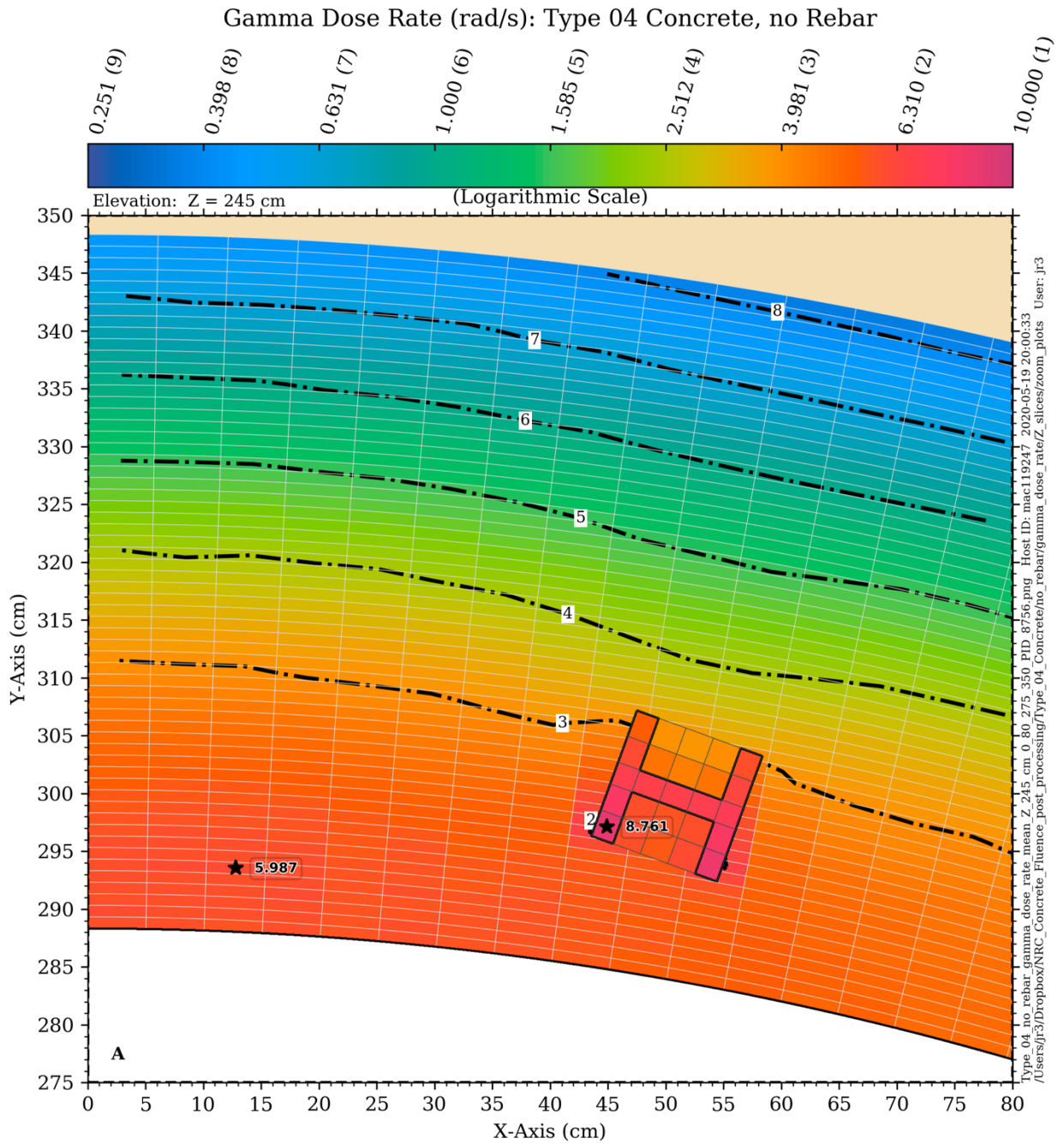

Figure 6-51 Gamma dose rate contours at an elevation of 245 cm: Type 04 concrete with no rebar

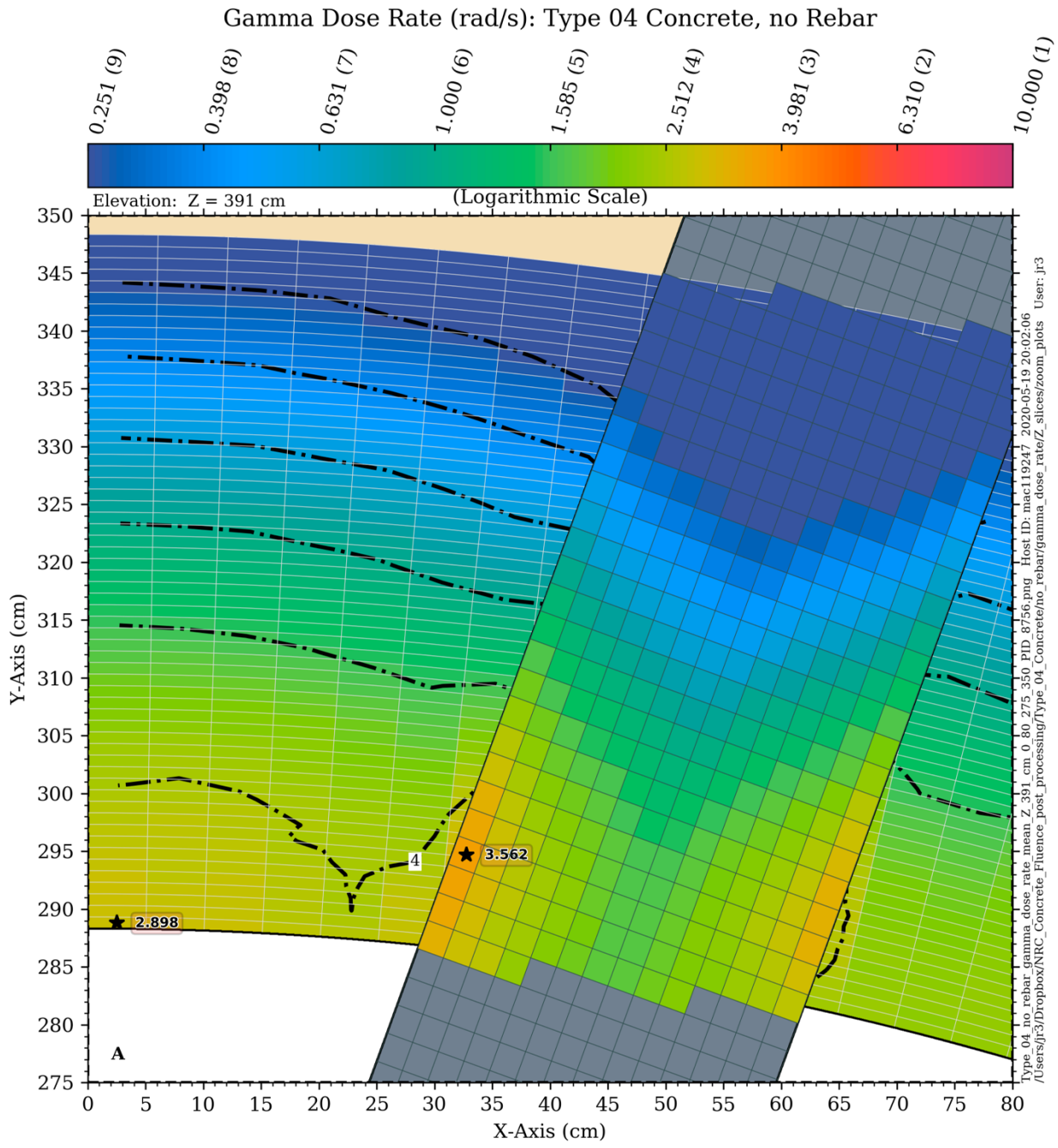

Figure 6-52 Gamma dose rate contours at an elevation of 391 cm: Type 04 concrete with no rebar

6.3 Bioshield with a Steel Liner

The presence of a 0.25-inch stainless steel liner on the inner surface of the bioshield was evaluated for the base case model. As shown in Figure 6-53 and Figure 6-54, the liner has a slight effect on neutron flux levels for E > 1.0 MeV and for E > 0.1 MeV. (These figures also show the effect of reflective thermal insulation, which is discussed in Section 6.4 The addition of the liner reduces the neutron flux levels in each of those energy ranges by 5–10%. The attenuation coefficients from a weighted least-squares fit are essentially identical, with differences of less than 3%.

The addition of the liner does cause a localized increase in the total heating rate and the gamma dose rate near the inner surface of the concrete, as shown in Figure 6-55 through Figure 6-58. These increases are due to capture gamma production in the steel. There are some slight localized differences in the heating rate and gamma dose rate in the rebar relative to the base case model (without a liner), but those differences are not statistically significant.

Because both carbon steel and stainless steel could be used for bioshield liners, an additional analysis was performed using carbon steel rather than stainless steel. Changing the stainless steel to carbon steel had no effect on the neutron flux attenuation. The only notable effect on the total heating rate and gamma dose rate was within the liner itself. Both the total heating rate and the gamma dose rate in the liner are reduced by ~9% with a carbon steel liner relative to a stainless steel liner.

6.4 Reflective Thermal Insulation in the Cavity Gap

The presence of reflective thermal insulation was evaluated for the base case model by adding a 3-inch layer of reflective thermal insulation in the cavity gap near the RPV (see Figure A-13). The insulation is modeled as a homogenized steel/air mixture with a steel volume fraction of 3%. As shown in Figure 6-53 and Figure 6-54, the insulation has essentially no effect on the neutron flux levels in the bioshield.

The addition of the insulation also has no statistically significant effect on the total heating rate or the gamma dose rate in the bioshield.

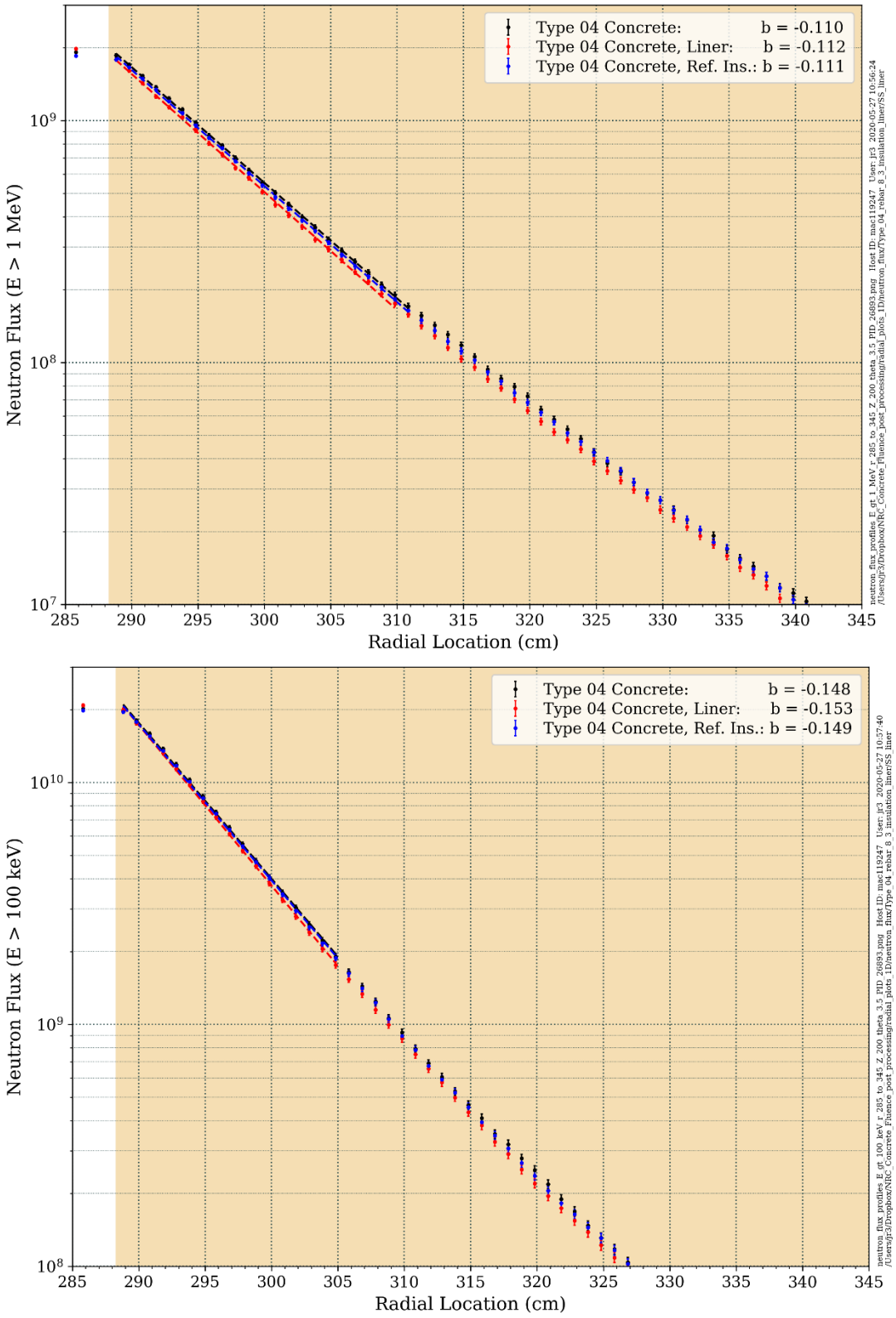

Figure 6-53 Neutron flux radial profiles in Type 04 concrete at an elevation of 200 cm and an azimuthal angle of 3.5º (This plot shows the effect of a stainless steel liner and the effect of reflective thermal insulation)

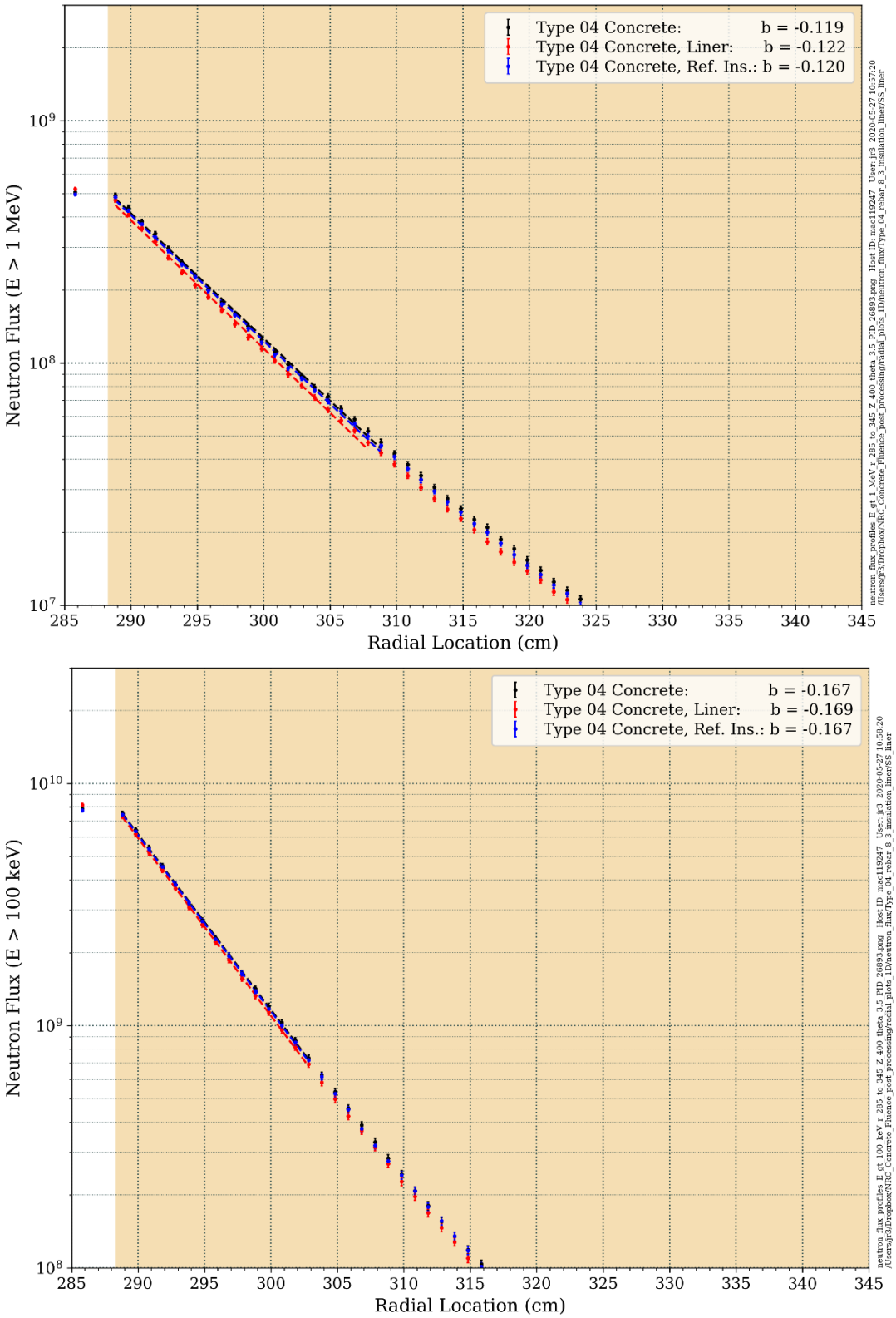

Figure 6-54 Neutron flux radial profiles in Type 04 concrete at an elevation of 400 cm and an azimuthal angle of 3.5º (This plot shows the effect of a stainless steel liner and the effect of reflective thermal insulation)

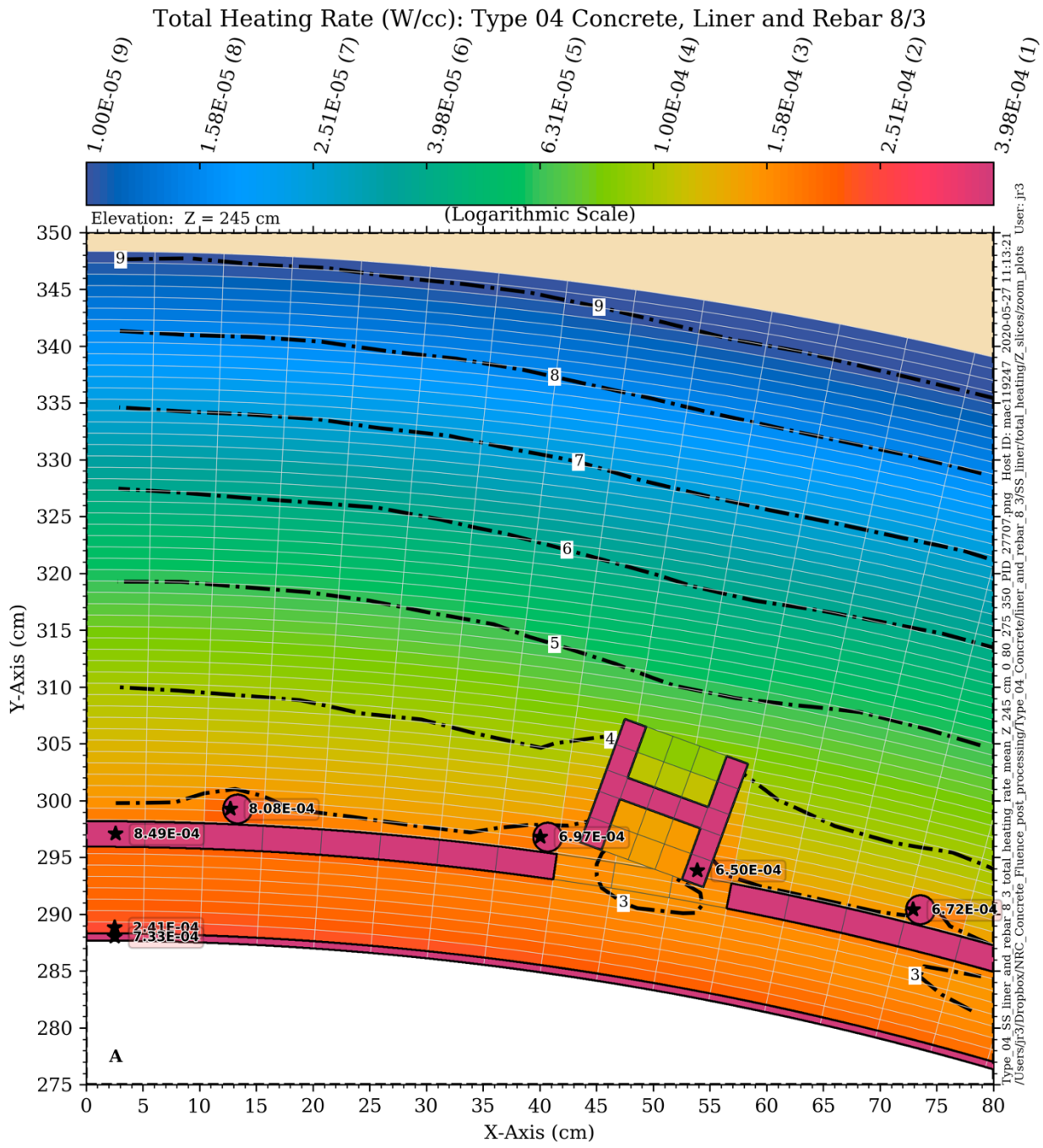

Figure 6-55 Total (neutron + gamma) heating rate contours at an elevation of 245 cm: Type 04 concrete with #8 rebar and a 3-inch concrete cover (This model also includes a 0.25-inch stainless steel liner on the inner radius of the concrete)

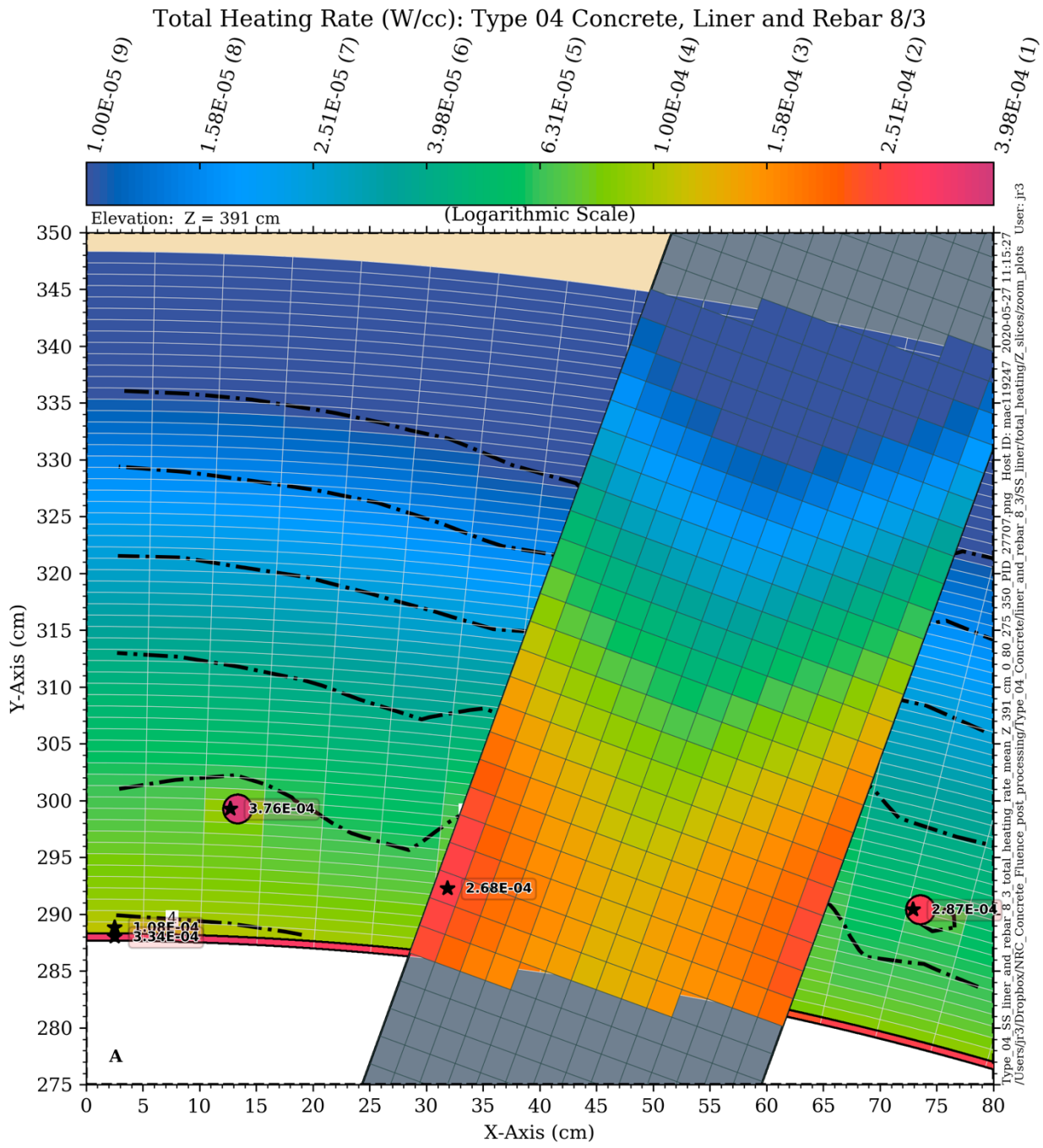

Figure 6-56 Total (neutron + gamma) heating rate contours at an elevation of 391 cm: Type 04 concrete with #8 rebar and a 3-inch concrete cover (This model also includes a 0.25-inch stainless steel liner on the inner radius of the concrete)

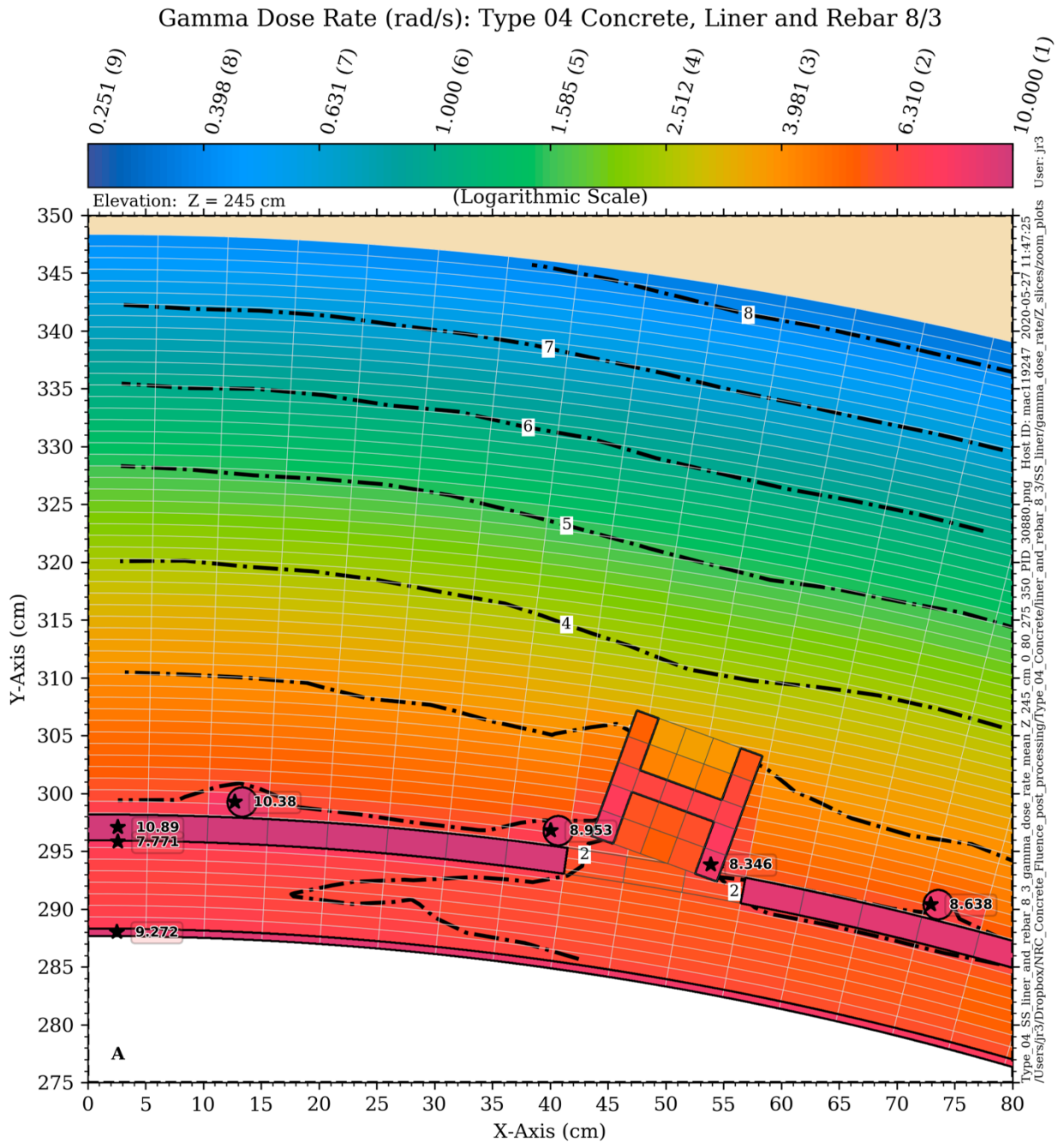

Figure 6-57 Gamma dose rate contours at an elevation of 245 cm: Type 04 concrete with #8 rebar and a 3-inch concrete cover (This model also includes a 0.25-inch stainless steel liner on the inner surface of the concrete)

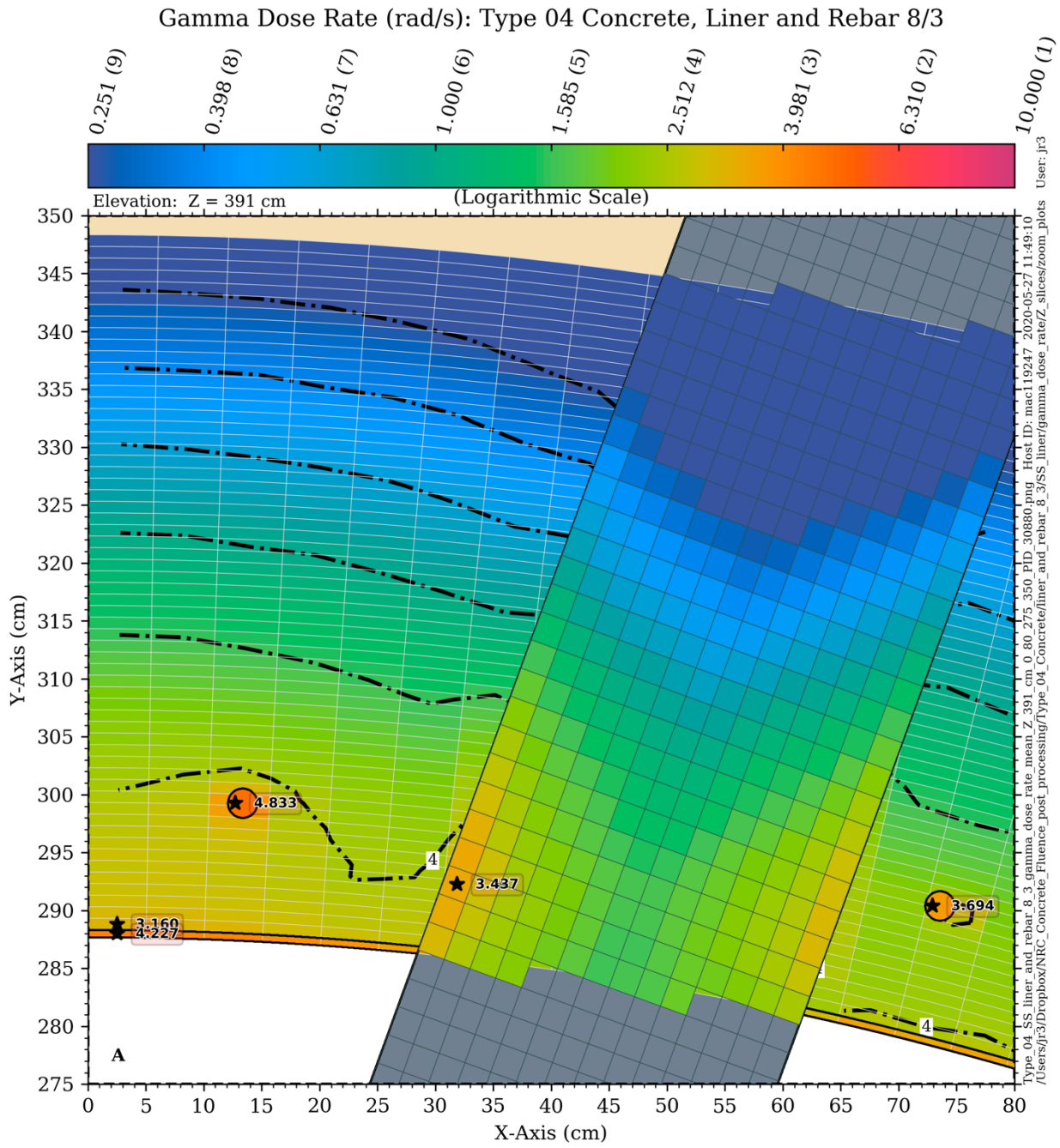

Figure 6-58 Gamma dose rate contours at an elevation of 391 cm: Type 04 concrete with #8 rebar and a 3-inch concrete cover (This model also includes a 0.25-inch stainless steel liner on the inner surface of the concrete)

6.5 Cavity Gap Width

The effect of the cavity gap width on neutron flux levels, heating rates, and gamma dose rates was assessed by constructing three versions of the three-loop PWR model: a minimum cavity gap width of 13 cm, a baseline width of 71 cm (used for the analyses in Sections 6.1 and a maximum width of 120 cm (see Section 5.5 Because varying the gap width affects the geometry of the RPV support system[5], these models have no structural steel in the bioshield or in the cavity gap. Consequently, no comparisons are made for these models in the extended beltline region. Plan views of the two non-baseline models (i.e., the 13-cm gap and the 120-cm gap model) are shown in Figure A-14 and Figure A-15.

Changing the cavity gap width has two fundamental impacts on neutron and gamma fluxes in the bioshield. While increasing the gap width reduces the maximum incident neutron and gamma fluxes at the inner surface of the bioshield, the ratio of the incident flux for one cavity gap width to another at any elevation is not constant but varies with the azimuthal location. Consequently, it is possible that at some locations the incident neutron flux (or heating rate or dose rate) can be equivalent or nearly so for different cavity gap widths. At an azimuthal angle of 3.5º (near the X-axis), the incident neutron flux levels for the three cavity gap widths (13 cm, 71 cm, and 120 cm) decrease as the gap width increases (Figure 6-59). At an azimuthal angle of 44.5º, however, the differences in the incident neutron flux levels for the three cavity gap widths are substantially reduced (Figure 6-60).

Figure 6-61 illustrates the azimuthal variation in the neutron fluxes for E > 1.0 MeV and E > 0.1 MeV at the inner surface of the bioshield. At angles near the X- and Y-axes, where the maximum incident flux levels occur, the incident flux for the 13-cm gap is approximately 70% higher than the incident flux for the 71-cm gap for E > 1.0 MeV, and approximately 85% higher for E > 0.1 MeV. At 45º, where the minimum incident fluxes occur, the difference between the 13-cm and 71-cm gap widths is less than 10% for E > 1.0 MeV, and there is no difference for these two gap widths for E > 0.1 MeV.

This behavior can be explained using the concept of particle *importance*. A particle's importance is a measure of how likely it is to contribute to a quantity of interest, such as the flux or heating rate at a particular location within a particular energy range. For example, a neutron with an energy of 2 MeV in the core has a greater probability of reaching the bioshield in comparison to a neutron with an energy of 0.1 MeV at the same location in the core. The 2-MeV neutron thus has a greater importance than the 0.1-MeV neutron. Similarly, a neutron with an energy of 2 MeV at the outer edge of a peripheral fuel assembly has a greater probability to reaching the bioshield compared with a neutron of the same energy in an inner assembly.

The particle importance as a function of space and energy can be obtained by solving the *adjoint* form of the Boltzmann transport equation. In an adjoint calculation, the adjoint source is the quantity of interest at a specified location or locations. For example, if the quantity of interest is the neutron flux for E > 1 MeV at a specific location in the bioshield, the adjoint source is taken to be the flux of neutrons with energy greater than 1 MeV at that location.

As an example, we consider the neutron flux incident to the bioshield at an angle of 45º, where the difference in the incident fluxes for the three cavity gap widths is minimized (Figure 6-61). The adjoint flux for energy ranges of E > 1.0 MeV and E > 0.1 MeV was solved for the 13-cm and 120-

[5] A review of the geometry plots in Appendix A shows that it would not be possible to model the short column support system with a 13-cm cavity gap.

cm gap models using the Denovo discrete ordinates radiation transport code. The adjoint source region, which is the inner surface of the bioshield at 45º, is the location for which the neutron importance in the fuel assemblies is calculated. Figure 6-62 and Figure 6-63 show the adjoint neutron flux for E > 1.0 MeV at an elevation of 200 cm. In each plot, the adjoint flux levels are normalized to the maximum adjoint flux level (or importance) within the core. Comparison of these figures shows that the neutron flux incident to the concrete at 45º for the 13-cm gap is due primarily to only a few assemblies near 45º, while the incident flux for the 120-cm gap has significant contributions from the outer assemblies along the entire periphery of the core.

There are thus two “competing effects” with regard to the bioshield incident flux along the 45º angle. As the cavity gap width increases, the incident flux tends to decrease due to the increased distance. At the same time, though, increasing the gap width expands the range of fuel assemblies that provide significant contributions to the incident flux at the 45º location.

The radial and azimuthal variations in the total heating rate and gamma dose rate are shown in Figure 6-64, Figure 6-65, and Figure 6-66. The general trend of the azimuthal variation of the total heating rate and gamma dose rate as a function of cavity gap width is similar to that of the neutron flux, though the variation of the total heating rate and gamma dose rate is slightly greater than that of the neutron flux. The radial attenuation rates of the total heating rate (which is largely due to gamma heating) and the gamma dose rate are significantly less than the attenuation rates of the neutron flux for E > 1.0 MeV and E > 1 keV. This is consistent with results presented in Section 6.1 .

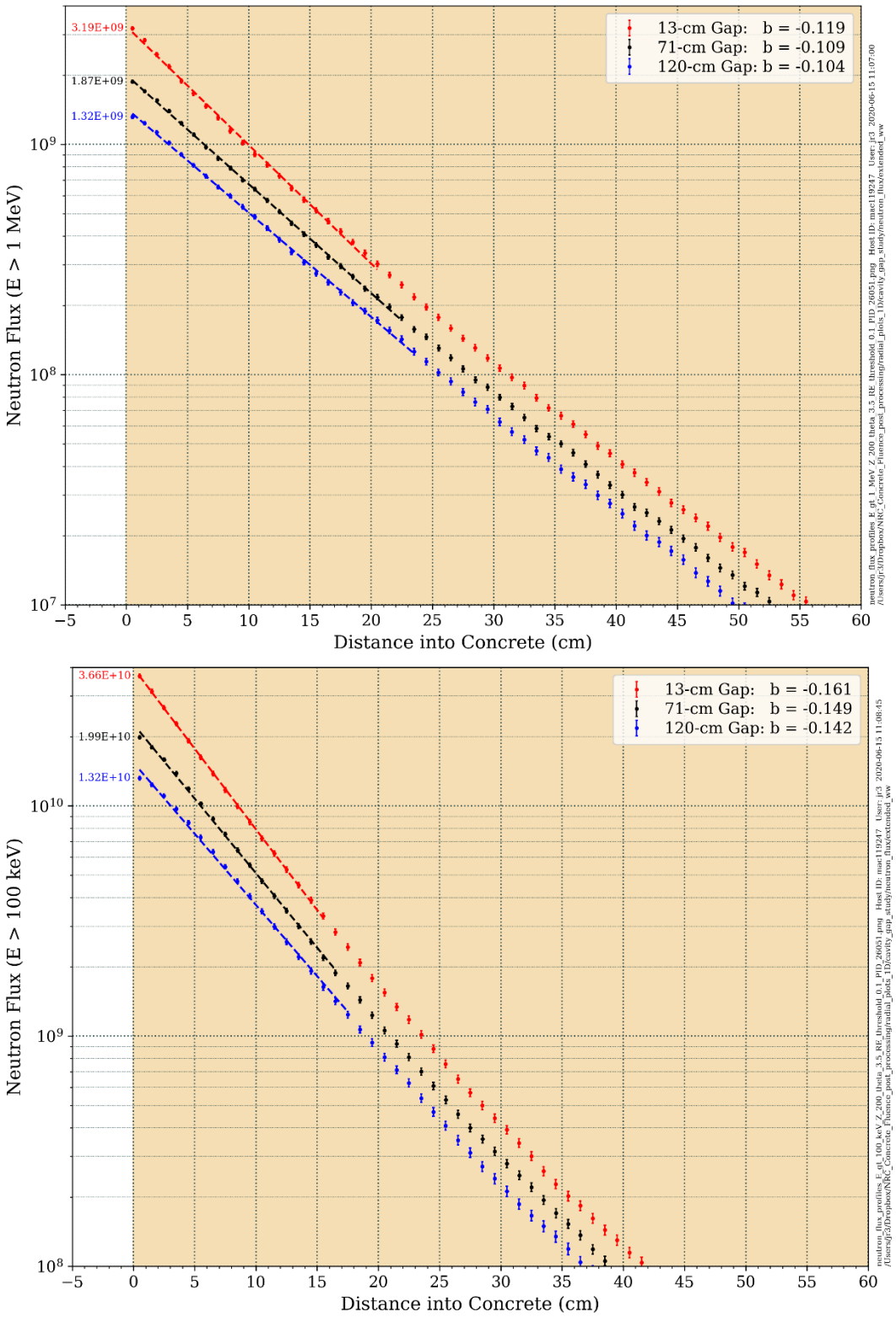

Figure 6-59 Neutron flux radial profiles (E > 1.0 MeV and E > 0.1 MeV) in the bioshield for three cavity gap widths at an elevation of 200 cm and an azimuthal angle of 3.5º (Type 04 concrete. See Section 6.1.1 for a discussion of the parameter "b")

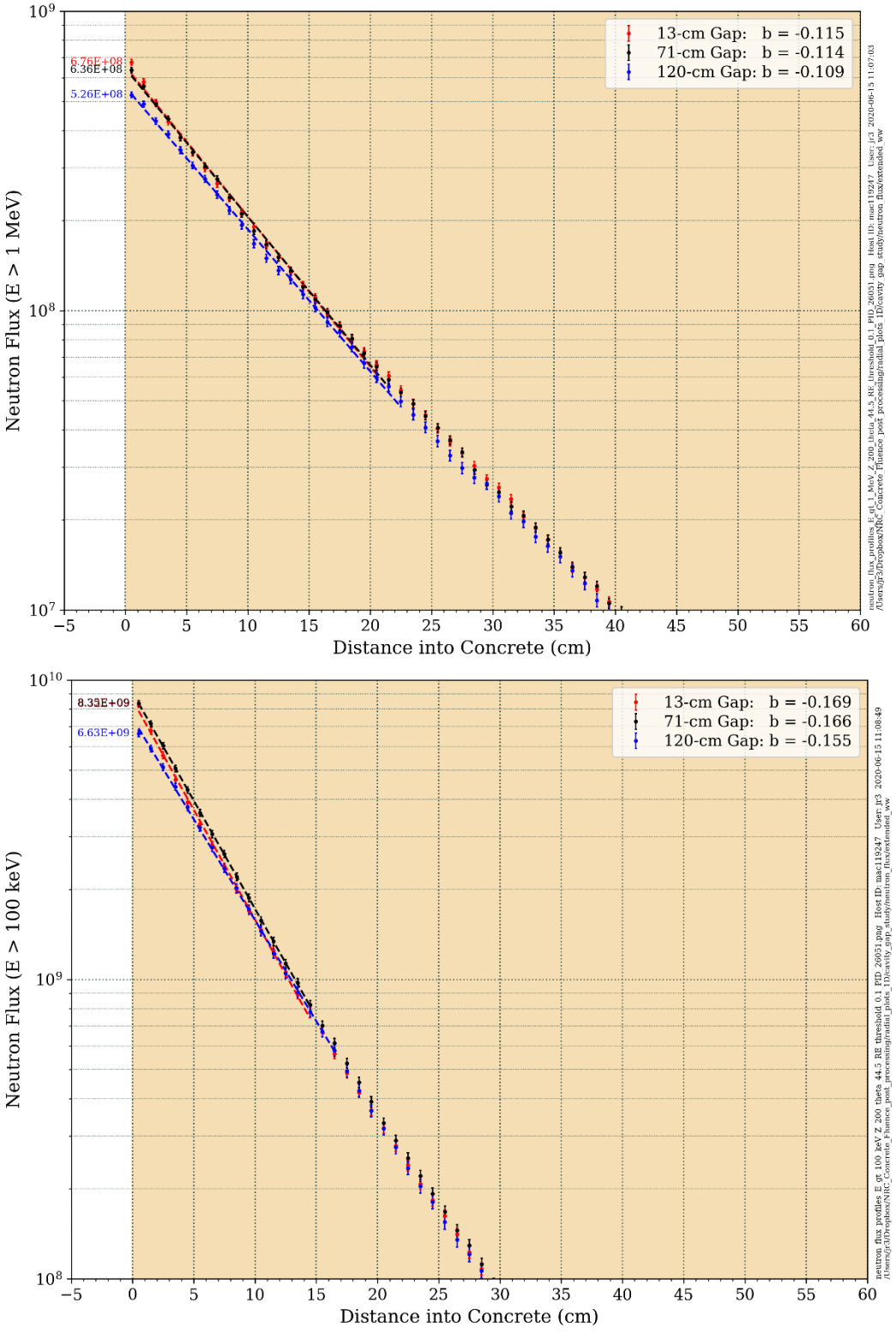

Figure 6-60 Neutron flux radial profiles (E > 1.0 MeV and E > 0.1 MeV) in the bioshield for three cavity gap widths at an elevation of 200 cm and an azimuthal angle of 44.5º (Type 04 concrete. See Section 6.1.1 for a discussion of the parameter "b")

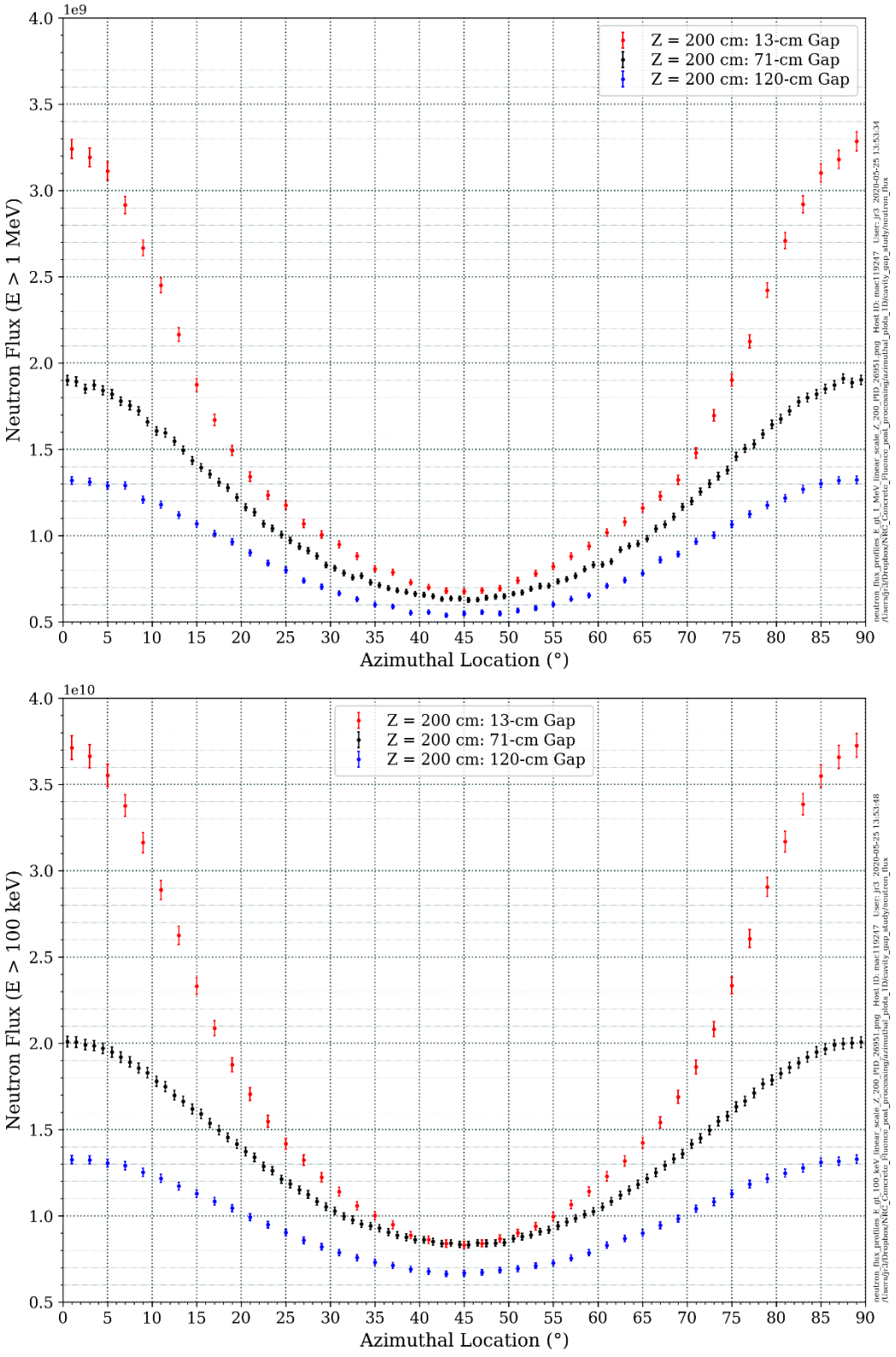

Figure 6-61 Azimuthal variation of the neutron flux at the inner surface of the bioshield for three cavity gap widths at an elevation of 200 cm (Type 04 concrete)

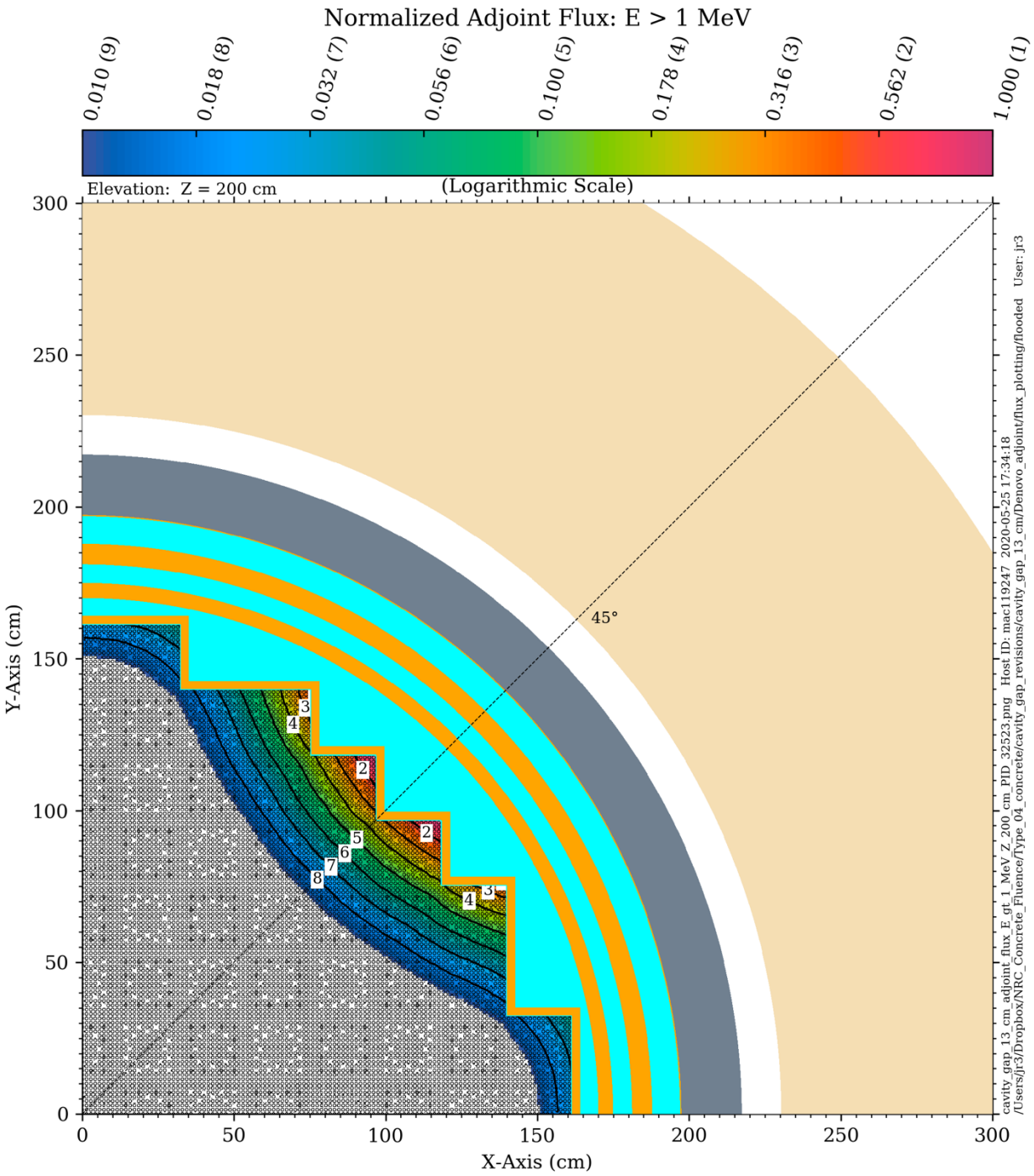

Figure 6-62 Adjoint neutron flux for E > 1.0 MeV for a cavity gap width of 13 cm (The adjoint source location is at the inner surface of the bioshield at an azimuthal angle of 45º. Adjoint flux values are normalized to the maximum adjoint flux within the fuel assemblies.)

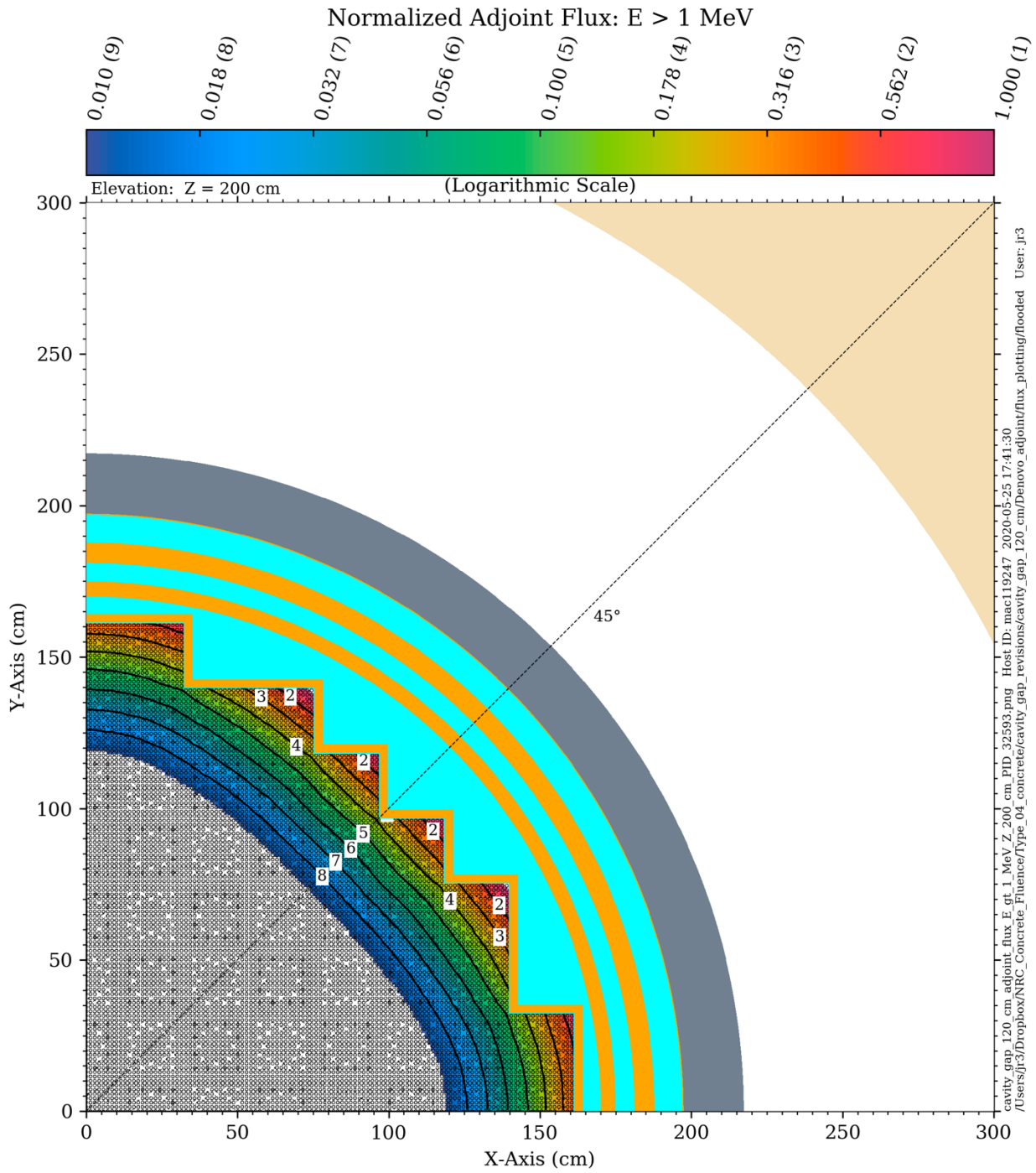

Figure 6-63 Adjoint neutron flux for E > 1.0 MeV for a cavity gap width of 120 cm (The adjoint source location is at the inner surface of the bioshield at an azimuthal angle of 45º. Adjoint flux values are normalized to the maximum adjoint flux within the fuel assemblies.)

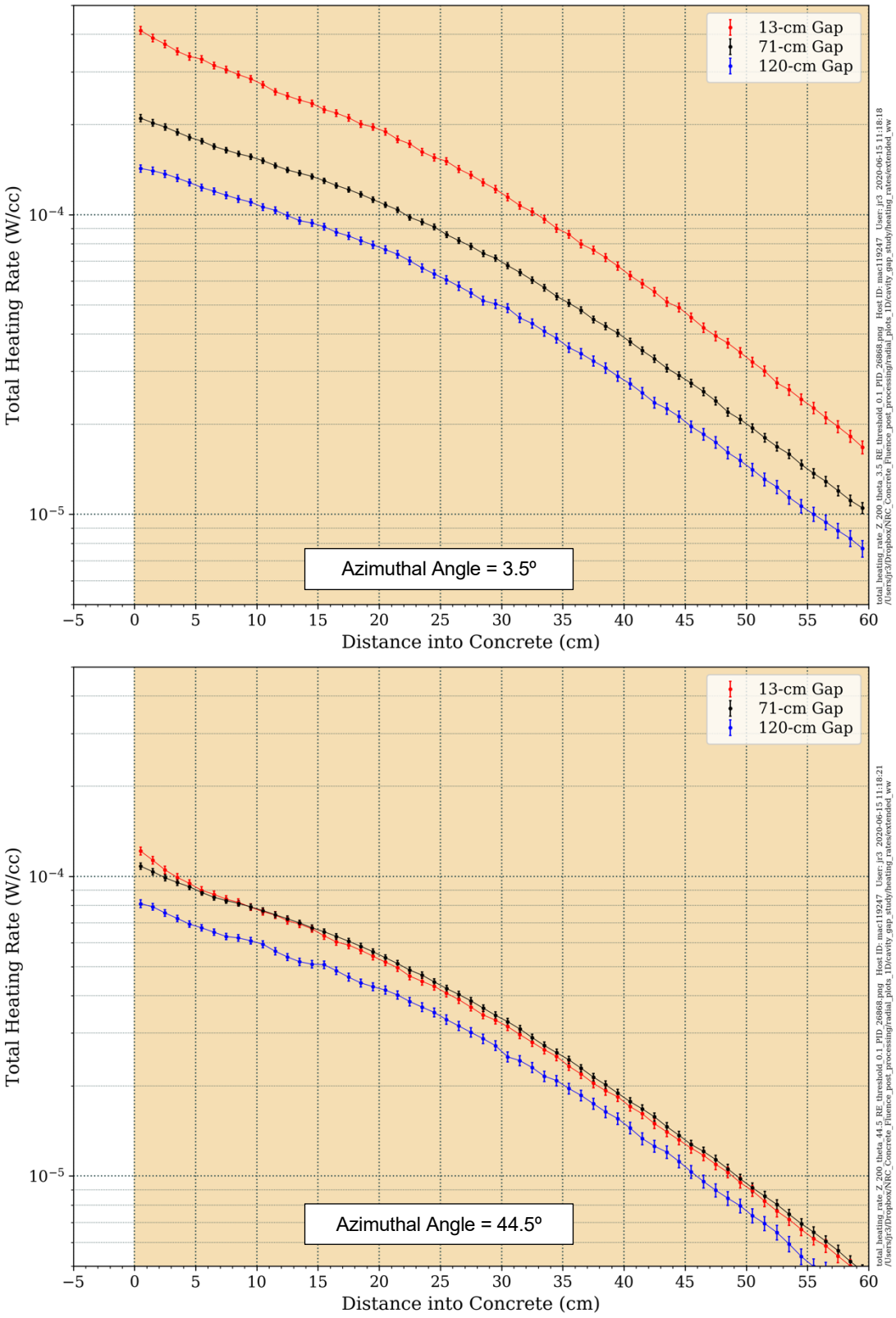

Figure 6-64 Total heating rate radial profiles in the bioshield for three cavity gap widths at an elevation of 200 cm and azimuthal angles of 3.5º and 44.5º

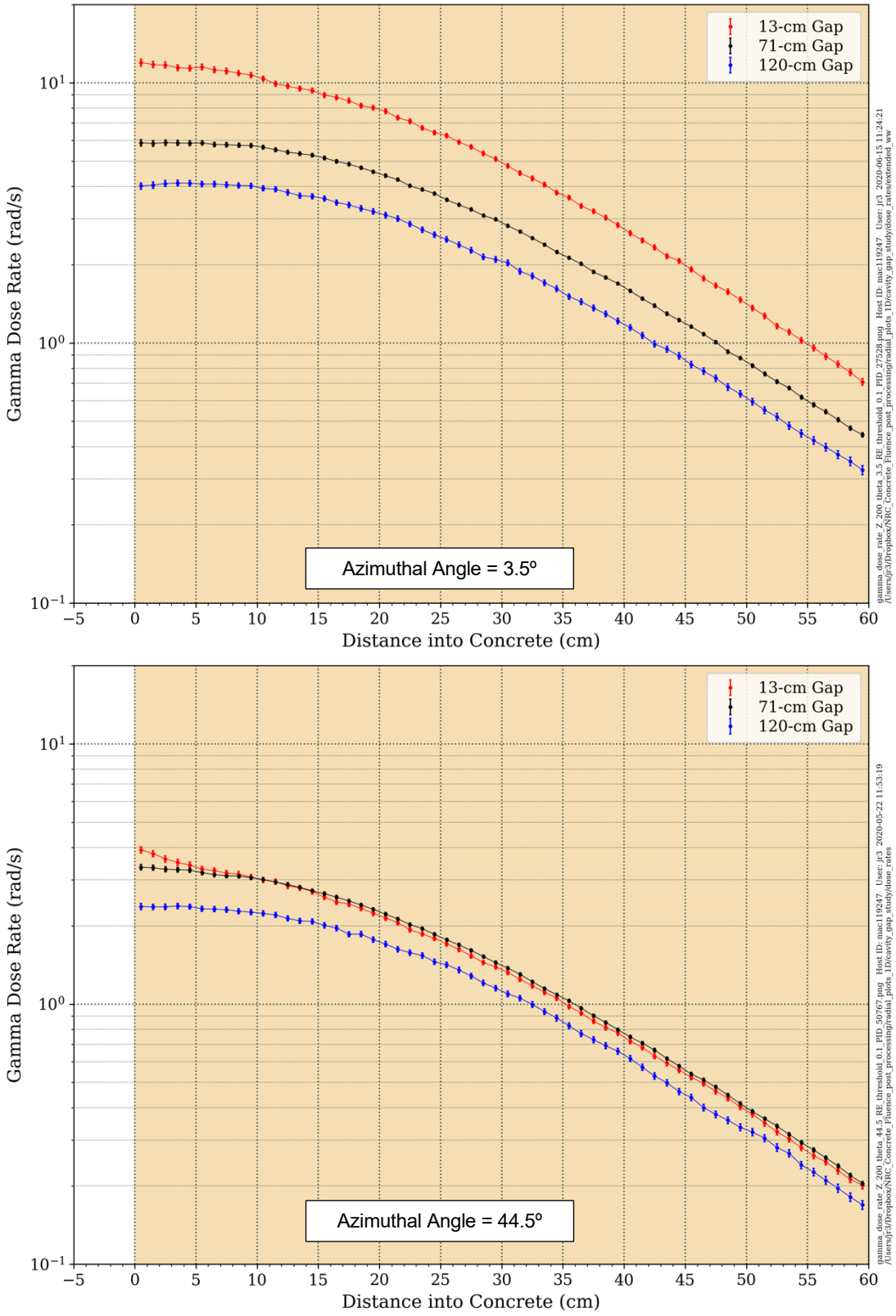

Figure 6-65 Gamma dose rate radial profiles in the bioshield for three cavity gap widths at an elevation of 200 cm and azimuthal angles of 3.5º and 44.5º

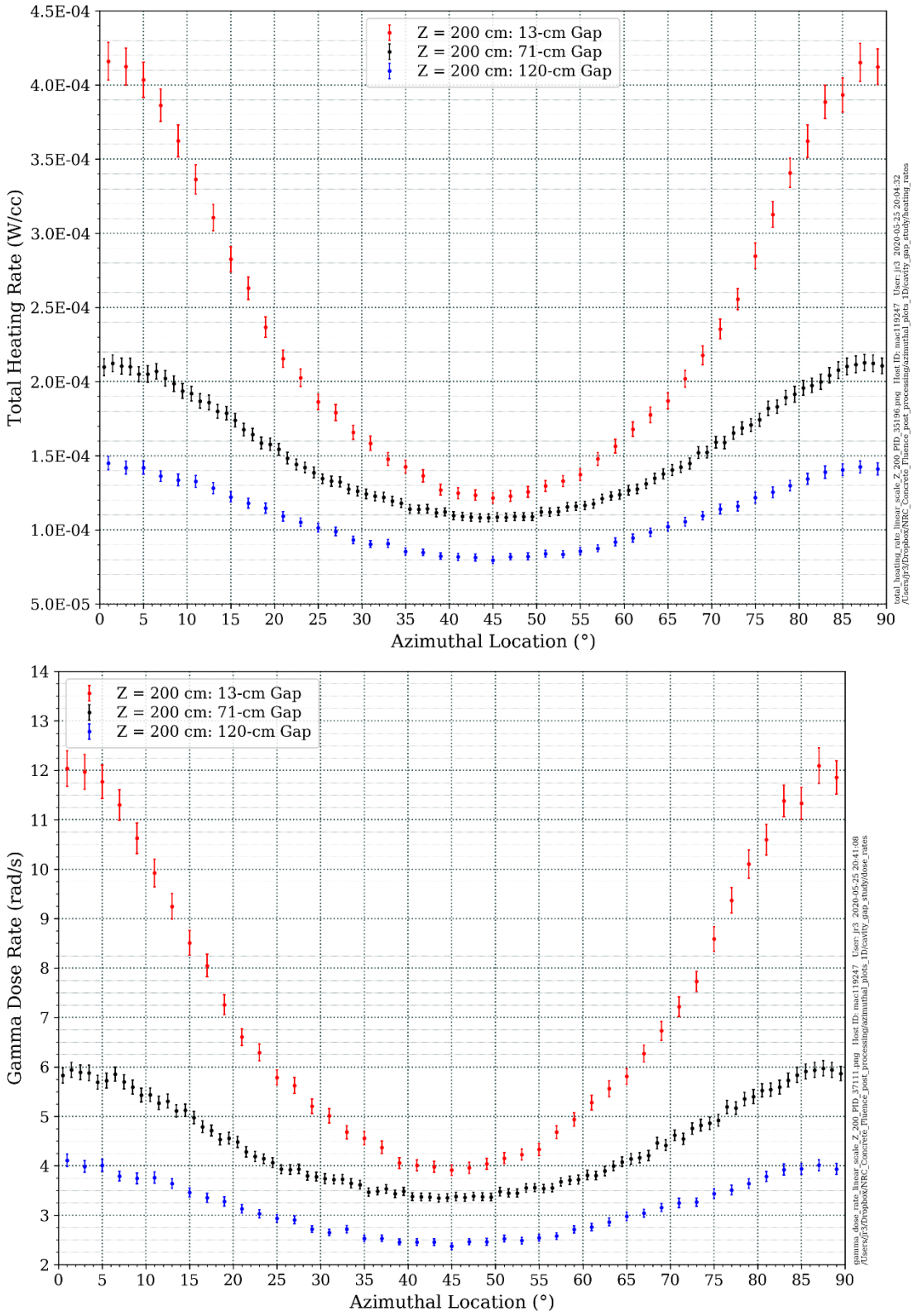

Figure 6-66 Azimuthal variation of the total heating rate and gamma dose rate at the inner surface of the bioshield for three cavity gap widths at an elevation of 200 cm (Type 04 concrete)

7 CONCLUSIONS AND FUTURE WORK

The objectives of this study were to determine the appropriate methodologies for evaluating the neutron flux for energies above 1.0 MeV and above 0.1 MeV, total heating rates, and gamma dose rates in the bioshield and associated steel structures (rebar, embedded support columns, and cantilever beams) within and outside the beltline region. Having determined the appropriate methodology, a model representative of a three-loop PWR was used to assess the effects of the following parameters.

1) The composition of the concrete, with particular emphasis on the hydrogen contents
2) The size and location of rebar (hoop and vertical) within the bioshield
3) The presence of a stainless steel or carbon steel liner on the inner surface of the bioshield
4) The presence of reflective thermal insulation in the cavity gap
5) The width of the cavity gap

The results of these parameter studies are summarized below, followed by a recommendation on the appropriate analysis methodology and suggestions for future work.

7.1 Summary of Parameter Study Findings

7.1.1 Concrete Composition

It is well known that the attenuation of neutrons through concrete is strongly dependent on the hydrogen content of the concrete [44]. Higher hydrogen concentrations in concrete lead to more rapid attenuation of the neutron flux for energies of interest with regard to concrete radiation damage (E > 0.1 MeV). However, this rapid attenuation produces pronounced peaks in the thermal flux (represented by E < 1 eV in this study), which result in higher capture gamma production rates, higher total heating rates, and higher gamma dose rates in the inner region of the bioshield. These effects are clearly demonstrated in Sections 6.1.1 through 6.1.6 This suggests that if the hydrogen content of the concrete for a specific plant analysis is not known, multiple concrete compositions could be evaluated to ensure that the worst-case radiation metrics (neutron flux, total heating rate, and gamma dose rate) are considered.

7.1.2 Size and Location of Reinforcing Steel (Rebar)

The primary radiation damage impact resulting from rebar in concrete is production of capture gammas as thermal neutrons, which have been moderated and thermalized by scattering in the concrete, undergo radiative capture reactions in the steel. This absorption produces a range of capture gamma energies, which can be as high as ~8 MeV. These capture gammas become the dominant contributor to the total heating rate and the gamma dose rate at a relatively short distance into the bioshield (see Figure 6-20).

For each of the four concretes evaluated in this study, the highest total heating rates and gamma dose rates occur within the rebar. Variations in the rebar size (diameter) and location (amount of concrete cover) were evaluated for the Type 04 concrete. Increasing the diameter of the rebar from 1 inch (#8 rebar) to 1.75 inches (#14 rebar) with the same 3-inch concrete cover results in a decrease in the peak total heating rate and peak gamma dose rate.

Increasing the concrete cover for the #14 rebar from 3 inches to 10 inches results in a reduction in both the peak total heating rate and the peak gamma dose rate. This is largely due to the movement of the rebar to a depth beyond where the thermal flux peak occurs (see Figure 6-15). This movement to a region of lower thermal flux reduces the intensity of the capture gamma source in the rebar.

7.1.3 Presence of a Steel Bioshield Liner

The addition of a 0.25-inch steel liner (either carbon steel or stainless steel) on the inner surface of the bioshield results in a slight (5–10%) decrease in the neutron flux for E > 1.0 MeV and for E > 0.1 MeV. The more significant effect of the steel liner is a localized increase in the total heating rate and the gamma dose rate near the inner surface of the concrete due to neutron capture in the liner.

7.1.4 Presence of Reflective Thermal Insulation in the Cavity Gap

The presence of a 3-inch layer of reflective thermal insulation near the RPV resulted in no statistically significant differences in neutron flux, total heating rates, or gamma dose rates in the bioshield.

7.1.5 Cavity Gap Width

The effect of the cavity gap width was evaluated using three models: a 13-cm gap, a 71-cm gap, and a 120-cm gap. While increasing the gap width results in reductions in the maximum neutron flux, total heating rate, and gamma dose rate in the bioshield, those reductions are not uniform around the periphery of the bioshield inner surface. Changes in the cavity gap width have the most pronounced effect at azimuthal angles with the minimum amount of water between the outer fuel assemblies and the inner surface of the RPV (e.g., near 0º and near 90º). At azimuthal angles near 45º, which is the location where the maximum amount of water occurs between the outer fuel assemblies and the inner surface of the RPV, there is little difference in the neutron flux for E > 1.0 MeV and for E > 0.1 MeV between the 13-cm-gap model and the 71-cm-gap model, and the differences in the total heating rate and gamma dose rate are small. Consequently, when considering the effect of a change in the cavity gap width, it must be remembered that the effect is azimuthally dependent.

7.2 Recommendations on Analysis Methodology

The primary analysis methods that are currently applied to calculation of neutron and gamma fluxes, heating rates, and dose rates are discrete ordinates calculations, Monte Carlo calculations, and hybrid calculations. Monte Carlo methods have long been considered to be superior to discrete ordinates methods. This is primarily because discrete ordinates calculations require discretization of the space, energy, and angle variables to produce a set of equations that are solved iteratively. In contrast, Monte Carlo calculations provide a more “exact” solution, as they use geometry described by linear and quadratic surfaces (planes, spheres, cylinders, cones, ellipsoids, hyperboloids, and paraboloids) rather than cartesian or cylindrical mesh structures, and CE cross sections rather than MG cross sections that are average values which may not be appropriate at all locations in a given model.

Until fairly recently, Monte Carlo calculations were considered to be prohibitively expensive in terms of computing resources. The advent of hybrid methods provides the ability to perform high-fidelity Monte Carlo calculations on a routine basis. Thus, the hybrid methodology was applied to

this study and is the recommended methodology for analyses of this type. As noted in Section 3.4 a recent hybrid radiation transport analysis of the PCA benchmark yielded calculational results that were generally within 5% of measured data, even in the simulated cavity gap region.

7.3 Suggestions for Future Work

While the results of this study provide valuable insights into the effect of parametric changes on neutron fluxes, total heating rates, and gamma dose rates in a representative LWR bioshield, there are additional areas of research that may be useful to pursue. Key areas of research that would help to provide further insights into radiation effects in concrete bioshields include the following.

- Non-uniform hydrogen content in the bioshield concrete

  As was noted in Section 5.1 the hydrogen content in each of the four concrete types is modeled uniformly throughout the bioshield. It is possible that as the concrete ages and is subject to both environmental and radiation heating effects, it may lose moisture in a non-uniform manner. Thus, it is possible that a more appropriate modeling of the concrete would be to include radial (and perhaps azimuthal) variation of the hydrogen content.

- Coupled radiation transport/thermal analysis to predict temperature distributions and resulting loss of moisture

  Because changes in the hydrogen content of the concrete affect the rate of neutron attenuation, the location and magnitude of the peak thermal flux, and the distribution of capture gamma sources, there may be a “coupling” effect that should be considered. For example, drying of the concrete near the inner surface of the bioshield would lead to reduced neutron attenuation in the inner portion of the shield and a shift in the location of the peak heating rates. This in turn would lead to increased hydrogen loss in different areas of the concrete, which would in turn result in a reduced rate of attenuation of the neutron flux. Consequently, radiation-induced damage of the concrete may occur at increased depths in the concrete. It may be possible to perform an iterative analysis sequence that would include radiation transport calculations to obtain heating rate distributions and thermal calculations to obtain the temperature distribution and resulting loss of moisture in the concrete. The new hydrogen distribution would then be used to calculate updated neutron fluxes and total heating rates.

- Evaluation of dpa rates in the bioshield concrete with hybrid radiation transport

  Remec et al. [18] evaluated dpa rates for several minerals that are common constituents of concrete using discrete ordinates calculations and a 2D/3D flux synthesis method. A similar analysis could be performed using hybrid radiation transport to provide higher-fidelity solutions, particularly in locations outside the beltline where the 2D/3D synthesis method may not be appropriate. (As noted in Section 2.1 the notion of dpa is less meaningful for damage in ionic bonding dominated calcareous (amorphous) aggregates.)

- Obtain measurement data which can be used to benchmark calculational predictions

  Obtaining measured data for the radiation quantities of interest (neutron flux, gamma dose rates, and total heating rates) in the bioshield concrete, rebar, and RPV support structures would be very helpful in developing uncertainty estimates for the ability of transport calculations to predict each of those metrics.

- Investigate whether changes in the concrete due to degradation and cracking affect neutron and gamma transport within the concrete.

8 REFERENCES

[1] U.S. Nuclear Regulatory Commission, "Status of Initial License Renewal Applications and Industry Initiatives," https://www.nrc.gov/reactors/operating/licensing/renewal/applications.html, March 3, 2020.

[2] U.S. Nuclear Regulatory Commission, "Status of Subsequent License Renewal Applications," https://www.nrc.gov/reactors/operating/licensing/renewal/subsequent-license-renewal.html, April 16, 2020.

[3] U.S. Nuclear Regulatory Commission, "A Review of the Effects of Radiation on Microstructure and Properties of Concretes Used in Nuclear Power Plants," NUREG/CR-7171, November 2013, ADAMS Accession No. ML13325B077.

[4] U.S. Nuclear Regulatory Commission, "Expanded Materials Degradation Assessment (EMDA)," NUREG/CR-7153, Vol. 4, October 2014, ADAMS Accession No. ML14279A430.

[5] U.S. Nuclear Regulatory Commission, "Calculational and Dosimetry Methods for Determining Pressure Vessel Neutron Fluence," Regulatory Guide 1.190, ADAMS Accession No. ML010890301.

[6] U.S. Nuclear Regulatory Commission, "H. B. Robinson-2 Pressure Vessel Benchmark," NUREG/CR-6453, February 1998.

[7] U.S. Nuclear Regulatory Commission, "Impact of ENDF/B-VI Cross-Section Data on H. B. Robinson Cycle 9 Dosimetry Calculations," NUREG/CR-6071, October 1993, ADAMS Accession No. ML14188B165.

[8] Esselman,T. and Bruck, P., *Expected Condition of Concrete Exposed to Radiation at Age 80 Years of Reactor Operation*, ORNL/TM-2018/769, Oak Ridge National Laboratory, January 2018.

[9] U.S. Nuclear Regulatory Commission, "Impact of Radiation Embrittlement on Integrity of Pressure Vessel Supports for Two PWR Plants," NUREG/CR-5320, January 1989.

[10] Remec, I., Rosseel, T.M., Field, K.G., and Le Pape, Y., "Characterization of Radiation Fields in Biological Shields of Nuclear Power Plants for Assessing Concrete Degradation," *Proceedings of the 15th International Symposium on Reactor Dosimetry, 18-23 May 2014*, Curran Associates, Inc., 2016.

[11] Hilsdorf, H.K., Kropp, J., and Koch, H.J., "The Effects of Nuclear Radiation on the Mechanicals Properties of Concrete", *American Concrete Institute Special Publication*, SP-55-10: 223–251.

[12] Kontani, O., Ichikawa, Y., Ishizawa, A., Takizawa, M., and Sato, O., "Irradiation Effects on Concrete Structures," *International Symposium on the Ageing Management and Maintenance of Nuclear Power Plants*, *27-28 May 2010*, Mitsubishi Research Institute, 2011.

[13] Fujiwara, K., Itoa, M., Sasanumab, M., Tanakac, H., Hirotanid, K., Onizawae, K., Suzukie, M. and Amezawaf, H. "Experimental Study of the Effect of Radiation Exposure to Concrete," *20th International Conference on Structural Mechanics in Reactor Technology (SMiRT 20)*, *9-14 August 2009*, NC State University Libraries, https://repository.lib.ncsu.edu/handle/1840.20/23584, 2009.

[14] Dubrovskii, V. B., Ibragimov, Sh.Sh., Kulakovskii, M.Ya., Ladygin, A.Ya., and Pergamenshchik, B.K., "Radiation Damage in Ordinary Concrete," *Atomnaya Energiya*, Vol. 23, No.4: 310-316.

[15] Field, K.G., Remec, I., and Le Pape, Y., "Radiation Effects in Concrete for Nuclear Power Plants – Part I: Quantification of Radiation Exposure and Radiation Effects," *Nuclear Engineering and Design*, 282:126-143.

[16] Le Pape, Y., Field, K.G., and Remec, I., "Radiation Effects In Concrete For Nuclear Power Plants – Part II: Perspective from Micromechanical Modeling," *Nuclear Engineering and Design* 282:144-157.

[17] U.S. Nuclear Regulatory Commission, "Review of Radiation-Induced Concrete Degradation and Potential Implications for Structures Exposed to High, Long-Term Radiation Levels in Nuclear Power Plants," ADAMS Accession No. ML2002F057.

[18] Remec, I., Rosseel, T.M., Field, K.G., and Le Pape, Y., "Radiation-Induced Degradation of Concrete in NPPs," *Proceedings of the 16th International Symposium on Reactor Dosimetry, 7-12 May 2017*, ASTM International, 2018.

[19] Soo, P., Milian, L.M., "The Effect of Gamma Radiation on the Strength of Portland Cement Mortars," *Journal of Materials Science Letters*, 20:1345-1348.

[20] Sopko, V., Trtík, K., Vodák, F., "Influence of γ Irradiation on Concrete Strength," *Acta Polytechnica*, Vol. 44 No. 1/2004:57-58.

[21] Kontani, O., Sawada, S., Maruyama, I., Takizawa, M., and Sato, O., "Evaluation of Irradiation Effects on Concrete Structure - Gamma-Ray Irradiation Tests on Cement Paste-", *Proceedings of the ASME 2013 Power Conference (POWER 2013), 29 July – 1 August 2013*, American Society of Mechanical Engineers, 2013.

[22] Maruyama, I., Kontani, O., Ishizawa, A., Takizawa, M., Sato, O., "Development of System for Evaluating Concrete Strength Deterioration Due to Radiation and Resultant Heat," *IAEA-CN-194-093*, *3rd International Conference on NPP Life Management (PLIM) for Long Term Operations (LTO), 14-18 May, 2012*, IAEA, 2012.

[23] Maruyama, I., Kontani, O., Sawada, S., Sato, O., Igarashi, G., Takizawa, M., "Evaluation of Irradiation Effects on Concrete Structure – Background and Preparation of Neutron Irradiation Test," *Proceedings of the ASME 2013 Power Conference POWER2013*, 29 *July – 1 August 2013*, American Society of Mechanical Engineers, 2014.

[24] Risner, J., Daily, C., Davidson, E., and Yang, J., "Reactor Pressure Vessel Fluence Evaluation Methodology Guidance," ORNL/SPR-2017/355, Oak Ridge National Laboratory, September 2017.

[25] Oak Ridge National Laboratory Presentation, "01/13/2016 Neutron Fluence Computation (Part 2 of 2)," 2016, ADAMS Accession No. ML17038A136.

[26] Oak Ridge National Laboratory Presentation, "Topic 3 Quadrature Studies," 2018, ADAMS Accession No. ML18159A008.

[27] Oak Ridge National Laboratory Presentation, "Deterministic Monte Carlo Comparisons," 2018, ADAMS Accession No. ML18159A010.

[28] I. K. Abu-Shumays. Compatible Product Angular Quadrature for Neutron Transport in x-y Geometry. *Nuclear Science and Engineering*, 64:299–316, 1977.

[29] I. K Abu-Shumays. Angular Quadratures for Improved Transport Computations. *Transport Theory and Statistical Physics*, 30(2 and 3):169–204, 2001.

[30] Evans, T.M., Stafford, A.S., Slaybaugh, R.N., and Clarno, K.T., “Denovo: A New Three Dimensional Parallel Discrete Ordinates Code in SCALE,” *Nuclear Technology*, 171(2):171-200.

[31] Pandya, T.M., Johnson, S.R., Davidson, G.G., Evans, T.M., and Hamilton, S.P., “Shift: A Massively Parallel Monte Carlo Radiation Transport Package,” *Joint International Conference on Mathematics and Computation (M&C), Supercomputing in Nuclear Applications (SNA) and the Monte Carlo (MC) Method, 19-23 April 2015*, CD-ROM, 2015.

[32] U.S. Nuclear Regulatory Commission, “Production and Testing of the VITAMIN-B7 Fine-Group and BUGLE-B7 Broad-Group Coupled Neutron/Gamma Cross-Section Libraries Derived from ENDF/B-VII.0 Nuclear Data,” NUREG/CR-7045, September 2011, ADAMS Accession No. ML11294A199.

[33] Oak Ridge National Laboratory Report ORNL/TM-2005/39, Version 6.2.3, “SCALE Code System,” March 2018.

[34] Remec, I. and Kam, F.B.K., “Pool Critical Assembly Pressure Vessel Facility Benchmark,” NUREG/CR-6454 (ORNL/TM-13205), Oak Ridge National Laboratory (1997).

[35] Kulesza, Joel A. and Martz, Roger L., “Evaluation of the Pool Critical Assembly Benchmark with Explicitly Modeled Geometry using MCNP6,” *Nuclear Technology*, 197:3, 284-295.

[36] U.S. Nuclear Regulatory Commission, Safety Evaluation Report with Open Items Related to the Subsequent License Renewal of Turkey Point Generating Units 3 and 4, Docket Nos. 50-250 and 50-251, Florida Power & Light Company, May 2019, ADAMS Accession No. ML19078A012.

[37] U.S. Nuclear Regulatory Commission, Safety Evaluation Report Related to the Subsequent License Renewal of Peach Bottom Atomic Power Station, Units 2 and 3, Docket Nos. 50-277 and 50-278, Exelon Generation Company, LLC, Final Report, February 2020, ADAMS Accession No. ML20044D902.

[38] U.S. Nuclear Regulatory Commission, Safety Evaluation Report Related to the Subsequent License Renewal of Surry Power Station, Units 1 and 2, Docket Nos. 50-280 and 50-281, Virginia Electric and Power Company, Final Report, March 2020, ADAMS Accession No. ML20052F523.

[39] *Turkey Point Units 3 and 4 Updated Final Safety Analysis Report - Unit 4 Cycle 29 Update and License Renewal 10 CFR 54.37(b)* 38 *Report,* Docket Nos. 50-250 and 50-251, Florida Power & Light Company, Homestead, FL, 2018. ADAMS Accession Nos. ML18117A091 (Chapter 3), ML18117A092 (Chapter 4), and ML18117A093 (Chapter 5).

[40] Surry, Units 1 & 2, UFSAR, Revision 39, Chapter 3, Reactor, 09/27/2007, ADAMS Accession No. ML072980798.

[41] Donald C. Cook Nuclear Plant. Units 1 & 2, Revision 27 to UFSAR, Chapter 3, Figure 3.2.1-12, 10/24/2016, ADAMS Accession No. ML16336A592.

[42] H. B. Robinson Steam Electric Plant, Unit 2, UFSAR, Revision 27, Chapter 4, Reactor, 09/25/2017, ADAMS Accession No. ML17298A851.

[43] Le Pape, Y., Senior Research and Development Staff, Concrete Specialist, Oak Ridge National Laboratory, personal communication, January 6, 2020):

[44] American Nuclear Society, “Nuclear Analysis and Design of Concrete Radiation Shielding for Nuclear Power Plants,” ANS/ANS-6.4-2006 (R2016), La Grange Park, IL.

[45] AEC Research and Development Report, “A Summary of Shielding Constants for Concrete,” ANL-6443, Reactor Technology (TID-4500, 16th Ed., Amended), November 1961.

[46] Pacific Northwest National Laboratory Report, “Compendium of Material Composition Data for Radiation Transport Modeling,” PIET-43741-TM-963, PNNL-15870 Rev. 1, March 2011. (S. W. Mosher, 2015)

[47] A. H. Fero, “Use of SSTRs and a Multi-Component Shield Assembly to Measure Radiation Penetrating the Reactor Biological Shield in the Presence of Radiation Streaming from Other Sources,” *Reactor Dosimetry: Radiation Metrology and Assessment, STP 1397, The Tenth International Symposium on Reactor Dosimetry, 12-17 September 1999*, American Society for Testing and Materials, 2001.

[48] R. E. Ginna Nuclear Power Plant Revision 28 to UFSAR, Chapter 5, Sections 5.1 thru 5.8, 5/2019, ADAMS Accession No. ML19150A465.

[49] Beaver Valley Power Station, Unit 2, Rev. 24 to UFSAR, Chapter 5, Reactor Coolant System and Connected Systems, ADAMS Accession No. ML19151A195.

[50] Virgil C. Summer Unit 1 Updated Final Safety Analysis Report, Chapter 5, Reactor Coolant System, May 2019, ADAMS Accession No. ML19255F491.

[51] U.S. Nuclear Regulatory Commission, “PWR and BWR Pressure Vessel Fluence Calculation Benchmark Problems and Solutions,” NUREG/CR-6115, September 2001, ADAMS Accession No. ML012900043.

[52] 43CCC-767 ORNL RSICC Computer Code Collection, “ADVANTG 3.2.0, AutomateD VAriaNce reducTion Generator”, August 2019.

[53] CCC-850 ORNL RSICC Computer Code Collection, “MCNP6.2: Monte Carlo N-Particle® Transport Code System Version 6.2”, March 2018.

[54] Bell, George I. and Glasstone, Samuel, *Nuclear Reactor Theory*, Robert E. Krieger, 1982.

[55] Duderstadt, James J., and Martin, William R., *Transport Theory*, John Wiley and Sons, 1979.

[56] Lewis, E.E., and Miller, W.F., *Computational Methods of Neutron Transport*, American Nuclear Society, Inc., 1993.

[57] Jarrell, J.J., Adams, M. L., and Risner, J. M., “Application of Quadruple Range Quadratures to Three-dimensional Model Shielding Problems,” *Nuclear Technology*, 168(2):424–430, 2009.

[58] Mosher, S.W, Johnson, S.R., Bevill, A.M., Ibrahim, A.M, Daily, C.R., Evans, T.M., Wagner, J.C., Johnson, J.O., and Grove, R.E., *ADVANTG – An Automated Variance Reduction Parameter Generator*, ORNL/TM-2013/416 Rev. 1, Oak Ridge National Laboratory (2015).

9 GLOSSARY

bioshield	The concrete biological shield surrounding the reactor vessel of a light water reactor
capture gamma	A gamma photon that is emitted from a compound nucleus following radiative capture of a neutron
dose rate	The rate at which energy from ionizing radiation is deposited in a material on a mass basis. The unit used for dose rate in this report is rad/s, where 1 rad corresponds to the deposition of 100 ergs per gram of the material. The SI unit for dose is the gray (Gy), where 1 Gy is equal to an energy deposition of 1 joule per kilogram. 1 rad = 0.01 Gy.
gamma energy absorption coefficient (μ_{en})	An energy-dependent quantity which, when integrated with the energy-dependent gamma flux, yields the energy that is deposited in that material
gamma self-heating rate	The heating rate (W/cm^3) in the biological shield due to gamma photons produced by neutron interactions (primarily radiative capture and inelastic neutron scattering) within the biological shield
heating rate	The rate at which energy from ionizing radiation is deposited in a material on a volumetric basis. The unit used for heating rate in this report is W/cm^3.
incident gamma heating rate	The heating rate (W/cm^3) in the biological shield that is due to gamma photons produced in the core or due to neutron interactions (primarily inelastic neutron scattering and radiative capture) within the core, core structural components, and RV
ionizing radiation	Subatomic particles and electromagnetic radiation capable of causing ionization in a material
radiative capture	A type of neutron absorption reaction in which a gamma photon is instantaneously emitted from the compound nucleus formed by absorption of the neutron. In most nuclides, radiative capture occurs predominantly with low-energy neutrons.
S8, S16, QR8T, QR12T	Angular quadrature sets used in discrete ordinates calculations. See Appendix B.1.3 for details.

APPENDIX A
GEOMETRY PLOTS OF THE THREE-LOOP MODEL

Plan and elevation views of the three-loop model are provided in this Appendix. Figure A-1 through Figure A-10 are for the “base-case” model, which has Type 04 concrete and #8 rebar with a 3-inch concrete cover. Figure A-11 and Figure A-12 provide plan views of the model with #14 rebar with 3-inch and 10-inch concrete covers, respectively. Each of these plan views is at an elevation that includes vertical and hoop rebar and the embedded support columns for the short-column supports. Figure A-13 illustrates the addition of reflective thermal insulation in the base-case model. Figure A-14 and Figure A-15 show plan views of the models with 13-cm and 120-cm cavity gap widths, respectively. As noted in Section 6.5 these models contain no structural steel in the cavity gap or within the biological shield.

In each of the plan view plots, the dashed rectangle labeled “A” corresponds to the label “A” in the plan view plots of Section 6 This “zoom” region corresponds to the location with the maximum incident neutron and gamma levels at the inner surface of the bioshield and includes representative steel components of each type (rebar, column supports, and cantilever beams) that are included in the bioshield modeling.

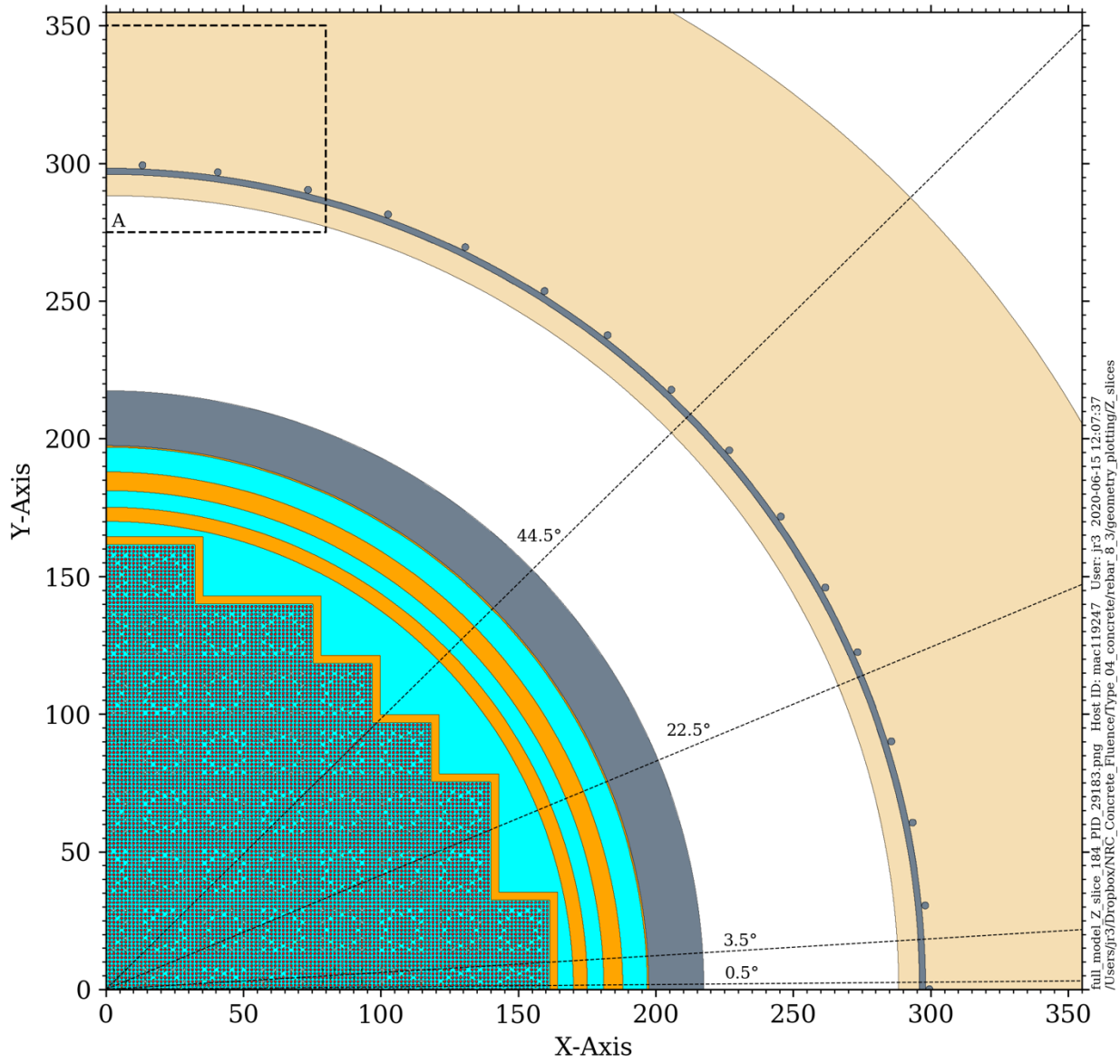

Figure A-1 Plan View of the Three-Loop PWR Model with #8 Rebar and a 3-inch Concrete Cover (Elevation at 184 cm)

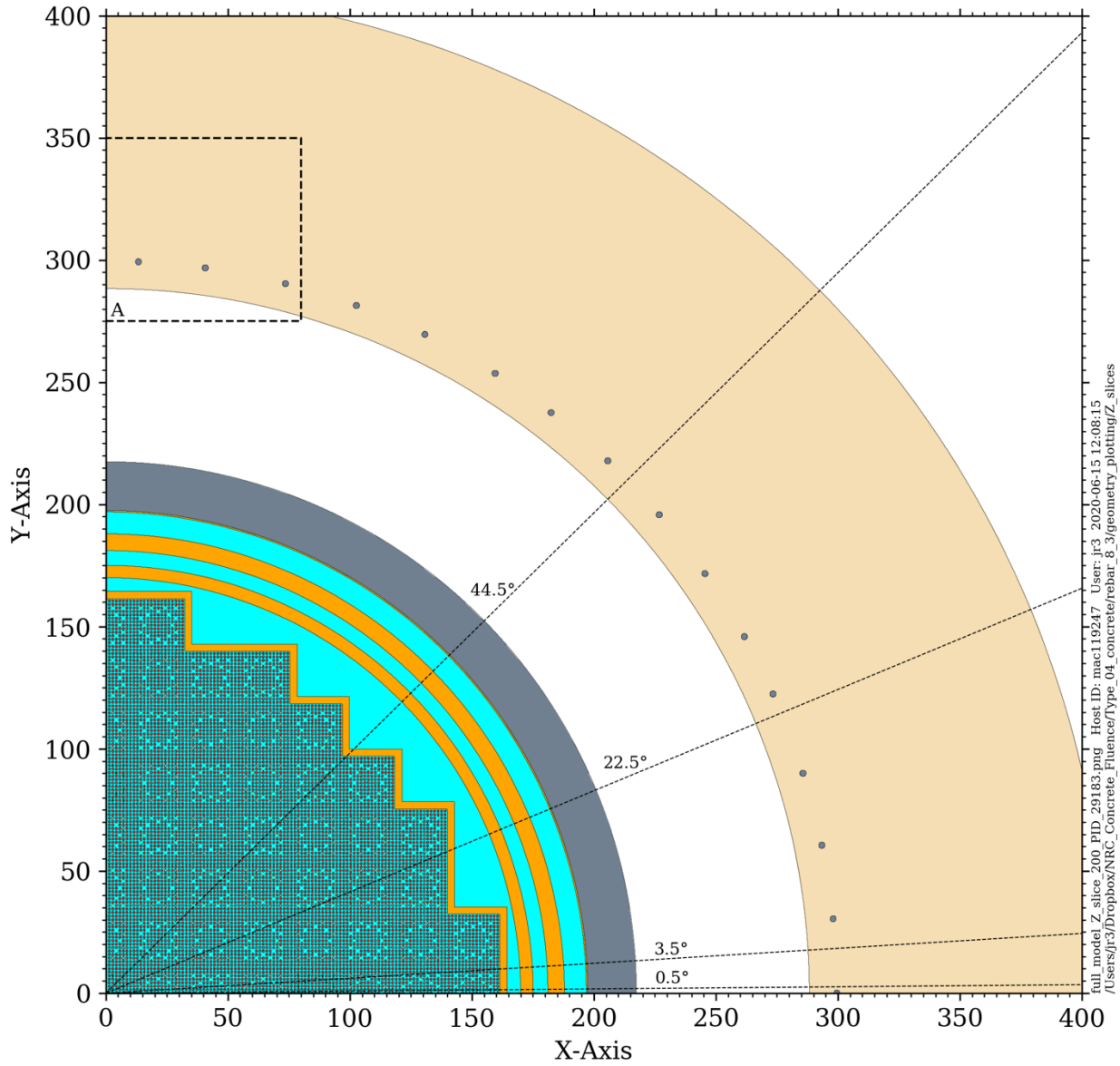

Figure A-2 Plan View of the Three-Loop PWR Model with #8 Rebar and a 3-inch Concrete Cover (Elevation at 200 cm)

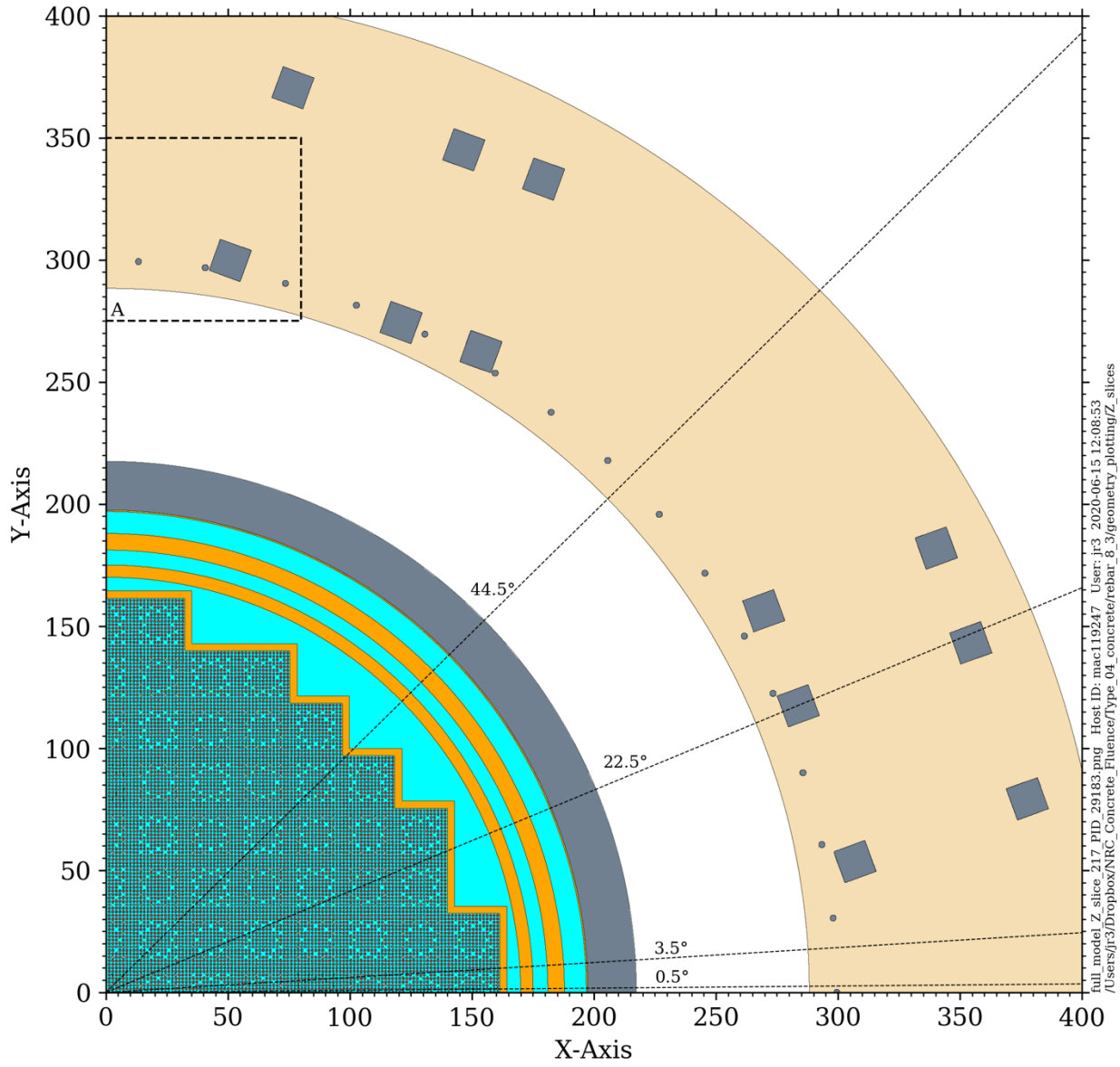

Figure A-3 Plan View of the Three-Loop PWR Model with #8 Rebar and a 3-inch Concrete Cover (Elevation at 217 cm and through the base plates of the support columns)

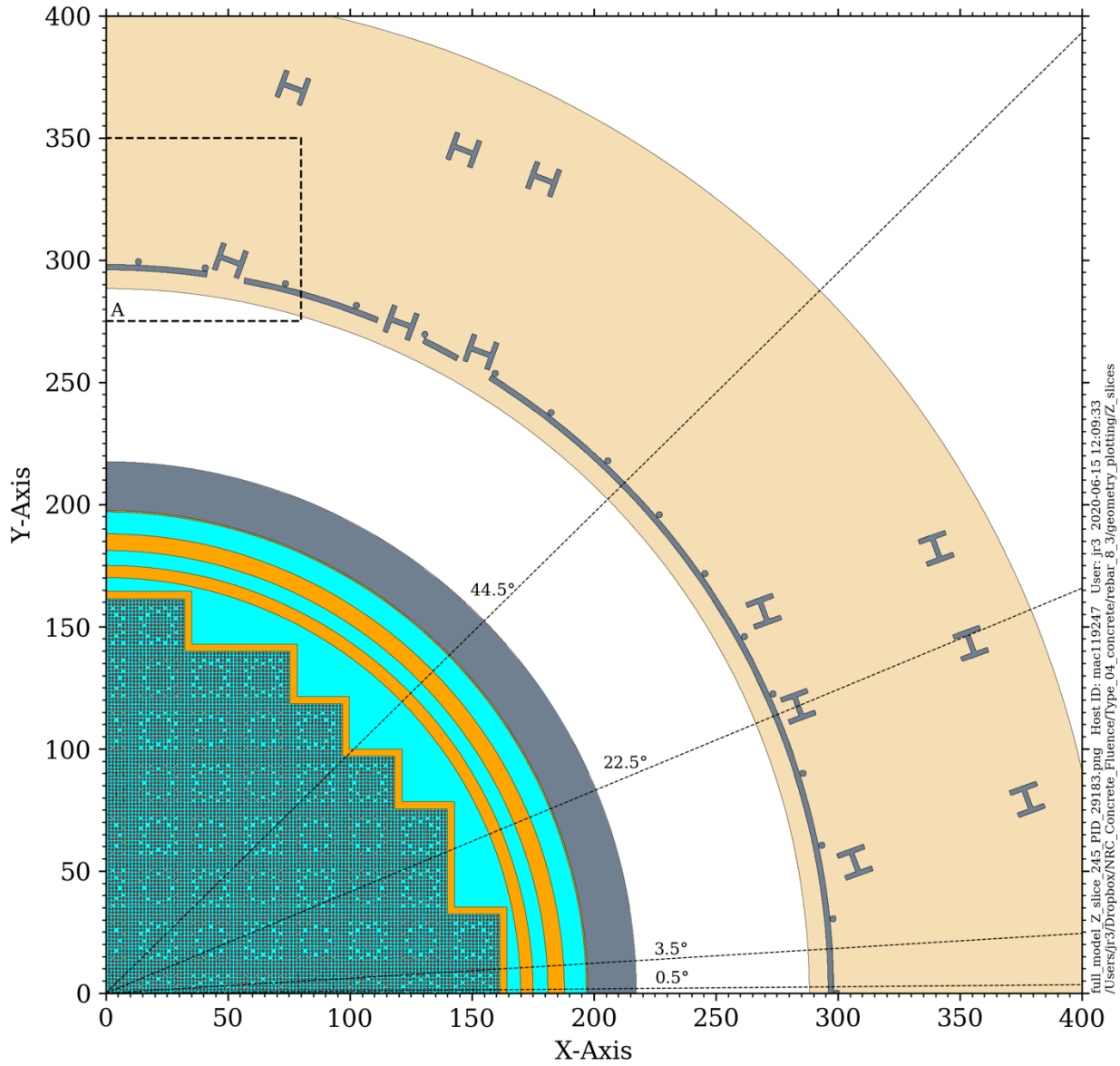

Figure A-4 Plan View of the Three-Loop PWR Model with #8 Rebar and a 3-inch Concrete Cover (Elevation at 245 cm)

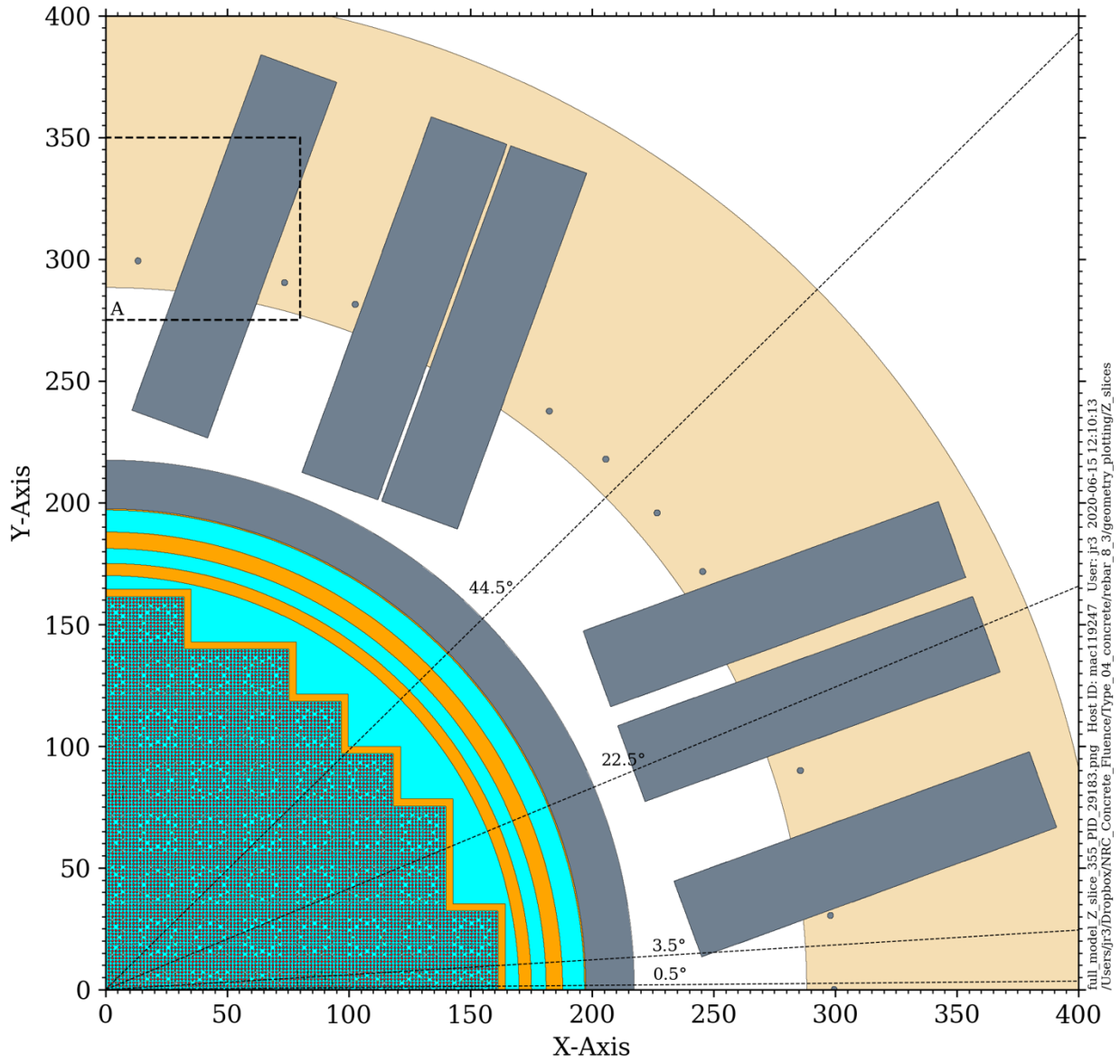

Figure A-5 Plan View of the Three-Loop PWR Model with #8 Rebar and a 3-inch Concrete Cover (Elevation at 355 cm and through the lower flange of the cantilever beams)

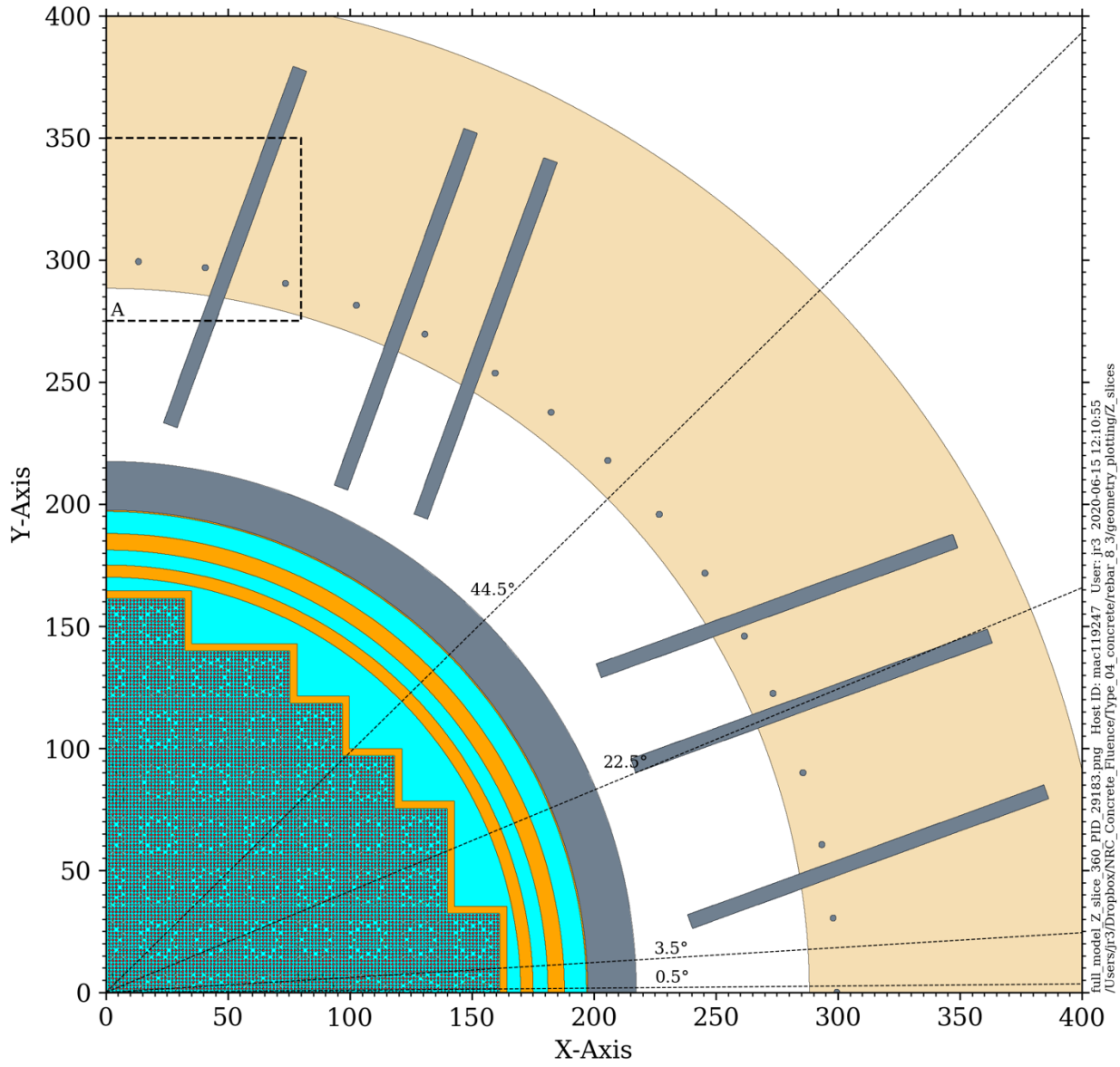

Figure A-6 Plan View of the Three-Loop PWR Model with #8 Rebar and a 3-inch Concrete Cover (Elevation at 360 cm and through the cantilever beam webs)

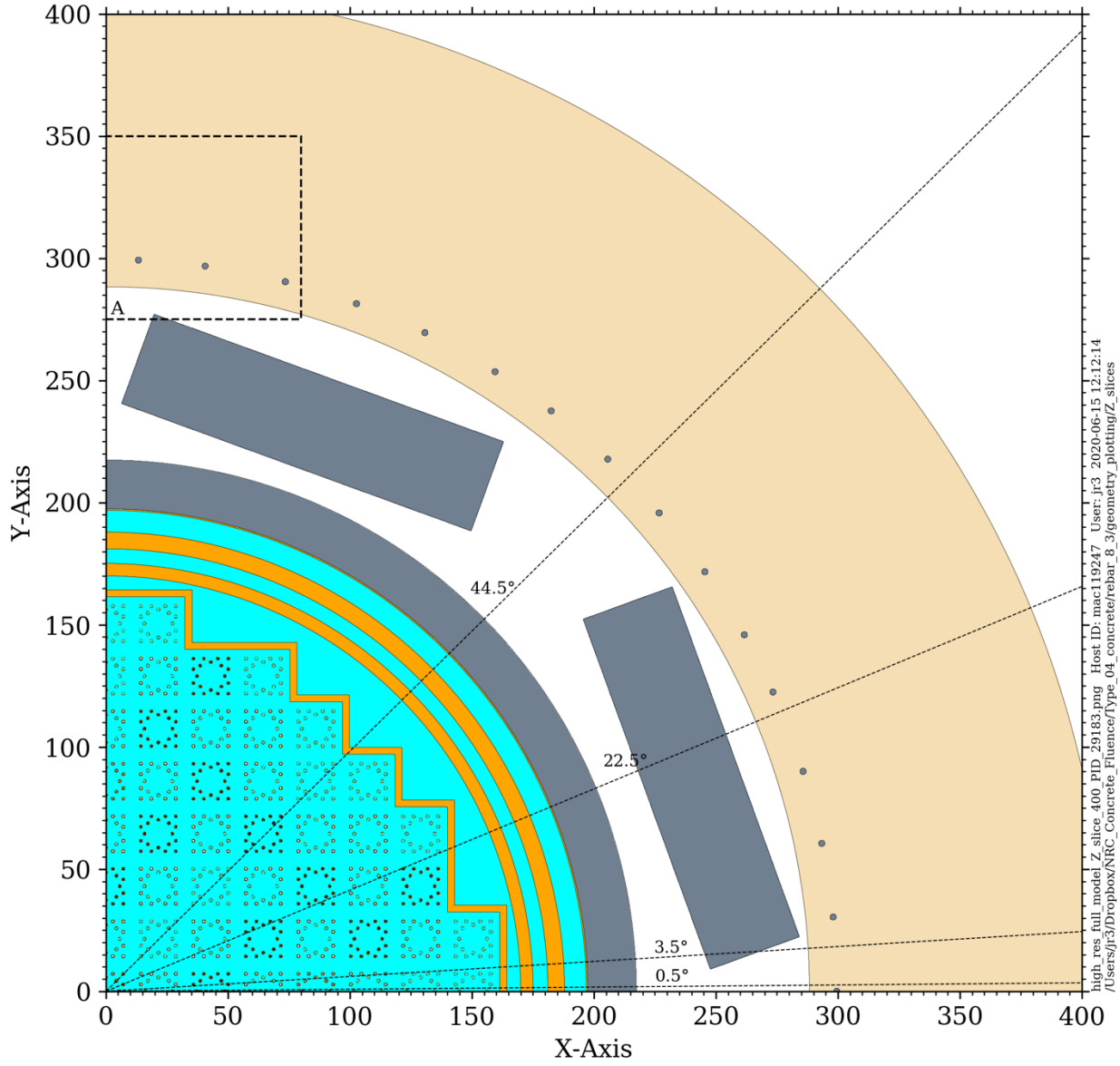

Figure A-7 Plan View of the Three-Loop PWR Model with #8 Rebar and a 3-inch Concrete Cover (Elevation at 400 cm)

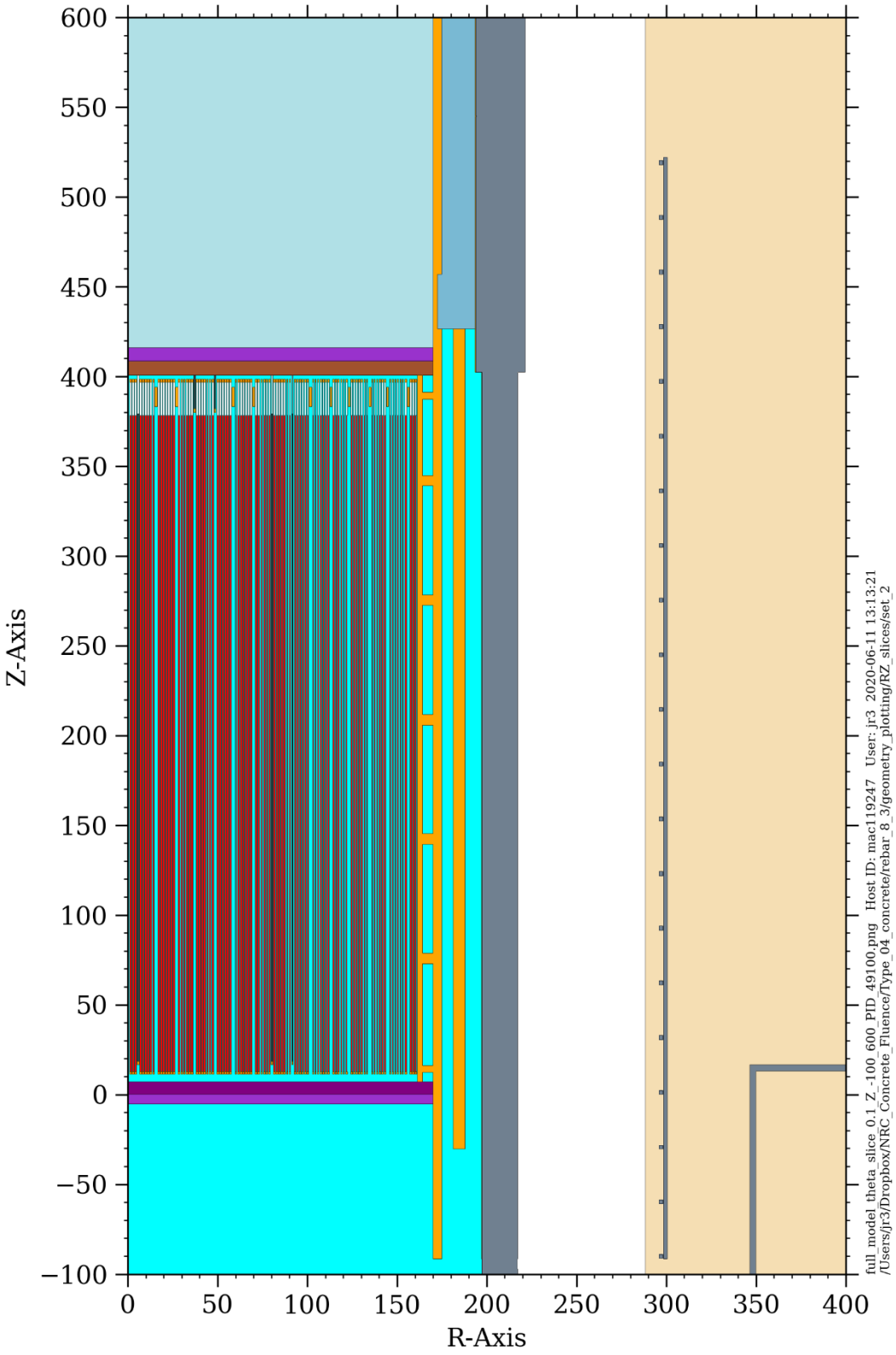

Figure A-8 Elevation View of the Three-Loop Model with #8 Rebar and a 3-inch Concrete Cover (Azimuthal angle of 0.1º)

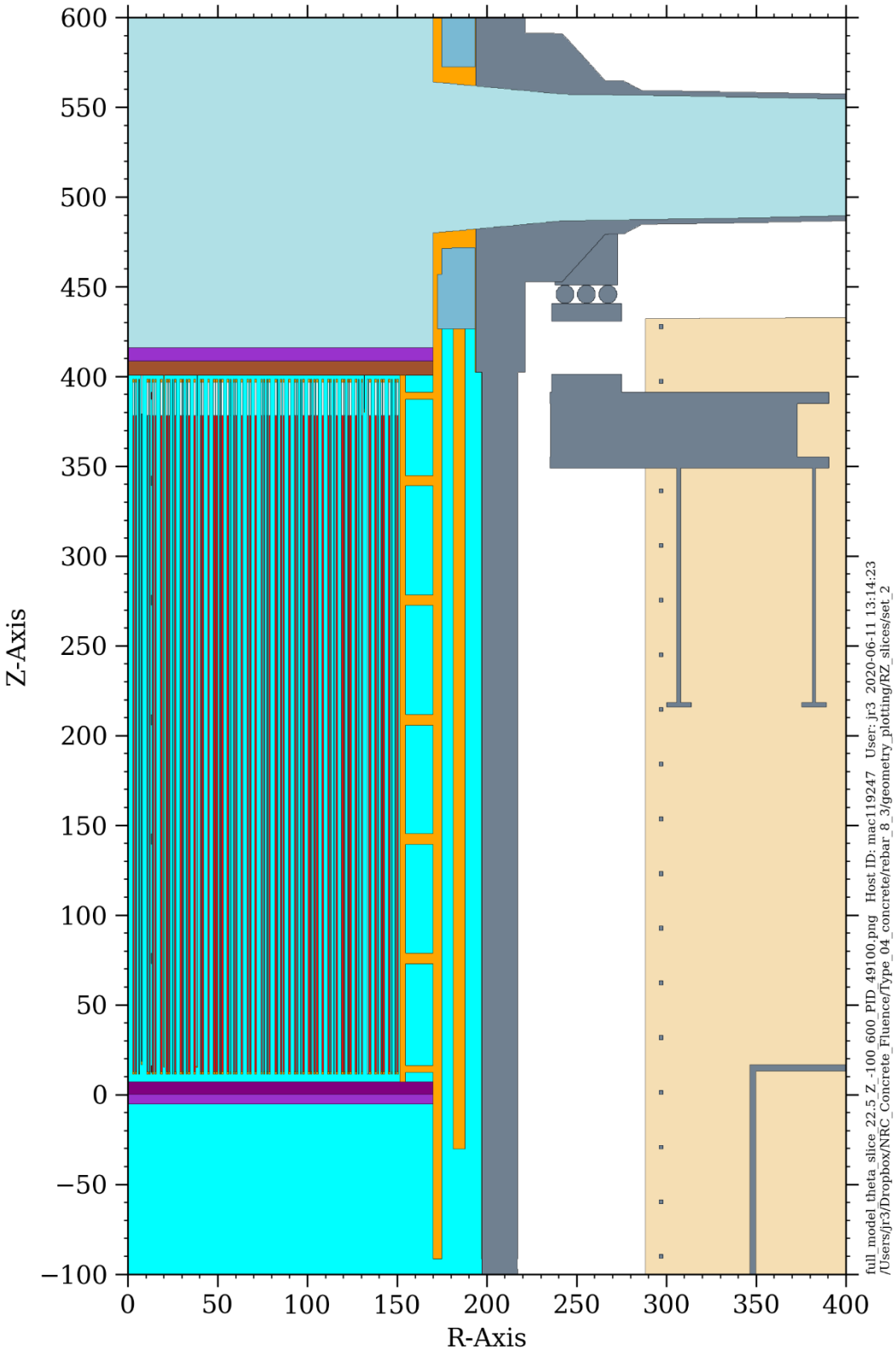

Figure A-9 Elevation View of the Three-Loop PWR Model with #8 Rebar and a 3-inch Concrete Cover (Azimuthal angle of 22.5º)

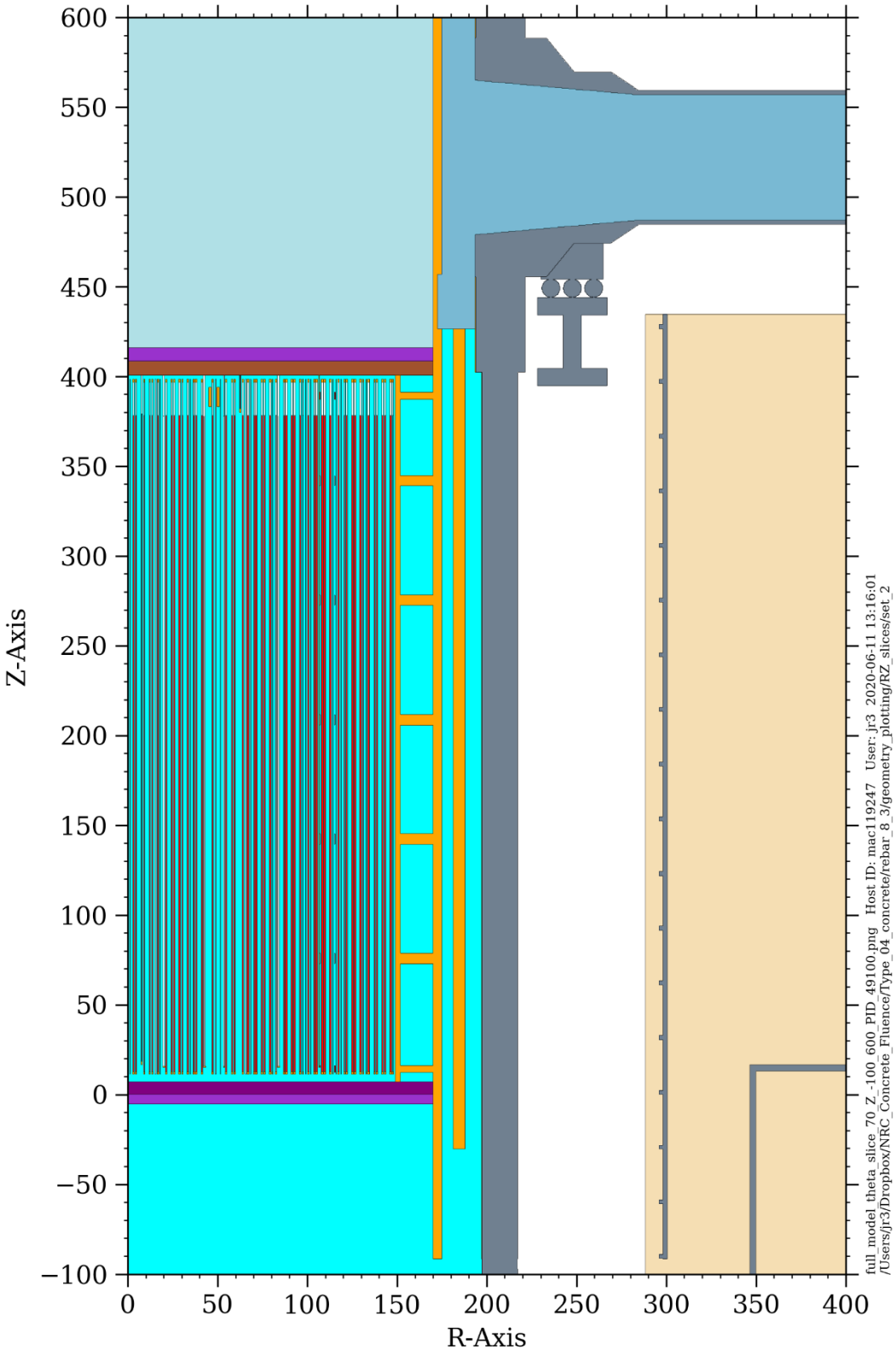

Figure A-10 Elevation View of the Three-Loop PWR Model with #8 Rebar and a 3-inch Concrete Cover (Azimuthal angle of 70º)

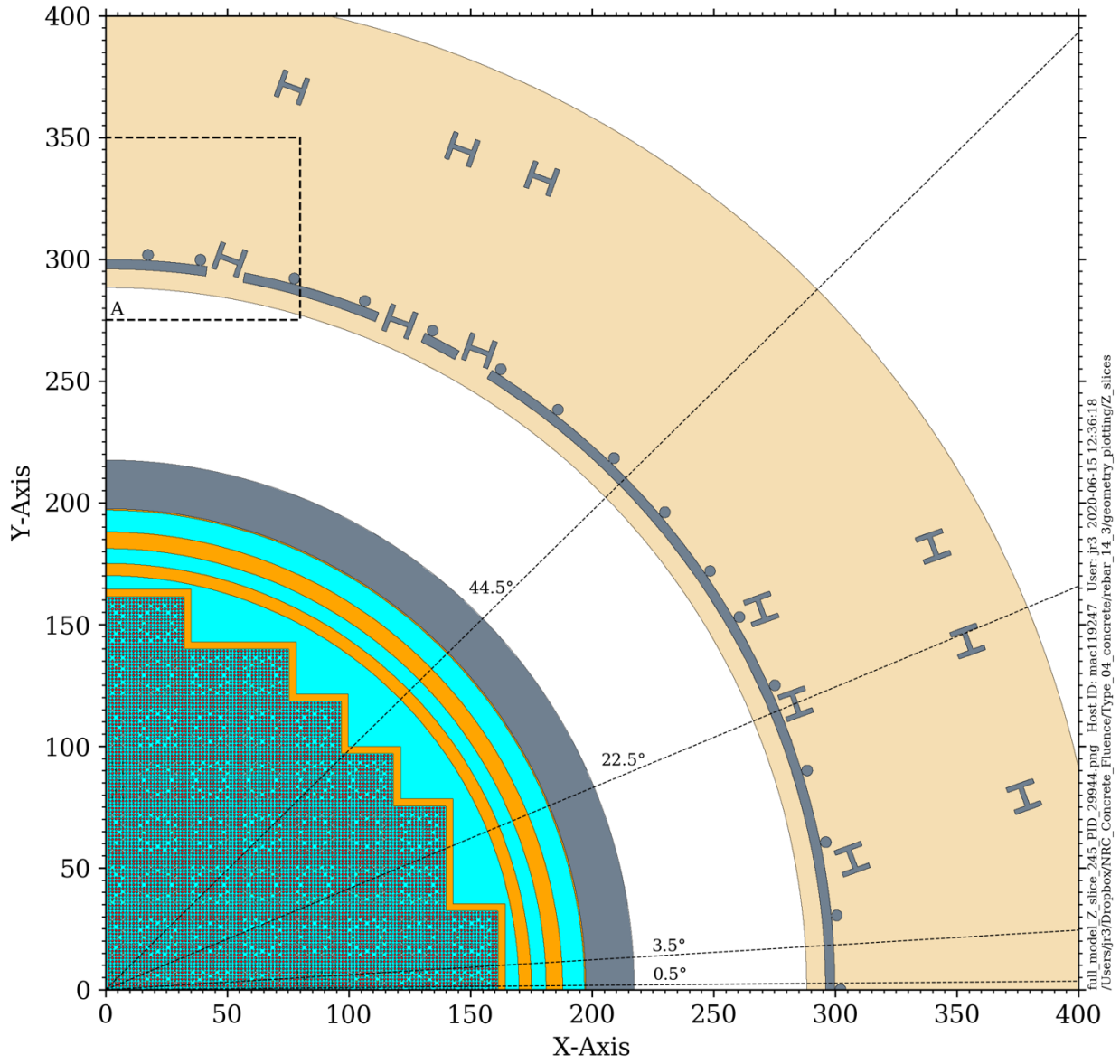

Figure A-11 Plan View of the Three-Loop PWR Model with #14 Rebar and a 3-inch Concrete Cover (Elevation at 245 cm)

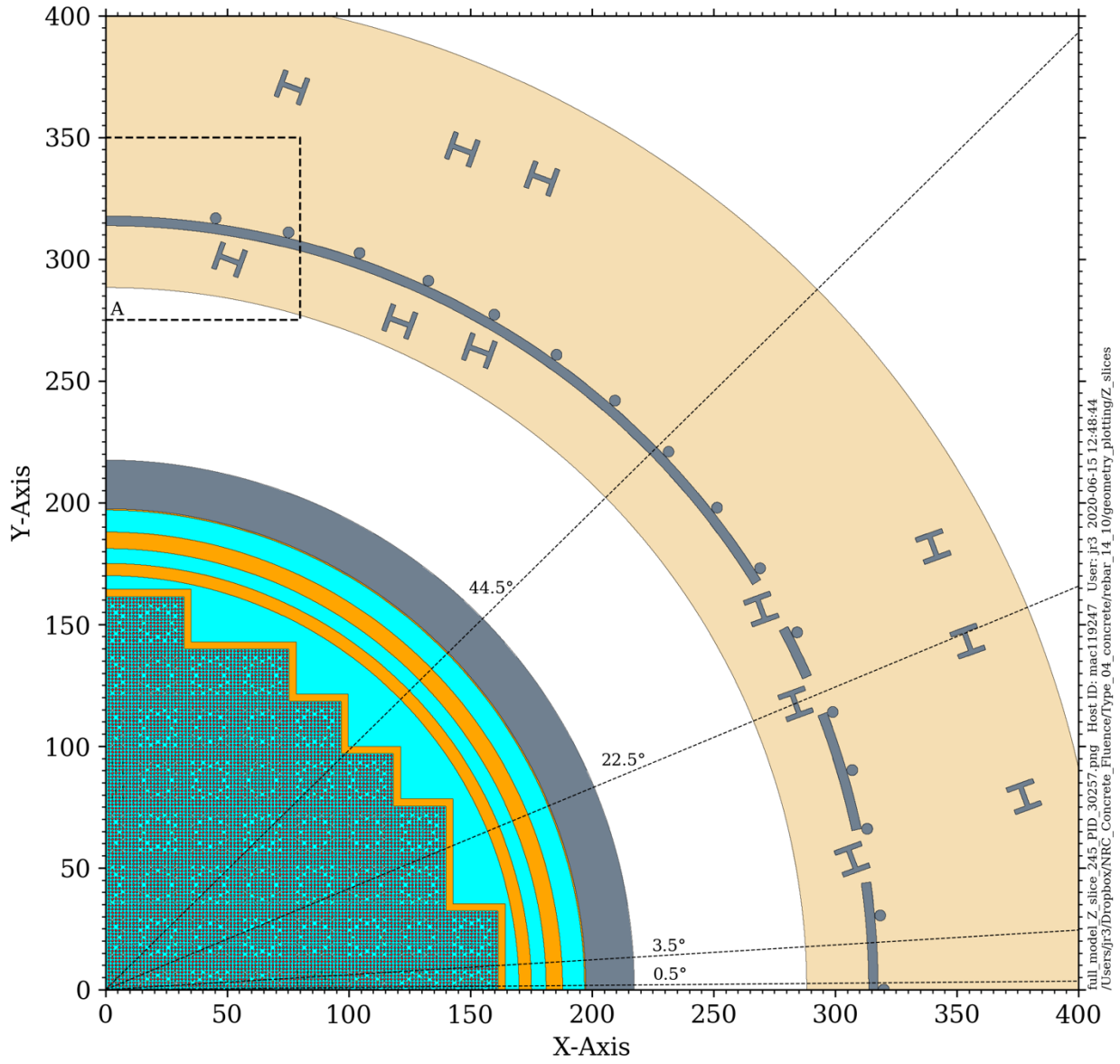

Figure A-12 Plan View of the Three-Loop PWR Model with #14 Rebar and a 10-inch Concrete Cover (Elevation at 245 cm)

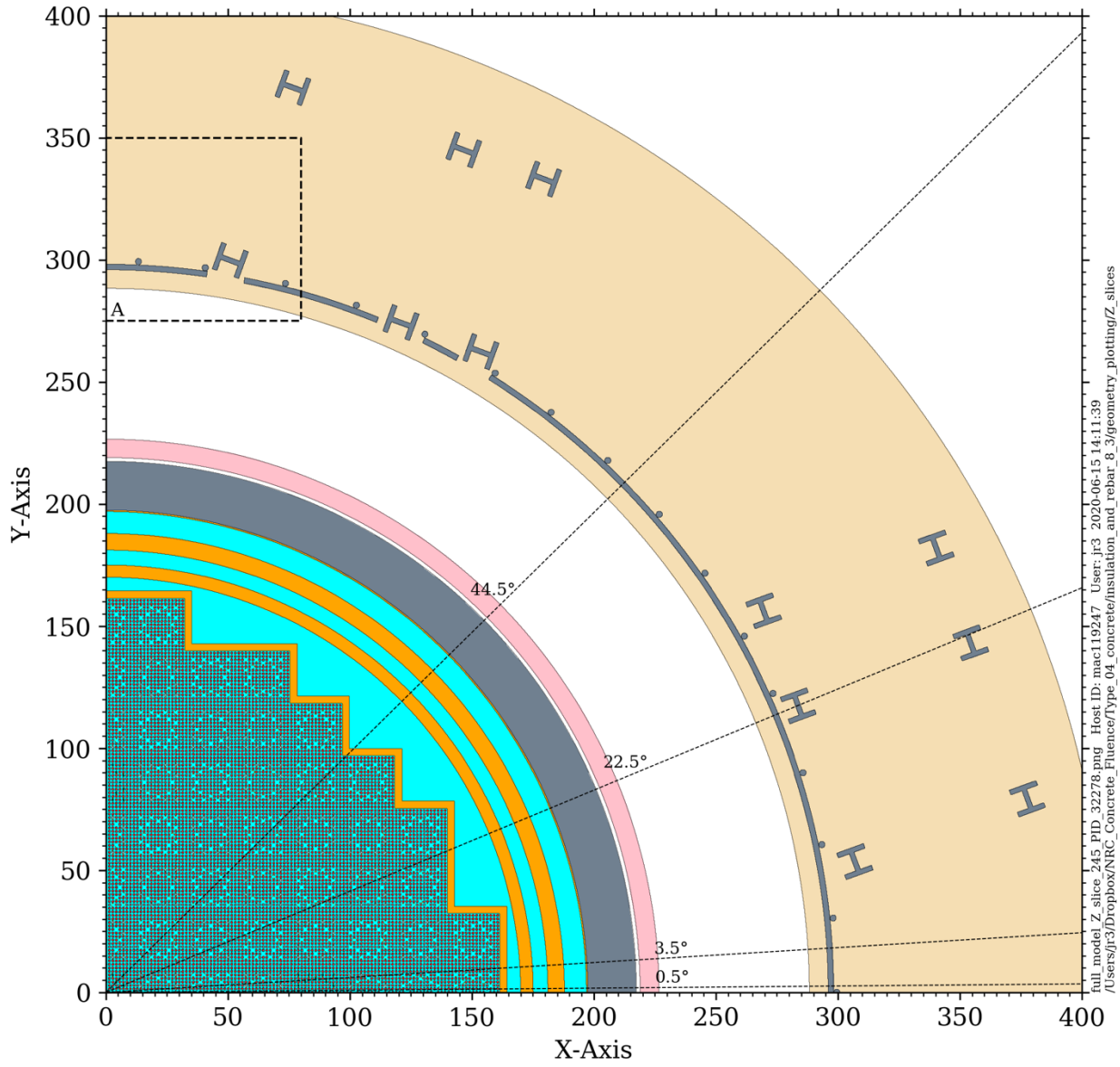

Figure A-13 Plan View of the Three-Loop PWR Model with Reflective Thermal Insulation and #8 Rebar with a 3-inch Concrete Cover (Elevation at 245 cm)

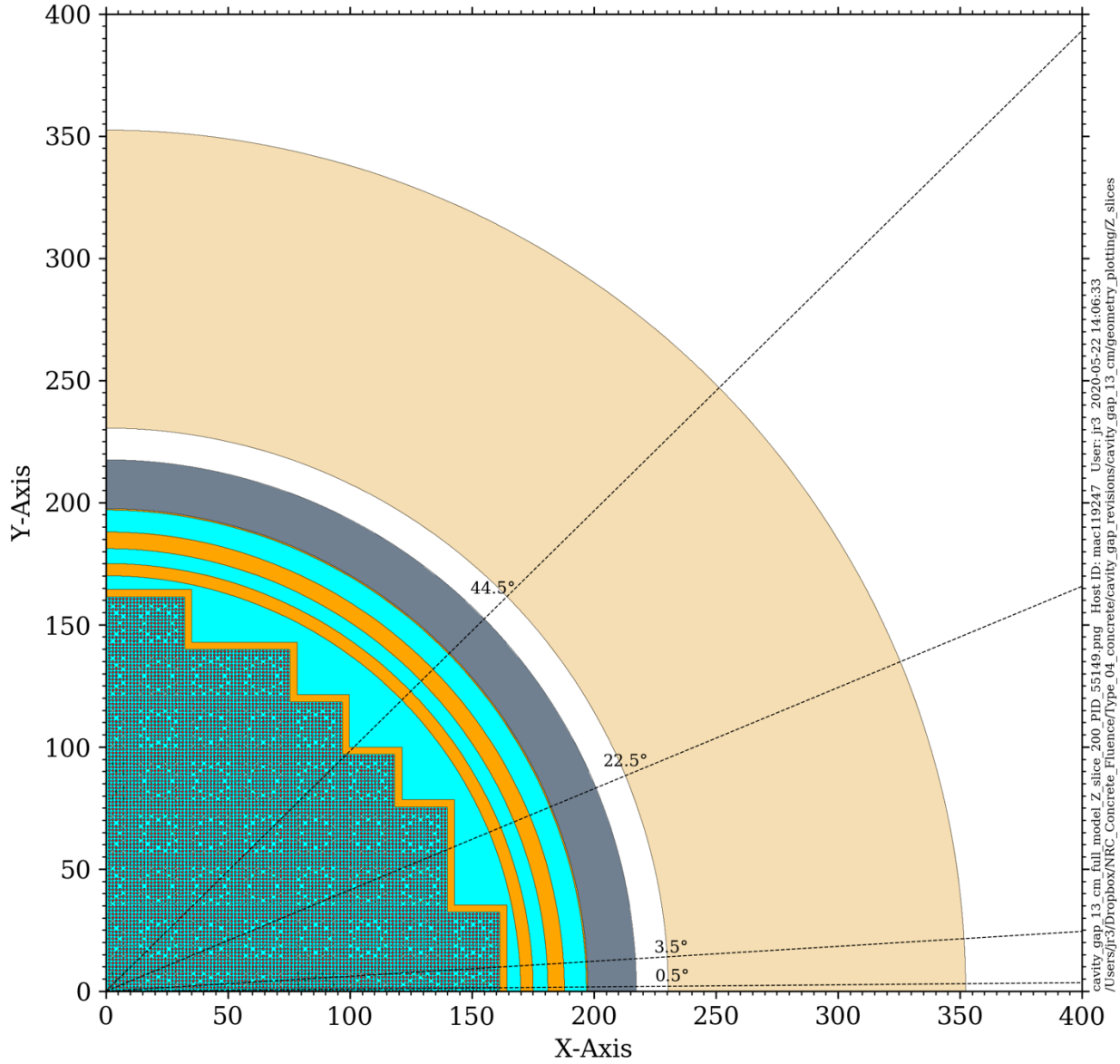

Figure A-14 Plan View of the Three-Loop PWR Model with a 13-inch Cavity Gap (Elevation at 200 cm)

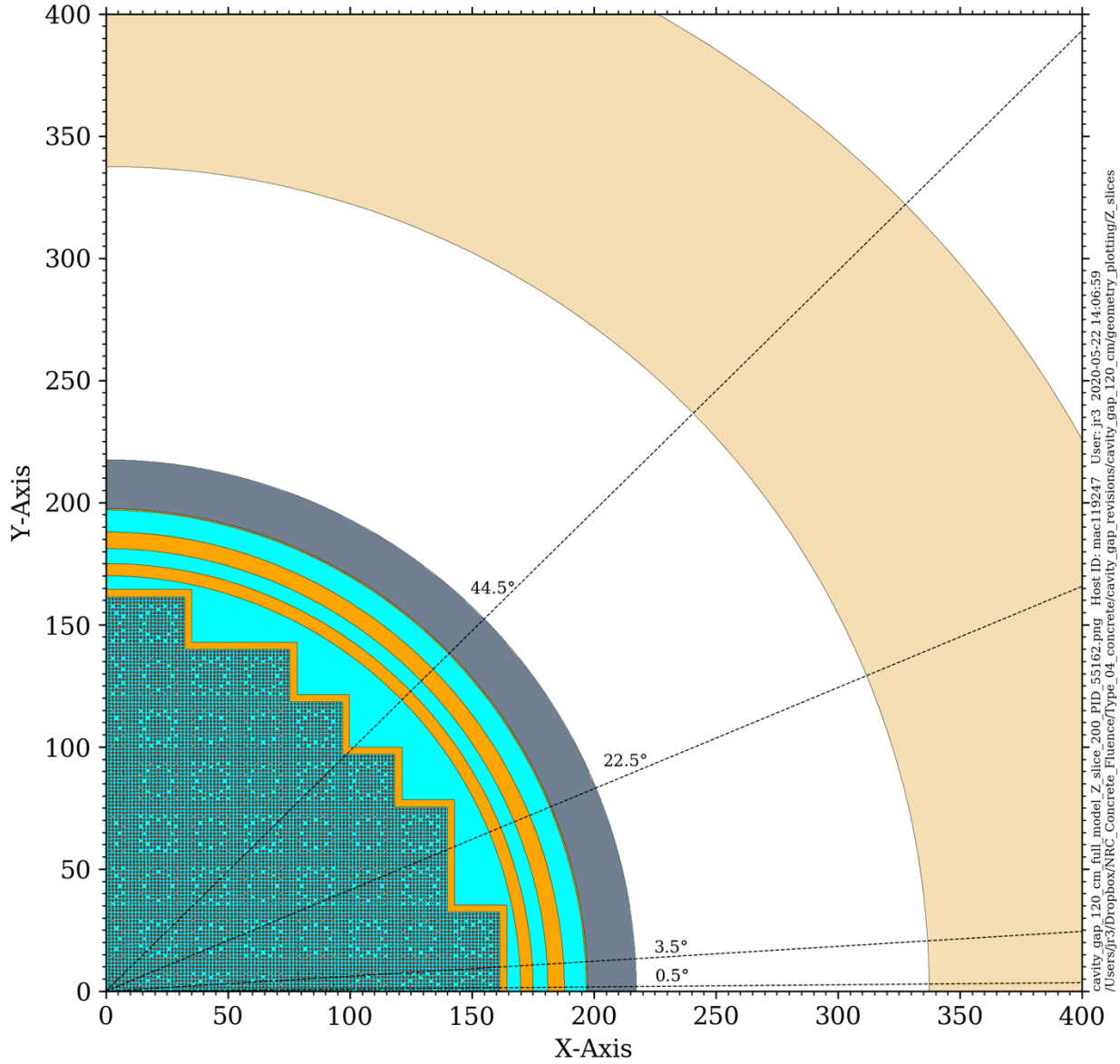

Figure A-15 Plan View of the Three-Loop PWR Model with a 120-inch Cavity Gap (Elevation at 200 cm)

APPENDIX B

DETERMINISTIC, STOCHASTIC, AND HYBRID SOLUTIONS OF THE RADIATION TRANSPORT EQUATION

Radiation shielding calculations are typically performed using one of two methodologies: *deterministic* or *stochastic*. In either case, the method is applied to obtain solutions to the steady-state Boltzmann transport equation. Detailed discussions of this equation and solution methods can be found in many references, including [54]–[56].

This appendix provides a brief overview of key aspects of these two methods. The intent of this overview is to provide a basic understanding of topics that are discussed are discussed in Sections 3 and 6

B.1 Deterministic Calculations

Modern computer codes based on deterministic methods are generally referred to as *discrete ordinates* or S_N codes. These codes are based on discretizing the spatial, energy, and angular variables in the Boltzmann equation and solving the resulting set of equations using numerical methods to obtain the particle flux as a function of position, direction, and energy.

B.1.1 Spatial Discretization

In discrete ordinates calculations the problem geometry is divided into *mesh cells*. For reactor shielding applications, the number of spatial mesh cells can range from thousands to millions. For the majority of discrete ordinates codes, a regular structured mesh is employed. Typical mesh geometries for these codes are 2D and 3D Cartesian geometry and 1D, 2D, or 3D cylindrical geometry.

Many shielding analyses are based on models with a variety of components, not all of which are best represented by a single coordinate system. For example, cylindrical geometry is well suited to modeling the cylindrical portions of an RPV or biological shield, but not the fuel assemblies, core internals, or, in the case of the model used in this study, the steel support columns that are embedded in the bioshield concrete.

B.1.2 Energy Discretization

Energy discretization in discrete ordinates calculations is based on the use of *multigroup* cross-section data. In this method, the variation of neutron and gamma cross sections is approximated by averaging the true (continuous energy) data over energy groups. The accuracy that can be obtained with a multigroup library is dependent on the energy variation in the CE data (which can be extremely complex) and on the 'weighting function' that is used to average the multigroup data. Figure B-1 shows the CE data for the total cross section for ^{56}Fe (the predominant isotope in elemental iron) as a function of neutron energy, as well as multigroup data from the VITAMIN-B7 and BUGLE-B7 libraries [32].

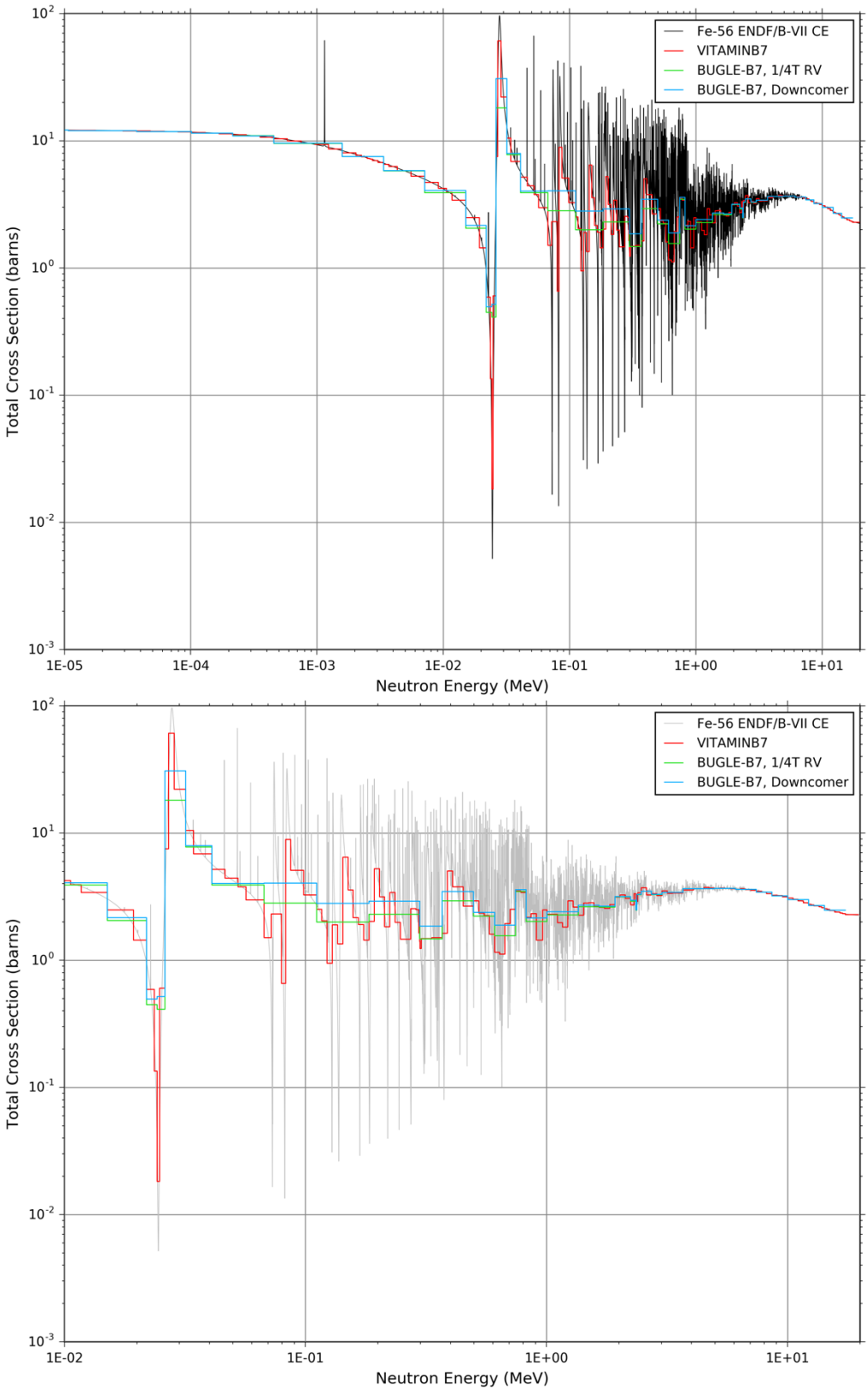

Figure B-1 Total Cross Section for ^{56}Fe from a CE Cross-Section Library and from Three MG Libraries

B.1.3 Angular discretization

In discrete ordinates radiation transport calculations, the directional variation of the neutron or gamma flux is represented using a set of discrete directions (or *ordinates*) to represent the continuous angular variable. The angular flux is calculated along each of these ordinates. The scalar flux, which is the typical quantity of interest in radiation shielding calculations, is obtained by integrating the discrete angular flux values using numerical quadrature, with each angular ordinate having a specified quadrature weight.

The selection of an appropriate quadrature set is dependent upon the characteristics of the problem being analyzed. *Level-symmetric* (S_N) quadrature sets have been widely used for many years for discrete ordinates calculations. While S_N sets are widely used for shielding calculations, they are not optimal for geometries where particle transport along directions near a coordinate axis, such as streaming of neutrons in the cavity gap between the RPV and the bioshield, is important. Abu-Shumays *quadruple range* (QR) quadratures [28], [29], [57] to provide superior accuracy for problems in which there are material discontinuities across octants of the unit sphere, such as the edges of fuel assemblies and gaps near any of the coordinate axes.

Figure B-2 and Figure B-3 illustrate S8 and S16 level symmetric quadratures, and QR8T and QR12T quadruple range quadratures. Level symmetric SN sets all include (N/2) levels in each octant of the unit sphere. Thus, an S8 quadrature has four levels and an S16 quadrature has eight. These quadratures are rotationally invariant (i.e., they are invariant under arbitrary 90º rotations about the coordinate axes).

The notation QRNT refers to a QR set with N polar angles (i.e., angles with respect to the Z axis) and a triangular arrangement of azimuthal angles on each polar level. Thus, a QR8T quadrature has the same number of polar levels and total angles as an S16 set. The QR sets are not rotationally invariant but instead have more angular ordinates near the coordinate axes.

The QR12T quadrature shown in Figure B-3 serves as the reference quadrature for comparisons of Denovo solutions with different quadratures in Section 3.1

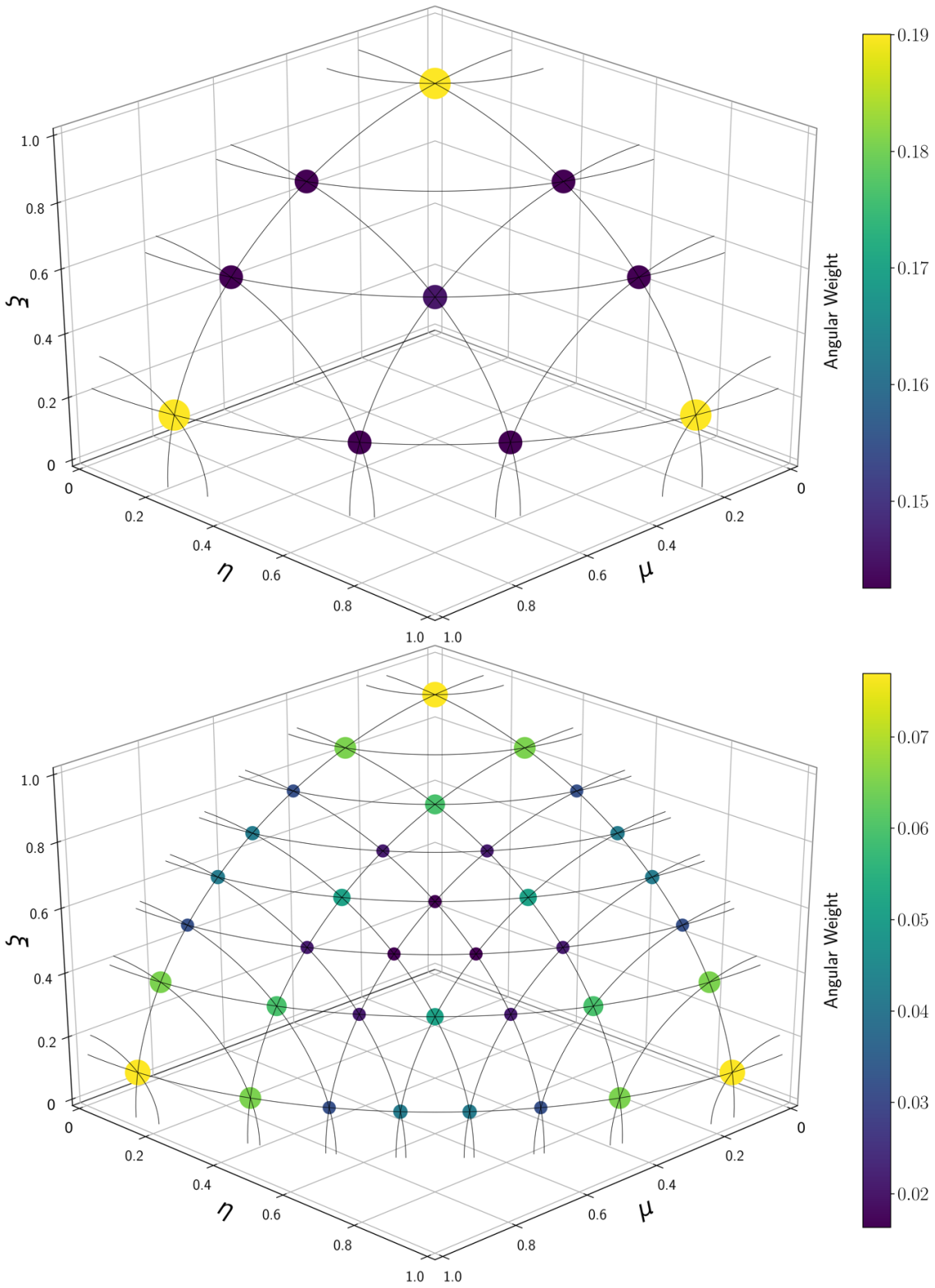

Figure B-2 Level Symmetric S8 and S16 Quadrature Ordinates (Directions) and Weights (The circles represent the direction vector cosines in x, y, and z on one octant of a unit sphere. The quadrature weights are indicated by the size and color of the spheres.)

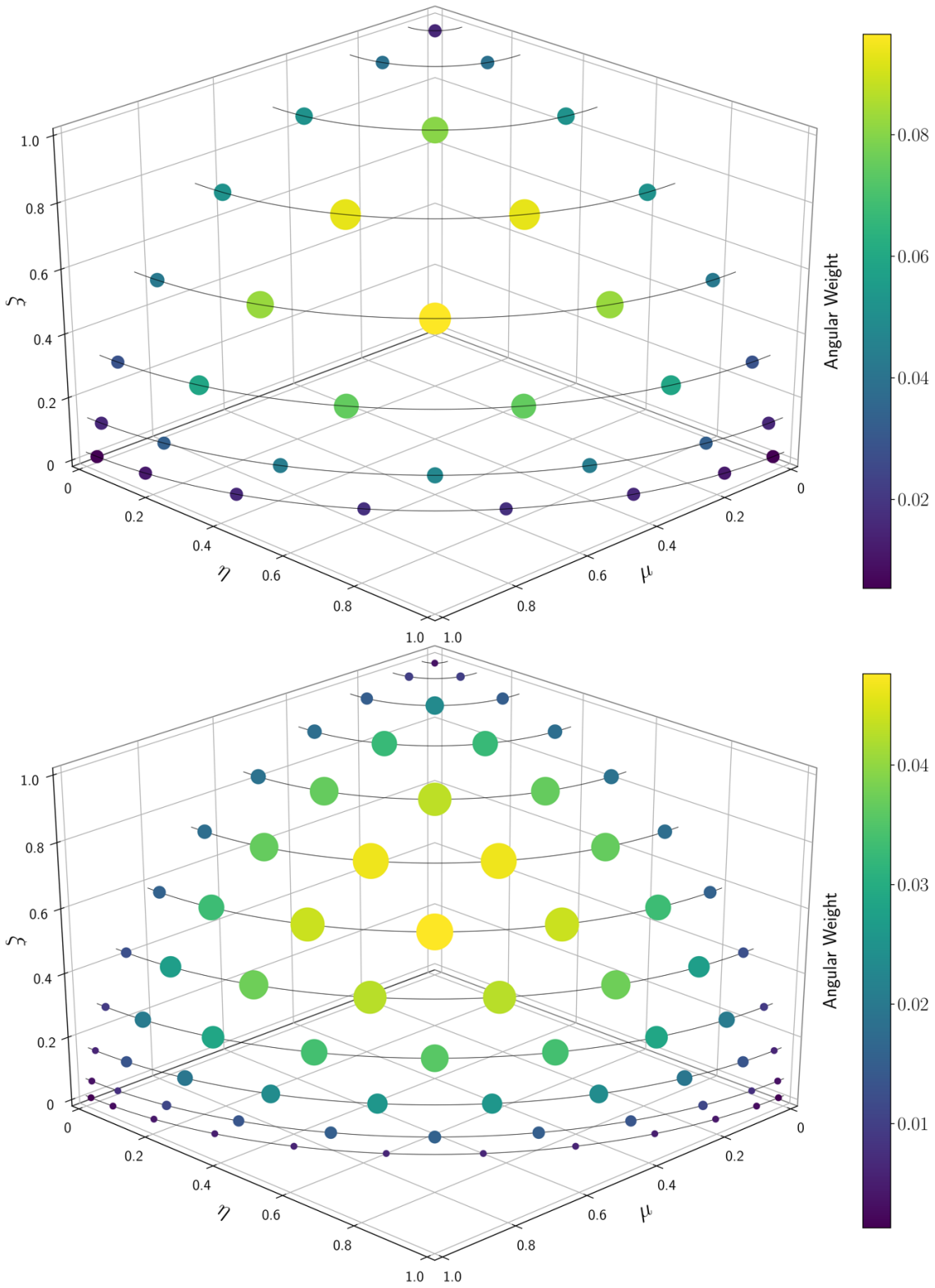

Figure B-3 Quadruple Range QR8T and QR12T Quadrature Ordinates (Directions) and Weights (The circles represent the direction vector cosines in x, y, and z on one octant of a unit sphere. The quadrature weights are indicated by the size and color of the spheres.)

B.2 Stochastic (Monte Carlo) Calculations

Radiation transport computer codes based on stochastic methods, including MCNP® and Shift, are generally referred to as Monte Carlo codes. Unlike discrete ordinates calculations, which solve a system of equations to obtain the flux distribution in space, energy, and angle, Monte Carlo calculations are based on the simulation of individual particle *histories*. Each history is based on sampling probability distribution functions (PDFs) that govern each event as a particle is born (e.g., a neutron is created by fission), undergoes various interactions (e.g., scattering) as it is transported through the model phase space, and is finally absorbed or escapes the boundary of the model.

As particle histories are accumulated, the model phase space is populated with a distribution of particle positions, energies, and directions. The population in one or more regions of interest can be obtained through the use of particle *tallies*. These tallies, which are discussed below, can be very localized or can encompass large portions of the model.

Monte Carlo calculations inherently provide higher-fidelity solutions than discrete ordinates calculations, as they do not require the discretizations in energy, space, and angle that are imposed by all discrete ordinates codes. Because of this, Monte Carlo simulations are generally considered to be the most accurate method for high-fidelity radiation transport calculations.

Monte Carlo calculations can use either CE or MG cross section data. Continuous energy cross-section libraries are generally used, as they eliminate the approximations encountered with MG libraries and hence provide more accurate solutions.

Unlike discrete ordinates calculations, in which the problem geometry is defined based on a mesh grid, Monte Carlo calculations provide the ability to exactly model the majority of the geometric features in most radiation transport problems. Both MCNP® and Shift allow modeling of linear and quadratic surfaces (planes, spheres, cylinders, cones, ellipsoids, hyperboloids, paraboloids) as well as elliptical or circular torii with axes parallel to the X-, Y-, or Z-axis.

This aspect of Monte Carlo modeling is particularly beneficial in fluence, heating rate, and dose rate analyses in the bioshield for the model used in the current study, as the concrete, liner (if present), rebar, embedded support columns, and cantilever beams can all be represented with none of the meshing artifacts that occur with discrete ordinates codes. For example, the embedded support columns could not be properly represented using either a cartesian or cylindrical mesh in a discrete ordinates code.

B.2.1 Monte Carlo tallies

The population in one or more regions of interest can be obtained through the use of particle *tallies*. Typical tally types in Monte Carlo codes include *cell tallies*, *surface tallies*, and *mesh tallies*.

Cell tallies are used to obtain the particle flux or response in one or more cells that are part of the model geometry definition. For example, if a segment of rebar in the biological shield is modeled as a single cell, a cell tally for that rebar will provide the average flux (or heating rate or dose rate) for the entire rebar segment.

Surface tallies are used to obtain the particle flux or response crossing a given surface that is a boundary between two adjacent cells.

Mesh tallies provide estimates of the flux in every voxel of a cartesian or cylindrical mesh that is superimposed over the problem geometry. MCNP® allows mesh tallies to be translated and rotated relative to the origin of the coordinate system. This allows cartesian mesh tallies to be used for the embedded steel columns and cantilevers, which are not orthogonal to the coordinate axes, in the current analysis.

In the limiting case, a mesh tally can provide a global solution with spatial resolution that can be comparable to, or even finer than, the spatial mesh of a discrete ordinates calculation of the same model. Until fairly recently, the use of mesh tallies in many Monte Carlo simulations was impractical because the problem run times that would be necessary to achieve acceptable convergence were unacceptably long. With the advent of hybrid radiation transport methods (see B.3), highly detailed mesh tallies are now feasible for many shielding analyses.

Monte Carlo tallies provide estimates of the mean (μ) and variance (σ^2) for the tally quantities of interest. The standard approach for reporting tally results is to provide the mean and the relative error. The tally relative error *RE* is defined as

$$RE = \frac{\sigma}{\mu},$$

where σ, the standard deviation, is the square root of the variance. It is also common to report confidence intervals based on the estimated mean and standard deviation. A typically reported quantity is the 95% confidence interval CI_{95}, where

$$CI_{95} = [\mu - 1.96\sigma, \mu + 1.96\sigma].$$

Monte Carlo cell, surface, and mesh tallies are generally considered to be reliable provided the relative error for each tally value is less than 10%. In the present analysis, relative errors of less than 2% were typically obtained, and relative errors of less than 1% were common in the locations where the peak flux, heating rate, and dose rate values occur. An example of a dose rate tally at an elevation that includes vertical and hoop rebar as well as embedded support columns is discussed in Section B.4

B.3 Hybrid Radiation Transport

The primary limitation in the use of Monte Carlo radiation transport analyses has historically been the amount of computer time required to obtain a well-converged solution (i.e., a solution with acceptable relative errors), particularly for deep penetration shielding calculations that use mesh tallies to obtain the solution over a large portion of the calculational model. A variety of *variance reduction* (VR) methods have been developed over the years in an attempt to reduce the computational time required to obtain satisfactory relative errors.

Hybrid radiation transport methods refer to a class of techniques that are used to obtain a solution to the Boltzmann transport equation using a combination of deterministic and stochastic calculations. The deterministic calculations in a hybrid calculation sequences are used to generate VR parameters that are then used in a Monte Carlo transport calculation to obtain the

desired quantities of interest. Details of the hybrid radiation transport method can be found in [58]. The hybrid calculations in the current analysis were performed using the ADVANTG and MCNP® codes.

B.4 Example Mesh Tally Results

A combination of cylindrical and cartesian mesh tallies was used for the neutron flux, total heating rate, and gamma dose rate calculations. Values in the bioshield concrete were obtained using a cylindrical mesh tally with radial intervals of 1 cm from the inner surface of the concrete to a depth of 60 cm, axial intervals of approximately 2.5 cm, and azimuthal intervals of 1º. The cylindrical mesh tallies for the rebar hoops have a single radial interval, axial intervals of approximately 2.5 cm, and azimuthal intervals of 1º. The cylindrical mesh tallies for the vertical rebar have a single radial and azimuthal interval, and axial intervals of approximately 2.5 cm. The cartesian mesh tallies for the embedded support columns and cantilever beams have intervals that are typically in the range of 2–2.5 cm.

Figure B-4 shows the gamma dose rate at an elevation of 245 cm for a case with Type 04 concrete and #8 rebar with a 3-inch concrete cover. This view includes vertical and hoop rebar segments and an embedded support column. The radial and azimuthal mesh lines are shown in light gray. The data are presented using a flooded contour plot, in which the color in each mesh tally cell indicates the magnitude based on the colorbar at the top of the plot. Contour lines are also shown, with the number of each contour line corresponding to the parenthetical values on the colorbar scale.

The relative errors in the gamma dose rate for this location are shown in Figure B-5. As noted in Section B.2.1 the relative errors for this tally data are less than 2%, and typically less than 1%.

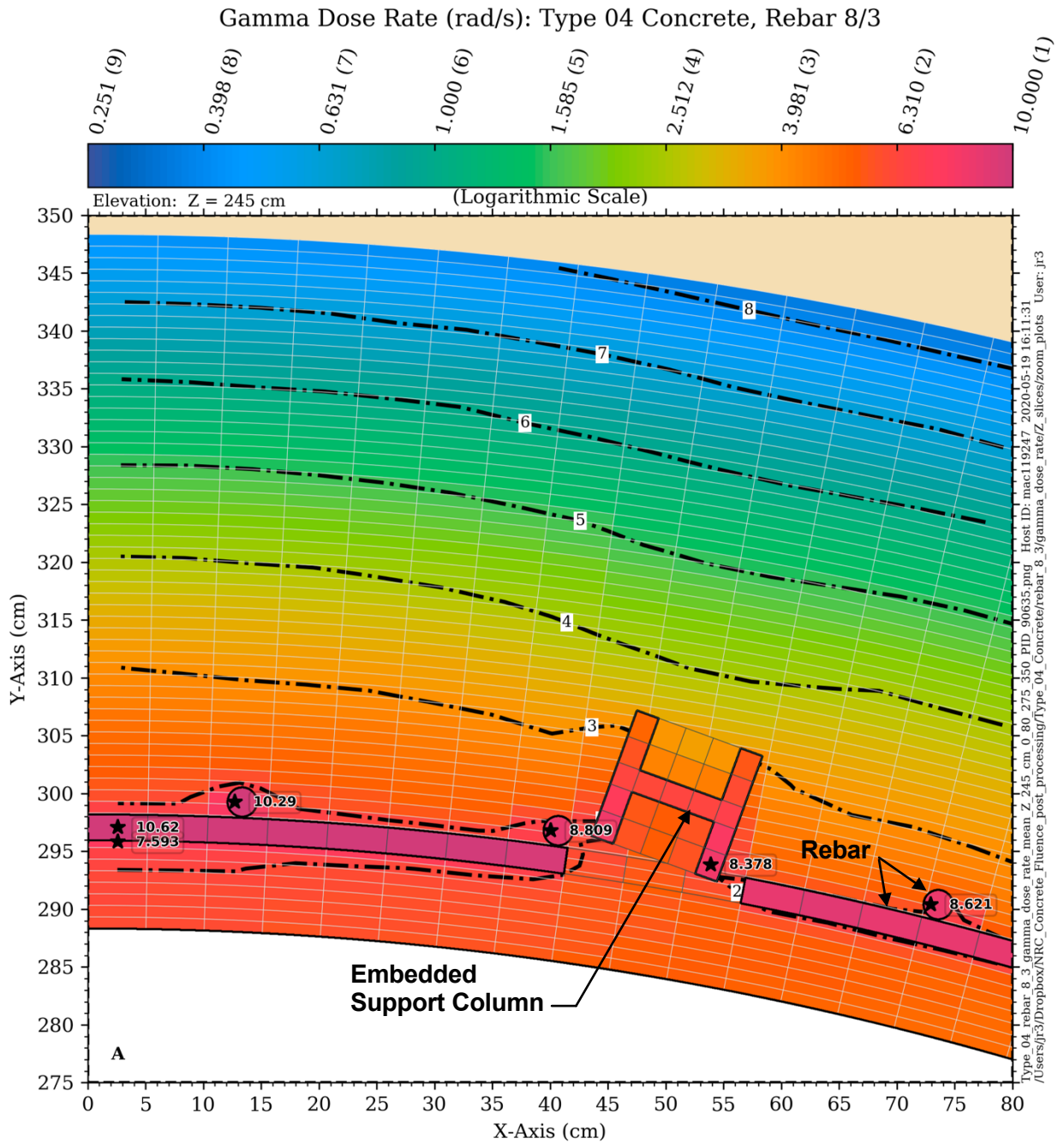

Figure B-4 Gamma Dose Rate (rad/s) at an Elevation of 245 cm (Type 04 concrete with #8 rebar and a three-inch concrete cover. The data is based on cylindrical mesh tallies for the hoop and vertical rebar and a cartesian mesh tally for the support column. The value shown for each mesh cell is the average gamma dose rate in that cell. The values marked with a star are the maximum gamma dose rates in the concrete, rebar hoop, vertical rebar, and embedded support column. Note the 'break' in the rebar hoop to avoid interference with the support column.)

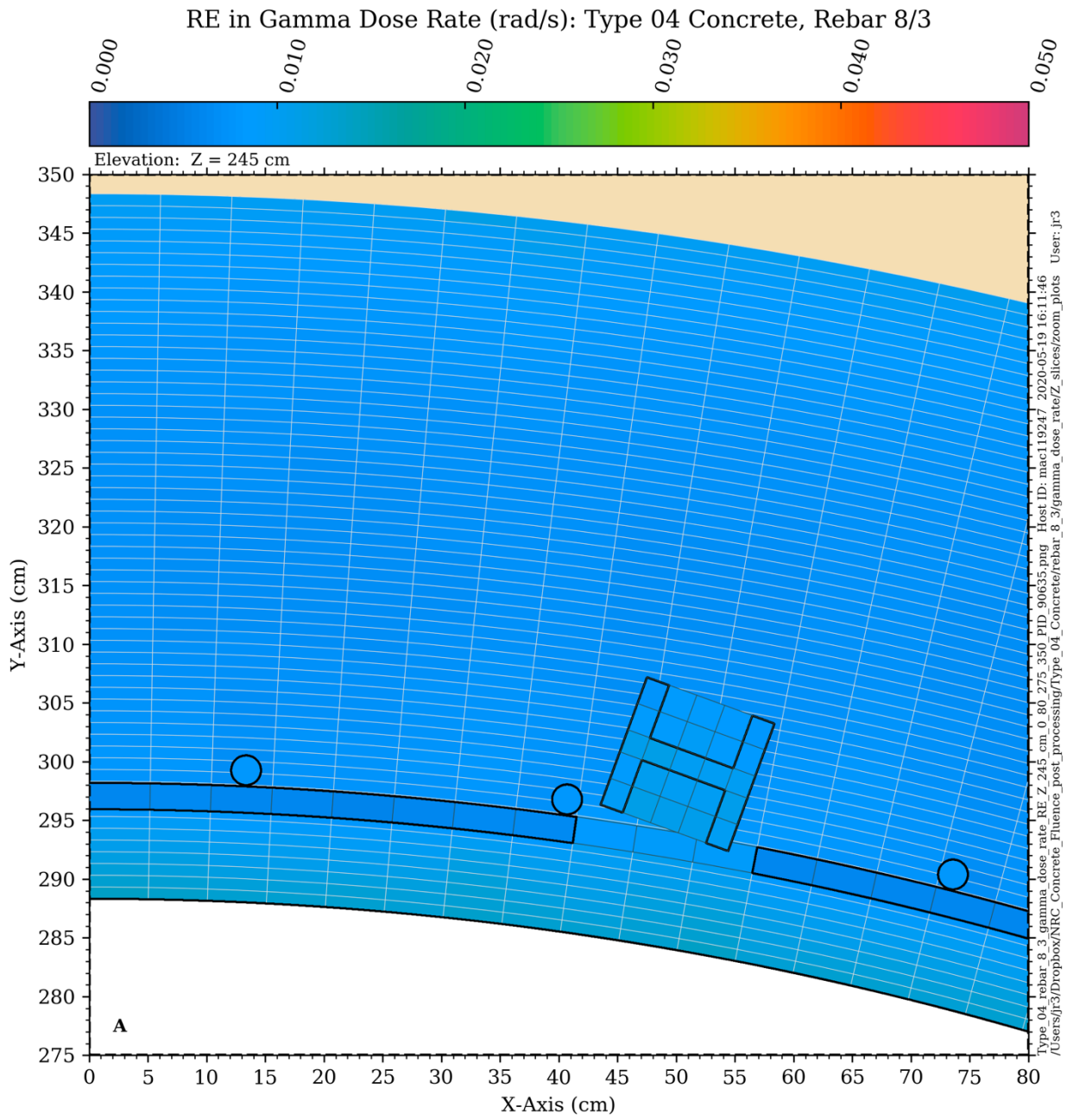

Figure B-5 Relative Error in the Gamma Dose Rate at an Elevation of 245 cm (Type 04 concrete with #8 rebar and a three-inch concrete cover. The data is based on cylindrical mesh tallies for the hoop and vertical rebar and a cartesian mesh tally for the support column. The value shown for each mesh cell is the relative error (RE) at the 1σ level in that cell.)

NRC FORM 335
(12-2010)
NRCMD 3.7

U.S. NUCLEAR REGULATORY COMMISSION

BIBLIOGRAPHIC DATA SHEET

(See instructions on the reverse)

1. REPORT NUMBER
(Assigned by NRC, Add Vol., Supp., Rev., and Addendum Numbers, if any.)

NUREG/CR-7281

2. TITLE AND SUBTITLE

Radiation Evaluation Methodology for Concrete Structures

3. DATE REPORT PUBLISHED

MONTH	YEAR
July	2021

4. FIN OR GRANT NUMBER

5. AUTHOR(S)

J. Risner, A. Alpan, and J. Yang

6. TYPE OF REPORT

Technical

7. PERIOD COVERED (Inclusive Dates)

8. PERFORMING ORGANIZATION - NAME AND ADDRESS (If NRC, provide Division, Office or Region, U. S. Nuclear Regulatory Commission, and mailing address; if contractor, provide name and mailing address.)

Oak Ridge National Laboratory
Oak Ridge, TN 37831-6283

9. SPONSORING ORGANIZATION - NAME AND ADDRESS (If NRC, type "Same as above", if contractor, provide NRC Division, Office or Region, U. S. Nuclear Regulatory Commission, and mailing address.)

Division of Engineering
Office of Research
U.S. Nuclear Regulatory Commission
Washington, D.C. 20555-0001

10. SUPPLEMENTARY NOTES

M. Sircar

11. ABSTRACT (200 words or less)

The ability to accurately calculate neutron fluence levels, radiation heating rates (neutron and gamma), and gamma dose rates in the concrete biological shields (bioshields) of light water reactors has become increasingly important as plant life extensions of 60 years have become common and extensions to 80 years of operation are proceeding This study evaluates the impact of concrete composition, the size and location of reinforcing steel, the presence of a bioshield liner or reflective thermal insulation, and the size of the reactor cavity gap on neutron flux, total heating rate (the rate of radiation energy deposition), and gamma dose rate using parametric studies with a representative three-loop pressurized water reactor (PWR) model. The analyses are performed using state-of-the-art hybrid radiation transport calculations, which provide the ability to explicitly model complex geometries and eliminate the discretization effects in space, energy, and angle that are present in the commonly used discrete ordinates transport methodology. The results of these analyses provide insights into the effect of material and geometrical variations in the representative PWR model on the magnitude of the neutron flux, heating rate, and gamma dose rate incident to the bioshield as well as their attenuation through the reinforced concrete structure.

12. KEY WORDS/DESCRIPTORS (List words or phrases that will assist researchers in locating the report.)

neutron fluence
gamma dose rate
radiation heating
concrete bioshield
subsequent license renewal

13. AVAILABILITY STATEMENT

unlimited

14. SECURITY CLASSIFICATION

(This Page)
unclassified

(This Report)
unclassified

15. NUMBER OF PAGES

16. PRICE

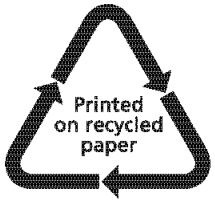

Federal Recycling Program

UNITED STATES
NUCLEAR REGULATORY COMMISSION
WASHINGTON, DC 20555-0001

OFFICIAL BUSINESS